Search for Singly Produced Vector-Like Down-Type Quarks in Single-Lepton Final States with ATLAS

Dissertation
zur Erlangung des akademischen Grades

doctor rerum naturalium

(Dr. rer. nat.)

im Fach Physik

Spezialisierung: Experimentalphysik

eingereicht an der

Mathematisch-Naturwissenschaftlichen Fakultät
der Humboldt-Universität zu Berlin

von

M.Sc. Laura Rehnisch

Präsident der Humboldt-Universität zu Berlin
Prof. Dr. Jan-Hendrik Olbertz

Dekan der Mathematisch-Naturwissenschaftlichen Fakultät
Prof. Dr. Elmar Kulke

Gutachter/innen:	1. Prof. Dr. Heiko Lacker
	2. Prof. Dr. Arno Straessner
	3. Prof. Dr. Johannes Haller
Tag der mündlichen Prüfung:	15.02.2016

Für Papa.

Abstract

A search for vector-like and excited down-type ($Q = \pm 1/3$) quarks with the ATLAS detector is presented in this thesis. The existence of these quarks is predicted by various models beyond the Standard Model, motivated by some limitations of that theory. Quarks from two specific models, b^* and B, are searched for in single production mode, as this is predicted to yield higher cross-sections than pair production in the investigated mass range. The search focuses on decays of the heavy quarks to a W boson and a top quark, the latter of which subsequently decays almost exclusively into another W boson and a bottom quark. Requiring one of the two W bosons to decay leptonically leads to final states containing exactly one lepton (electron or muon in this case), several jets, one of which can be identified as originating from a bottom quark, and some amount of missing energy in the transverse plane stemming from the neutrino of the leptonic W decay. The reconstructed mass of the heavy quark is used to discriminate between signal and background.
This search was performed on $20.3\,\mathrm{fb}^{-1}$ of proton-proton collision data collected at the Large Hadron Collider in the year 2012 with a centre-of-mass energy of 8 TeV. No significant excess of the data over the background could be observed and therefore exclusion limits were set on model parameters. The search presented here makes use of the boosted event topology that is prominent in the explored range of signal masses, allowing it to by far exceed the exclusion bounds obtained in the preceding search for the b^* model on the 2011 data set, and producing results that are comparable to those from a recent search performed with the CMS detector on the 2012 data set. Additionally, it is the first search in the single production mode for the B model.

Zusammenfassung

In dieser Arbeit wird die Suche nach vektorartigen und angeregten Quarks mit einer elektrischen Ladung von $Q = \pm 1/3$ mit dem ATLAS-Detektor vorgestellt. Die Existenz solcher Quarks wird von verschiedenen Modellen jenseits des Standardmodells vorhergesagt, die bestimmte Schwächen der Theorie beseitigen können. Es wird nach der Einzelproduktion von Quarks aus zwei verschiedenen Modellen, b^* und B, gesucht, da für diesen Produktionsmodus höhere Wirkungsquerschnitte im untersuchten Massenbereich vorhergesagt sind als für die Paarproduktion. Die Suche beschränkt sich auf Zerfälle der neuen Quarks in W-Bosonen und Top-Quarks, wobei letztere wiederum fast ausschließlich in W-Bosonen und Bottom-Quarks zerfallen. Verlangt man nun, dass eines der W-Bosonen leptonisch zerfällt, erhält man Endzustände mit einem Lepton (Elektron oder Myon in diesem Fall), mehreren Jets, von denen einer als von einem Bottom-Quark stammend identifiziert werden kann, und fehlender Energie in der Transversalebene, die durch das beim leptonischen Zerfall entstandene und nicht detektierbare Neutrino hervorgerufen wird. Die daraus berechnete invariante Masse des neuen Quarks wird zur Unterscheidung zwischen Signal und Untergrund verwendet.

Die Suche wurde auf dem am Large Hadron Collider im Jahr 2012 aufgenommenen $20.3\,\mathrm{fb}^{-1}$ großen Datensatz von Proton-Proton-Kollisionen bei einer Schwerpunktsenergie von $8\,\mathrm{TeV}$ ausgeführt. Es wurde kein signifikanter Unterschied zum vorhergesagten Untergrund gemessen und deshalb Ausschlussgrenzen für Parameter der untersuchten Modelle berechnet. Da die vorgestellte Suche Gebrauch von der *geboosteten* Topologie der Signalereignisse im untersuchten Massenbereich macht, übertreffen die Ergebnisse bei Weitem die Ausschlussgrenzen für b^*, die in der Vorgängersuche auf dem Datensatz von 2011 erhalten wurden und sind vergleichbar mit kürzlich auf dem Datensatz von 2012 mit dem CMS-Detektor gewonnenen Ergebnissen. Darüber hinaus ist es die erste Suche nach einzeln produzierten B-Quarks.

Contents

List of Figures

Chapter 1.

Introduction

With the start of its operation in the year 2009, the Large Hadron Collider (LHC) has provided an insight into by then unexplored energy regimes and thus opened up a field of measurements and searches in particle physics with unprecedented accuracy and reach with centre-of-mass energies up to 8 TeV and instantaneous luminosities of up to $8 \times 10^{33}\,\mathrm{cm}^{-2}\mathrm{s}^{-1}$ in the first years of operation. The two main goals of the two general-purpose detectors at the LHC, ATLAS (A Large Toroidal LHC ApparatuS [1]) and CMS (Compact Muon Solenoid [2]), are precision measurements of quantities predicted by the Standard Model of particle physics, as well as searches for new physics phenomena. The Standard Model is an experimentally well-tested theory, which has been supported by numerous measurements performed by various experiments. One long sought-after goal to make the picture of the Standard Model complete was achieved in 2012, when both, ATLAS and CMS, declared the discovery of a Higgs-like boson [3, 4]. Intense investigations which are still ongoing, have strengthened the evidence that it indeed is the boson predicted by the Standard Model.
However, even though the theory is mature and in most parts well-tested, it still leaves open several unanswered questions. For example, it is lacking an explanation why the Higgs mass of about 125 GeV [5], compared to the Planck mass, is as small as the experiments have shown, and the vacuum expectation value – the minimum of the vacuum energy of the Higgs field – is so low, an effect also known as the hierarchy or naturalness problem. This problem is addressed by various models beyond the Standard Model which predict new physics phenomena at the TeV scale.
Many of these models predict new fermionic particles, which can have both, left-handed and right-handed couplings to the W boson. These so-called vector-like quarks [6] are colour-triplets and, depending on the model, can occur in singlets or multiplets and with

different electric charges.
As the Yukawa coupling of the top quark is quite large, the above mentioned models provide a sizeable mixing of the new quarks with the third family of the Standard Model. Hence, searches for such particles make use of the decay topologies of the top and the bottom quark.
Vector-like quarks appear in a variety of models, some of which also predict excited quarks. While excited quarks are singly-produced in strong interactions via an anomalous coupling to gluons, vector-like quarks can be produced in pairs at the LHC via the strong interaction or singly via the weak interaction, the latter process being dominant at higher vector-like quark masses. In both cases, the production is followed by a decay of the new heavy quark to Standard Model particles and gauge or Higgs bosons.
In this thesis, a search for single production of vector-like and excited quarks with an electric charge of $\pm 1/3$ is presented, which subsequently decay into a top quark and a W boson. The top quark itself decays to another W boson and a b-quark in nearly 100% of the cases. Events with exactly one lepton (an electron or a muon) are selected, requiring one of the W bosons to decay leptonically, while the other W boson decays hadronically. In addition, the events are required to contain 2 or 3 jets emerging from the hadronic decay products of the daughter particles, and some amount of missing energy in the transverse plane, caused by the neutrino from the leptonic W decay which due to its long interaction length escapes the detection. The search is performed using $20.3\,\mathrm{fb}^{-1}$ of proton-proton data collected with the ATLAS experiment at a centre-of-mass energy of 8 TeV during the year 2012. Two different new heavy particles are searched for: The excited quark b^* [7] with vector-like couplings and the vector-like quark B [8], which are predicted by different models, but have very similar decay kinematics making a combined search possible. The only difference, which is taken into account in the selection criteria, is the presence of additional jets in the B case, which are very likely to have low transverse momenta and will therefore be found close to the beam axis. These so-called forward jets emerge from the t-channel production of the B quark, while the b^* quark is produced via an s-channel process.
While a search for b^* with subsequent decay to W boson and top quark has been carried out by ATLAS using the 7 TeV data set collected in 2011 [9] and by CMS using the 8 TeV data set [10], all previous searches for B focused on pair production, and the search presented in this thesis is the first one for single production of B. As the existence of both types of quarks has been excluded for lower masses by previous searches, the higher mass range, especially above 1 TeV, opens up the possibility to make use of the boosted event topologies

which arise when the decay products of a high-momentum particle are more and more collimated, such that hadronic decay products can no longer be resolved as separate jets in the detector, but are merged into one. This effect is made use of in this analysis by asking for the presence of a high-momentum jet with a large radius and by applying selection criteria on angular distances between the different objects in the events, which enhance the fraction of boosted events. As a result, the background-to-signal ratio can be well reduced, as such events are rare in the SM.

The largest part of the irreducible background comes from top-quark pair production, followed by associated production of a W boson and jets and by single-top production in the Wt channel. Minor backgrounds are production of Z bosons in association with jets, production of two gauge bosons (ZZ, WZ, WW) and QCD multijet events events, where one jet is misreconstructed as a lepton. Except for the QCD multijet background, which is determined via a data-driven method, the background processes are modelled using Monte-Carlo simulations. The normalisation of the simulated backgrounds is obtained by a fit of the background-only hypothesis to data in kinematic regions depleted from potential signal contributions. In order to show that the two main backgrounds are well understood, two regions are defined which are enriched with either top-quark pair production or W+jets events. The background and data spectra are also fed into the binned likelihood fit, which – in the absence of a data excess – is used to set a limit on the mass and/or coupling parameters of the new quarks.

This thesis is organised in the following way: Chapter 2 gives an overview over the theoretical foundations, the models and a more detailed theoretical motivation for such a search. Chapter 3 describes the experimental setup, while Chapter 4 gives some details on data acquisition and reconstruction as well as on event simulation. In Chapter 5 the reconstruction of the physics objects is described, that are used in the analysis, while the analysis strategy and obtained results are discussed in Chapter 6. Eventually, Chapter 7 will summarise the findings and give an outlook for future LHC runs.

Chapter 2.

Theoretical Aspects and Motivation

2.1. The Standard Model

The Standard Model of Particle Physics, which is based on relativistic quantum field theory (which combines special relativity and quantum mechanics), describes the fundamental particles with spin 1/2 and the interactions between them carried by spin 1 gauge bosons. It incorporates the electromagnetic, weak and strong forces and their implications on particle states observed in nature. The Standard Model (SM) was developed as a Yang-Mills gauge theory (a theory with non-Abelian gauge invariance, as discussed further down) [11] based on the special unitary symmetry groups $SU(N)$. According to Noether's theorem [12], symmetries are connected to conserved quantities. In the SM, these symmetries are gauge symmetries of the quantum fields, while the conserved quantities are different kinds of charges that allow for interactions of the fields. For a particle to be able to take part in a given interaction, it has to carry the corresponding charge. The reason for using unitary groups is the requirement that the norm be conserved, such that the probability of a state $|\psi\rangle$ under a gauge transformation $\mathcal{M}$ is invariant:

$$\langle\psi|\psi\rangle \stackrel{!}{=} \langle\psi|\mathcal{M}^\dagger\mathcal{M}|\psi\rangle \Rightarrow \mathcal{M}^\dagger\mathcal{M} = \mathbb{1}. \tag{2.1}$$

The specific gauge group of the SM is

$$SU(3)_C \otimes SU(2)_L \otimes U(1)_Y, \tag{2.2}$$

where $SU(3)_C$ describes the strong interaction based on the colour charge (C) and $SU(2)_L \otimes U(1)_Y$ describes the unification of the electromagnetic and weak interactions (EW theory), which was developed by Glashow, Weinberg and Salam [13]. Y denotes the weak hypercharge, the generator of the $U(1)$ group, and L denotes the coupling to left-handed fermions only. Left- and right-handed components of spinors ψ are defined by the left- and right-handed projection operators in the following way:

$$\psi_L = P_L\psi = \frac{1-\gamma^5}{2}\psi, \tag{2.3}$$

$$\psi_R = P_R\psi = \frac{1+\gamma^5}{2}\psi. \tag{2.4}$$

The fermions described by the SM can be divided into two main groups: six quarks that carry a colour charge and therefore take part in the strong interaction and six colourless leptons. The leptons themselves can be sub-divided into three charged and three neutral ones (neutrinos), while all quarks carry electric charges which are multiples of 1/3 of the elementary charge. Each of these particles has an associated anti-particle with the same mass and spin, but reversed additive quantum numbers like e.g. electrical charge. Anti-quarks additionally carry anti-colour.
In addition to quarks and leptons, which are organised in three families (also denoted as generations) with increasing mass, the SM also contains several gauge bosons, with different electric and colour charges. Figure 2.1 gives an overview over the particle content, listing also mass, spin and electrical charge. Neutrinos were believed to be massless for a long time, but the observation of neutrino oscillations shows that they need to have non-vanishing masses. As of today, no exact values for the neutrino masses are known, however, and the limits deduced in experiments involving the respective lepton flavour are shown in Figure 2.1 as well.

Ordinary matter is only made of fermions from the first generation, as atoms contain electrons and nuclei consisting of neutrons (quark content udd) and protons (uud)[1]. Electron neutrinos are emitted in β decays, e.g. when a neutron transforms into a proton via the emission of an electron and an electron anti-neutrino. Particles of the second and third

[1]These so-called valence quarks, which fix the quantum numbers of the nuclei, are surrounded with an infinite number of virtual quarks and anti-quarks of all possible flavours, the so-called sea quarks, which arise from gluon splittings.

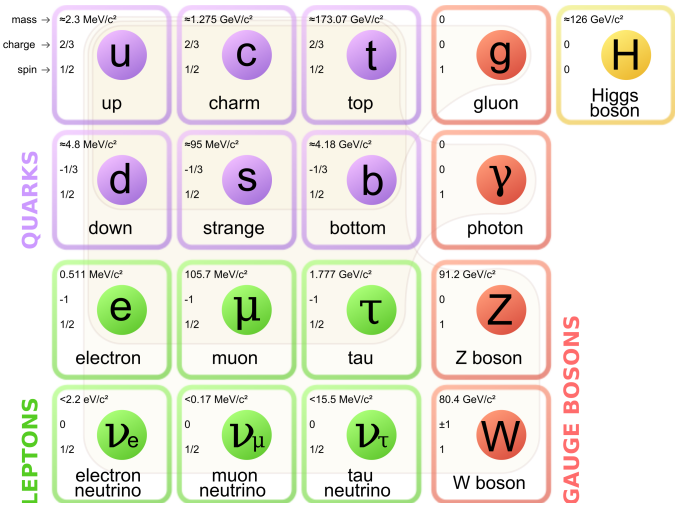

Figure 2.1.: Particle content of the Standard Model [14].

generation do not exist under normal conditions on earth and have to be produced in the laboratory, such as in collider experiments, in order to study them. The fact that the quarks of the higher families have larger masses, is also reflected in their later discoveries. As the last one to complete the picture that we have today, the top quark was experimentally observed only in 1995.

The forces among quarks and leptons can be described as mediated via several gauge bosons, which are also shown in Figure 2.1: The electromagnetic interaction can be described the exchange of virtual massless photons, γ, the weak interaction as the exchange of virtual massive charged (W^+, W^-) or neutral (Z^0) bosons and the strong interaction as an exchange of virtual massless gluons, g. While the strong interaction is limited to quarks and gluons, all quarks and charged leptons take part in the electromagnetic interaction and all quarks and leptons are affected by the weak interaction. The formalism of the fundamental interactions is described in more detail in the following sections. Most of the information there is taken from [15] and the notation therein is mainly adopted.
The remaining particle in Figure 2.1, the Higgs boson H, is the excitation of an ubiquitous scalar field, which plays an important role for the validity of the SM and is described further down in section 2.1.2.

It is important to note that the SM is a renormalisable quantum field theory. This means, that physical observables do not depend on UV modes of their radiative corrections and that singularities in those quantum corrections to masses or coupling strengths arising from integration over all energy scales can be subtracted by factorising the finite from the divergent parts of the integrals and subtracting the divergent parts by introducing appropriate counter terms. In the following section, the formalism of the different parts of the theory are introduced in more detail.

2.1.1. Electroweak Interaction

The electroweak theory is a generalisation of quantum electrodynamics and the weak interaction based on the symmetry group $SU(2)_L \otimes U(1)_Y$. This unified theory was developed by Glashow [16], Salam [17] and Weinberg [13] in the 1960s and is therefore also referred to as *GSW model*. The associated charges with this interaction are the weak isospin I and the hypercharge Y. In charged- and neutral-current interactions, involving left-handed particles, the hypercharge and the third component of the weak isospin are conserved quantities. The weak isospin is a concept analogous to isospin of nuclei. Left-handed fermions are grouped into weak isospin doublets within one family of quarks or leptons ($I = 1/2$). The third component of the weak isospin is defined to be $I_3 = +1/2$ for up-type quarks and neutrinos and $I_3 = -1/2$ for down-type quarks and charged leptons. Right-handed fermions are weak isosinglets ($I = 0$), the electroweak theory is therefore considered a chiral theory. The hypercharge Y is derived from the electric charge Q and the third component of the weak isospin as $Y = 2Q - 2I_3$, which means that within one doublet, the hypercharge is the same for both particles ($Y = 1/3$ for quarks and $Y = -1$ for leptons), as $\Delta Q = 1$ within one doublet. Flavour changing transitions from one particle of a doublet to the other one are possible by changing the third component of the weak isospin by $|\Delta I_3| = \pm 1$, which is realised by emitting a $W^{\pm}$ boson, the mediator of the weak interaction, with $I = 1$. The electromagnetic interaction is mediated by massless photons, γ, which couple to electrically charged particles. Table 2.1 summarises the electroweak quantum numbers of all fermions in the Standard Model.

In order to understand the formalism, it is a natural choice to start from the quantum field theory of purely electromagnetically interacting particles, the so-called quantum

Table 2.1.: SM fermions and their electroweak quantum numbers: electric charge Q, weak isospin I and its third component I_3 and hypercharge Y. Left-handed fermions carry a weak isospin of $1/2$ and are thus organised in weak isodoublets, while right-handed fermions are weak isosinglets.

Fermion fields			Q	I	I_3	Y
$\begin{pmatrix} u \\ d \end{pmatrix}_L$	$\begin{pmatrix} c \\ s \end{pmatrix}_L$	$\begin{pmatrix} t \\ b \end{pmatrix}_L$	$+2/3$ $-1/3$	$1/2$	$+1/2$ $-1/2$	$1/3$
u_R	c_R	t_R	$+2/3$	0	0	$+4/3$
d_R	s_R	b_R	$-1/3$	0	0	$-2/3$
$\begin{pmatrix} \nu_e \\ e \end{pmatrix}_L$	$\begin{pmatrix} \nu_\mu \\ \mu \end{pmatrix}_L$	$\begin{pmatrix} \nu_\tau \\ \tau \end{pmatrix}_L$	0 -1	$1/2$	$+1/2$ $-1/2$	-1
e_R	μ_R	τ_R	-1	0	0	-2

electrodynamics (QED) and only later move on to also include the weak interaction.
From Noether's theorem we know that symmetries are related to conserved physical quantities. For example, the Lagrangian density (short: Lagrangian) of a free fermion,

$$\mathcal{L} = i\bar{\psi}\gamma_\mu\partial^\mu\psi - m\bar{\psi}\psi, \tag{2.5}$$

is invariant under the phase transition

$$\psi(x) \to e^{i\alpha}\psi(x) \tag{2.6}$$

of the complex fermion field ψ, with a global phase α. As this phase cannot be measured, it has no physical meaning and can thus be fixed for all space and time, which leads to the term *global gauge invariance*. Phase transformations with just one single parameter are part of the $U(1)$ group, the unitary Abelian symmetry group QED is based on.
However, when requiring the Lagrangian to be invariant also under local phase (or *gauge*) transformations, i.e. with a space-time dependent phase $\alpha(x)$, this statement no longer holds. As the transformation law is now different for each point in space-time, the derivative loses its physical meaning. To restore it, a factor compensating for the difference in phase transformations from one point to the next (a so-called comparator) has to be introduced,

with the help of which a *covariant derivative* D_μ of the form

$$D_\mu \equiv \partial_\mu - iqA_\mu \tag{2.7}$$

is defined in order to replace ∂_μ. It transforms covariantly under phase transitions, just like ψ:

$$D_\mu \psi(x) \to e^{i\alpha(x)} D_\mu \psi(x). \tag{2.8}$$

It contains the charge q and the newly introduced vector field A_μ, that transforms in such a way, that the terms cancel, which were previously breaking the invariance,

$$A_\mu \to A_\mu - \frac{1}{q}\partial_\mu \alpha(x), \tag{2.9}$$

and is therefore called a *gauge field*. It can be thought of as the physical photon field, but then a kinetic term needs to be added to the Lagrangian. As this term has to be invariant under Eq. 2.9, and from the properties of the introduced comparator, if follows that the kinetic term has to involve the gauge invariant field strength tensor

$$F_{\mu\nu} = \partial_\mu A_\nu - \partial_\nu A_\mu. \tag{2.10}$$

The complete local gauge invariant Lagrangian of QED therefore reads:

$$\mathcal{L} = \bar{\psi}(i\gamma^\mu \partial_\mu - m)\psi + q\bar{\psi}\gamma^\mu A_\mu \psi - \frac{1}{4} F_{\mu\nu} F^{\mu\nu}. \tag{2.11}$$

It should be noted that no mass term can be added for A_μ without violating the gauge invariance, which is in accordance with our observation that photons are massless.
In a similar fashion, a gauge theory can be built around the combined symmetry group $SU(2)_L \otimes U(1)_Y$ of the unified electroweak interaction. The generators of the $SU(2)_L$ group, T^a, can be expressed by the Pauli matrices σ_a via $T^a = \sigma_a/2$ $(a = 1, 2, 3)$. It is important to note that the symmetry group is non-Abelian, as the generators (and as a consequence all elements of the group) do not commute with one another:

$$\left[T^a, T^b\right] = i\epsilon^{abc} T^c, \tag{2.12}$$

with ϵ^{abc} being the structure constant of the group. The weak isospin Y is the generator of the $U(1)_Y$ group. The phase $\alpha(x)$, which was already introduced above, is now complemented with the analogous phase of $SU(2)_L$, that has to be a 3-component vector: $\vec{\beta}(x)$, such that the final local gauge transformations of $SU(2)_L \otimes U(1)_Y$ acting on left- and right-handed spinors ψ_L and ψ_R read:

$$\begin{aligned} \psi_L(x) &\to e^{ig\vec{\beta}(x)\vec{T}+ig'\alpha(x)Y}\psi_L(x), \\ \psi_R(x) &\to e^{ig'\alpha(x)Y}\psi_R(x). \end{aligned} \tag{2.13}$$

In equations 2.13, the coupling strengths g and g' have been factored out of the phases $\alpha(x)$ and $\vec{\beta}(x)$, in order to underline the different strengths of the two interactions. An important point to notice is that the $SU(2)_L$ part of the unified interaction does not act on right-handed spinors, which makes the weak interaction a chiral theory.
As the Lagrangian again is not invariant under this transformation, a covariant derivative has to be introduced, similar to the pure $U(1)$ case:

$$D_\mu \equiv \partial_\mu + igW_\mu^a T^a + ig'\frac{1}{2}YB_\mu. \tag{2.14}$$

W_μ^a and B_μ are the newly introduced gauge fields for $SU(2)_L$ and $U(1)_Y$, respectively. They transform under $SU(2)_L \otimes U(1)_Y$ as

$$\begin{aligned} W_\mu^a &\to W_\mu^a + \frac{1}{g}\partial_\mu\beta^a + \epsilon^{abc}W_\mu^b\beta^c \\ B_\mu &\to B_\mu + \frac{1}{g'}\partial_\mu\alpha^a. \end{aligned} \tag{2.15}$$

Analogous to the $U(1)$ case, two corresponding kinetic terms are needed as well to give the gauge fields physical meanings:

$$\mathcal{L}_{W,B}^{kin} = -\frac{1}{4}W_{\mu\nu}^a W^{\mu\nu,a} - \frac{1}{4}B_{\mu\nu}B^{\mu\nu}. \tag{2.16}$$

They contain the field tensors

$$\begin{aligned} B_{\mu\nu} &= \partial_\mu B_\nu - \partial_\nu B_\mu \text{ and} \\ W_{\mu\nu}^a &= \partial_\mu W_\nu^a - \partial_\nu W_\mu^a - g\epsilon^{abc}W_\mu^b W_\mu^c. \end{aligned} \tag{2.17}$$

The last term of $W^a_{\mu\nu}$ arises from the non-Abelian nature of $SU(2)_L$. With the kinetic terms, the four gauge fields can be interpreted as the fields of the gauge bosons of the electroweak interaction.
Assuming massless spinor fields, all described ingredients lead to the local gauge invariant Lagrangian of the EW theory:

$$\begin{aligned}\mathcal{L}_{EW} = \bar{\psi}_L \gamma^\mu \left[\partial_\mu + igW^a_\mu T^a + ig' \frac{Y_L}{2} B_\mu\right] \psi_L + \bar{\psi}_R \gamma^\mu \left[\partial_\mu + ig' Y_R B_\mu\right] \psi_R \\ - \frac{1}{4} B_{\mu\nu} B^{\mu\nu} - \frac{1}{4} W^a_{\mu\nu} W^{\mu\nu,a}.\end{aligned} \tag{2.18}$$

2.1.2. Generation of Particle Masses

As stated earlier, the renormalisability of the SM is an important property of the theory. It was indeed shown by t'Hooft [18] and Veltman that any Yang-Mills theory with massless gauge bosons is renormalisable. Indeed, the Lagrangian of the EW interaction (Eq. 2.18) does not contain mass terms for the gauge bosons, as they would violate the gauge invariance under $SU(2)_L \otimes U(1)_Y$ transformations. A similar reasoning is applicable to fermions ψ, for which a simple Dirac mass term $\Delta\mathcal{L}_{Dirac} = -m_\psi \bar{\psi}\psi = -m_\psi(\bar{\psi}_L \psi_R + \bar{\psi}_R \psi_L)$ would break $SU(2)_L$ symmetry as well, due to the different transformation properties of the left- and right-handed components.
However, as stated above, the observed particles described by the SM have non-vanishing masses, except for the massless gluon and photon. This should lead to the conclusion that $SU(2)_L$, associated with massive mediator particles, is not a symmetry of nature. Another interpretation, avoiding the need to discard $SU(2)_L$ as a fundamental symmetry, is that there must be a mechanism that spontaneously breaks this symmetry. This is done by the *Higgs mechanism*, which was proposed independently by Brout and Englert [19], Higgs [20] and Hagen, Guralnik and Kibble [21] in 1962. The main idea is that the gauge bosons obtain their masses by spontaneous symmetry breaking and coupling to a scalar field, the so-called Higgs field. Interactions with this field are also responsible for the masses of the fermions via the so-called *Yukawa coupling*. The details of the formalism are discussed in the following.

Gauge Boson Masses

The first ingredient for the generation of the masses of W and Z bosons is the introduction of an additional global $SU(2)_L$ gauge invariant term $\Delta\mathcal{L}_\Phi$ to the electroweak Lagrangian in Eq. 2.18:

$$\Delta\mathcal{L}_\Phi = (D_\mu\Phi)^\dagger(D^\mu\Phi) - V(\Phi^\dagger\Phi), \tag{2.19}$$

with Φ being an $SU(2)_L$ doublet of scalar fields

$$\Phi = \begin{pmatrix}\Phi_a \\ \Phi_b\end{pmatrix} = \frac{1}{\sqrt{2}}\begin{pmatrix}\Phi_1 + i\Phi_2 \\ \Phi_3 + i\Phi_4\end{pmatrix}, \tag{2.20}$$

and the potential (later to be known as Higgs potential)

$$V(\Phi^\dagger\Phi) = \mu^2\Phi^\dagger\Phi + \lambda(\Phi^\dagger\Phi)^2, \tag{2.21}$$

the first term of which is a mass term (with μ^2 having units of mass squared) and the second one describes the self-interaction of the field Φ (λ being a parameter denoting the strength of quartic self-interactions). In order to make the Lagrangian of this scalar field (Eq. 2.19), which is invariant under global $SU(2)_L$ transformations, also invariant under local gauge transformations, a covariant derivative D_μ and three gauge fields W_μ^a are introduced. With help of this Lagrangian, mass generation of the gauge bosons can be explained without spoiling the $SU(2)_L$ gauge symmetry. In order to do this, however, some considerations of the potential are necessary:
In the interesting case $\mu^2 < 0$ and $\lambda > 0$, the vacuum expectation value of Φ is non-zero, as the minimum of the potential V is sitting at the vacuum state Φ_{vac} with

$$|\Phi_{vac}| = \sqrt{-\frac{\mu^2}{\lambda}}. \tag{2.22}$$

This ground state violates $SU(2)_L$ symmetry, which is why this mechanism is called *spontaneous symmetry breaking*.
The field Φ can now be expanded around its minimum, which in *unitary gauge* [22, p. 175]

can be chosen as

$$\begin{aligned} \Phi_1 = \Phi_2 = \Phi_4 = 0 \text{ and} \\ \Phi_3^2 = -\frac{\mu^2}{\lambda} \equiv v, \end{aligned} \tag{2.23}$$

where v denotes the vacuum expectation value. The vacuum state, about which Φ is expanded, therefore is

$$\Phi_0 \equiv \sqrt{\frac{1}{2}} \begin{pmatrix} 0 \\ v \end{pmatrix}. \tag{2.24}$$

At first order, Φ only consists of the (Higgs) field $h(x)$, which describes a shift from the vacuum:

$$\Phi(x) = \sqrt{\frac{1}{2}} \begin{pmatrix} 0 \\ v + h(x) \end{pmatrix}. \tag{2.25}$$

Substituting this new field Φ into the extended Lagrangian $\mathcal{L} = \mathcal{L}_{EW} + \mathcal{L}_{\Phi}$ leads to a mass term for the Higgs field $h(x)$ and mass terms for the three W_μ^a, that can be identified as longitudinal polarisations of the $W^\pm$ and Z bosons. The mass term in the Lagrangian becomes

$$\begin{aligned} |(-igT^a W_\mu^a - ig' B_\mu Y)\Phi|^2 = (\frac{1}{2}vg)^2 W_\mu^+ W^{\mu,-} \\ + \frac{1}{8}v^2 (W_\mu^3, B_\mu) \underbrace{\begin{pmatrix} g^2 & -gg' \\ -gg' & g'^2 \end{pmatrix}}_{\text{mass matrix}} \begin{pmatrix} W^{3,\mu} \\ B^\mu \end{pmatrix} \end{aligned} \tag{2.26}$$

with the massive fields

$$W_\mu^\pm = \frac{1}{\sqrt{2}}(W_\mu^1 \mp i W_\mu^2), \tag{2.27}$$

which can be interpreted as $W^\pm$ bosons with mass $m_W = vg/2$. One should notice that in Eq. 2.26 $W^{3,\mu}$ and B^μ are no fields of defined mass as the mass matrix is not diagonal.

Diagonalisation leads to the expression

$$\begin{pmatrix} A_\mu \\ Z_\mu \end{pmatrix} = \begin{pmatrix} cos\theta_W & sin\theta_W \\ -sin\theta_W & cos\theta_W \end{pmatrix} \begin{pmatrix} B_\mu \\ W^3_\mu \end{pmatrix} \tag{2.28}$$

relating the physical fields of a massless photon (A_μ) and a massive Z boson (Z_μ with mass $m_Z = \sqrt{g^2 + g'^2}v/2$) with the previously introduced fields via the Weinberg angle θ_W, which is connected to the coupling strengths g and g' and the electric charge e via

$$e = gsin\theta_W = g'cos\theta_W. \tag{2.29}$$

All massive gauge bosons now have mass terms and the resulting Lagrangian is invariant under $SU(2)_L \otimes U(1)_Y$ transformations.
Additionally, one can calculate the energy of the vacuum expectation state via $m_W = vg/2$, using the measured values of the Weinberg angle, the electric charge and the W boson mass to be

$$v = \frac{2m_W}{g} = \frac{2m_W sin\theta_W}{e} \approx 246\,\text{GeV}. \tag{2.30}$$

Fermion Masses

A similar strategy as for the masses of the gauge bosons can be employed to generate fermion masses, for which a Dirac mass term in the Lagrangian was forbidden by $SU(2)_L$ gauge invariance as well. A nice feature of the SM is, that for this purpose the same Higgs doublet is sufficient. To generate the mass of a lepton with flavour $\ell = e, \mu, \tau$, the following $SU(2)_L \otimes U(1)_Y$-invariant term is added to the EW Lagrangian:

$$\mathcal{L}_3 = -G_\ell \left[(\bar{\nu}_\ell, \bar{\ell})_L \begin{pmatrix} \Phi_a \\ \Phi_b \end{pmatrix} \ell_R + \bar{\ell}_R (\bar{\Phi}_a, \bar{\Phi}_b) \begin{pmatrix} \nu_\ell \\ \ell \end{pmatrix}_L \right]. \tag{2.31}$$

The doublet has the correct quantum numbers to couple to $\bar{\ell}_L \ell_R$. Analogous to the procedure for gauge boson mass generation, the symmetry is broken and Eq. 2.25 is substituted into

the Lagrangian, which then looks like

$$\mathcal{L}_3 = -\frac{G_\ell}{\sqrt{2}} v(\bar{\ell}_L \ell_R + \bar{\ell}_R e_L) - \frac{G_\ell}{\sqrt{2}}(\bar{\ell}_L \ell_R + \bar{\ell}_R \ell_L) h. \tag{2.32}$$

We can now choose the coupling strength G_ℓ to satisfy

$$m_\ell = \frac{G_\ell v}{\sqrt{2}}, \tag{2.33}$$

such that the lepton mass can be generated via

$$\mathcal{L}_3 = -m_\ell \bar{\ell}\ell - \frac{m_\ell}{v} \bar{\ell}\ell h. \tag{2.34}$$

Analogously, the masses of the quarks are generated. The only difference is that here also right-handed up-type fermions must be considered for mass generation. Thus, a conjugated Higgs doublet needs to be constructed, based on Φ:

$$\Phi_c = -i\tau_2 \Phi^* = \begin{pmatrix} -\bar{\Phi}_a \\ \bar{\Phi}_b \end{pmatrix}, \tag{2.35}$$

(τ_2 denoting the second Pauli matrix) which transforms under $SU(2)$ transformations in the same way as Φ and, when breaking the symmetry, becomes

$$\Phi_c = \frac{1}{\sqrt{2}} \begin{pmatrix} v + h \\ 0 \end{pmatrix}. \tag{2.36}$$

It can thus be used to construct the gauge invariant Lagrangian

$$\begin{aligned} \mathcal{L}_4 = & -Y_d(\bar{u}, \bar{d})_L \begin{pmatrix} \Phi_a \\ \Phi_b \end{pmatrix} d_R - Y_u(\bar{u}, \bar{d})_L \begin{pmatrix} -\bar{\Phi}_a \\ \bar{\Phi}_b \end{pmatrix} u_R + h.c. \\ = & \underbrace{-m_d \bar{d}d - m_u \bar{u}u}_{\text{mass terms}} \underbrace{-\frac{m_d}{v}\bar{d}dh - \frac{m_u}{v}\bar{u}uh}_{\text{interaction terms}} + h.c., \end{aligned} \tag{2.37}$$

with h.c. denoting the hermitian conjugate. However, instead of the mass eigenstates $(u, d)_L$, $(c, s)_L$ and $(t, b)_L$ weak interactions act on the flavour eigenstates (weak eigenstates) $(u, d')_L$, $(c, s')_L$ and $(t, b')_L$, which are linear combinations of the mass eigenstates. This

fact is explained in more detail in section 2.1.3. Considering this, Eq. 2.37 becomes

$$\mathcal{L}_4 = -Y_d^{ij}(\bar{u}_i, \bar{d}'_i)_L \begin{pmatrix} \Phi_a \\ \Phi_b \end{pmatrix} d_{jR} - Y_u^{ij}(\bar{u}_i, \bar{d}'_i)_L \begin{pmatrix} -\bar{\Phi}_a \\ \bar{\Phi}_b \end{pmatrix} u_{jR} + h.c., \tag{2.38}$$

with $i, j = 1, ..., 3$ running over the number of quark doublets. One can then write the quark Lagrangian in diagonal form in the following way:

$$\mathcal{L}_4 = -m_d^i \bar{d}_i d_i \left(1 + \frac{h}{v}\right) - m_u^i \bar{u}_i u_i \left(1 + \frac{h}{v}\right), \tag{2.39}$$

where

$$m_{u/d}^i = Y_{u/d}^i \frac{v}{\sqrt{2}} \tag{2.40}$$

with $Y_{u/d}$ being the so-called *Yukawa coupling* strengths and $v = 246\,\text{GeV}$ the Higgs vacuum expectation value. Adding this quark-mass generating part to the EW Lagrangian as well leaves it invariant under $SU(2)_L \otimes U(1)_Y$ transformations. We thus have a complete description of the electroweak interaction including the Higgs mechanism to generate massive gauge bosons and fermions, as they are observed by experiments. One should note, though, that the theory does not predict the values of the particle masses, as the introduced coupling parameters are arbitrary in size. Despite that fact, the Higgs mechanism is an important building block of the Standard Model of elementary particles. A great achievement thus was the discovery of a Higgs boson at the LHC by ATLAS and CMS in 2012, that to date looks very much like the SM Higgs boson, even though precision measurements of the Higgs sector are still ongoing with larger data sets.

2.1.3. Flavour Changing Transitions

By coupling to the W boson, a quark can undergo a charged current transition and change its flavour. The naive assumption that this only happens within one generation of quarks has been falsified by experimental results already in the 1960s. This lead to the insight, that the quark states taking part in the weak interaction are a superposition of different mass eigenstates, which was first formulated by Cabibbo in 1963 [23] when only three flavour quantum numbers were known, and later extended to the six-quark case by Kobayashi and

Maskawa in 1973 [24]. The weak (or flavour) eigenstates of the down-type quarks, d', s' and b', which the up-type quarks couple to in weak interactions, are connected to their mass eigenstates d, s and b via a unitary ($U^\dagger U = \mathbb{1}$) 3×3 matrix in the following way:

$$\begin{pmatrix} d' \\ s' \\ b' \end{pmatrix} = V_{CKM} \begin{pmatrix} d \\ s \\ b \end{pmatrix} = \begin{pmatrix} V_{ud} & V_{us} & V_{ub} \\ V_{cd} & V_{cs} & V_{cb} \\ V_{td} & V_{ts} & V_{tb} \end{pmatrix} \begin{pmatrix} d \\ s \\ b \end{pmatrix}. \tag{2.41}$$

The matrix V_{CKM} is the so-called *Cabibbo-Kobayashi-Maskawa (CKM) matrix*. The matrix element $|V_{ij}|$ is thus a measure for the probability of a transition from one quark i to another quark j and the interaction term with the positive W bosons (e.g.) reads

$$\Delta\mathcal{L}_{W^+} = \frac{g}{\sqrt{2}} W^+_\mu J^\mu, \tag{2.42}$$

in which the weak current J^μ has the form

$$J^\mu = \begin{pmatrix} \bar{u} & \bar{c} & \bar{t} \end{pmatrix} \frac{\gamma_\mu(1-\gamma^5)}{2} V_{CKM} \begin{pmatrix} d \\ s \\ b \end{pmatrix}. \tag{2.43}$$

The choice that for up-type quarks flavour and mass eigenstates coincide ($u = u'$, $c = c'$, $t = t'$), while down-type quarks are mixed, is purely conventional.
The sizes of the different matrix elements have been measured in various experiments. As of today, the known values are the following ones [25]:

$$V_{CKM} = \begin{pmatrix} 0.97427 & 0.22534 & 0.00351 \\ 0.22520 & 0.97344 & 0.0412 \\ 0.00867 & 0.0404 & 0.999146 \end{pmatrix}. \tag{2.44}$$

The diagonal elements are close to one, making transitions within one family much more likely than inter-generational ones. One can also observe the trend that transitions skipping one family are highly suppressed. Third generation quarks hardly ever undergo transitions to lighter families.
The unitarity of the CKM matrix leads to an interesting feature of the SM. Eq. 2.41 can

also be expressed as

$$d'_i = \sum_j V_{CKM,ij} d_j, \tag{2.45}$$

with i running over the three quark generations. As V_{CKM} is unitary, the following equality holds:

$$\sum_i \bar{d'}_i d'_i = \sum_{i,j,k} \bar{d}_j V^\dagger_{CKM,ij} V_{CKM,ik} d_k = \sum_j \bar{d}_j d_j, \tag{2.46}$$

which means that there are no transitions like $s \leftrightarrow d$ at tree-level, that change flavour but not charge (*flavour changing neutral currents, FCNC*). Such FCNC can be realised via loop diagrams, which are suppressed with respect to tree level ones.

2.1.4. Quantum Chromodynamics

The remaining one of the fundamental interactions described by the SM is the strong force. It is described by quantum chromodynamics (QCD) of which the name refers to the Greek word for colour, because its associated charge is the colour charge. The symmetry requires strong interactions to be invariant under colour transformations. There are three conserved colour charges, which is why QCD can be described using the gauge group $SU(3)_C$. A quark carries one of the colour charges r, g or b, while an anti-quark carries one of the anti-colours $\bar{r}$, $\bar{g}$ or $\bar{b}$. Quarks can be expressed in the fundamental representation of $SU(3)$ in the following way:

$$r = \begin{pmatrix} 1 \\ 0 \\ 0 \end{pmatrix}, \; g = \begin{pmatrix} 0 \\ 1 \\ 0 \end{pmatrix}, \; b = \begin{pmatrix} 0 \\ 0 \\ 1 \end{pmatrix}. \tag{2.47}$$

The colour can be changed in strong interactions by exchanging or emitting gluons (massless spin-1 particles), which themselves carry colour charges. As they have to carry both, a colour and an anti-colour, in order to keep colour conserved at fundamental vertices, there are nine possible charges a gluon can have. Using group-theory expressions this can be written as $\mathbf{3} \otimes \bar{\mathbf{3}} = \mathbf{8} \oplus \mathbf{1}$, which means that the fundamental representation of $SU(3)$

together with its adjoint yields a colour octet with net colour charge and a colour singlet. Being colour-neutral, the latter one does not participate in the strong interaction, leaving us with eight different gluons.

The formalism of quantum chromodynamics can be developed in a similar way around the underlying symmetry group $SU(3)$, as it has been done in the previous section with $U(1)$ for QED by requiring the free Lagrangian

$$\mathcal{L}_0 = \bar{q}_j(i\gamma^\mu\partial_\mu - m)q_j, \tag{2.48}$$

with q_j $(j = 1, 2, 3)$ being the colour fields, to be invariant under local phase transformations:

$$q(x) \to e^{i\alpha_a(x)T_a}q(x). \tag{2.49}$$

The generators of the group, T_a, with $a = 1, ..., 8$, can be represented by the Gell-Mann matrices λ_a via $T_a = \lambda_a/2$. One should notice, that they do not pairwise commute, which means that $SU(3)$ is non-Abelian, like $SU(2)$:

$$[T_a, T_b] = if_{abc}T_c, \tag{2.50}$$

with f_{abc} being the structure constants of the group.

Local phase transformations do not leave the Lagrangian unchanged. Thus, in order to restore invariance, a covariant derivative

$$D_\mu = \partial_\mu + igT_aG^a_\mu, \tag{2.51}$$

which introduces eight gauge fields G^a_μ, is introduced, analogous to the $SU(2)_L$ case.

Analogously as well, the field strength tensor needs to get a special transformation property, in order to associate the gauge fields with physical gluon fields and to keep the Lagrangian invariant:

$$G^a_\mu \to G^a_\mu - \frac{1}{g}\partial_\mu\alpha_a - f_{abc}\alpha_bG^c_\mu. \tag{2.52}$$

The extra term, arising due to the non-Abelian nature of $SU(3)$, analogous to the $SU(2)_L$ case, is responsible for gluon self-interactions, which is a fundamental difference to QED based on the $U(1)$ symmetry group. Using all of the above mentioned ingredients, one is left with the local gauge invariant Lagrangian of QCD:

$$\mathcal{L}_{QCD} = \bar{q}(i\gamma^\mu \partial_\mu - m)q - g(\bar{q}\gamma^\mu T_a q)G^a_\mu - \frac{1}{4}G^a_{\mu\nu}G^{\mu\nu}_a, \tag{2.53}$$

the field strength tensor $G^a_{\mu\nu}$ contains the kinetic terms for the gluons and the gluon self-interactions. Again, local gauge invariance prohibits the introduction of a mass term, such that gluons are required to be massless.

The coupling constant of the strong interaction, α_s, is experimentally found to be highly dependent on the energy range (or distance), it is therefore said to be *running*. α_s becomes larger with decreasing energy or increasing distances. This leads to a phenomenon called *confinement*, which means that quarks are asymptotically free only at very small distances, which is why no single quarks or gluons are observed in nature. Instead they cluster together in so-called hadrons, of which there are two kinds: Baryons made of three quarks, and mesons, which are combinations of a quark and an anti-quark. This phenomenon is explained by the theoretical assumption that only colour singlet states can exist in nature, and that the three colours together or a colour and the corresponding anti-colour add up to zero colour charge. This behaviour, which gives rise to a rich phenomenology, as gluons themselves carry colour charges, can be described by an effective potential between coloured objects:

$$V(r) \sim -\frac{C_1}{r} + C_2 \cdot r, \tag{2.54}$$

with C_1 and C_2 being constant factors. The first term on the right-hand side is the asymptotically free part, while the second term describes the confinement of quarks at large distances. An energy scale Λ_{QCD} can be found which separates the high-energy regime, where quarks are asymptotically free, from the low-energy regime. This energy scale at which the coupling constant is of the order of $\alpha_s \sim 1$, can experimentally be determined to be $\Lambda_{QCD} \sim 200\,\text{MeV}$.

2.1.5. Limitations of the Standard Model

The Standard Model of particle physics is well-tested and is widely considered one of the best theories ever developed, as many of its predictions have been confirmed by experiments to a high precision and no falsifying experimental results have been found in the laboratory so far. However, there are still some open theoretical questions and experimental observations which can not be explained by the SM:
The potentially most striking issue on the theoretical side is that the SM does not include one of the four known fundamental forces, gravity. The related fact that gravity is many orders of magnitude weaker than the weak force, can not be explained either. Therefore it is conjectured that the SM is an effective theory in the low-energy limit (well below the Planck scale of $10^{19}\,\text{GeV}$), in which gravity can be safely ignored. This potentially leads to new particles being present at that scale. An intermediate step towards a theory that describes all fundamental forces would be a so-called *Grand Unified Theory* (GUT), which unites the strong and electroweak interactions. The energy scale at which this happens would be the scale at which to expect new particles, as they are needed to alter the running of the coupling constants, such that the unification can take place. However, the assumption that such a scale connected to new physics must exist leads to quadratic divergences in the quantum corrections to the Higgs mass, mainly stemming from top-quark loop contributions. While the masses of fermions and vector bosons are protected against linearly and quadratically divergent corrections by the requirement of gauge invariance, the Higgs self-energy corrections are quadratically divergent, as there is no such protective symmetry in the scalar sector. To obtain the experimentally observed Higgs mass of $\sim$125 GeV, there must be unnaturally large *fine-tuning* between the bare Higgs mass and the large quantum corrections, a fact which is commonly referred to as the *naturalness* or *hierarchy problem*.
A question triggered by the ad-hoc addition of the Higgs field as the only fundamental scalar field to the SM, is whether it might arise within an effective theory due to the breaking of some larger underlying symmetry.
The model is furthermore lacking an explanation for the existence of different lepton and quark flavours as well as the number of fermion generations and the quantisation of the hypercharge Y.
An unattractive feature of the SM is the large number of free parameters like particle masses and coupling strengths and another mismatch between theory and experiment is the so-called *strong CP problem*: the fact that while theoretically possible in QCD, the strong

interaction does not seem to violate the symmetry with respect to the product of charge and parity quantum numbers (CP).
The SM also predicts neutrinos to be massless, which is found not to be true in nature by the observation of neutrino oscillations [26]. The unexplained fact that the observed neutrino masses are many orders of magnitude smaller than the other lepton masses, can indicate that neutrinos might be the key to new physics phenomena.
Puzzles prompted by experimental observations are the baryon-antibaryon asymmetry in the universe and the fact that only a small fraction of about 4.9% of the energy-matter content of the universe (the so-called *baryonic matter*) is described by the SM. The remaining 95.1% are shared among *dark energy* (68.3%) and *dark matter* (26.8%) [27], both of which are not part of the SM.

Various hypothetical extensions of the SM have been developed, addressing several of the above mentioned puzzles. The next section will focus on the subgroup of models beyond the SM which address the naturalness problem, as they have implications for experimental searches for new particles, one of which is carried out in the course of this thesis.

2.2. Possible Extensions of the Standard Model

If the amount of fine-tuning allowed in the calculation of the Higgs mass is limited to 10%, one can infer that the scale up to which the SM is valid, should be of the order of 1 TeV [28]. A sign for new physics to set in would be the presence of new particles with a mass close to that scale. As this mass range lies within the reach of the LHC, such new states could be discovered there and should be searched for.
Apart from this general motivation, several extensions of the SM addressing the naturalness question also specifically introduce new fermions [29, 30]. There are e.g. theories including extra dimensions [31] or supersymmetry, which predicts a partner for every SM particle with special coupling properties [32]. There are also theories with modified Higgs sectors, which e.g. describe an excitation of the Higgs field not as an elementary state, but as a composite object [8, 33]. These composite Higgs models can also be embedded in Grand Unified Theories based on the E_6 group [34]. Other theories, referred to as *Little Higgs* models, suggest that the Higgs boson is a pseudo-Goldstone boson stemming from a global symmetry breaking [35]. In all of these theories, extra quarks are predicted, which can be searched for by experiments. Even though it is widely accepted, that the Standard Model

contains six quarks, the number of quark generations is not predicted by the theory. It is therefore sensible to search for new quarks at higher energy ranges, as they are likely to be heavier than the SM quarks known as of today. A simple extension of the existing quark and lepton sector by a chiral fourth generation, however, has been excluded by the Higgs discovery [36]. New heavy quarks are thus required to have different properties than the known ones. The heavy fermions predicted by the above mentioned models have special properties which makes them escape constraints from Higgs data, as described in more detail in the following section. These so-called *vector-like quarks* can stabilise the electroweak vacuum [37] and especially the introduction of heavy top-partners is responsible for the cancellation of the divergent contributions from the top quark to radiative corrections of the Higgs mass. They are therefore very promising candidates for new heavy quarks to look for in collider searches. However, in many models these top-partners come in multiplets with bottom-partners or even quarks with exotic charges. This justifies the experimental search also for down-type fermions, which could be easier to find experimentally than the top partners, in case that the usual mass hierarchy within a doublet also holds for vector-like quarks. Such a search is carried out in this work.

2.2.1. Vector-Like Quarks

Vector-like quarks (VLQ) are hypothetical heavy quarks, theorised in all above mentioned extensions of the SM. The property which distinguishes them from SM quarks is that Ψ_L and Ψ_R have the same $SU(2)_L \otimes U(1)_Y$ quantum numbers, such that left- and right-handed components behave equally under the associated gauge transformations. Thus, while SM quarks couple chirally to the W boson,

$$J^{\mu+} = \bar{u}\gamma^{\mu}(1-\gamma^5)d = \bar{u}_L\gamma^{\mu}d_L, \tag{2.55}$$

vector-like quarks couple via a vector current,

$$J^{\mu+} = \bar{u}_L\gamma^{\mu}d_L + \bar{u}_R\gamma^{\mu}d_R = \bar{u}\gamma^{\mu}d, \tag{2.56}$$

which is the origin of the name. Differently from their SM counterparts, VLQ can occur as weak isosinglets, -doublets or -triplets. If the scalar sector only comprises $SU(2)_L$ doublets, as it is the case in the SM, seven different multiplets are possible [38]:

- singlets: $T^0_{L,R}$, $B^0_{L,R}$
- doublets: $(X\ T^0)_{L,R}$, $(T^0\ B^0)_{L,R}$, $(B^0\ Y)_{L,R}$
- triplets: $(X\ T^0\ B^0)_{L,R}$, $(T^0\ B^0\ Y)_{L,R}$,

where the superscript 0 denotes a weak eigenstate. As X and Y cannot mix via the mass matrix due to their exotic charges, weak and mass eigenstates are the same, such that no distinction is necessary. Considering only models, where one of these multiplets, e.g. the $T^0_{L,R}$ singlet, is added to the SM particle content, one is faced with the possibility that the resulting physical up-type mass eigenstates (u, c, t, T) might contain non-vanishing $T^0_{L,R}$ components. This mixing of vector-like with SM quarks would lead to modifications of their couplings to the Z boson, which in turn would introduce tree-level FCNC [39]. However, such coupling deviations are highly constrained for up and charm quarks by the LEP experiments [25]. Much weaker constraints exist on potential coupling modifications for the top quark. Together with existing similar (even though weaker) knowledge about the down-type quarks, this leads to the general assumption that vector-like quarks preferentially mix with the third generation only. This is supported by the fact that in most models the mixing is proportional to the ratio m_q/M_{VLQ} between the mass of the SM and the new heavy vector-like quark [40, 41], which is negligible for the first two generations, and by the fact that no tree-level flavour changing transitions are observed among SM quarks. FCNC transitions between vector-like and third generation quarks however, are introduced by the above mentioned mixing. This is an important property of VLQ models, as it increases the number of production and decay modes and therefore leads to a larger number of final states that are experimentally accessible. In fact, the flavour changing neutral current decays of vector-like quarks to SM quarks are comparable to the charged current ones [6]. Another means of easily understanding the occurrence of FCNC at tree level is that in the presence of a VLQ multiplet the CKM matrix (as introduced in Eq. 2.41) is no longer unitary, such that the FCNC-suppressing argument discussed in section 2.1.3 no longer holds.
One has to note, however, that all above mentioned arguments only hold in the simplified case of only one additional multiplet of VLQs, which is an assumption widely made in the interpretation of search results. In more realistic models, the mixing scenario and implications thereof would be much more involved.
At hadron colliders vector-like quarks can be produced in pairs via the strong interaction or, due to the mixing with SM quarks, singly via the weak interaction. Figure 2.2 shows a relative comparison of the production cross-sections of the two production modes for various

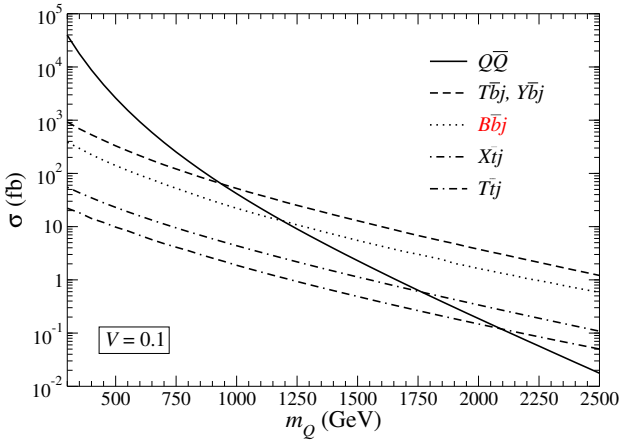

Figure 2.2.: Comparison of the pair-production cross-section ($Q\bar{Q}$) and the single-production cross-sections for various vector-like quarks (T, B, X, Y) in different production modes for a mixing with the third generation of $V = 0.1$ at a centre-of-mass energy of $\sqrt{s} = 8\,\text{TeV}$ [6]. The legend indicates the final-state particles of the respective t-channel production, j denotes a light-flavour jet. One channel considered in the course of this thesis is indicated in red.

VLQ multiplets for a mixing with the third generation of $V = 0.1$. For low vector-like quark masses, pair production has a higher cross section, but due to phase space restrictions, the single-production mode takes over with increasing mass. The position of the intersection point depends on the mixing parameter V. For smaller mixing with the third generation, pair production is dominant up to higher masses.

As we have seen in section 2.1.2, adding Dirac mass terms for chiral quarks to the Lagrangian breaks local gauge symmetry. A Higgs field thus had to be introduced for the mass generation. Due to their different transformation properties, however, this is not the case for vector-like quarks. As left- and right-handed components, Ψ_L and Ψ_R respectively, transform in the same way under local $SU(2)_L$ transformations,

$$M_{VLQ}\bar{\Psi}\Psi \xrightarrow{\substack{\Psi_L \to e^{i\vec{\alpha}(x)\cdot\vec{T}}\Psi_L \\ \Psi_R \to e^{i\vec{\alpha}(x)\cdot\vec{T}}\Psi_R}} M_{VLQ}\bar{\Psi}\Psi, \tag{2.57}$$

the mass terms are gauge invariant, such that no EWSB is necessary to introduce VLQ masses. Vector-like quarks thus do not have to couple to the Higgs field to obtain their masses (they only couple via mixing), which is why the $gg \to H$ production rate does not have to be affected by the potential existence of these quarks. In fact, it has been shown

that VLQ, even though they enter the loop diagrams in the $gg \to H$ production amplitudes, give negligible contributions due to their decoupling behaviour and cancellations [40]. The effects on Higgs decay rates were also shown to be below the measurement precision achieved at LHC experiments. Unlike chiral fourth generation quarks, vector-like quarks are therefore not excluded by the discovery of a Higgs boson with SM-like production and decay rates.

For the interpretation of search results two different strategies can be followed: An interpretation can be done in the context of a minimum renormalisable extension of the SM including VLQ [40] or in the context of (e.g. composite Higgs) models including also non-renormalisable terms in the Lagrangian, which is then expected to be valid only up to some scale at which new physics phenomena set in [42, 43]. While the former one is the more general approach, the latter one yields higher production cross-sections. In order to obtain a reasonable sensitivity, the search for vector-like quarks presented in this thesis is interpreted using cross sections calculated in a composite Higgs model, even though the signal Monte-Carlo samples (as described in section 6.1 in Chapter 6) were produced in the context of the general model. Besides the vector-like quark B, the search also considers excited quarks with vector-like couplings, b^*. Details on the the underlying models, the two predicted down-type ($Q = -1/3$) quarks and their similarities as well as the implications on the search for their decay to third generation quarks are presented in the following sections.

Vector-Like Quark B

As mentioned before, vector-like quarks are predicted - among other models - in so-called *composite Higgs* models. They assume that instead of being an elementary particle, the Higgs boson is a bound state of strongly interacting dynamics at the TeV scale [8]. As such a composite object, its mass would no longer be sensitive to radiative corrections above that scale, analogously to the pion mass stabilisation in QCD. This model is thus a means of addressing the naturalness problem.
The specific model considered in this search [8] is based on a *two-site* (TS) description, where an elementary sector which contains the SM fermions, is linearly coupled to a composite sector containing the Higgs boson via mixing. Besides the Higgs boson, the composite sector also comprises heavy vector-like quarks, which the composite operator $\mathcal{O}$ can excite from the vacuum. The linear coupling between the heavy fermions and the SM quarks,

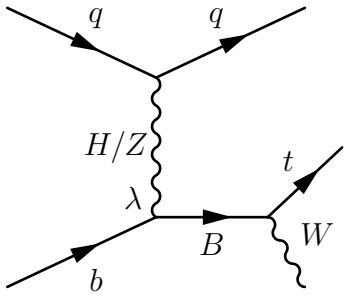

Figure 2.3.: t-channel production of a single B quark in association with two SM quarks with low transverse momentum and subsequent decay to Wt.

which transports the electroweak symmetry breaking to the latter ones, can be phrased as

$$\Delta\mathcal{L} = \lambda\bar{\psi}\mathcal{O} + h.c., \tag{2.58}$$

[8], with λ being the coupling strength. After diagonalisation of the mass matrix the SM quarks also have composite contributions, a scenario often referred to as *partial compositeness* of the SM. We should note, that heavier SM quarks (b, t) – due to their larger mixing with the new fermions – have a larger degree of compositeness, while the lighter families are nearly purely elementary. The Lagrangian of that model can be schematically expressed by

$$\mathcal{L} = \mathcal{L}_{elementary} + \mathcal{L}_{composite} + \mathcal{L}_{mixing}, \tag{2.59}$$

where the coupling between elementary and composite fields, as described in Eq. 2.58, only takes place in the mass mixing part $\mathcal{L}_{mixing}$.
The underlying symmetry groups in the model are $SU(3)_c \otimes SU(2)_L \otimes U(1)_Y$ for the elementary (SM without Higgs boson) sector and $SU(3)_c \otimes SO(4) \otimes U(1)_X$ for the composite sector, where $SO(4) \sim SU(2)_L \otimes SU(2)_R$ includes an additional $SU(2)_R$ symmetry not present in the SM, and X being defined via $Q = I_L^3 + I_R^3 + X = I_L^3 + Y$, the generalisation of the (hyper) charge concept for the new symmetry group. The composite sector comprises several multiplets of composite fermions, but as the analysis presented in this thesis will only investigate down-type vector-like quarks, we will focus on the B quark with electric charge $Q = -1/3$. The diagram for B production with subsequent decay to Wt, as considered in this search, can be found in Figure 2.3.

Apart from the charged one, the B quark has two neutral decay modes and the branching fractions at high VLQ masses are approximately [8]:

$$BF(B \to qH) : BF(B \to qZ) : BF(B \to qW) \approx 1 : 1 : 2.$$

The decay widths depend quadratically on the coupling parameter λ in the part of the Lagrangian describing the coupling to the third SM quark generation,

$$\Delta\mathcal{L} = -\lambda(\bar{b}_L \Phi_0 B_R + \bar{t}_L \Phi^+ B_R) \tag{2.60}$$

with $\lambda = Y_* s_1 c_{bR}$. Y_* is the Yukawa coupling among composite states, $s_1 \equiv sin\phi_L$ with ϕ_L parametrising the degree of compositeness of the (t_L, b_L) doublet and $c_{bR} \equiv cos\phi_{bR} \approx 1$ with ϕ_{bR} parametrising the degree of compositeness of b_R. The coupling λ of the B with the gauge bosons and the SM quarks thus affects both the decay and single-production rate. Table 2.2 lists the product of single-production cross-section and decay branching fraction to Wt (the only decay mode considered in this analysis) for various B masses and values of λ, for which the 2×2 mass matrix of the B and the b-quark has been diagonalised. The calculation was carried out in the 5-flavour scheme with the MSTW2008LO PDF (parton distribution function[2]) set.

As a benchmark model in the search presented in this thesis, $\lambda = 2$ is assumed. Current exclusion limits for B production were set by ATLAS in a pair-production search at a centre-of-mass energy of $\sqrt{s} = 8\,\text{TeV}$. Assuming $BF(B \to Wt) = 100\%$, B masses below 810 GeV are excluded and for the case of branching ratios corresponding to those of an $SU(2)$ singlet state, masses below 640 GeV are excluded [45]. The most stringent exclusion limits on the B mass to date were obtained in a pair-production search by CMS performed at a centre-of-mass energy of $\sqrt{s} = 8\,\text{TeV}$, which excludes B masses below 900 GeV assuming $BF(B \to bH) = 100\%$ and below 740 GeV for smaller branching fractions [46].

[2]An explanation of parton distribution functions is given in section 4.2.1 in Chapter 4

m_B [GeV]	$\sigma \times \mathrm{BR}(B \to Wt)$ [fb]			
	$\lambda = 2$	$\lambda = 3$	$\lambda = 4$	$\lambda = 5$
400	710	—	—	—
600	220	250	—	—
800	52	97	95	—
1000	15	30	43	39
1200	4.8	10.2	16	20
1400	1.7	3.6	5.9	8.2

Table 2.2.: Cross section times branching fraction for $pp \to B \to Wt$ for different B masses and coupling values λ at a centre-of-mass energy of $\sqrt{s} = 8\,\mathrm{TeV}$ [8, 44], calculated with the MSTW2008LO PDF set. For certain values of λ and masses of B the cross section becomes unphysical, if $\lambda \cdot v/\sqrt{2} > m_B - m_b$ with the vacuum-expectation value v and the mass of the b quark m_b. This is denoted in the table with "—". More details on the cross-sections can be found in section 6.1, the theoretical uncertainties are listed in Table 6.2.

Vector-Like and Excited Quark b^*

The other model being considered in the search presented in this thesis predicts excited quarks, of which we will also concentrate on the down-type ones, referred to as b^*. The possibility of excitations of quarks would show, that instead of elementary particles, quarks of the SM are composite objects. As excited quarks couple to the gauge bosons in a vector-like manner [47], as all vector-like quarks, b^* quarks are not excluded by the Higgs discovery, in contrast to sequential fourth-generation quarks.
The model considered here [7][3] describes an effective scenario, where the b^* quark is the only relatively light state below a cutoff Λ. As for all excited quarks, the b^* couplings to SM quarks and gauge bosons are of magnetic moment type [47], which can be seen from the part of the Lagrangian describing the coupling to gluons, which already takes into account the fact that the b^* only mixes with third generation quarks [7]:

$$\mathcal{L} = g_s \bar{b^*} \gamma^\mu G_\mu b^* + \frac{g_s \lambda}{2\Lambda} G_{\mu\nu} \bar{b} \sigma^{\mu\nu} (\kappa_L^b P_L + \kappa_R^b P_R) b^* + h.c. \tag{2.61}$$

[3] Please note that in the cited theory publication the excited quark was called B', which was changed to b^* in this context, in order to better emphasise its excited-quark properties and to disentangle it from the vector-like quark B which is also investigated in the same search.

Here g_s is the strong coupling constant, G_μ the gluon fields, $G_{\mu\nu}$ the field strength tensor for the gluon, Λ the scale of the process (being set to the mass of the new quark and thus being well below the assumed cutoff), P_L and P_R the helicity projection operators with the respective strengths κ_L and κ_R (both set to 1.0 for the benchmark process under investigation) and λ is a free parameter depending on the physics above the cutoff that was integrated out and is set to $\lambda = 1.0$ [47]. This chromomagnetic anomalous magnetic moment vertex gbb^* is responsible for comparatively high cross sections, which result in good sensitivity for the model (which is quantified in Chapter 6).
The decay of the excited quarks into third generation quarks and gauge bosons via the electroweak interaction can be parametrised in the following way:

$$\mathcal{L} = \frac{g_2}{\sqrt{2}} W_\mu^+ \bar{t} \gamma^\mu (f_L P_L + f_R P_R) b^* + h.c., \tag{2.62}$$

where g_2 is the electroweak coupling constant, W_μ^+ the field strength of the W boson, and f_L and f_R the strengths of the left-handed and right-handed coupling to W bosons, respectively. In this search, a benchmark scenario of $f_L = f_R = 1$, which denotes the pure vector-like case, has been considered. Only b^* decays into W boson and t quark have been taken into account, as this decay mode accounts for the largest fraction of decays for high b^* masses (see Figure 2.4). This way, the final state of b^* decays is very similar to the final state of B decays, which motivates a common search involving both models. For this scenario, as well as for the purely left-handed or purely right-handed coupling cases, the product of cross section and branching fraction into Wt, calculated in a 5-flavour scheme using the MSTW2008LO PDF set, is listed in Table 2.3 for various signal masses. The Feynman diagram of the production and decay to Wt of a b^* quark is shown in Figure 2.5.

Previous mass limits obtained by ATLAS in a search for single production of b^* in single-lepton and dilepton final states at a centre-of-mass energy of $\sqrt{s} = 7\,\text{TeV}$ are 870 GeV for the purely left-handed coupling case and 1030 GeV for the vector-like coupling scenario, respectively [9]. The most stringent limit to date of 1530 GeV for the vector-like coupling scenario was obtained in a search by the CMS collaboration [10].

Before describing the search strategy and results in detail, the next chapters introduce the experimental setup and the techniques used to simulate and reconstruct the various physics objects needed in order to carry out a successful search for new particles.

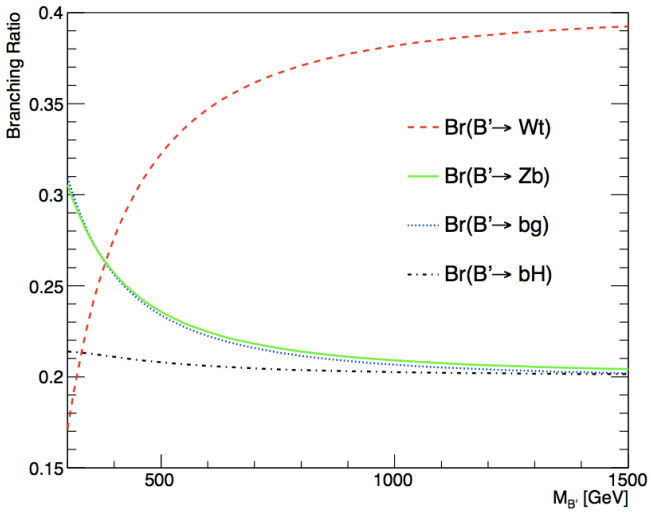

Figure 2.4.: Branching fractions for excited b^* quarks. For higher masses, the decay mode to Wt is dominant [7]. Please note that what is called B' in reference [7] where this plot is taken from is called b^* throughout this thesis.

m_{b^*} [GeV]	$\sigma \times BR(b^* \to Wt)$ [fb]	
	$f_{\mathrm{L(R)}} = 1,\ f_{\mathrm{R(L)}} = 0$	$f_L = f_R = 1$
400	115×10^3	196×10^3
600	183×10^3	35×10^3
800	3.9×10^3	7.5×10^3
1000	1.0×10^3	2.0×10^3
1200	310	610
1400	110	210
1800	16	30

Table 2.3.: Cross section times branching ratio for $b^* \to Wt$ for different b^* masses and b^*Wt couplings at a centre-of-mass energy of $\sqrt{s} = 8\,\mathrm{TeV}$, calculated with the MSTW2008LO PDF set. Here $\kappa_L = \kappa_R = 1$ is assumed [7]. More details on the cross sections can be found in section 6.1, the theoretical uncertainties are listed in Table 6.1.

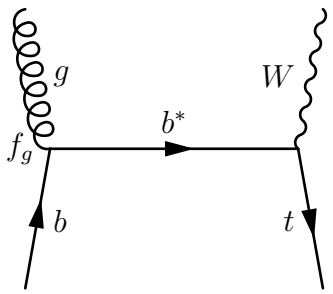

Figure 2.5.: s-channel production of a single b^* quark decaying to Wt with $f_g = \kappa_L = \kappa_R$.

Chapter 3.

The ATLAS Experiment

3.1. ATLAS at the LHC

ATLAS is one of four experiments situated at the Large Hadron Collider (LHC) at CERN, Geneva. The LHC was built to either collide protons in bunches of up to 10^{11} with centre-of-mass energies of up to 14 TeV at a rate of 40 MHz with a design luminosity of $10^{34}\,\mathrm{cm}^{-2}\mathrm{s}^{-1}$ or heavy ions, especially lead nuclei, at 5.5 TeV per nucleon pair at a design luminosity of $10^{27}\,\mathrm{cm}^{-2}\mathrm{s}^{-1}$. In the year 2012, when the data analysed in this thesis was taken, proton bunches with a spacing of 50 ns were collided at a centre-of-mass-energy of 8 TeV and instantaneous luminosities of up to $8 \times 10^{33}\,\mathrm{cm}^{-2}\mathrm{s}^{-1}$ were reached.

The LHC was built into the already existing tunnel of the former LEP experiment with a circumference of 26.7 km and, besides the large storage ring, consists of several pre-accelerators shown in Figure 3.1. The data taking was started in the year 2009. With its unprecedented high energy and luminosity, the LHC was designed to extend the frontiers of particle physics. Besides two rather specialised experiments, LHCb [49] and ALICE [50], it hosts the two general purpose detectors ATLAS and CMS, which are meant to verify each other's physics results in order to exclude potential biases induced by unexpected detector effects. In this chapter, the characteristics of the ATLAS experiment will be discussed in detail.

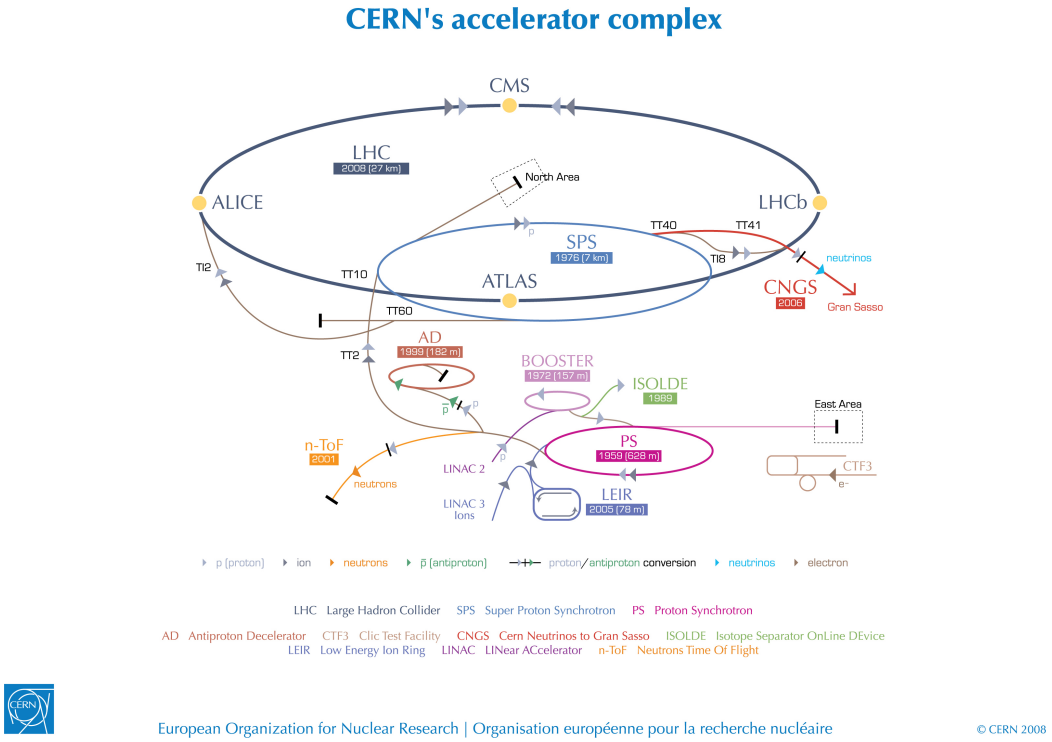

Figure 3.1.: Overview of the CERN accelerator complex [48].

3.2. The ATLAS Detector

As a general purpose detector, ATLAS is designed for investigations of a wide variety of physics processes, such as precise measurements of Standard Model parameters as well as new physics phenomena. It is built in cylindrical symmetry around the beam axis with a barrel part around the interaction point and one end-cap at either side and has nearly a 4π coverage. In order to detect the different final-state particle-species, ATLAS is made up of several subsystems, which fulfil different tasks, assembled in an onion shell structure. Figure 3.2 gives an overview over the whole system.
The information given in this chapter is mostly based on [1].

3.2.1. Coordinate System

A cylindrical coordinate system is used for the description of positions and directions of particles in the detector. The z coordinate is defined along the beam axis, with positive z values representing points in the clockwise direction around the LHC ring. Φ is the

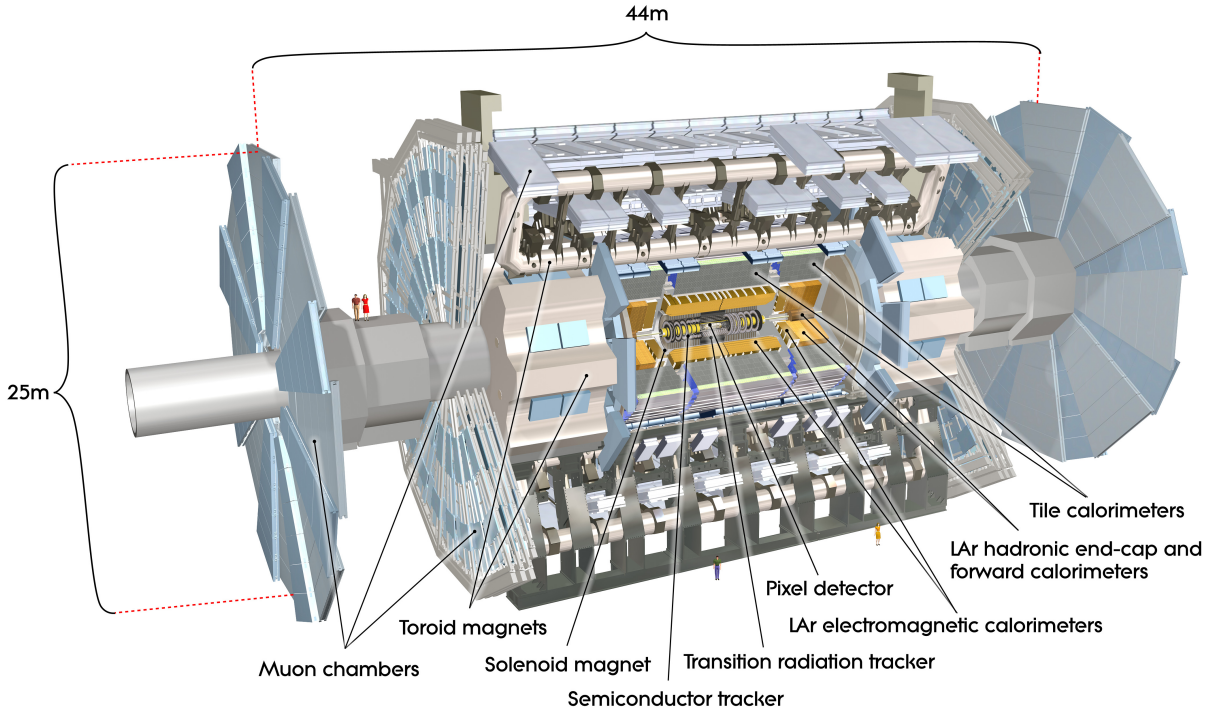

Figure 3.2.: Cut-away view of the ATLAS detector [1].

azimuthal angle perpendicular to the z-axis and θ is defined as the polar angle between the positive z-axis and the particle direction. As differences in the angle θ are not invariant under Lorentz boosts in the z direction, which typically occur in proton-proton collisions at such high energies, an alternative quantity, the pseudorapidity η, is used instead. It is defined as

$$\eta = -ln\left(tan\frac{\theta}{2}\right), \tag{3.1}$$

which is equal to the rapidity y

$$y = \frac{1}{2}ln\frac{E+p_z}{E-p_z} \tag{3.2}$$

in the massless limit. The relation between η and the polar angle θ is visualised in Figure 3.3

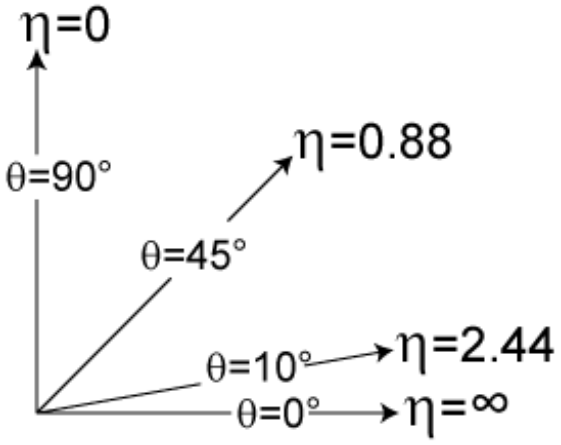

Figure 3.3.: Pseudorapidity η for various values of the polar angle θ [51].

Another commonly used quantity is ΔR, the distance of two points in $\eta - \Phi$ space, defined as

$$\Delta R = \sqrt{(\Delta\Phi)^2 + (\Delta\eta)^2}. \tag{3.3}$$

As the longitudinal momenta of the incoming partons are unknown, while the transverse momenta are zero before the collision, energy and momentum of the detected particles are only measured in the plane perpendicular to the z-axis (transverse plane):

$$p_T = \sqrt{p_x^2 + p_y^2} \tag{3.4}$$

and

$$E_T = E \cdot sin\theta = \frac{E}{cosh\eta}. \tag{3.5}$$

3.2.2. Inner Detector

The innermost system in the onion-shell structure of ATLAS is the Inner Detector (ID) which is responsible for track and momentum reconstruction of charged particles as well as for precise vertex reconstruction. It consists of three independent, complementary subdetectors: silicon pixels and strips (SCT) as well as a transition radiation tracker (TRT). The ID is contained in a cylindrical volume of a length of 3.5 m and a radius of 1.15 m and is permeated by a 2 T magnetic field. Figure 3.4 shows an overview of the Inner Detector

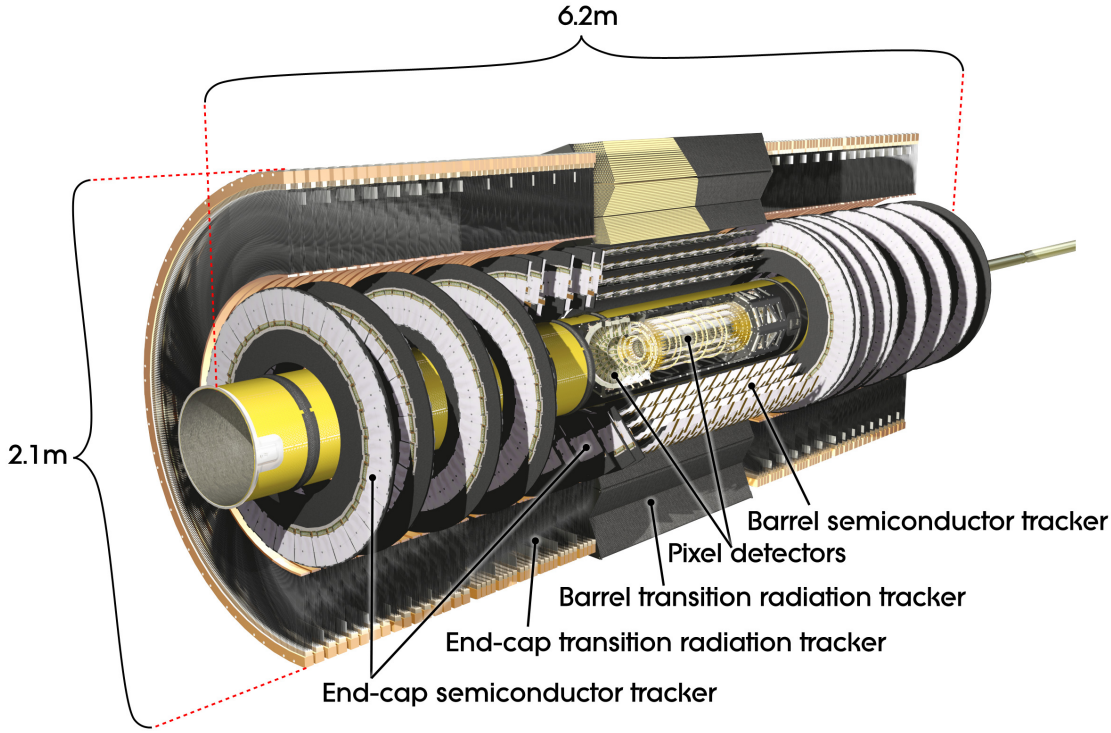

Figure 3.4.: Cut-away view of the ATLAS Inner Detector [1].

with its components.

The region closest to the interaction point is covered by 3 layers of pixel detectors which provide the high granularity necessary in the region with the highest track density emerging from the ∼1000 particles being produced every 50 ns. It is followed by 4 double-layers of silicon strips. The two silicon subdetectors cover the region $|\eta| < 2.5$ and are arranged in concentric cylinders in the barrel region, while they are mounted on disc-like structures in the end-cap regions. The outermost region of the ID consist of the TRT with a large number of axial straws of 4 mm diameter. Figure 3.5 shows the sensors and structural elements that a charged particle with high transverse momentum traverses, when it emerges from the interaction point.

The Pixel Detector

The pixel detector is the subdetector with the highest granularity as it is operated just outside the beam pipe in an area of very high particle fluences. Its main purpose is the

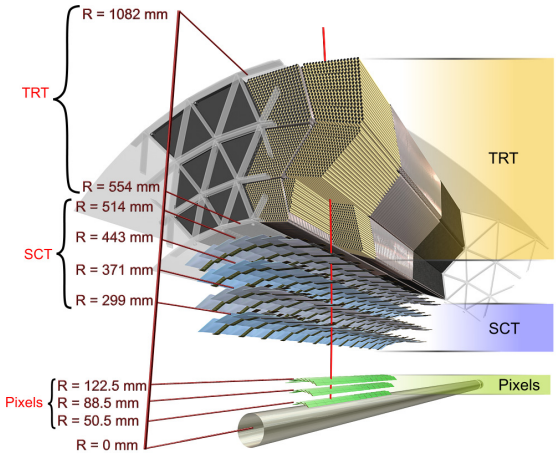

Figure 3.5.: Sensors and structural elements of the barrel part of the ATLAS Inner Detector traversed by a charged particle of 10 GeV p_T [1].

reconstruction of primary and secondary vertices and thus to enable technologies to identify jets[1] arising from b-hadron decays, which manifest in vertices that are slightly displaced from the one of the primary interaction (b-tagging). In order to distinguish these jets from light-quark or gluon jets, a spatial resolution of ∼10 µm is required.

The design of the pixel sensors is mostly driven by considerations of the high radiation doses of 1 MeV neutron equivalent fluence of up to $\sim 8 \times 10^{14}\,\mathrm{cm}^{-2}$ that these detectors will need to withstand within multiple years of operation. The dose is so high that the innermost layer had to be replaced during the first long shutdown in the years 2013 and 2014 after the first three years of operation. The pixel sensors are 250 µm thick oxygenated n-type wafers with readout pixels on the n^+-implanted side. This design is of advantage, as the detectors can also be operated with good charge-collection efficiency after inversion of the n-type bulk to p-type, which is an effect arising after a certain level of irradiation.

The pixel detector consists of 1744 identical sensors, $19 \times 63\,\mathrm{mm}^2$ in size, with 47232 pixels each. Due to space issues, some of the pixels on each sensor are ganged, leading to a total of 46080 readout channels. At the start of the first data-taking period, the sensors were operated with ∼150 V, but due to increasing radiation damage over time, which changes the effective doping concentration, a bias voltage of 600 V will be necessary after 10 years of operation. Most pixels (90% of the total number) have a size of 50×400 µm, which is driven by the pitch of the readout electronics, while the remaining ones which are sitting in the area of the readout chip on the sensor, are larger: 50×600 µm. Each pixel is bump-bonded

[1] A jet is a collimated particle bunch arising from the showering and hadronisation of a final state quark or gluon, see section 5.4.

to an element of the front-end electronics through a hole in the passivation layer.
A pixel sensor is connected to 16 front-end electronics chips with 2880 readout channels each and a flex-hybrid (flexible polyimide printed-circuit board) with a module control chip to form a pixel module. These modules are grouped onto staves (barrel) and end-cap sectors and arranged in three barrel layers and three layers per end-cap. The modules are oriented such that the amount of material between the pixel module and the interaction point is minimised. In order to keep temperature-dependent annealing of radiation damages, while keeping the leakage current, that increases linearly with the radiation dose, at low levels, the modules are cooled down to an operating temperature between -10°C and -5°C.

The SCT

The next layer outside the pixel detector is the so-called SCT, a silicon strip detector, which consists of 15912 sensors, which, in order to optimise cost and reliability, are produced using a classic single-sided p-in-n technology. The sensors consist of 285 µm thick silicon wafers with a strip pitch of 80 µm in the barrel region, which was defined by the required granularity, occupancy and noise performance. In this region, pairs of 6 cm long sensors are daisy-chained together. The end-cap sensors have radial strips with constant azimuthal angle with a mean pitch of ∼80 µm. The sensors are operated with a bias voltage between ∼150 V and 350 V, depending on the amount of irradiation. Binary signal readout chips (ASICs) are glued onto a polyimide hybrid, which in turn is glued onto the sensor. The electrical connection between the components is established via wire bonds. A barrel module consists of four sensors, two on either side sharing one common hybrid. 380 µm thick thermal pyrolitic graphite (TPG), which the sensors are glued onto, provides thermal and mechanical stability. The sensors on the double-sided modules are oriented such, that there is a small stereo angle of 40 mrad between the strips on the two sides, in order to measure two directions. In the barrel part, strips on one side are aligned parallel to the beam direction, measuring $R - \Phi$. The 2112 modules in the barrel region are grouped on so-called *staves*, which are then used for macro assembly.
In the end-cap region, there are three different wedge-shaped module types, given by geometric requirements for the end-cap disks (outer, middle and inner rings). Double-sided modules consisting of two sensors each also have a built-in stereo angle of 40 mrad, one set of strips being radially aligned.
The spatial resolution of a single SCT module has been measured to be ∼16 µm in $R - \Phi$,

given by the binary readout of the two sensors (for each one of which the resolution should be $\sim$pitch$/\sqrt{12}$), improved by the $\pm$20 mrad rotation of the sensors. The resolution is slightly enlarged by a small fraction of multiple hits and is not degraded significantly after irradiation. The Lorentz angle for a magnetic field of 2 T, however, changes from 4.2° before irradiation to 2.7° after irradiation. The SCT modules are designed to operate at a temperature of -7 °C and the temperature difference between modules should not exceed 5 °C, in order to minimise the overall leakage current. This is ensured by extracting the dissipated heat via evaporating C_3F_8 at ~ -25 °C circulating in cooling pipes attached to each module.

The Transition Radiation Tracker

The outermost ID system is the TRT which is mainly used for electron identification via transition radiation and tracking in general. The basic TRT detector elements are polyimide drift (straw) tubes of 4 mm diameter. Their walls are made of two 25 µm thick polyimide films, each of which is coated on one side with 0.2 µm of aluminium and protected by a $\sim$5 µm thick graphite-polyimide film. On the other side, the polyimide film is coated by 5 µm polyurethane, which heat-seals the films when they are glued back-to-back to one another. This design is optimised for good electrical and mechanical properties with minimal material. Mechanical stabilisation of the straws, which are cut in length of 144 cm for the barrel and 37 cm for the end-cap region, is assured by carbon fibres. The anodes are 31 µm thick, gold-plated tungsten wires, supported at the straw end by an end-plug. They are kept at ground potential and connected to the front-end electronics. The cathodes are operated at -1530 V in the gas mixture of 70% Xe, 27% CO_2 and 3% O_2 with 5 -10 mbar over-pressure, where they reach a gain of 2.5×10^4. Electrons issued by transition radiation photons within the gas mixture are collected with a maximum time of $\sim$48 ns and an operational drift-time accuracy of $\sim$130 µm is reached at operating conditions. Each straw has an intrinsic $R-\Phi$ resolution of 130 µm. Since low-energy transition radiation photons are absorbed in the gas mixture and therefore produce much higher signals than minimum ionising particles, the distinction between the two types is done on a straw-by-straw basis by using separate high and low thresholds in the front-end electronics.
In the barrel region, straws are divided electrically by a fused glass capillary at their centre to reduce the occupancy and supported mechanically via a plastic insert which is glued to the inner wall of the straw. Each barrel straw is therefore inefficient near its centre. The

anode straws with a remaining active length of ±71.2 cm are read out from either end. In the inner barrel layers, the straws are even divided into three segments, of which only the 31.2 cm of each end-segment are kept active.
To ensure stable operation, the gas mixture has to be re-circulated and the gas quality is continuously monitored. Pollution from permeation through the straw walls is avoided by operating the straws in a CO_2 envelope.
In the barrel region, the TRT contains up to 73 layers of straws which are interleaved with 19 µm polypropylene fibres, while in the end-caps there are 160 straw planes interleaved with foil. Fibres and foils provide the transition radiation which is needed for electron identification. A charged particle with $p_T > 0.5\,\text{GeV}$ and $|\eta| < 2.0$ traverses at least 36 straws, except in the transition region between barrel and end-cap ($0.8 < |\eta| < 1.0$), where this number is reduced down to 22 traversed straws. Electrons with energies above 2 GeV are expected to yield seven to ten high-threshold hits on their way through the TRT.
In the barrel part, the TRT consists of three rings with 32 modules each, supported at each end by a space frame for mechanical stability. The straws within a module form a uniform array with mean spacing of ∼7 mm. The 400 µm thick carbon fibre module shells are tested to have maximum distortions of < 40 µm under full load, in order to assure wire straightness and thus stable operation. At typical LHC rates, the ionisation current generates some significant heat inside the straws. The temperature gradient along each straw is required to be less than 10 °C to assure gas uniformity. This is achieved by removing the heat from the barrel straws by conduction through the CO_2 gas envelope. The module shells are cooled by two cooling pipes each, which also serve as return pipes for the C_6F_{14} cooling circuits of the front-end electronics. The central component of a TRT barrel module is the high-voltage plate, on top of which a printed circuit board, the tension plate, is mounted, which assures a stable wire tension and provides electrical connections.
In the end-cap region, the TRT consists of two sets of independent wheels, the inner one of which hosts 12 wheels, each with 8 layers with a distance of 8 mm to each other. The outer set consists of eight wheels, with 8 straw layers each, with a wider mean spacing of 15 mm. Each layer contains 768 radially oriented straws with uniform azimuthal spacing. The space between the straw layers is filled with radiator foils separated by a polypropylene net. Each layer is rotated by 3/8 of the inter-straw azimuthal spacing with respect to its neighbour to ensure optimal uniformity in the number of crossed straws for high-p_T tracks pointing back to the interaction point. The high-voltage and signal connections are provided by a flex-rigid printed circuit board, via two separate layers. Each four-plane wheel hosts 32

such boards, each of which serves a Φ sector of 96 straws. The dissipated heat from the straws in the end-cap region is evacuated through the CO_2 gas envelope flowing along the straws from the inner to the outer radius. Heat is also extracted from the gas between neighbouring wheels by heat exchangers cooled with C_6F_{14}.

Tracking and Primary Vertex Reconstruction

Information from the three above mentioned subsystems of the ID is combined in the inside-out track reconstruction, which is divided into three major parts [52]:

- The first stage is the pre-processing step, in which silicon detector raw data information is grouped into clusters and raw timing information from the TRT is transformed into drift circles. Three-dimensional representations of SCT and Pixel measurements, so-called *space points*, are created.
- The second stage is the track-finding step, in which different tracking algorithms are implemented. The default strategy is used to find prompt tracks originating from an area close to the interaction region. This is a multistep process itself. At first, space points in the three pixel layers and the first SCT layer are combined to form track seeds. An extension through the other SCT layers results in track candidates. These candidates are then fitted using a Kalman filter-based approach [53], outlier clusters are removed, cluster-to-track association ambiguities are resolved (by re-fitting the track candidates and creating a likelihood ranking for hits to describe the real trajectory) and fake tracks are removed from the collection of track candidates. These steps are achieved by using several quality criteria like distances of hits to tracks or limits on the number of clusters to be shared between different tracks and on the number of holes per track (a hole being defined as a silicon sensor traversed by a track, but not giving a hit). The tracks selected by those criteria are then extrapolated into the TRT in order to add drift-circle information. The last step is a track refit taking into account the full information provided by the three subdetectors. The refitted tracks are compared to the silicon-only tracks using fit-quality information in order to label hits in track extensions which result in bad fits as outliers, that are then kept as part of the track, but are no longer used in the fit.

- The third stage is the post-processing step, in which a vertex finder reconstructs primary vertices using the tracks which were obtained in the previous step. After that, dedicated algorithms for the reconstruction of photon conversions and secondary vertices are run.

In the 2012 data taking period there was not only one single proton-proton interaction per bunch crossing, but on average 20, a phenomenon known as pileup. This causes the necessity of efficient vertex reconstruction algorithms in order to disentangle the primary vertex stemming from the hard interaction from the various pileup vertices. This procedure is explained in [54]. The underlying iterative vertex finding algorithm, as presented in [55], uses the interpolation of the reconstructed tracks to the beam pipe as seeds for the vertices. For each of these seeds, a χ^2 fit is performed on the neighbouring tracks to measure the compatibility with the fitted vertex. Tracks exceeding 7σ are excluded from the particular vertex and used as a new seed. This step is repeated until no further vertices can be found. Tracks used as input for the primary vertex algorithms have to fulfil the following criteria:

- $p_T > 150\,\text{MeV}$,
- $|d_0| < 4\,\text{mm}$,
- $\sigma(d_0) < 5\,\text{mm}$,
- $\sigma(z_0) < 10\,\text{mm}$,
- ≥ 4 hits in the SCT detector,
- ≥ 6 hits in pixel and SCT detectors combined,

with d_0 and z_0 being the transverse and longitudinal impact parameters of the tracks with respect to the centre of the luminous region and $\sigma(d_0)$ and $\sigma(z_0)$ being the corresponding uncertainties (estimated in the track fit). As the hard scattering process typically leads to final state particles with large p_T, the reconstructed vertex with the highest sum of transverse momenta of the associated tracks is chosen as the primary vertex of the event. In this analysis, primary vertices are required to have at least four associated tracks with $p_T > 400\,\text{MeV}$ each. This is a means to reject non-collision backgrounds.

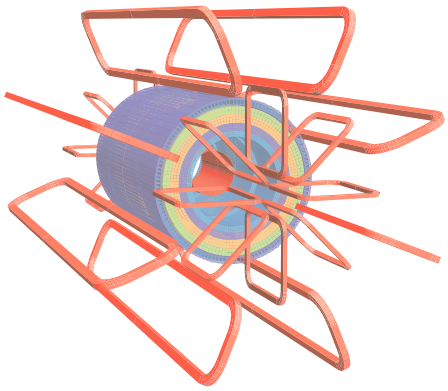

Figure 3.6.: Geometry of the magnet windings and the tile calorimeter steel. Eight barrel toroid coils, interleaved with the end-cap coils, are visible, while the solenoid windings are situated within the calorimeter volume [1].

3.2.3. Magnet System

In order to provide the bending power for charged particle tracks, ATLAS is equipped with a powerful magnet system, consisting of a solenoid, as well as a barrel and two end-cap toroids. Both sub-systems will be briefly described in the following. An overview of the geometry of the whole system can be seen in Figure 3.6.

Central Solonoid

The central solenoid is responsible for bending tracks in the Inner Detector, which it encloses, with a 2 T field parallel to the beam axis. It is barrel-shaped with a length of 5.8 m, an inner diameter of 2.46 m and a thickness of about 10 cm. As it is placed in front of the electromagnetic calorimeter, one of the main design goals was to minimise the material thickness, such that it only contributes a total of ∼0.66 radiation lengths at normal incidence of a track. This is especially achieved by reducing the number of vacuum walls, by letting the solenoid share a vacuum vessel with the electromagnetic calorimeter, and placing a 2 mm heat shield between the magnet and the inner cryostat wall. The solenoid consists of a single-layer coil, wound with a high-strength Al-stabilised NbTi conductor, which is a design to achieve high field with low material. The solenoid is surrounded by a 12 mm thick Al 5083 support cylinder. The nominal current in the solenoid is 7.73 kA. Charging and discharging the solenoid takes about 30 minutes. When a quench occurs, the temperature of the cold mass is enhanced to a safe value of 120 K, after which it takes

about one day to re-cool the system to the operational temperature of 4.5 K.
In the Inner Detector cavity, for which the solenoid is providing the magnetic field, the driving design consideration was the absolute accuracy of the momentum scale of charged particles, which is why a very uniform field is needed. A target of $\sim 5 \times 10^{-4}$ was set on the uncertainty of the bending power determination, such that it nearly does not have any influence on the momentum resolution uncertainty, as the other source of this uncertainty, the relative alignment of ID components, was unlikely to improve beyond the 1 µm level. This stringent requirement is met by in-situ mapping with dedicated instrumentation within the ID cavity right after installing the solenoid. Potential long-term drifts of the absolute scale are determined with high accuracy by permanently installed NMR probes.

Barrel and End-Cap Toroids

The toroids' magnetic field of about 0.5 T in the barrel region and 1 T in the end-caps is meant to deflect tracks of muons that are to be detected in the muon spectrometer which is the outermost subsystem of ATLAS. The barrel toroid, as can be seen in Figure 3.7, consists of eight coils which are encased in individual racetrack-shaped stainless-steel vacuum vessels. The total barrel toroid system has a length of 25.3 m, and inner and outer radii of 9.4 m and 20.1 m, respectively. Its magnetic field is filling all the cylindrical volume outside the calorimeters and both end-cap toroids. Like the coils of the end-cap toroid, the ones of the barrel part are made of pure Al-stabilised Nb/Ti/Cu conductor windings. The nominal current in the barrel toroid is 20.5 kA, which can be ramped up to within 2 hours. A fast dump within 2 minutes can be achieved in case of a quench. The safe cold-mass temperature achieved by such a dump, which immediately forces the magnet into a normal-conducting state, is 58 K.

The end-cap toroids generate the magnetic field needed for the bending of muon tracks in the end-cap regions. As can be seen from Figure 3.8, it consists of eight square coil units as well as eight keystone wedges. They can slide along supporting rails in order to ease the opening of the detector for maintenance work. With a total weight of 240 t, the end-cap toroids were the heaviest sub-system in ATLAS. This had to be accounted for during the integration by leaving space for slight deformation of the support structure after inserting the end-cap toroids, which was achieved with high precision. The nominal current in the end-cap toroid is 20.5 kA as in the barrel part.

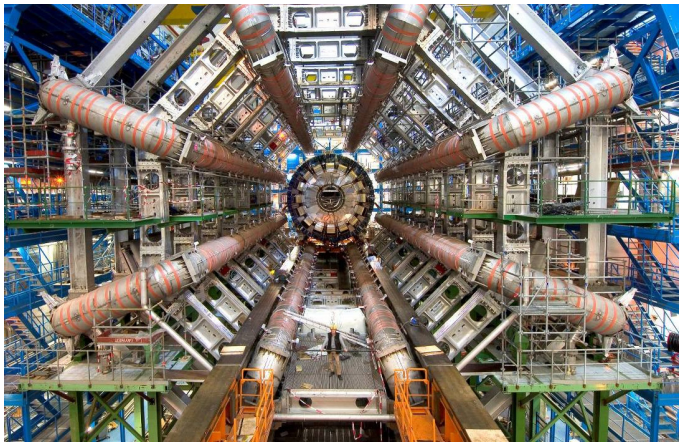

Figure 3.7.: Barrel toroid as installed in the underground cavern, the scale is indicated by the person standing in the middle [1].

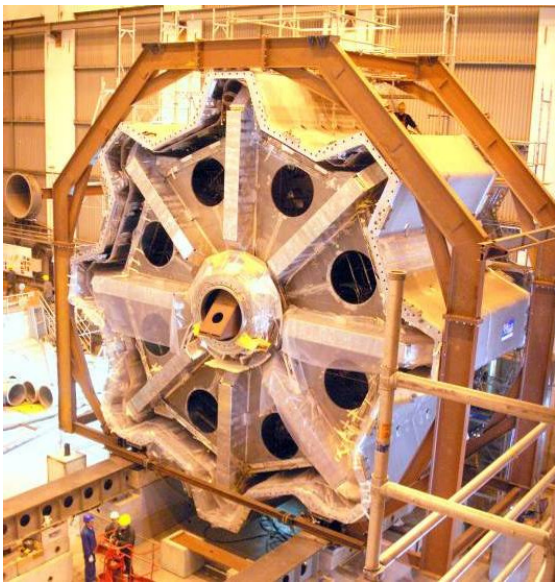

Figure 3.8.: End-cap toroid cold mass inserted into the cryostat. The eight flat, square coil units and eight keystone wedges (with the circular holes) are visible [1].

In the muon spectrometer region, the magnetic field is much more inhomogeneous than in the ID region. The extraction of the muon momentum from MDT (Monitored Drift Tube, see 3.2.5) measurements, the field integral between consecutive chambers has to be known to great precision along the muon trajectory. As the field is non-uniform in this area, the field gradient can reach up to 1 mT/mm. This leads to the fact that local bending power uncertainties translate into fluctuations of the momentum scale from one spatial region into another, adding up in quadrature to the overall muon momentum resolution. For one muon trajectory, there are three sources of uncertainty on the measured curvature: Field measurement errors, accuracy on the alignment of muon chambers and magnet coils as well as trajectory measurement errors. As a design goal, the total muon momentum resolution uncertainty from these three sources combined was meant to not exceed 5%. As the field in the toroids is that non-uniform over a large volume, in-site measurements would not have been a useful choice to obtain precise field maps. Instead, the toroids are equipped with about 1840 B-field sensors. This setup meets the specifications mentioned above, given that the sensors' measurements are accurate up to $\sim$1 mT and the field direction is measured within $\pm$ 3 mrad.

3.2.4. Calorimeters

For the energy measurement of the particles produced in pp collisions, a calorimeter system designed to capture electromagnetic and hadronic particle showers and to absorb their full energy is necessary. The ATLAS calorimeter system covers an η range up to 4.9 and uses different techniques, such that it is suited for the various physics processes as well as for the varying radiation environment. It consists of an electromagnetic and a hadronic calorimeter, which will be described in the following. Figure 3.9 gives an overview over the calorimeter system.

In the η range of the Inner Detector, the granularity of the electromagnetic calorimeter is high enough for precise electron and photon measurements, while in the remaining part the calorimeters are coarser, but sufficient for jet reconstruction and E_T^{miss} measurements[2]. The calorimeter depth is an important design criterion, as it has to be assured that electromagnetic and hadronic showers are reasonably well contained and punch-through

[2] E_T^{miss} denotes missing transverse momentum in the transverse plane, as will be discussed in section 5.6 in Chapter 5.

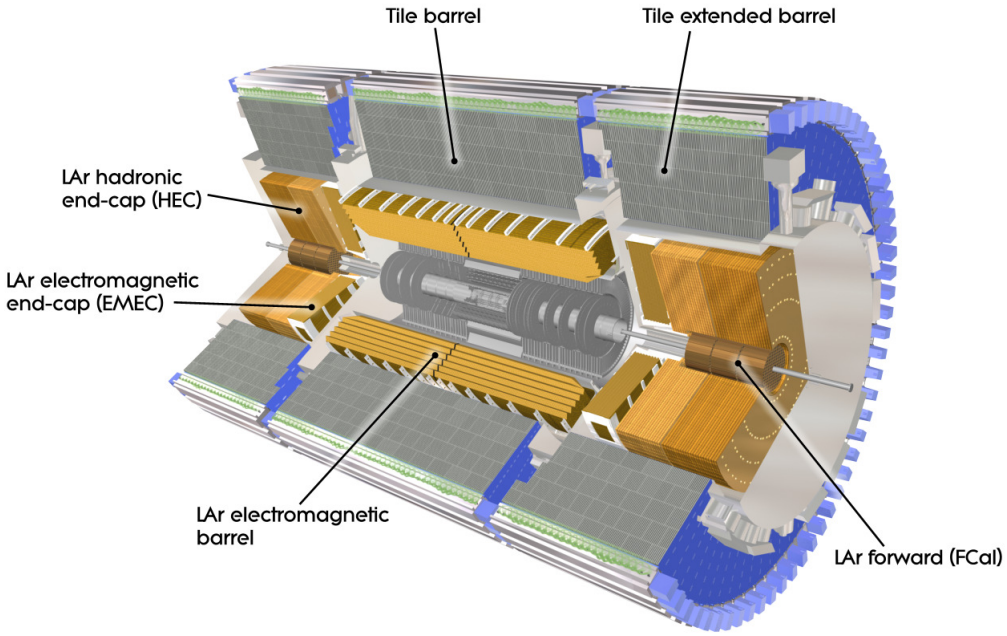

Figure 3.9.: Cut-away view of the ATLAS calorimeter system [1].

into the Muon System is limited. Therefore the total thickness of the barrel calorimeter has been chosen to be $> 22\,X_0$ and of the end-caps $> 24\,X_0$. This translates to approximately 9.7 interaction lengths (λ) in the barrel and 10 λ in the end-caps, which is sufficient to achieve good resolution for high-p_T particle jets.

Electromagnetic Calorimeter

The electromagnetic calorimeter (ECAL), which is situated outside the Inner Detector, is a detector with lead absorbers and LAr as active material, assembled in accordion shape, with kapton electrodes and lead absorbers over the full range of its coverage. It is divided into a barrel part ($|\eta| < 1.475$) and two end-caps ($1.375 < |\eta| < 3.2$), each one of which is sitting inside its own cryostat. They share a vacuum vessel with the central solenoid in order to cut down on two vacuum walls and thus to reduce material. The barrel part is divided into two half-barrels of inner and outer diameters of 2.8 m and 4 m, respectively, and a length of 3.2 m each, which leaves a small gap of 4 mm in the centre. One half-barrel has a weight of 57 t and is made up of 1024 absorbers. Each end-cap is made up of two coaxial wheels, the boundary between which sits at $|\eta| = 2.5$. Each wheel has a thickness of

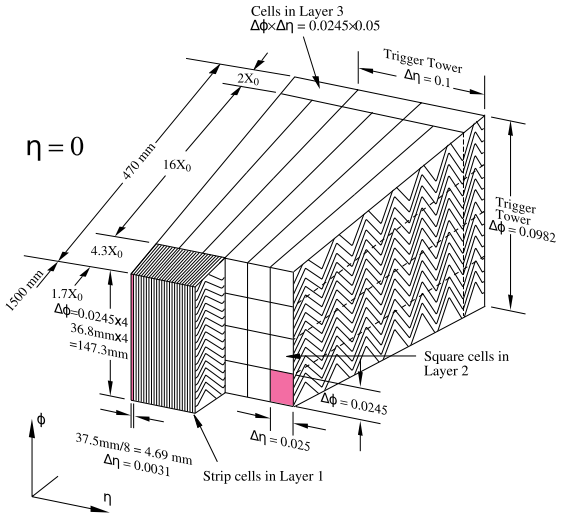

Figure 3.10.: Sketch of a barrel module of the ATLAS ECAL [1].

63 cm and weighs 27 t. As there is material of up to several X_0 in front of the calorimeter in the transition region between barrel and end-cap part, a LAr presampler was installed in front of the end-cap calorimeter in order to improve the energy measurement in this region. Each end-cap outer wheel consists of 768 absorbers interleaved with electrodes and each inner wheel of 256 absorbers. Similarly to the barrel part, the end-cap calorimeter is divided into three layers in depth within the precision region of $1.5 < |\eta| < 2.5$, with decreasing granularity going from the interaction point to the outer layers.

The accordion geometry, which is displayed in Figure 3.10, assures total Φ symmetry without azimuthal cracks and thus uniform performance. The accordion structure is designed such that the liquid-argon gap is kept constant in the barrel part and it increases in amplitude with increasing radius to account for the increasing gap in the end-cap part. For the high-granularity range ($|\eta| < 2.5$), the barrel calorimeter is divided into three sections in depth, the first one of which has the finest segmentation in η, while the second one usually contains the bulk of the shower and the third layer, usually only collecting the tail of the shower, is least granular. In the very central region of $|\eta| < 1.8$, an additional presampler detector made of an active LAr layer of 1.1 cm (0.5 cm) thickness in the barrel (end-cap) region is installed in front of the first layer of the rest of the calorimeter in order to correct for energy losses from photons and electrons upstream of the calorimeter. It is made of 32 identical sectors of 3.1 m length and 0.28 m width per half-barrel, covering a region of $\Delta\eta \times \Delta\Phi = 1.52 \times 0.2$.

The lead absorbers are 1.53 mm thick in the region of $|\eta| < 0.8$ and 1.13 mm for $|\eta| > 0.8$. This decrease in thickness compensates the otherwise increasing sampling fraction for larger $|\eta|$ values. The lead plates in the end-caps have a thickness of 1.7 mm for $|\eta| < 2.5$ and 2.2 mm for $|\eta| > 2.5$, respectively. The readout electrodes made of three copper layers separated by insulating polyimide sheets are placed in the gaps between the absorbers.

Hadronic Calorimeter

The hadronic calorimeter (HCAL), which is placed outside the ECAL, consists of three subsystems: the tile calorimeter, the liquid-argon hadronic end-cap calorimeter (HEC) and the liquid-argon forward calorimeter (FCal).
The tile calorimeter is a sampling calorimeter with steel absorbers and scintillators as active material. It covers the region of $|\eta| < 1.7$ and is made up of a 5.8 m long central barrel and two 2.6 m long extended barrels, all of which are having an inner and outer radius of 2.28 m and 4.25 m, respectively. The radial depth is about 7.4λ. Each of the 64 tile calorimeter modules is a wedge made of steel plates and scintillating tiles covering $\Delta\Phi \sim 0.1$. Homogeneous azimuthal coverage is assured by the orientation of the tiles (radial and normal to the beam pipe) and by wavelength-shifting fibre readout at the end of the tiles. The way the readout fibres are grouped to readout photo multiplier tubes (PMTs), assures a projective geometry in η. In the gap region between barrel and extended barrel (the so-called *crack region*), some of the lost energy is recovered by special instrumentation in that area, consisting of steel-scintillator sandwiches of which the sampling fraction is accustomed to the available space. In order to minimise inactive material, the mechanical structure of the tile calorimeter is designed to be self-supporting and the steel girder, each module sits on is also used as a flux return for the solenoid magnet. The tile calorimeter is also equipped with three calibration systems, which - among other tests - are used to set the PMT gains to uniform values of $\pm 3\%$.
As an active medium, in total more than 460k 3 mm thick scintillator tiles of eleven different sizes (for eleven radial positions in one wedge) are used. In the base material polystyrene, crossing ionising particles induce the production of UV light, which is converted to visible light by wavelength-shifting fluor, which the polystyrene is doped with. The scintillation light is collected and converted into longer wavelength light by wavelength-shifting fibres put into contact with the tile edges. The fibres are aluminated at the end opposite to the PMT in order to increase the light output.

The hadronic end-cap calorimeter is a sampling calorimeter made of copper and liquid-argon covering the range $1.5 < |\eta| < 3.2$. For each end-cap, the HEC consists of a front wheel and a rear wheel, each one consisting of 32 identical wedge-shaped modules. The sampling fraction in the front wheels is larger (4.4%) than in the rear wheels (2.2%), to account for the higher particle density closer to the interaction point. The 8.5 mm thick gaps between the 25 mm thick copper plates are each divided into four different LAr drift zones by three electrodes. The signals collected by this electrode structure are amplified by GaAs amplifiers, which assure an optimum signal-to-noise ratio in cold environments. The signal which is finally read out is summed over eight or sixteen pads (one pad being etched onto the central foil in each gap), which form a readout section. An important consequence of the HEC is its possibility to measure any radiative energy loss and to detect muons, which will be important for the correct measurement of E_T^{miss} (as will become clear in section 5.6). The forward calorimeters are designed to build a quite hermetic system with the HEC, which minimises energy losses in cracks between the different components and backgrounds that reach the muon system. They cover a range of $3.1 < |\eta| < 4.9$. At the high pseudorapidity the FCal modules are situated at, they are exposed to high particle fluxes, which is the reason for their liquid-argon gaps being designed to be small. These smaller gaps avoid problems induced by ion build-up, while providing the highest possible density. Each of the two FCals is made up of three consecutive 45 cm deep modules: An electromagnetic module (FCal1) and two hadronic ones (FCal2, FCal3). FCal1 consists of copper absorbers, while FCal2 and FCal3 are mainly made of tungsten absorbers, a design which is a trade-off between resolution and heat removal on one hand and minimisation of the lateral spread of hadronic showers on the other hand. In FCal2 and FCal3 the amount of tungsten is maximised in order to optimise for a high absorption length. The modules are made of two copper end-plates each, spanned by electrode structure of co-axial tungsten rods and a copper tube separated by plastic fibre. Signals are read out on different sides of the different FCal parts, in order to spare out the region of highest radiation damage. The signals are then routed to the FCal summing modules where they are summed before they leave the detector.

3.2.5. Muon System

The muon spectrometer, which is designed to detect particles which penetrate the calorimeter system, is the outermost subsystem of the ATLAS detector. It measures particle momenta

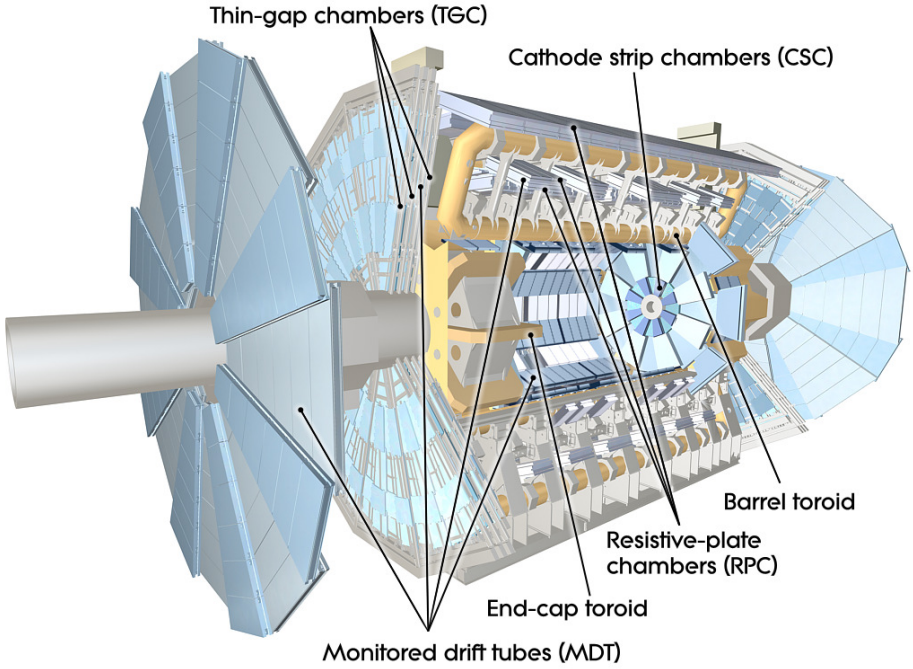

Figure 3.11.: Cut-away view of the ATLAS muon system [1].

in the region $|\eta| < 2.7$ and is used within the trigger system (see section 3.3) in the region $|\eta| < 2.4$. The main design goal was a p_T resolution of 10% for 1 TeV tracks, while staying performant down to muon momenta of a few GeV. Figure 3.11 shows an overview of the muon system. The Φ symmetry of the toroid is mirrored in the symmetric design of the muon system, which consists of eight octants. Each of these octants is itself divided into a larger and a smaller sector, which are assembled such that they overlap in order to assure maximum coverage.

The muon spectrometer which is split into four layers and different detector types consists of two subsystems: precision-measurement tracking chambers, which are complemented by trigger chambers. The tracking chambers are again subdivided into monitored drift tube chambers (MDTs), which are responsible for precision momentum measurements within $|\eta| < 2.7$ for the outer three layers, and cathode strip chambers (CSCs), which complete the coverage in the innermost chamber layer, covering the range $2.0 < |\eta| < 2.7$, where the MDTs only extend up to $|\eta| < 2.0$. The reason for this choice is the higher rate capability and time resolution of the CSCs. The MDTs are made of three to eight layers of pressurised drift tubes with a diameter of ∼30 mm, operating with a 93/7 ratio of Ar and CO_2 gas. A central tungsten-rhenium wire with a diameter of 50 µm sitting at a potential

of 3080 V is responsible for collecting the electrons stemming from ionisation processes. As the cylindrical geometry results in radial electric fields, the measurement accuracy hardly depends on the muon's incident angle, which assures a homogeneous drift-time resolution. Per tube, the average momentum resolution is 80 µm, which corresponds to 35 µm per chamber. A disadvantage of the geometry, though, are relatively long drift times from the wall to the wire, which open up the possibility of not only one threshold crossing per track, but several ones after each other. As only the arrival time of the closest track segment to the wire is relevant to assign a track coordinate, an adjustable dead-time was implemented in the front-end electronics in order to avoid unnecessary data volume inflation. The long drift times of up to 700 ns are also partly due to the non-linearity of the chosen gas admixture, which causes a reduction of spatial resolution especially at high rates above 150 $\mathrm{Hz/cm^2}$. However, the admixture is beneficial since no deposits on wires have ever been observed and the formation of polymers is not possible. Thus, in order to restore the resolution in the region with the highest track density, the MDTs are partly replaced by CSCs. CSCs are multiwire proportional chambers with radially oriented wires (parallel to the central wire). The cathode planes are segmented into strips in orthogonal direction, in order to measure also the second coordinate. With this technique, much higher counting rates of up to 1000 $\mathrm{Hz/cm^2}$ can be dealt with. With a readout pitch of ∼5 mm, which is a trade-off between too high costs for the readout electronics and achieved resolution, the CSC has a resolution of 60 µm per plane in the bending direction, to be compared to the 80 µm per MDT tube layer. The good two-track resolution, small electron drift times of less than 40 ns and low neutron sensitivity because of the small gas volume are additional factors that make the CSC suitable for high particle density regions. Another advantage is the possibility to combine the measurements of the two coordinates via the pulse height in order to circumvent ambiguities arising from more than one track being present at a time. The trigger chambers consist of resistive plate chambers (RPCs) covering the range $|\eta| < 1.05$ and thin gap chambers (TGCs) in the range $1.05 < |\eta| < 2.4$. They allow for triggering on muons, which comes with the requirement of track info being passed on within a few tens of nanoseconds after the muon has passed. Other requirements are bunch-crossing identification, measurement of the second coordinate in the non-bending projection to complement the MDT measurement and robustness against random hits stemming from photon or neutron background. Another requirement for the trigger chambers is to provide acceptance over a wide η and the full Φ range, which is challenging as the muon momentum for a given p_T is strongly dependent on the η value. As the bending power does not increase

as much with increasing η, an η-dependent increase of granularity is needed in the end-caps, in order to match the p_T resolution of the barrel part. All of these requirements are met using two different technologies.

The RPCs, three concentric double-layers of which are used in the barrel region, have no wires, which makes them robust against small deviations from planarity. They provide good spatial and time resolution and a sufficiently good rate capability for the central region, where particle fluxes are not that high. The RPCs are gaseous detectors of two parallel resistive plastic laminate plates in a distance of 2 mm to one another. In the electric field between the plates, avalanches towards the anode form along the tracks of ionising particles. The signals are read out via capacitive coupling to metallic strips located on the outer sides of the plates. The gas admixture of $C_2H_2F_4$/Iso-C_4H_10/SF_6 in a 94.7/5/0.3 ratio provides a plateau for safe avalanche building while keeping cost and inflammability low. The strong and uniform electric field inside an RPC cell leads to the fact that all primary electron clusters simultaneously cause avalanches, such that one single signal is produced after the passage of an ionising particle. The charge multiplication continues until the arrival at the anode, which is why the gas gain primarily depends on the distance between the track and the anode. In the end-cap region, four layers of TGCs are used, which operate on the same principle as multiwire proportional chambers, and provide the high rate capability needed in the very forward region. In the barrel part, the first two RPC layers are forming a sandwich with the middle MDT layer, while the third RPC layer is located close to the outermost MDT layer. In the end-cap region the first TGC layer is in front of and the second and third one behind the second MDT wheel, while the fourth layer is situated in front of the innermost layer of muon tracking chambers. The main requirements for the TGCs are good time resolution, in order to tag beam-crossings, and fine granularity in order to provide a relatively sharp cut-off in the momentum of the triggered muon. A TGC's specific feature is that the distance between wires and cathode is smaller than the distance between neighbouring wires. These wires are grouped into sets of varying size depending on η, matching the change in required momentum resolution and granularity over the pseudorapidity range. A good time resolution is achieved for the majority of tracks by the small wire-to-wire distance and the high electric field. The only kind of tracks, for which the time resolution is worse, are the ones with normal incidence between two wires, as the drift field vanishes in these regions. However, tracks from the interaction point, that traverse the TGC wheels, have incident angles of at least 10°, such that at least some part of the track will be outside of such a low-field region.

Both trigger chambers provide signals with a small spread of 15 ns to 25 ns, which allows to tag different bunch crossings. A common issue for the trigger chambers is the inhomogeneous magnetic field distribution in the transition between barrel and end-cap systems, which leads to nearly zero bending power in some regions. In order to avoid fake trigger signals which are wrongly attributed to high-p_T tracks, this region is excluded from the trigger algorithm. Another feature concerning both types of trigger chambers is the coincidence condition established separately in η and Φ directions, in order to suppress fake triggers due to random combinations of converted photons. The trigger algorithm is a set of coincidences of the last three trigger chamber layers, taking into account the bending of a track in order to judge whether a certain p_T criterion is satisfied.

3.3. Data Acquisition and Trigger

As proton bunches are crossing within the ATLAS experiment with a frequency of about 40 MHz, a strategy had to be developed to cope with the enormous amount of resulting data, which is impossible to fully store on disk. A three-fold trigger system is therefore implemented, to filter out only potentially interesting events for data analyses and by doing so to drastically reduce the amount of data to be stored. It consists on a custom-made hardware-based Level-1 (L1) trigger and a high-level trigger (HLT) consisting of the software-based Level-2 (L2) trigger and the Event Filter (EF), which is based on offline reconstruction algorithms. The L1 trigger scans the data for signatures of high-p_T particles (muons, electrons/photons, jets and hadronically decaying τ leptons) and events with large (missing) transverse energy, by using only reduced-granularity information from a subset of detectors (RPC and TGC for muons and all calorimeter subsystems for the other objects). By this procedure, the rate is reduced to about 75 kHz, which is the maximum accept rate of the L1 trigger that the readout system can handle, as the data acquisition (DAQ) system receives and buffers the event data at this rate until the next steps in the trigger chain have decided whether or not to further keep them. If the L1 trigger has identified one of the possible trigger objects described above, a region of interest (RoI) is built around it, given by a certain region in η and Φ. This RoI is used to seed the L2 trigger, which uses information about coordinates, energy, and signature types to further reduce the amount of data. The decision is based on a set of selection criteria on p_T thresholds and alike, which reduces the rate to 3.5 kHz. All events passing the L2 criteria are handed to the event

builder, from which the assembled events are shipped by the DAQ system to the EF. The EF uses detailed offline analysis methods and further selects events which fulfil certain criteria to reduce the rate further to 200 Hz. The full granularity and precision of the calorimeters and muon chamber information is used for both HLT decisions. Events selected by the HLT are then moved to permanent storage. Such an event has an approximate size of 1.3 MB.
The set of thresholds and selection criteria for the different trigger stages is defined in the so-called trigger menu. A menu can consist of up to 256 different items, each item being a combination of requirements on the input data. This way, various requirements for different kinds of physics analyses can be met. For the development of different items, which is an iterative process, rejection and rate capabilities are taken into account. A trigger item corresponds to a certain physics object to be selected. They are denoted by a nomenclature in which the object's symbol is preceded by the required multiplicity and followed by a short notation for the energy threshold. For example, the item `2e5` describes the requirement for two electrons with an energy of at least 5 GeV to be present in the event, for the event to be selected. The trigger item passed by the event is also written out such that in the later stage of the offline analysis a decision can be taken which triggers to use. An option to further reduce the needed storage space and especially to account for varying luminosity and background conditions, is the so-called *pre-scaling* of trigger menu items. This means that of the events passing a given set of selection criteria, only a randomised subset (defined in size by the chosen pre-scale factor) is stored.
In this analysis, single electron and single muon triggers are used, the parameters of which are described in section 5.2.4 and 5.3.4.

3.4. Luminosity Determination

Due to the relation between the integrated luminosity L, the event count N and the cross section σ of a process,

$$N = \sigma \cdot L, \tag{3.6}$$

it is very important to precisely determine the luminosity provided by the LHC in order to perform cross-section measurements of SM processes, but also to precisely determine the background yield in new physics searches. This quantity is the time integral of the

instantaneous luminosity $\mathscr{L}$,

$$L = \int \mathscr{L} dt, \tag{3.7}$$

and – for a pp collider – can e.g. be measured from

$$\mathscr{L} = \frac{R_{inel}}{\sigma_{inel}}. \tag{3.8}$$

Here, R_{inel} and σ_{inel} are the rate and cross section of inelastic proton-proton collisions. For a ring collider like the LHC this can be rewritten as

$$\mathscr{L} = \frac{\mu n_b f_r}{\sigma_{inel}}, \tag{3.9}$$

with μ being the average number of inelastic interactions per bunch crossing, n_b the number of colliding bunch pairs (in case of asymmetrically filled beams this is the number of bunches in the beam filled with less bunches) and f_r the revolution frequency of a bunch. For a given detector and algorithm, this translates into

$$\mathscr{L} = \frac{\mu_{vis} n_b f_r}{\sigma_{vis}}, \tag{3.10}$$

where the relation between the true and the visible quantities is $\mu(\sigma)_{vis} = \epsilon\mu(\sigma)$ with ϵ being the efficiency of a particular detector and reconstruction algorithm.
The luminosity measurement in ATLAS, as described in [56], is based on Eq. 3.10: the observed inelastic interaction rate per crossing, μ_{vis}, is an observable quantity which is continuously measured during data taking by various independent detectors and algorithms, both of which will be briefly described further down. To relate that quantity to the instantaneous luminosity, it has to be calibrated via a rather laborious measurement of the latter one, which corresponds to retrieving the missing factor, the visible cross section σ_{vis}. This measurement of the instantaneous luminosity is performed by dedicated beam-separation scans, exploiting the following relation between the luminosity and certain beam parameters:

$$\mathscr{L} = \frac{n_b f_r n_1 n_2}{2\pi \Sigma_x \Sigma_y}. \tag{3.11}$$

Here, $n_{1/2}$ are the numbers of protons per bunch in the two beams and $\Sigma_{x/y}$ are the convolved beam widths in the two directions perpendicular to the beam axis. In so-called *van der Meer (vdM)* (beam separation) scans, which are part of the underlying method proposed by van der Meer [57], these widths are measured by separating the two beams by steps of known distance. By doing so, the maximum value of the visible interaction rate, μ_{vis}^{max}, is determined and used in the relation

$$\sigma_{vis} = \frac{2\pi\Sigma_x\Sigma_y}{n_1 n_2}\mu_{vis}^{max}, \tag{3.12}$$

which is obtained by equating Eq. 3.10 and 3.11. An independent measurement of the bunch population product $n_1 n_2$ provides the last missing ingredient to calculate the luminosity. These dedicated processes can not be performed during normal data taking periods and are usually only done once or twice a year using special beam optics. In future data taking periods, the *vdM* scans will be replaced by a measurement of the luminosity scale by a dedicated detector, ALFA (Absolute Luminosity For ATLAS [58]), which is located 240 m from the interaction point, on either side. It uses a roman-pot technique which means that its volume is separated from the beam, but can be moved very close to it (down to 1 mm). The roman pot contains a scintillating-fibre tracker for particle detection.
Once the above described calibration process has been done for a given detector and algorithm, the observed inelastic interaction rate per bunch crossing, μ_{vis}, obtained with that particular setup can be used as a continuous luminosity monitor. For its determination, several algorithms are made use of: So-called *event counting* algorithms, which detect the presence of at least one inelastic *pp* collision in a given bunch crossing by using pre-defined criteria. However, with increasing interaction rates, these algorithms saturate, once the average number of inelastic collisions per bunch crossing approaches one, which was the case for the data analysed in this thesis. For this region, more granular algorithms exist, like *hit counting* or even *particle counting* algorithms. They identify the number of inelastic interactions by the number of readout channels which are above a certain threshold or (for detectors with very fine granularity) how many particles enter the detector. These algorithms saturate at much larger values of μ_{vis}.
For the measurement of μ_{vis} two independent detectors have been used in the 2012 data taking period, which measure the rates on a bunch-by-bunch basis. LUCID (LUminosity measurement using a Cherenkov Integrating Detector, [59]) is a Cherenkov detector, of which the two parts are situated 17 m upstream/downstream the interaction point. It

consists of 16 aluminium tubes filled with C_4F_{10} gas, which are placed around the beam pipe with the tubes parallel to the beam pipe. LUCID covers the very forward region $5.6 < |\eta| < 6.0$. It measures charged particles by detecting their emitted Cherenkov light and amplifying it in photo multipliers. BCM (Beam Conditions Monitor, [60]) is a detector consisting of four diamond sensors which are sitting on either side of the interaction point at $|\eta| = 4.2$. Besides its main purpose, the monitoring of beam conditions and the triggering of beam aborts if necessary, it is also capable of measuring the bunch-by-bunch interaction rates. Measurements carried out by the tile and forward hadronic calorimeters are used to crosscheck the results obtained by the above mentioned detectors.
For the measurement of the total integrated luminosity, a systematic uncertainty of 1.8% has to be taken into account, which is derived from the systematic effects of both luminosity detectors and algorithms used [56].
Once the luminosity is precisely measured, it can be used to scale simulated background and signal processes to their respective cross sections, which is crucial for nearly all ATLAS data analyses. The procedure of event simulation will be described in the next chapter.

Chapter 4.

Data Sample and Event Simulation

4.1. Data Sample

In the 2012 data taking period, the ATLAS detector collected more than 93% of the collision events provided by the LHC with a centre-of-mass energy of $\sqrt{s} = 8\,\text{TeV}$. Sorting out events collected with an incomplete set of subdetectors or unstable detector conditions, 95.3% of the collected data can be used for physics analyses. These events add up to a total integrated luminosity of $20.3\,\text{fb}^{-1}$. The very high data collection efficiency of the ATLAS detector can be read off from Figure 4.1.

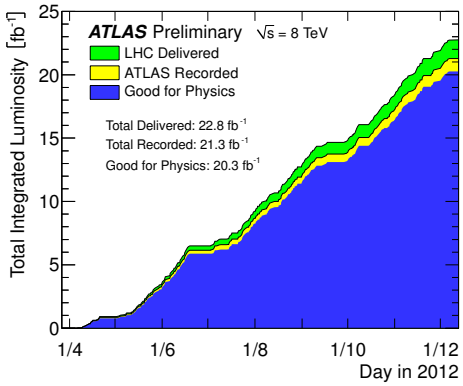

Figure 4.1.: Integrated luminosity provided by the LHC and collected by ATLAS during the data taking period in the year 2012 [61].

As in this analysis events with electrons or muons in the final state were selected, the Egamma and Muons stream[1] were used, established by the trigger system as described in section 3.3. The total number of events in these streams for the full data taking period are listed in Table 4.1.

Table 4.1.: Total event number per stream for the 2012 data taking period, with data quality sufficient for physics analyses.

data stream	Egamma	Muons
number of events	699 783 096	665 809 664

In order to structure the collected data, events are grouped into so-called *runs* during data taking, each run corresponding to one LHC fill. The runs have ascending numbers and within each run, the events are numbered as well. In order to identify a given event, one thus has to know the pair of run and event number. This information is stored along the physics data of every event and can thus be used later during the analysis, to select single events for testing purposes or to make sure that each event is only counted once.
At LHC run conditions it is not assured that one event only consists of contributions from one single proton-proton collision. At instantaneous luminosities of up to $8 \times 10^{33}\,\mathrm{cm}^{-2}\mathrm{s}^{-1}$, it is very likely that pileup occurs, i.e. more than two protons from two given proton bunches collide. The distribution of the number of interactions per bunch crossing for the 2011 and 2012 data taking periods is shown in Figure 4.2. This leads to the presence of several primary interaction vertices at a time, which is shown as well. The vertex with the highest sum of transverse momenta of all associated tracks is chosen, and the event is stored. However, the event can have contributions from particles stemming from one of the other vertices. This phenomenon is commonly called *in-time pileup*.

An event can in addition also have contributions from particles stemming from a proton-proton collision from an earlier bunch crossing. This is referred to as *out-of-time pileup*. Both sources of pileup need to be corrected for on the analysis level in order to be able to apply conservation laws which only apply to separated proton-proton interactions.

[1] A *stream* is a collection of data events that have passed a particular trigger decision. Events that have fired one of the muon triggers (as will be described in section 5.3.4) end up in the Muons stream, while the Egamma stream contains all events that have fired one of the electron triggers (as will be described in section 5.2.4). The overlap between both streams is removed during the analysis in order to avoid double counting.

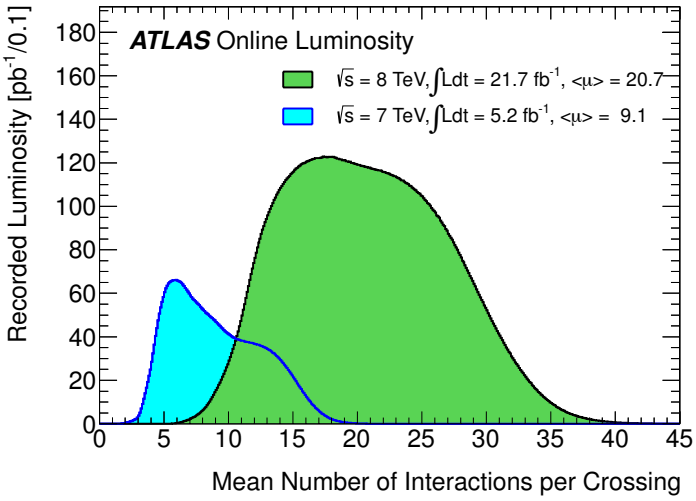

(a)

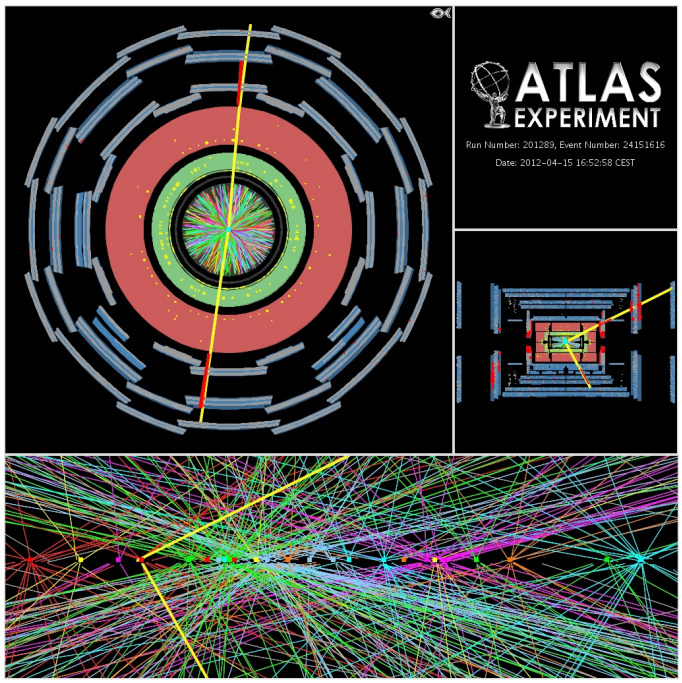

(b)

Figure 4.2.: (a) Luminosity-weighted distributions of the mean number of interactions per bunch crossing in the 2011 and 2012 proton-proton data sets. The mean number of interactions per crossing corresponds to the mean of a Poisson distribution of the number of interactions per crossing calculated for each bunch. On average, there were more than 20 interactions per bunch crossing in the 2012 data [61]. (b) Event display of a candidate for a $Z \to \mu^+\mu^-$ event from the 2012 data set. The top-left panel shows a cross section of the transverse plane, while the bottom panel shows the spatial distribution of the 25 reconstructed vertices along the beam axis [62].

Dedicated pileup-suppression techniques have been developed and will be described in more detail in the respective sections of the reconstruction of various physics objects in chapter 5. The collected data set is complemented by simulated data sets needed for a thorough understanding of the physics processes present in the real proton-proton collision data, which will be described in the next sections.

4.2. Event Generation

In order to determine, whether the measured data is in accordance with known Standard Model processes or potentially compatible with a new physics process under study, one has to simulate proton-proton collision events for the known processes and for the new one. The details of this procedure, which is carried out using Monte-Carlo event generators, will be described in this section. While the majority of events produced at the LHC are stemming from soft QCD processes, which have to be modelled with phenomenological models, in the simulation of a typical new physics or corresponding background event, several steps have to be followed [63]:

- The **hard subprocess** is the interaction of two partons (either from the valence quarks *uud* or sea quarks, anti-quarks or gluons) from the colliding protons, in which heavy objects like e.g. W bosons or objects with high p_T are created, or where a large amount of momentum is transferred to the produced particles. It is the core of the simulation procedure, as it is the part that is determined by the user's choice of the kind of process of interest. Usually, a large number of events of a certain kind of hard subprocess are generated at once, resulting in what is commonly called a *Monte-Carlo sample* of the given physics process, rather than producing generic events, which would result in small numbers of the respective processes under study.
- A **parton shower algorithm** is then needed, as the partons going into and partly also resulting from the hard process can radiate gluons, which in turn can radiate gluons or produce quark-antiquark pairs. This leads to cascades, or *showers*, of partons. These showers are simulated using step-wise Markov chains, where at each stage it is randomly chosen whether or not a new parton (pair) is added. The algorithm starts from the momentum scale defined by the hard process, evolving forward for the outgoing partons and backwards for the incoming ones.

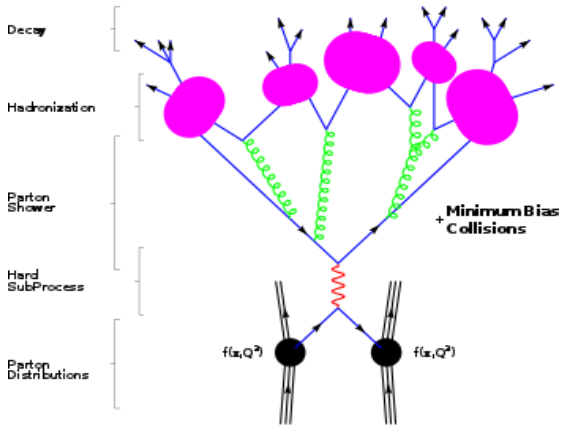

Figure 4.3.: Basic structure of a generated event, from the hard subprocess of two partons through showering and hadronisation to the decay of the formed hadrons [65].

- It is possible, that more than one parton pair from the incoming protons interact. These multiple partonic interactions and all other activity unrelated to the hard subprocess, generally referred to as **underlying event**, need to be modelled as well, as they can contribute to all kinds of observables.
- After hitting a certain threshold in the downwards evolution of the momentum scale during the showering process, QCD becomes strongly interacting and can no longer be described perturbatively. At this point, a non-perturbative model takes over, describing the **hadronisation** of coloured partons into colourless hadrons.
- Many of the hadrons produced in the previous step are unstable resonances, which is why at the last stage **hadron decays** need to be modelled, resulting in lighter hadrons, which are long-lived enough to reach the detector. In ATLAS simulations, a hadron is considered stable, if its decay length satisfies $c\tau > 10\,\text{mm}$ [64].

The various steps, which are also sketched in Figure 4.3 are discussed in more detail in the following sections with most of the information taken from [63], after a short discussion of parton distribution functions and the choice of two scales which are important for event generation.

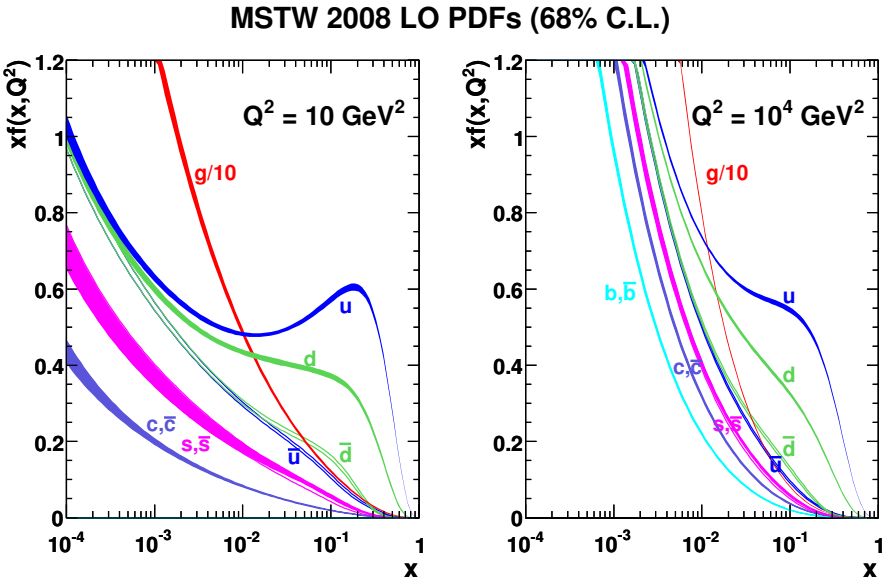

Figure 4.4.: MSTW2008LO parton distribution functions at $Q^2 = 10\,\mathrm{GeV}^2$ (left) and $Q^2 = 10^4\,\mathrm{GeV}^2$ (right) [66].

4.2.1. Parton Distribution Functions

In a collision of two protons, the longitudinal proton momenta P are shared among their constituents. Each parton carries a momentum fraction xP, x being the Bjorken variable. As the hard subprocess is initiated by single partons, these momentum fractions define the kinematics of the resulting events and are therefore an important object to various studies. The distribution functions of x for the various parton species can not be described by perturbative QCD, because the interactions inside the proton happen at a low momentum transfer Q which goes in line with large strong couplings $\alpha_s(Q)$. The so-called parton distribution functions (PDF) are thus not calculable from first principles and have to be determined by experiments. They are measured in deep inelastic electron-proton scattering experiments, at electron-proton colliders or fixed target experiments. Several groups are analysing data and providing PDF and the corresponding uncertainties to the particle physics community, such as MSTW [66] or CTEQ [67, 68]. Figure 4.4 shows the PDF $f_i(x)$ multiplied by the momentum fraction x as provided by the MSTW group as well as their 68% confidence intervals for the different parton species at two different momentum scales.

The function $f_i(x, Q^2)$, with Q^2 being the scale of the scattering off the parton, corresponds to the probability density of finding a parton of a given kind at a momentum

fraction x inside the proton. The region of small x is dominated by gluons, while quarks also populate the region of higher x values.

Factorisation and Renormalisation Scales

When considering gluon radiation of the partons contributing to the collision event, the resulting modifications to the calculated cross section have to be accounted for. Soft (low p_T) gluons, however, can not be described by perturbative QCD. One therefore defines a momentum scale, the so-called *factorisation scale* μ_F, below which gluon radiations are factored into the PDF. As this scale is an unphysical parameter, its choice is somewhat arbitrary and should not alter the overall result of the cross-section calculation, as it just shifts contributions from one part of the calculation to another. However, it could be shown that a reasonable choice of the factorisation scale is $\mu_F = Q$, where Q denotes the typical momentum scale of the process of interest [69]. For the s-channel production of a heavy quark, as it is studied in this thesis in the case of the b^* quark, the scale is given by the particle mass.
The *renormalisation scale* μ_R is the scale to which α_s is expanded and is chosen in order to avoid divergences at low Q^2. For further reading please see [15]. It is also commonly chosen to be of the order of the process' inertial momentum scale Q.
Both scales have to be chosen in order to fully define the formula for obtaining the cross section, which will be given in the following section.

4.2.2. Generation of the Hard Process

As stated earlier, the processes of interest at the LHC occur at high energy scales, which means that the QCD quanta are asymptotically free and reactions can be described by perturbation theory. This gives rise to the possibility of computing the features of the subprocesses of interest by using Feynman diagrams. The computation of the cross section

for a scattering subprocess $ab \to n$ is formally done via the factorisation formula:

$$\begin{aligned}\sigma &= \sum_{a,b} \int_0^1 dx_a dx_b \int f_a^{h_1}(x_a, \mu_F)\, f_b^{h_2}(x_b, \mu_F)\, d\hat{\sigma}_{ab\to n}(\mu_F, \mu_R) \\ &= \sum_{a,b} \int_0^1 dx_a dx_b \int d\Phi_n f_a^{h_1}(x_a, \mu_F)\, f_b^{h_2}(x_b, \mu_F) \times \frac{1}{2\hat{s}} |\mathcal{M}_{ab\to n}|^2 (\Phi_n; \mu_F, \mu_R),\end{aligned} \tag{4.1}$$

with

- $f_{a/b}^{h_{1/2}}$ being the parton distribution function (PDF), depending on the fraction x of the parent hadrons, $h_{1/2}$, momentum and the factorisation scale μ_F,
- $\hat{\sigma}_{ab\to n}$ being the partonic cross section of the process $ab \to n$, depending on the factorisation scale and renormalisation scale μ_R as well as on the momenta given by the final-state phase space Φ_n. It can be divided into a product of the parton flux $1/(2\hat{s}) = 1/(2x_a x_b s)$ (s being the hadronic centre-of-mass energy squared) and the square of the corresponding matrix element, $|\mathcal{M}_{ab\to n}|^2$.
- The matrix element can be re-written as a sum over Feynman diagrams:

$$\mathcal{M}_{ab\to n} = \sum_j \mathcal{F}_{ab\to n}^{(j)}. \tag{4.2}$$

- The differential phase space element $d\Phi_n$ over the n final-state particles can be expressed as

$$d\Phi_n = \prod_{i=1}^{n} \frac{d^3 p_i}{(2\pi)^3 2E_i} \cdot (2\pi)^4 \delta^{(4)}(p_a + p_b - \sum_{i=1}^{n} p_i), \tag{4.3}$$

  with p_a and p_b being the initial-state momenta, given by $x_a P_a$ and $x_b P_b$ with the respective Bjorken variables $x_{a/b}$ being integrated over and $P_{a/b}$ being the fixed hadron momenta.

Eq. 4.1 is valid to all orders in perturbation theory. However, most of the current matrix element Monte-Carlo generators are generating processes at leading order (LO), which approximately gives the correct distributions of observables, but a generally lower normalisation compared to higher order calculations. To account for these missing higher order contributions, usually the LO cross section is multiplied with a factor greater than

one, the so-called *k-factor*.
There are some multi-purpose event generators on the market like Sherpa [70], HERWIG++ [71] or Pythia (6 and 8) [72, 73], with all matrix elements for $2 \to 1$, $2 \to 2$ and $2 \to 3$ processes built in for all Standard Model and some new physics processes. However, for higher final state multiplicities, dedicated generators have to be used, either stand-alone or interfaced to a multi-purpose generator, like Alpgen [74] or MadGraph/MadEvent [75], which are both used in this analysis and which are specialised for the matrix element generation in multi-particle processes. These specialised Monte-Carlo generators perform the phase-space integration by dedicated MC integration techniques (for more details, please refer to [63]). This is necessary, as the number of Feynman diagrams contributing to a given process $ab \to n$ increases with $n!$ and textbook methods of squaring the amplitude via completeness relations cannot be used for $n > 4$ processes.

4.2.3. Shower Modelling

The hard scattering process generated according to fixed-order matrix elements, as discussed in the previous section, can approximately describe the momenta of the outgoing jets, but is lacking a description of the jet substructure as well as of any accompanying particles, which is important for a complete picture of the produced event. It is technically impossible to represent these parts by matrix elements, as they would need to be of very high order which makes the calculation time-consuming and inefficient. Instead, they can be provided by parton shower algorithms, which describe the momentum-transfer evolution from the scale of the hard process down to a scale Q_0 of about $\sim$1 GeV, at which confinement sets in and hadronisation takes over. There are two kinds of algorithms for the parton shower simulation:

- **Collinear final state evolution:**
  This approach can be exemplified by the simple process $ee \to q\bar{q}$. The differential cross section for the next-to-leading order (NLO) process, the $q\bar{q}$ pair being accompanied by an additional gluon g, is given by

$$\frac{d\sigma_{q\bar{q}g}}{dcos\theta dz} \approx \sigma_{q\bar{q}} C_F \frac{\alpha_s}{2\pi} \frac{2}{sin^2\theta} \frac{1+(1-z)^2}{z}, \tag{4.4}$$

  where the phase space is parametrised in terms of θ, the opening angle between the the quark and the radiated gluon and z, the energy fraction of the gluon with respect

to the quark it was radiated off. $C_F = (N_c^2 - 1)/N_c$ is a colour factor for N_c colour charges. At LO, the cross section is proportional to the one for $q\bar{q}$ production $\sigma_{q\bar{q}}$. The NLO differential cross section (Eq. 4.4) diverges for collinear ($\theta = 0$ or $\theta = \pi$) or soft ($z = 0$) gluon emissions. These divergences are compensated by introducing a cutoff parameter Q_0, below which a radiated gluon can no longer be resolved from the emitting (anti-) quark. The choice of this parameter is free and is adjusted such that the data is best described. In order to get an equation that can be implemented and iterated in a Monte-Carlo algorithm and is valid for all kinds of processes, Eq. 4.4 can be generalised to give the cross section for any hard process producing partons of flavor i with a cross section of σ_0, to be accompanied by the radiation of a parton j:

$$d\sigma \approx \sigma_0 \sum_{partons,i} \frac{\alpha_s}{2\pi} \frac{d\theta^2}{\theta^2} dz P_{ij}(z, \Phi) d\Phi. \tag{4.5}$$

Here, P_{ij} is a universal, but flavour- and spin-dependent splitting function describing the dependence of the cross section on the energy fraction and the angle between the two partons i and j.
One can start from Eq. 4.5 to derive the probability that no gluon is radiated above a certain scale. The derivative of this quantity, in turn, describes the probability for the first branching after the hard process. It is therefore the basic building block of the parton shower algorithm. This is used in an iterative approach by taking the final state after each radiation, as the 'hard process' state for the next decision and every time deciding probabilistically whether or not a gluon is emitted. This way, a parton shower is established, which dies out when reaching the cutoff Q_0.
It should be noted that the parametrisation does not necessarily have to be performed in the angle θ between the partons, but that the transferred momentum q or the p_T of the emitted parton are also valid choices. In the collinear limit, all of them should give the same result as the following holds:

$$\frac{d\theta^2}{\theta^2} = \frac{dq^2}{q^2} = \frac{dp_T^2}{p_T^2}. \tag{4.6}$$

In the non-collinear case, however, the different parametrisations can give slightly differing results.

- **Dipole approach:** An alternative formulation of the parton shower process is the so-called dipole approach, which describes the emission from sets of colour dipoles. In

the large-N_c limit, i.e. when an unlimited number of colour charges is assumed, an arbitrarily complicated parton system's colour structure can be broken down to a set of colour lines. Each of these lines connects an incoming quark, outgoing antiquark or gluon with and outgoing quark, incoming antiquark or another gluon, with each of these lines building a colour-anticolour dipole and emitting independently. The dipole approximation is valid in a region, where the momentum transfer from the emitting line to the gluon is much smaller than any scales involved in the production of the respective line. It is therefore a natural choice to use p_T-ordering in this approach, which gives the same result at LO as other ordering schemes (see Eq. 4.6).
A majority of recent implementations of parton showers make use of the dipole approach, such as e.g. PYTHIA 8.

Another source for activity in an event are interactions of partons of the proton remnants, which do not take part in the hard scattering process. As these multiple partonic interactions (MPI) happen at much smaller momentum scales, they cannot be treated by perturbative QCD, but have to be described by phenomenological MPI models. This underlying event is also simulated during the parton shower step in the event generation process.

4.2.4. Hadronisation

At the end of the parton shower evolution, one is left with single coloured partons, which do not exist in nature. The formation of colourless hadrons is therefore the next step in the event generation. As the momentum scale after the showering is low, this step has to be described using phenomenological models, of which the parameters are tuned to data. There are two types of models for the development of such a hadronic final state, which are implemented in modern day event generators:

- The **string model** is based on the linear confinement between a quark-antiquark pair at large distances (see Eq. 2.54). The interaction of a quark and an antiquark moving apart can be illustrated as a colour flux tube stretching between the two partons (see Figure 4.5(a)). The potential stored in this tube of lateral dimension of about 1 fm is $V(r) = \kappa r$, with the string tension κ being the amount of energy per unit length which amounts to $\kappa \approx 1\,\mathrm{GeV/fm}$. The additional Coulomb term needed at small distances has been found to be negligible in the overall description of the hadronisation process. When the two partons separate further and the energy stored in the string increases,

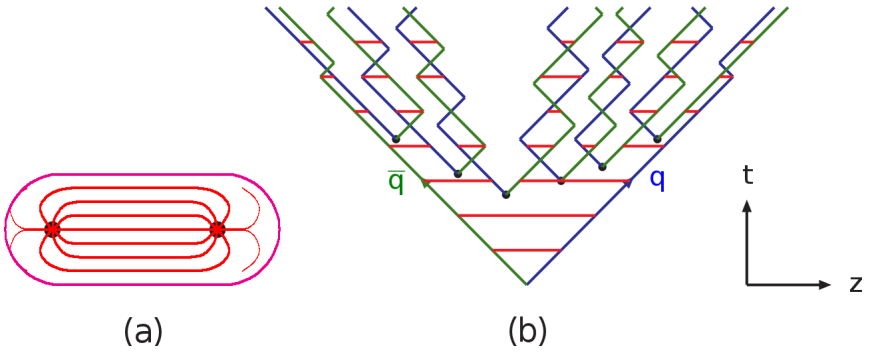

Figure 4.5.: (a) A flux tube spanned between a quark and an antiquark. (b) The motion and breakup of a string system, with the two transverse degrees of freedom suppressed (the diagonal lines are (anti)quarks, horizontal ones snapshots of the string field) [63].

a maximum energy is reached at which the string breaks to produce a new $q'\bar{q}'$ pair to form the colourless parton pairs $q\bar{q}'$ and $q'\bar{q}$. This maximum potential is one of the parameters adjusted to data. As the newly formed parton pairs continue moving along the original momentum direction, a new colour flux tube is built, which gives rise to an iterative procedure (see Figure 4.5(b)). The hadronisation process ends, when the string tensions drop below a certain cutoff parameter, which is also subject to tuning to data. Other tuning parameters used in this class of models, are the probabilities for spin-0 or spin-1 hadron formation and the quark flavour composition of the formed hadrons.

- The other class of models are the **cluster models**. They are based on the finding that the colour structure of the parton shower at any given point in the evolution can be described by colour singlet combinations of partons (clusters) with an asymptotically universal mass distribution, i.e. with the evolution scale Q_0 being much smaller than the hard process scale Q and the distribution being independent of Q. This property of parton showers is referred to as *pre-confinement* [76]. The step from such clusters to physical final state objects, like mesons and baryons, has to be modelled.
  In this model, the large-N_c limit is employed, i.e. the limit of infinitely many colour charges, instead of three. In this limit, to leading order in N_c, radiated gluons can be represented as colour-anticolour lines connected by common vertices (see Figure 4.6). When drawing this colour structure into a plane, colour-anticolour partners are adjacent. Such adjacent partners have a high probability of forming colour singlets (clusters). Meson and baryon flavours and multiplicities are determined using the above mentioned universal mass scale, i.e. massive clusters decay into lighter ones until stable *light*

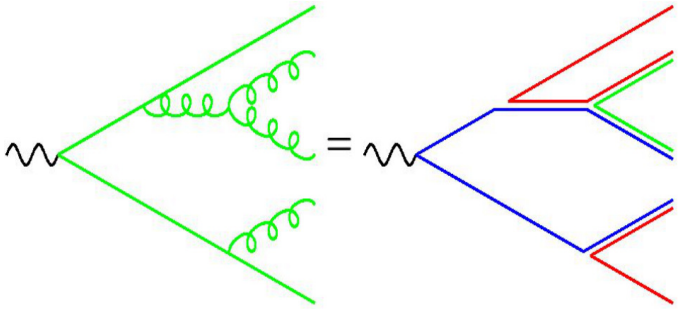

Figure 4.6.: Colour structure of a parton shower to leading order in N_c [63].

states are reached, which do not decay further.
Generators using an implementation of a cluster model are e.g. HERWIG++ and SHERPA.

A comparison of the two model families shows that, while the cluster model describes the observed hadron collider data slightly worse than the string model, it deals with less tunable parameters [63]. Independent of the chosen hadronisation model, the decays of the particles into stable ones at the end of the hadronisation process are simulated by taking into account the known branching fractions, which are provided by the Particle Data Group [25].

Figure 4.7 shows a graphical representation of a simulated $pp \to t\bar{t}H$ event including all previously discussed generation steps, illustrating the event generation procedure.

4.2.5. Generators Used in this Analysis

For the various SM background and signal processes used in this analysis, a number of different matrix element and event generators have been used. Their properties are shortly discussed in the following, while a description of the physics processes along with tables listing which generator the individual ones have been produced with, can be found in sections 6.1 and 6.5.

- **PYTHIA8** is a LO multi-purpose event generator, starting from the matrix element for the hard scattering through parton shower and hadronisation. A list of more than 200 SM and beyond the Standard Model (BSM) $2 \to 1$, $2 \to 2$ and $2 \to 3$ processes are

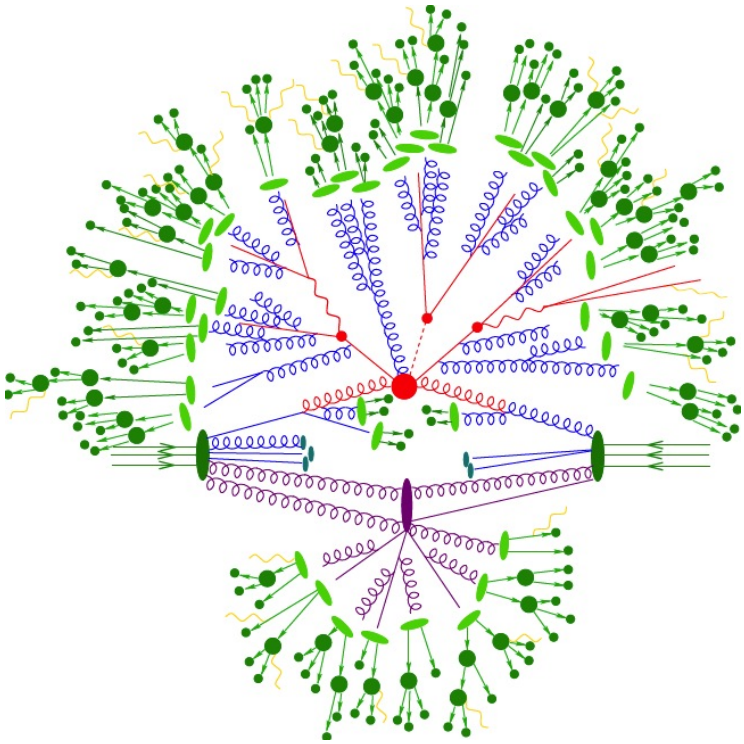

Figure 4.7.: Pictorial representation of a $t\bar{t}h$ event as produced by an event generator. The various steps of the generation process are shown: The hard interaction (big red blob), decay of top quarks and Higgs boson (smaller red blobs), QCD radiation (red), hadronisation of final-state partons (light green blobs) and hadron decays (dark green blobs). A secondary interaction, which takes place before the hadronisation of final-state partons, is also displayed (purple blob) [70].

implemented. It is the first PYTHIA version written in `C++`, as opposed to `Fortran`, in which the preceding versions were written.
Parton showers in PYTHIA8 [73] are implemented via the dipole approach, which results in p_T-ordered showers. For showers coming from initial state radiation, a backwards evolution is used, starting from the hard scattering and then dressing the incoming partons with additional radiation. The hadronisation is based on the string model.

- **MADGRAPH5** [75] is a `Python`-based LO matrix element generator. It only produces the hard subprocess and therefore has to be interfaced to one of the multi-purpose generators for the parton shower and hadronisation steps. MADGRAPH is usually combined with PYTHIA8. It has the advantage that user-defined $2 \to n$ processes can be generated. Computer code is generated for the evaluation of the matrix elements of all contributing Feynman diagrams, which is then used within the `MadEvent` package, where the diagrams are evaluated and the kinematics for the event generation are calculated. For this analysis, the signal samples of the excited vector-like quark b^* were generated using the combination of MADGRAPH5 and PYTHIA8.

- **PROTOS** is a LO matrix element generator specifically developed for BSM models like single vector-like quark production and needs to be interfaced to a general-purpose generator for showering and hadronisation. For this analysis, a combination of PROTOS and PYTHIA has been used for the production of the vector-like quark B samples.

- **POWHEG-BOX** [77, 78] is a generator specifically developed around the so-called Powheg method (POsitive Weight Hardest Emission Generator) to generate the hardest emission first, with NLO accuracy, which is then embedded in a shower from one of the general-purpose generators.

- **ALPGEN** [74] is a LO matrix element generator specialised for final states with several hadronic jets, where its fixed-order matrix element is supposed to yield a better description of the data, than the shower approximation of PYTHIA or HERWIG. ALPGEN is usually interfaced to PYTHIA for the parton shower and hadronisation steps.

- **HERWIG++** is a flexible multi-purpose generator for the generation of SM and supersymmetry processes. It is written in `C++`.

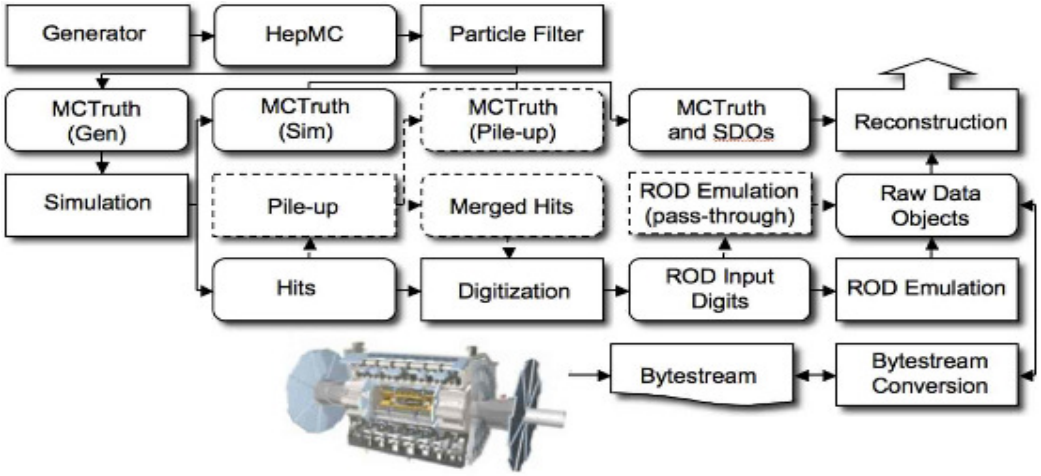

Figure 4.8.: The flow of the ATLAS simulation software, from event generators (top left) through reconstruction (top right). Algorithms are placed in square-cornered boxes, data objects are represented by rounded boxes. Optional parts (e.g. pileup addition) are shown in hashed boxes [64].

4.3. ATLAS Simulation

After the event generation up to hadronisation and decay of short-lived particles, the detector response has to be simulated as well, in order to compare simulated events with those from recorded data. Events on hadron level are therefore fed into the simulation framework of the ATLAS detector, before they can enter the same object reconstruction procedures as real data events, which will be described in Chapter 5. The detector simulation consists of two major parts: First, the interactions of the various particles with the detector material are simulated and unstable hadrons produced in the hadronisation step decay further into particles which are stable on scales of the size of the detector. For this simulation step, one of two options can be chosen: a time-consuming high-precision one and a faster one based on parametrisations. These two steps will be described further in the following sections. Secondly, the response of the detector components and electronics is modelled by digitising the simulated physics quantities. An overview over the simulation structure, from event generation to reconstruction, is sketched in Figure 4.8.
Most of the information in this section is taken from [64].

4.3.1. Full Detector Simulation

The standard (or full) detector simulation of ATLAS is based on the GEANT4 [79] toolkit, which provides physics models as well as tools for particle transportation through a given geometry. The geometry used here resembles the real ATLAS detector as much as possible. It is assembled from basic building blocks provided by GEANT4, described by a number of properties such as shape, material composition or other physical properties. The description of the ATLAS detector with its variety of materials consists of hundreds of thousands of such physical volumes. Such a detailed description is crucial for correctly modelling the various physics quantities of interest, such as track reconstruction efficiency or calorimeter response. For a given geometry, different *conditions* can be set from a condition database, including e.g. misalignment or dead channels. This is needed in order to exactly mimic the running conditions during data taking in the simulation step. The list of physics models included in GEANT4 contains all possible interactions of the different particle species with the materials present in the detector and infra-structure around it, as well as possible decay modes and branching fractions of unstable hadrons.
As an input to the detector simulation, the generator output is taken, usually in HepMC data format [80]. At this stage, a certain subset of the generated events can be selected, e.g. leptonic final states or events in which a given particle exceeds some chosen p_T threshold. It is useful to constrain the events going into the detector simulation to what is sensible for the analysis to look at, as this is the most time- and CPU-consuming step in the chain. Another means of reducing the computation time is to limit the pseudorapidity range of the passed-on particles to $|\eta| < 6$. At this stage, the primary vertex of the generated event is statistically widened to resemble the luminous region in the ATLAS detector.
After passing through the detector simulation, the event is stored in *hits* format. A hit represents an energy deposit in the sensitive region of the detector together with its time and position. Such a hits file contains some meta data and the hits produced by the simulation. It has a size of 2MB for a typical top-pair event and can be passed on to the digitisation step which will be described further down. Besides that, these files contain the so-called Monte-Carlo *truth* information. This is a record of the qualities of all (stable and unstable) particles produced in the generation step as well as in the detector simulation, which can be used later on to verify the quality of the reconstruction and to determine reconstruction efficiencies. This information is also passed on to the next steps in the chain, such that it is available at analysis level.

4.3.2. Fast Detector Simulation

Due to the complexity of the detector geometry and the detailed description of interactions with the detector material, the complete GEANT4 simulation described in the previous section (referred to as full simulation) is very time-consuming. The large statistics of generated events needed for a large variety of physics processes result in the need of a fast simulation alternative. Two main bottlenecks can be identified: the tracking of particles traversing the calorimeter system, which accounts for 80% of the total CPU time and that of charged particles, accounting for 75% [64]. These slowest parts of the simulation process are sped up by introducing a number of different fast simulation packages. The one used to produce Monte-Carlo samples used in this thesis besides the full simulation, is the ATLFAST-II setup, which will be described in the following.
The difference between the full simulation and ATLFAST-II is the handling of interactions in the calorimeter. Instead of a complete simulation for every single particle, parametrisations of the lateral and longitudinal energy profile are used to directly deposit the energy of single particle showers. These parametrisations are based on a large sample of GEANT4-simulated single photons and charged pions over a wide range of energy and evenly distributed in η and Φ and are finely binned in the particle energy and pseudorapidity to account for the detailed description of the calorimeter material. Furthermore, they are binned in the longitudinal shower depth, as the deposited energy strongly depends on the origin of the shower in the calorimeter. The photon parametrisation is used to approximate all electron and photon showers and all hadronic showers are approximated by the charged pion parametrisation. The calorimeter geometry used is the slightly simplified reconstruction one, which has a granularity of the size of the readout cells.
During the simulation process, the parametrisation of the respective kind that is closest in energy and pseudorapidity to the incident particle is taken. Total shower depth and energy are then taken from the stored histograms and rescaled to the particle's energy.
Using this fast simulation alternative, the calorimeter simulation time of a typical top-pair event is reduced from a few minutes to a few seconds. This way, a lot of CPU time can be saved without sacrificing much of the performance, such that ATLFAST-II Monte-Carlo samples can be used for most physics analyses. If, however, the analysis is sensitive to quantities related to a detailed calorimeter description, the full simulation has to be employed. As the analysis in this thesis makes use of jets with a larger-than-standard

radius (as will be discussed in Chapters 5 and 6), that are not yet studied in detail in fast simulation, ATLFAST-II samples can only be used for very limited purposes here.

4.3.3. Digitisation

After having stored the hits from the simulation step, they need to be translated into detector responses, so called *digits*. Such a digit is usually produced, if a given readout channel registers a voltage or current to be over a certain threshold within a given time-window. For some subdetectors, the digit format only records the exceeded threshold, while for others, the signal shape is included in addition. The digitisation software is specific for every subdetector and includes characteristic features, such as electronics noise or channel-dependent variations. The simulation software was tuned such that the properties of the detector response match the ones measured in test beam and other test setups. Since real data events are always contaminated by events from other primary vertices or even bunch crossings, the simulated events also have to be overlayed with such pileup contributions. This is done in the digitisation step as well, by adding hits from additional events with a small time offset to the hits from the hard scattering event. Additional contributions, that arise from interactions between the beam and residual hydrogen, oxygen and carbon gasses in the beam pipe (beam gas), interactions between the beam and upstream accelerator elements (beam halo) and neutrons traversing some distance in the cavern and creating a constant background of low-energy electrons and photons from spallation (cavern background), are also added in a similar fashion during the digitisation.

4.3.4. Pileup Reweighting

As the production of Monte-Carlo simulation samples and thus the insertion of pileup events already took place before the end of the data taking period, the pileup conditions could only be mimicked based on assumptions. In order to exactly match the pileup conditions in the simulated samples to the ones in data, the MC events have to be reweighted according to the true conditions recorded. This is done by giving a weight to each event, based on the average number of proton-proton collisions in one event, μ, which is obtained per luminosity block (the smallest subdivision of data recording in which the instantaneous luminosity is

assumed to be stable).

Once the samples of simulated events are established by the steps described above, they are fed into the same reconstruction algorithms as the real data samples, in order to turn detector output into information about the physics objects responsible for the signals. This procedure will be described in the following chapter.

Chapter 5.

Identification and Reconstruction of Physics Objects

New heavy quarks, as they are searched for in this analysis, can not be detected directly due to their short lifetimes given by their comparatively high mass. The theory predicts them to decay into SM particles before reaching the detector, which can be used to reconstruct the properties of the mother particles. It is therefore crucial to have a good knowledge about the detection properties of the known particles. This translation between recorded detector signals and physics objects is taken care of by various specialised performance groups within the ATLAS collaboration and a set of recommended selection criteria for every kind of object is made available to the analysers. The definition of the physics objects used in this analysis is described in the following sections. Most of them are the object definitions recommended for analyses dealing with top quarks by the *ATLAS Top Group*. The reconstruction and identification of electrons and muons[1] are described in section 5.2 and 5.3. Tau leptons, which further decay before being detected, are not used in this work. Their discussion will therefore be dropped. Neutrinos escape the detection and give rise to an imbalance in the transverse momentum sum, which can be deployed and is described in section 5.6. Quarks or gluons appear in the detector after hadronisation as collimated particle bunches (so-called jets). Their reconstruction is discussed in section 5.4. In the following section, a technique used for measuring reconstruction efficiencies of several types of physics objects, the so-called 'Tag & Probe' method, is described.

[1]The terms electron, muon, neutrino and quark likewise denote the particle and the anti-particle throughout the thesis, unless stated otherwise.

5.1. Tag & Probe Method

The Tag & Probe (T&P) method is a technique to determine selection or reconstruction efficiencies in data. A selection efficiency can be described as

$$\epsilon_{sel} = \frac{N_{sel}}{N_{total}}, \tag{5.1}$$

where N_{sel} is the number of selected events (or particles, tracks, etc.) by a certain set of criteria under study and N_{total} is the total number of these objects before applying the selection. While N_{total} is accessible in MC simulations as the truth information on how many of these objects were generated, this is not the case for data, where one only knows the number of objects after a given selection. The T&P method provides a solution to circumvent this problem in scenarios which aim at the selection of two objects (or a composite object). This is done by creating a very clean sample of one of the objects, called the 'tag' sample, by using strong selection criteria and a 'probe' sample with looser requirements and defining a matching criterion for the two objects. This procedure can be best illustrated with the following typical example using $Z \to e^+e^-$ events, which provide clean lepton signatures. As a common criterion, the invariant mass of the Z boson is used. The sample of 'tag' electrons is made nearly background-free by strong cuts. The efficiency is then measured by selecting a 'probe' electron from the other sample which has to fulfil much looser requirements. N_{total} is defined as the number of events containing a 'tag' and a 'probe' electron with an invariant mass close to the Z-boson mass. If the 'probe' electron in addition fulfils all tight selection criteria, the event contributes to N_{sel}. This way, the efficiency can be measured in data and MC. As some parts of the detector cannot be perfectly modelled in the simulation, the efficiency in data and MC obtained by the T&P method do not necessarily agree. In this case, kinematics-dependent scale factors (SF) are applied to the MC events in order to correct for these differences.

5.2. Electrons

An excellent electron reconstruction and identification is crucial for analyses with electrons in their final states, as they need to be disentangled from jets (see section 5.4) containing many π^0 and a low number of charged particles, which cause very similar signatures in the

calorimeters. In the p_T range of 20 GeV-50 GeV the number of electrons stemming from prompt W decays is much lower than the number of jets from QCD processes, which is why the required jet rejection rate in that region is $\sim 10^{-5}$ [81]. New physics processes producing electrons can be even rarer.
The algorithms and selection criteria described in the following have been developed by the *ATLAS ElectronGamma Performance* working group.

5.2.1. Electron Reconstruction, Identification and Selection

For the reconstruction of electrons in the central part of the detector ($|\eta| < 2.47$), information from the ECAL on the deposited energy as well as information from the ID on tracks are used [82]. Energy deposits (clusters) with a total transverse energy of at least 2.5 GeV are searched for by a so-called *sliding-window* algorithm, and are used as seeds to build electromagnetic (EM) clusters. The size of the window used is 0.075×0.125 in $\eta \times \Phi$ space, which corresponds to the granularity of the middle layer of the calorimeter (see section 3.2.4). Monte-Carlo simulations have shown that the cluster reconstruction is very efficient (100% for electrons from W or Z decays with $E_T > 15$ GeV and slightly worse below that value). The seed clusters are then matched to the extrapolation of ID tracks to the middle layer of the calorimeter with a position-dependent $\Delta\eta \times \Delta\Phi$ window of 0.05×0.05 to 0.05×0.10. At least one track not stemming from a photon-conversion pair needs to be matched to the seed cluster to reconstruct an electron. In the event of multiple tracks being located in the matching window, the closest one in ΔR is chosen. In order to correct for bremsstrahlung losses in the ID, the track associated to the cluster is re-fitted. Starting with 2012 data, a dedicated reconstruction algorithm, the so-called Gaussian Sum Filter (GSF) [83] was used for this purpose. In some cases this leads to a discard of the best-matching track. The ratio of the cluster energy over the track momentum has to fulfill the relation $E/p < 10$ [81] to account for energy losses due to bremsstrahlung in front of the ECAL. The cluster is then re-built using a slightly larger window of a size of 3×7 longitudinal calorimeter cells in the barrel region and 5×5 in the end-caps, respectively, and the cluster energy is calculated from the estimated deposited energy in front of the ECAL, the measured energy in the cluster itself and the estimated depositions outside the cluster (lateral leakage) as well as beyond the calorimeter (longitudinal leakage). For the parameterisation of these energy contributions and thus for the correct reconstruction of the electron energy a very detailed knowledge of the active and inactive material in the

detector simulation is crucial.

The kinematic properties of the reconstructed central electron are taken from cluster (energy) and best-matched track information (η and Φ). The transverse energy of the electrons is defined as $E_T = E_{cluster}/cosh\eta_{track}$ with $E_{cluster}$ being the cluster energy and η_{track} the matched track's pseudorapidity.
In the forward region of the detector ($2.5 < |\eta| < 4.9$), the reconstruction is done without using track information, as the ID does not extend up to that η range. However, this procedure will not be discussed here, as this analysis only uses electrons from the central region.
An additional requirement used in this analysis is the exclusion of central electrons stemming from the so-called crack region. The region of $1.37 < |\eta| < 1.52$ contains support structures and cables, which worsens the reconstruction quality, and is therefore excluded. The energy of electrons reconstructed close to that crack-region, i.e. electrons reconstructed in $1.52 < |\eta| < 1.55$, is underestimated due to leakage into that region. A correction factor is therefore introduced for these electrons.
At this stage, electron candidates are referred to as *reconstructed electrons*. The corresponding reconstruction efficiencies, derived via the T&P method, can be found in Figure 5.1. Electrons used in this analysis are required to have a transverse energy of $E_T > 25\,\text{GeV}$.

However, even though the described reconstruction algorithm is highly efficient, it will likewise reconstruct background electrons (e.g. from photon conversions in the detector material or from Dalitz decays) as well as jets which cause similar energy deposits in the electromagnetic calorimeter. In order to suppress these processes and to enhance the fraction of prompt, isolated electrons stemming from the hard process (i.e. from W or Z decays), a cut-based approach was established. Three different sets of selection cuts based on calorimeter and tracking information are used to define different levels of background rejection: the so-called `loose++`, `medium++` and `tight++` cuts, with increasing rejection power, which will be described in the following. Electrons used in this analysis correspond to the `tight++` selection, while a set of looser criteria is used to estimate the background fraction from QCD multijet production, as described in section 6.5.1.

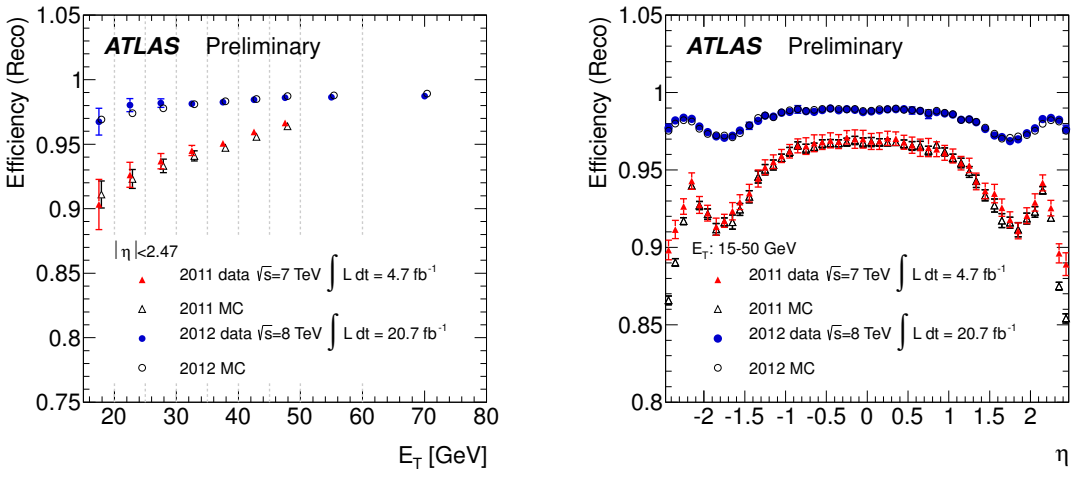

(a) (b)

Figure 5.1.: Reconstruction efficiency for electrons as a function of E_T integrated over the full pseudorapidity range (a) and as a function of η for $15\,\text{GeV} < E_T < 50\,\text{GeV}$ (b) for the 2011 and 2012 data sets [84].

The discriminating variables used for categorisation of electrons into the three above mentioned operating points can be divided into those making use of calorimeter properties, which are referred to as *shower shapes* and are generally η and E_T dependent, those using ID information, which are generally independent of the electron position and energy and those making use of a combination of ECAL and ID information. The definitions described in the following have been taken from [85] and references therein:

- R_{had1}, R_{had} (hadronic leakage): ratio of the energy deposit in the first sampling of the hadronic calorimeter behind the reconstructed EM cluster and the cluster energy, and a similar ratio using all layers of the hadronic calorimeter (in the transition region between barrel and end-cap HCAL, $0.8 < |\eta| < 1.37$). These values are small for signal electrons, as they deposit most of their energy in the ECAL.

- $w_{\eta 2}$ (width of second sampling): energy-weighted RMS of the η distribution of calorimeter cells in the second sampling, defined as $w_{\eta 2} = \sqrt{\frac{\sum_i \left(E_i \eta_i^2\right)}{\sum_i \eta_i} - \left(\frac{\sum_i E_i \eta_i}{\sum_i E_i}\right)^2}$, with the sums running over all cells in a 3×5 window and E_i and η_i being the energy and pseudorapidity of the cells. This variable takes smaller values for signal electrons than for background, which tends to cause more spread-out showers.

- R_η (energy ratio): ratio of the energies in different η-size cell windows (3×7 vs. 7×7 in $\eta \times \Phi$), the smaller one being included in the larger one. Again, the small spread of signal electron showers leads to smaller values of this variable than for background.

- $w_{s,tot}$ (shower width): shower width in the first calorimeter layer (strips) defined as $w_{s,tot} = \sqrt{\frac{\sum_i E_i (i - i^{max})^2}{\sum_i E_i}}$, the sums running over a 20×2 strips window in $\eta \times \Phi$, with i^{max} being the index of the strip with the largest energy deposit. Also in the strip layer the shower is more spread-out for background than for signal electrons.

- E_{ratio} (strip energy maxima): difference in energy between the two strips with the highest energy maxima normalised to their sum, $E_{ratio} = \frac{E^s_{1st\ max} - E^s_{2nd\ max}}{E^s_{1st\ max} + E^s_{2nd\ max}}$. Signal electrons sharply peak at one, while backgrounds have more contributions at smaller values.

- N_{PIX}, N_{SCT} (number of pixel and SCT hits): the requirement of a minimum number of pixel and SCT hits associated to a track is an important track quality criterion and suppresses conversion electrons while keeping the signal efficiency high.

- N_{BL} (b-layer hits): the number of hits in the first pixel layer (b-layer) further helps to suppress background from photon conversion as such conversions are unlikely to take place right after entering the first detector layer.
- d_0 (impact parameter): the distance of closest approach of the extrapolated track to the primary vertex is another means of suppressing conversion.
- *conversion bit*: the conversion bit is set if a track can be associated to a reconstructed photon conversion vertex.
- f_{TR} (TRT hit fraction): the fraction of high-threshold TRT hits indicates how much transition radiation has been emitted along a track, which is higher for electrons than for hadrons. This however, does not help to discriminate against background electrons.
- $|\Delta\eta|$(cluster, track): the η distance between the cluster and the associated track is smallest for signal electrons.
- $\Delta\Phi$(cluster, track): the Φ distance between the cluster and the associated track is also smaller for signal electrons than for background, even though this variable is less powerful than $|\Delta\eta|$.
- E/p: the distribution of the ratio of the electron energy measured in the calorimeter and the track momentum measured in the ID is different for background and signal electrons due to bremsstrahlung in the ID. The radiated photons are invisible for the ID, while their energy deposit ends up in the EM cluster, which is why electrons have typically larger E/p values and this variable can be used for discrimination.

Table 5.1 summarises which of the discussed selection criteria are used for the different electron selection operating points.

In addition to the `tight++` selection criteria, several other requirements are made in order to improve the electron selection: The impact parameter of the electron track, z_0, defined as the distance between the point of closest approach of the track extrapolation to the beam pipe projected onto the z-axis and the primary vertex, has to obey $|z_0| < 2\,\text{mm}$. The *ATLAS ElectronGamma Performance* working group also provides so-called object-quality maps, which mark regions in which minor hardware issues in the ECAL arose during data taking, e.g. dead front-end boards or regions where the voltage did not reach the

Table 5.1.: Summary of variables used to classify `loose++`, `medium++` and `tight++` electron working points, each one being a subset of the next in this order. Track quality criteria comprise the requirement of at least one pixel hit and and at least 7 hits in the overall silicon detector.

`loose++`
shower shapes: R_{had1}/R_{had}, $w_{\eta 2}$, E_{ratio}, $w_{s,tot}$
track quality criteria
$\lvert\Delta\eta\rvert < 0.015$
`medium++`
shower shapes: same variables as in `loose++` with tighter values
track quality criteria
$\lvert\Delta\eta\rvert$ <0.005
$N_{BL} \geq 1$ in $\lvert\eta\rvert < 2.01$
$N_{PIX} > 1$ in $\lvert\eta\rvert > 2.01$
loose f_{TR} requirement
$d_0 < 5\,\mathrm{mm}$
`tight++`
shower shapes: same variables as in `medium++` with tighter values
track quality criteria
$\lvert\Delta\eta\rvert$ <0.005
$N_{BL} \geq 1$ everywhere
$N_{PIX} > 1$ in $\lvert\eta\rvert > 2.01$
tight f_{TR} requirement
$d_0 < 5\,\mathrm{mm}$
E/p requirement
$\Delta\Phi$ requirement
conversion bit not set

nominal value. Electrons traversing one of these regions are rejected from the analysis. Some ECAL modules can also suffer from more serious hardware problems, so-called noise bursts, which heavily affect the calorimeter performance. Events, which are affected are

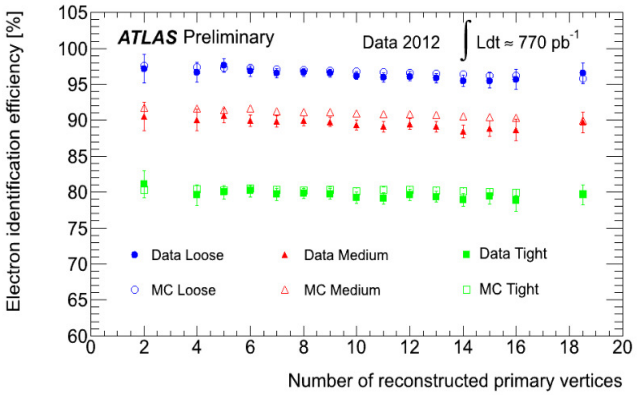

Figure 5.2.: Identification efficiency for tight++, medium++, loose++ electron selections (called Tight, Medium, Loose on the image) for a subset of 2012 data [86].

flagged as 'LArError' and are not considered for the analysis.
Figure 5.2 shows the electron identification efficiency in a subset of 2012 data and MC, obtained with the T&P method. The described identification criteria yield quite stable efficiencies over the range of reconstructed primary vertices of ≥95% (`loose++`), ∼90% (`medium++`) and ∼80% (`tight++`).

5.2.2. Electron Isolation

Another means of discriminating signal electrons from background is the isolation. Electrons from W or Z decays are usually well isolated in terms of activity close to their track or cluster, while background electrons, e.g. electrons from hadron decays, are produced along with other particles such that they are correlated with other electromagnetic activity in the event. This relation is quantified by summing over the energy in a cone around the electron cluster (calorimeter isolation) or over the p_T of tracks in a cone around the associated ID track (track-based isolation), omitting the energy deposit of the centre of the cluster and the momentum of the track itself, respectively. Typical cone sizes for this procedure are 0.2, 0.3 or 0.4 in units of ΔR. The final quantities used to cut on are the relative isolation criteria, i.e. the energy (momentum) sum divided by the electron E_T (p_T). In this analysis, a cone size of 0.2 has been used for the calorimeter isolation and one of 0.3 for the track-based isolation, as recommended by the *ATLAS Top Working Group*. In order to achieve a uniform isolation efficiency over wide ranges of η and E_T, instead of fixed

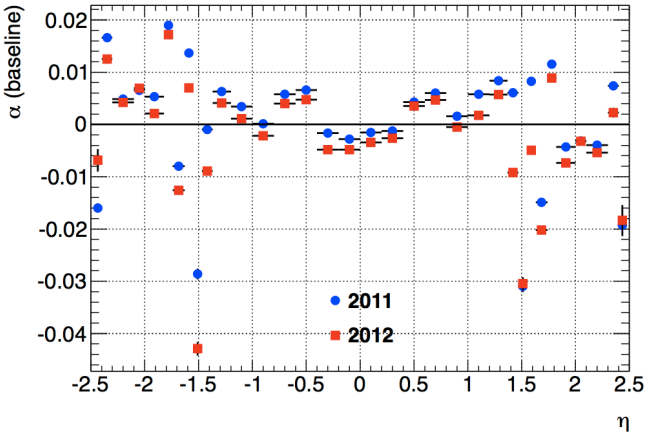

Figure 5.3.: Inter-calibration coefficients α as a function of η for 2011 (blue) and 2012 data (red) [89].

cut values, the cuts on these two variables were chosen such that they yield an isolation efficiency of 90%. Cut maps can be found in [87].

5.2.3. Electron Energy Scale and Resolution

As the electron energy is obtained from the energy deposit in the cluster, it needs to be calibrated in order to account for energy deposits in front of the ECAL, in the HCAL or outside the cluster. For this purpose, the so-called calibration hits method [88] is used, which defines several calibration coefficients. The values of these coefficients are obtained using special MC simulations with single electrons traversing the detector. A dedicated `Geant4` detector simulation is used in this case, which makes it possible to also quantify energy deposited in inactive material. The obtained coefficients are parametrised as functions of the cluster energy, the estimated energy deposited outside the clusters (but within the active calorimeter material), the estimated energy deposit in the HCAL and in front of the ECAL.
In addition to the calibration described above, a comparison of the shape of the Z peak in $Z \to e^+e^-$ events has been used to obtain an η-dependent factor α used to correct the electron energy in data, shown in Figure 5.3. The application of the factor $(1-\alpha)^{-1}$ leads to good agreement of the Z-peak shape in data and MC.

The electron energy resolution is parametrised as

$$\frac{\sigma_E}{E} = \frac{a}{\sqrt{E}} \oplus \frac{b}{E} \oplus c, \tag{5.2}$$

[82], with a (sampling term), b (noise term) and c (constant term) being η-dependent parameters. a and b are determined from $Z \to e^+e^-$ events in MC, while c is obtained comparing the $Z \to e^+e^-$ mass peak shape in data and MC via the following relation:

$$c_{data} = \sqrt{2 \cdot \left(\left(\frac{\sigma}{m_Z} \right)^2_{data} - \left(\frac{\sigma}{m_Z} \right)^2_{MC} \right) + c^2_{MC}}, \tag{5.3}$$

[82], with m_Z being the measured Z-boson mass [90], c_{MC} being a constant term of about 0.5% obtained from the simulation and σ being the Gaussian width of the experimental resolution. This resolution is determined by fitting a Breit-Wigner with a width fixed to the measured Z-boson width convolved with a Crystal Ball function to the invariant mass distributions in data.
In order to mimic the experimental resolution obtained from data for MC events, the simulated electron energy is randomly smeared on truth level by a Gaussian of width σ_E, which corresponds to the total energy resolution width in data.

5.2.4. Electron Trigger

An advantage of working with electrons is that they provide good trigger signals. As described in section 3.3, the trigger system in ATLAS consists of three stages: the fast and hardware-based L1, as well as L2 and EF, which are slower and deploy similar algorithms as in the offline reconstruction. Events used in the analysis are required to pass a trigger chain made up of these three consecutive levels. In this analysis, the lowest un-prescaled single electron and single muon triggers are used to select events with at least one of these leptons in the final state. It is required that at least one physics object in the event fulfils all trigger requirements (often denoted as "to fire the trigger"). The electron trigger requirements will be explained in the following and the ones of the muon trigger in section 5.3.
Electron events used in this analysis are required to pass one of two possible trigger chains (L1→L2→EF), which will be defined in the following:

- `L1_EM18VH` → `L2_e24vh_medium1` → `EF_e24vhi_medium1`:
  At L1 level, an energy deposit of at least 18 GeV in the ECAL (`18`) is required with a 'varied-threshold' correction for coarse dead material applied to the trigger threshold (`V`) and a veto on too large HCAL/ECAL energy deposit fractions in the region of the EM cluster (`H`). At L2 and EF level, the trigger item is required to be seeded from a varied-threshold L1 item with hadronic veto applied (`vh`). `24` in both, L2 and EF trigger items represents the $E_T > 24$ GeV threshold beyond which the trigger efficiency reaches its plateau and a selection mirroring the offline `medium++` criteria is also required on L2 and EF level (`medium1`). `i` on the EF level denotes the fact that a loose track-based isolation criterion has to be fulfilled.

- `L1_EM30` → `L2_e60_medium1` → `EF_e60_medium1`:
  At L1 level, a strict energy deposit requirement of at least 30 GeV without hadronic core veto is applied. On L2 and EF level, the E_T thresholds are also higher and no isolation criterion is required.

As the veto on the hadronic activity in the first trigger chain leads to inefficiencies in some kinematic regions, the second one was introduced. A logical OR combining the two chains yields the requirement imposed on an electron object to fire the trigger. The performance of the combination of these two trigger chains has been studied in Monte-Carlo simulations and is found to be very good [87].

5.3. Muons

Compared to electrons, muons give a cleaner signal in the detector due to their larger penetrating power and due to the fact that ATLAS contains a dedicated Muon Spectrometer (see section 3.2.5). However, a distinction between prompt muons from W or Z decays and those produced in hadron decays has to be made, which is taken care of by several muon reconstruction algorithms developed by the *ATLAS Muon Combined Performance* working group, which will be presented in the following.

5.3.1. Muon Reconstruction, Identification and Selection

For the reconstruction of muons in ATLAS, four different algorithms have been developed, making use of different kinds of detector information:

- **Standalone muons** (MS information only):
  In this algorithm, track segments in the MS are searched for by using a technique called 'Hough transformation' which is a method to look for lines and curves in pictures [91]. These segments are combined in a fit, taking into account the energy loss in the traversed detector components, based on parametrisations of the traversed material and the measured energy deposits in the calorimeter [92]. The resulting track of this muon candidate is then extrapolated to the beam pipe. This algorithm does, however, not provide good discrimination against background muons from hadron decays inside jets.

- **Combined muons** (ID and MS information):
  In order to better discriminate against background muons and to improve the momentum resolution, the standalone track can be supplemented by tracking information [93]. The matching criterion χ^2_{match} is defined as the difference between the vector of the MS track, $\mathbf{T}_{MS}$, and the vector of the ID track, $\mathbf{T}_{ID}$, weighted by the combination of their respective covariance matrices $\mathbf{C}_{MS}$ and $\mathbf{C}_{ID}$ [81]:

  $$\chi^2_{match} = (\mathbf{T}_{MS} - \mathbf{T}_{MS})^T (\mathbf{C}_{MS} + \mathbf{C}_{ID})^{-1} (\mathbf{T}_{MS} - \mathbf{T}_{MS}) , \tag{5.4}$$

  each vector containing five track parameters.

- **Segment tagged muons** (ID information only):
  In this approach, reconstructed ID tracks are extrapolated to the first layer of the MS, where a search for track segments is performed. There are two algorithms in order to match such segments with the ID track: either a χ^2 is calculated from the difference of the extrapolated track and the MS segment (`MuTag` [93]) or a neural network is employed for the tagging decision (`MuGirl` [94]). A track fulfilling these tagging requirements is considered corresponding to a muon candidate.

- **Calorimeter tagged muons** (ID and calorimeter information):
  This algorithm combines the above described tagged ID tracks with information from

the calorimeters. This approach is not used in the analysis described in this thesis and will thus not be further discussed.

The four algorithms described above are organised in two implementation families: `Muid` [95], which is used for the muons selected in this work, and `STACO` [81], which will not be further discussed.

Muon Quality Criteria

Analogous to the electron objects, muon objects are also classified in three different quality categories: `tight`, `medium` and `loose`. A `Muid` muon is considered `tight` if it fulfils at least one of the following logically linked requirements. It needs to be

- a combined muon OR
- a standalone muon with $|\eta| > 2.5$ of which the MS track has at least a sum of MDT+CSC hits of three OR
- a `MuGirl` muon with an extended track AND (at least two MDT+CSC hits OR less than six MDT+CSC holes along the track).

For this analysis, only tight combined muons are selected, except for the estimation of the QCD multijet background (see section 6.5.1), where looser selection criteria are applied. These muons are required to satisfy $p_T > 25\,\text{GeV}$ due to the trigger threshold, which will be discussed in section 5.3.4 and $|\eta| < 2.5$ due to the acceptance of the ID. The longitudinal impact parameter has to fulfil the same criterion as for electrons: $|z_0| < 2\,\text{mm}$. In order to improve the quality of the track associated to the muon, several additional criteria have to be fulfilled:

- $N_{PIX}^{hit} + N_{PIX}^{ds} > 0$ (sum of pixel hits and crossed dead pixel sensors)
- $N_{SCT}^{hit} + N_{SCT}^{ds} > 4$ (sum of SCT hits and crossed dead SCT sensors)
- $N_{PIX}^{hole} + N_{SCT}^{hole} < 3$ (sum of pixel and SCT holes)
- successful TRT extension (in TRT acceptance $0.1 < |\eta| < 1.9$):
  $N_{TRT}^{hit} + N_{TRT}^{outlier} > 5$ and $N_{TRT}^{outlier} < 0.9 \cdot \left(N_{TRT}^{hit} + N_{TRT}^{outlier}\right)$

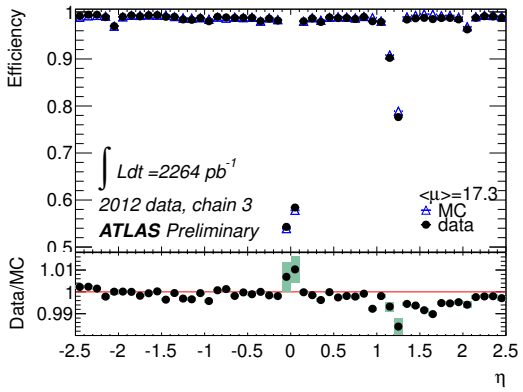

Figure 5.4.: Reconstruction efficiency for combined muons vs. the muon pseudorapidity in 2012 data and in MC [96]. 'chain 3' denotes a new algorithm family combining `Muid` and `STACO`, for which no separate plots were made publicly available. The combined family, however, has similar reconstruction efficiencies as the `Muid` family alone. The small (<1%) differences in data and MC efficiencies are accounted for by SF which are applied to the events in MC.

Figure 5.4 shows the reconstruction efficiencies for muons in data and MC obtained in $Z \to \mu^+\mu^-$ events using the T&P method [96].

5.3.2. Muon Momentum Scale and Resolution

The measurement of muon momentum scale and resolution is performed on opposite-sign dimuon events in data with an invariant mass close to the Z-boson mass, as described in [97]. The position and the width of the mass peak are sensitive to the momentum scale and resolution. The overall momentum scale and the resolution parameters, as defined in

$$\frac{\sigma\left(p\right)}{p} = \frac{p_0^{MS}}{p_T} \oplus p_1^{MS} \oplus p_2^{MS} \cdot p_T \tag{5.5}$$

for a given η value with p_0^{MS}, p_1^{MS} and p_2^{MS} being coefficients related to energy loss in the calorimeter, multiple scattering and intrinsic resolution terms, have been derived using a template fit to the invariant mass distribution. The resolution measured in a subset of 2012 data and in MC for various η values is shown in Figure 5.5. In order to account for the difference in data and MC, the momentum of simulated muons is additionally smeared. Figure 5.6 shows that data and MC distributions of the invariant dimuon mass agree very well after scaling and smearing the MC muon momentum, which justifies this treatment of

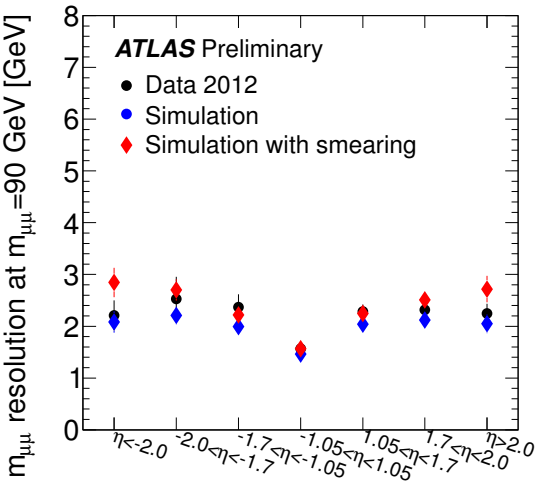

Figure 5.5.: Dimuon mass resolution measured in $Z \to \mu^+\mu^-$ events in MC and a subset of 2012 data. The muon momentum in the simulation is smeared in order to obtain a similar resolution as in data [96].

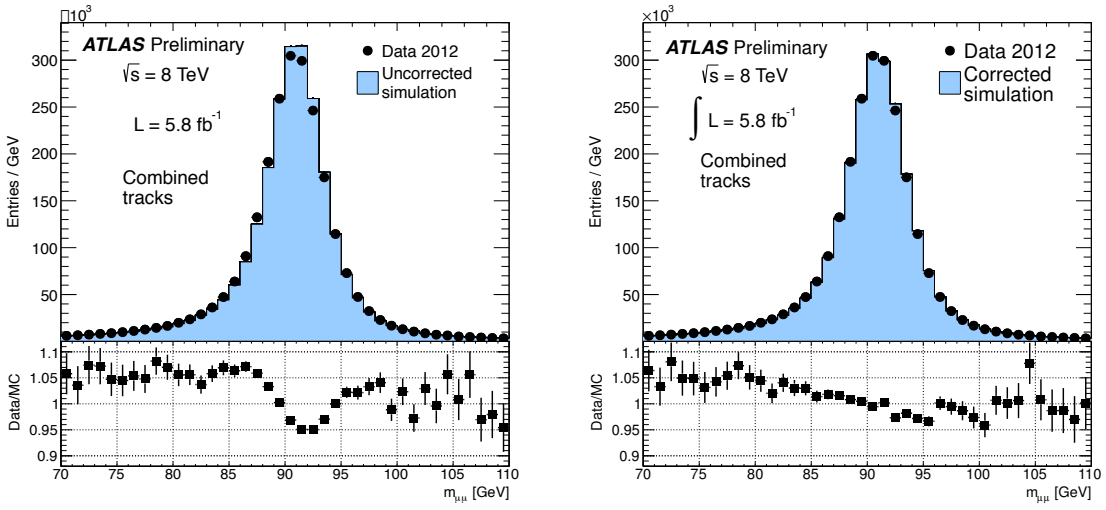

(a) (b)

Figure 5.6.: Dimuon mass distribution measured in $Z \to \mu^+\mu^-$ events in MC and a subset of 2012 data before (a) and after (b) scaling and smearing the muon momenta [98].

simulated muons.

5.3.3. Muon Isolation

In order to discriminate between signal muons and background ones stemming from hadron decays inside jets, an isolation criterion is applied. In contrast to the electron case, no fixed cone size is used for muons, but instead a p_T-dependent one. This yields an advantage in analyses with boosted muons, which arise primarily in decays of heavy objects, such as new heavy quarks. This approach, which has been proposed in [99], is called 'Mini-Isolation'. An isolation parameter, I_{mini}, is introduced in the following way:

$$I_{mini} = \sum_{tracks} \frac{p_T^{track}}{p_T^{\mu}}, \tag{5.6}$$

in which the sum runs over all tracks which fulfil $p_T > 1\,\text{GeV}$ and are found within a distance of $\Delta\text{R} < K_T/p_T^{\mu}$. p_T^{μ} is the muon momentum and K_T a scale parameter, such that the cone in which track momenta are summed over becomes smaller with increasing muon momentum. The tracks in the cone need to fulfil a number of additional requirements:

- $|d_0| < 10\,\text{mm}$
- $z_0 \cdot sin\theta_{track} < 10\,\text{mm}$
- $N_{SCT}^{hit} + N_{SCT}^{ds} \geq 4$
- $N_{PIX}^{hit} + N_{PIX}^{ds} \geq 4$

It was shown in [99] that an optimal muon isolation can be achieved for the choice of $K_T = 10\,\text{GeV}$ and $I_{mini} < 0.05$. These requirements are used for the muons selected for this analysis. The muon isolation performance has been measured using the T&P method in $Z \to \mu^+\mu^-$ events in a subset of 2012 data and MC. The efficiency is close to 1 over the full p_T range and extremely close in data and MC [87], such that no scale factor needs to be introduced in the analysis. A slight data-MC difference in the efficiencies in the low-p_T region will be accounted for with a systematic uncertainty (see section 6.7).

5.3.4. Muon Trigger

As previously described for electrons, there is also a single-muon trigger. Events have to have fired either of the two in order to be considered in this analysis. All three stages of

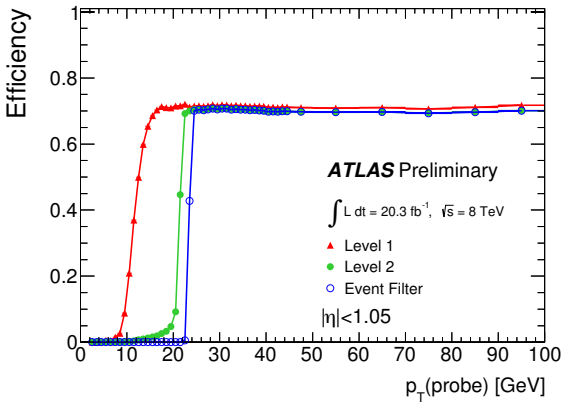

Figure 5.7.: Efficiency of the two single-muon trigger chains (convolved with a logical OR) measured with the T&P method in the full 2012 data set as a function of the p_T of the probe muon in the barrel part of the muon system [100].

the ATLAS trigger system are used for the decision: The hardware-based L1 trigger level searches for hit coincidences in the different layers of the muon spectrometer's RPC and TGC chambers (see section 3.2.5), which are defined as regions of interest (RoI) and used as the starting point for the next stage. The L2 trigger level takes these L1 RoIs and is using the full granularity of the muon system to select MDT regions that have been crossed by a muon track. After performing a track fit, these tracks are combined with ID tracks. As a last step, the EF uses the same algorithms that are used in offline muon reconstruction in the analysis. Similarly to the L2 stage, MS tracks are reconstructed and, after a full track fit, combined with tracks from the ID.
As for electrons, there are two separate trigger chains (L1→L2→EF) for muons, at least one of which an event has to pass in order to be selected:

- `L1_MU15` → `L2_mu24_tight` → `EF_mu24i_tight`
- `L1_MU15` → `L2_mu36_tight` → `EF_mu36_tight`

The two chains only differ in the p_T threshold of the considered muon candidates and in the isolation criterion in the first chain, indicated by the `i` of the EF item name. This isolation criterion was introduced in order to lower the p_T cut while still maintaining a good trigger efficiency. Both of these trigger chains have the lowest p_T thresholds to still be unprescaled over the full 2012 data taking period. The efficiency of the single-muon trigger as a function of the muon momentum is shown in Figure 5.7.

5.4. Jets

In the final state of a semi-leptonic b^*/B decay, one expects three partons: a b quark from the top-quark decay and two additional quarks from the hadronic W-boson decay. More partons can occur due to initial or final state radiation. Due to the structure of QCD (as discussed in section 2.1.4), single partons cannot propagate very far. They form showers which eventually hadronise and appear in the detector as collimated particle bunches, so-called jets. These jets leave energy deposits in the calorimeters, which are used to reconstruct them. This is more challenging than for single particles, as the reconstructed jet object needs to represent all kinematic properties of the parton shower, which in turn carries the quantities of the underlying single parton. For this purpose, several jet algorithms have been developed which will be discussed in the next section. It should be noted, however, that a jet is the outcome of such an algorithm as opposed to a 'real world' physics object, which is why the properties of the jet can depend on the algorithm it is formed with. The jet selection criteria and corrections were developed and provided by the *ATLAS Jet and Etmiss Performance* working group.

5.4.1. Jet Reconstruction and Selection

Jet finding and reconstruction algorithms should fulfil two conditions in order to be comparable to theoretical calculations:

- **Infrared safety:** Adding additional soft (low-p_T) particles, not originating from fragmentation of a hard-scattered parton, should not have an influence on the properties of the reconstructed jet.
- **Collinear safety:** The jet properties should not change depending on whether a certain amount of transverse momentum is carried by one single parton or by several collinear ones.

There are two general types of jet finding algorithms, fixed-cone jet finders and sequential recombination algorithms [81]. The former ones start from high-p_T seed clusters in the calorimeter, add all clusters in a cone of fixed size around that object and re-calculate the jet direction from these objects. These algorithms are not infrared safe, and produce overlapping jets, which is why they are not used in ATLAS. The implementation of a

sequential recombination algorithm in ATLAS is the so-called k_T algorithm, which fulfils both above mentioned conditions. For each input object (calorimeter clusters in this case) i, two quantities are calculated:

$$d_{ij} = min\left(k_{T,i}^{2p}, k_{T,j}^{2p}\right) \frac{\Delta R_{ij}^2}{R} \tag{5.7}$$

where j runs over all clusters for $j \neq i$, $k_{T,i(j)}$ being the transverse momentum of object $i(j)$, ΔR_{ij} the angular distance between the two objects and p and R algorithm parameters, which will be discussed further down.

$$d_{iB} = k_{T,i}^{2p} \tag{5.8}$$

is the squared transverse momentum of cluster i with respect to the beam pipe. After the full list of d_{ij} and d_{iB} is established, a minimum value, d_{min} is searched for. The next steps depend on the two possible outcomes:

- If d_{min} is one of the d_{iB}, this object is considered a jet and is removed from the list of clusters.
- If d_{min} is one of the d_{ij}, the two clusters i and j are merged and the list is re-established with the remaining clusters.

This iterative procedure is carried out as long as there are still clusters on the list. The two above mentioned parameters that appear in Eq. 5.7 and 5.8, R and p, have the following meaning: R is a measure for the resolution at which jets are resolved and thus for the approximate size of the jet. With increasing R, d_{ij} is smaller for a given pair of clusters and thus, more clusters are merged until the object is considered a final jet. R is therefore often denoted as the 'radius parameter' of a jet. p can take three distinct values, depending on which the algorithm can be classified into three different versions:

- $\mathbf{p = 1}$: This choice of p was used in the original k_T algorithm [101]. Soft (low-p_T) objects are merged first, i.e. the final merging step combines the hardest objects. This procedure back-tracks the evolution of a shower from a single parton that splits up and is therefore close to the real physics process. However, it has the shortcoming, that very soft objects i with $d_{iB} < d_{ij}$ for all other clusters j will never be merged with other clusters and thus result in single very soft jets.

- $\mathbf{p = -1}$: This choice of p reverts the ordering of the k_T algorithm and is therefore commonly called anti-k_T algorithm [102]. It clusters hard objects first, and a soft object is merged with a hard one rather than with another soft one (a hard object 'collects' all soft contributions in its vicinity) and thus the jet boundaries are not dependent on soft radiations. It is the default jet algorithm used in ATLAS and for the jets selected in this analysis. The anti-k_T algorithm produces fairly round jets, which is why it is justified to call the parameter R a radius.
- $\mathbf{p = 0}$: This choice of p, which makes the clustering step momentum-independent, is called the Cambridge/Aachen (or C/A) algorithm [103]. Here, the closest objects in η-Φ space are merged first, independent of their momenta.

At each clustering step, the four-momentum scheme is deployed, such that the four-momentum of the jet is given by the sum of four-momenta of its constituents at any time [104]. In order to suppress the usually soft jets stemming from the underlying event, jets are only considered in the analysis if their momentum satisfies $p_T > 25\,\text{GeV}$. This requirement is made on the corrected p_T, i.e. after applying the jet calibration, which will be described in section 5.4.2. Jets from the full pseudorapidity range up to $|\eta| < 4.5$ are used in this analysis.
The reconstruction efficiency was studied in dijet events in 2010 data [105]. This was done using the T&P method on so-called track jets, which are built using ID tracks as input for the jet algorithm instead of calorimeter clusters. The reconstruction efficiency has a plateau value of 1.0 for jets with $p_T > 30\,\text{GeV}$. As data and MC were found to behave very similarly, no correction scale factors have to be applied in the analysis.
Small differences are observed for $20\,\text{GeV} < p_T < 30\,\text{GeV}$ which are used as an estimate for the systematic uncertainty related to jet reconstruction (see section 6.7).

5.4.2. Jet Energy Scale and Resolution

Due to the nature of parton showers, the determination of the jet energy scale is more involved than the one of single charged particles like electrons or muons. A shower can be decomposed into two parts: the electromagnetic (em) and the non-electromagnetic (non-em) shower component. The em component is initiated by electromagnetically decaying hadrons (mainly π^0) and the non-em component by contributions from all other processes, mainly of nuclear nature (release of nucleons or nucleon aggregates from the nuclear bound state).

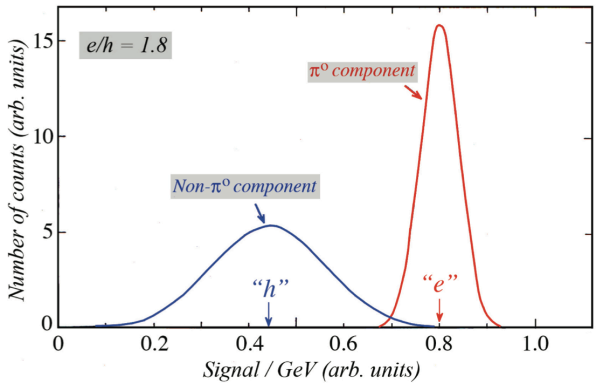

Figure 5.8.: Schematic representation of the response functions of a non-compensating calorimeter to the em and non-em components of hadronic showers. The ratio of the mean values of the two distributions is the e/h value [106].

The nuclear binding energy which has to be provided in order to enable such processes, however, will not be transformed into detector signals and is thus called 'invisible energy'. 15-55% of the non-em component will on average not be detected [104], which is why the calorimeter response (signal per deposited energy) of the non-em component is typically lower than the one of the em component. As can be seen from the schematic representation of the calorimeter response functions in Figure 5.8, the non-em component is also considerably broader than the em one, which is due to the large variety of nuclear reactions and thus a wide range of associated binding energy losses. The ratio of the mean values of both functions, commonly referred to as the e/h value, is a measure for the nature of the calorimeter. Calorimeters with $e/h \neq 1$ are called *non-compensating*. This is the case for the ATLAS calorimeter system, which is why a special calibration is needed in order to account for the non-measured jet energy. For this purpose, so-called *truth* jets are built using simulated stable particles as input to the jet algorithm instead of calorimeter clusters. This provides a handle on the the true energy of a jet, which can be used for calibration purposes. The different steps used for calibrating the jets, will be described in the following.

Energy depositions in the calorimeter used to form jets are usually reconstructed from topologically connected calorimeter cells with a significant signal above noise level (so-called topo clusters [107]) at the *electromagnetic energy scale* [108] (EM).

Jets formed from these clusters on the EM scale were only used for analyses of the very first Run 1 data. For more recent physics analyses, a cluster calibration is usually

applied. The calibration scheme used for clusters in this analysis is the so-called local cell weighting (LCW) scheme [104], which starts from topo clusters reconstructed at the EM scale, and uses additional information on the measured cluster topology (e.g. energy density in the calorimeter cells, fraction of energy deposited in different calorimeter layers or shower depth) in order to classify the clusters as being hadronic or electromagnetic. Based on this classification, energy correction factors are derived from single pion MC simulations, comprising dedicated corrections for non-compensation of the calorimeters, energy losses in inactive regions and signal losses due to noise threshold effects [104]. These calibrated clusters are then handed over to the jet algorithm of choice. Both kinds of jets, EM and LCW, then undergo a correction procedure in order restore the original jet properties known from truth particle level. This calibration consists of four steps:

- **pile-up correction:** The jet energy is affected by in-time and out-of-time pile-up. Correction factors depending on the number of primary vertices, the expected average number of interactions, η and p_T are derived from MC.
- **origin correction:** After their formation, calorimeter jets point to the centre of the detector. A correction is applied to make them point to the position of the primary vertex of the event. This correction does not alter the jet energy.
- **energy and η calibration:** The jet energy is corrected using MC information on the jet response, defined as the ratio of the calorimeter jet p_T and the particle (truth) jet p_T, depending on the jet pseudorapidity. This quantity, which can be derived for EM as well as for LCW jets, is shown in Figure 5.9. Its inverse in each bin is equal to the average jet energy scale correction factor.
- **residual in-situ corrections:** In this last step, residual corrections to account for data-MC differences are obtained in situ from p_T imbalances between a jet and a well-measured reference object and are applied to data only. For details on these techniques please refer to [104].

The resulting energy scale corrected jets are referred to EM+JES or LCW+JES calibrated jets, respectively, depending on the kind of clusters which were used as inputs to the jet algorithm.

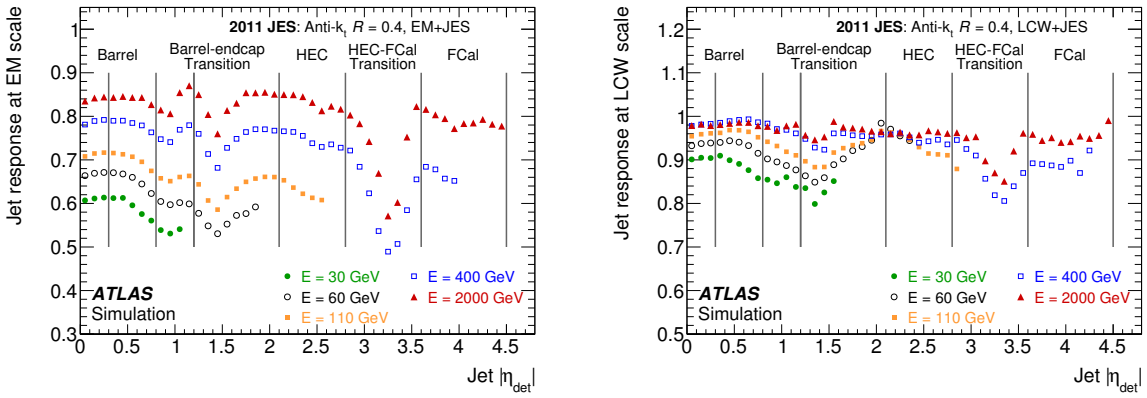

(a) (b)

Figure 5.9.: Average response of simulated jets formed from topo clusters as a function of the jet energy and the uncorrected η for anti-k_T jets with a radius parameter of $R = 0.4$ for the EM scale (a) and for the LCW scale (b). The vertical lines divide the pseudorapidity range in regions where the JES uncertainty is derived separately. The inverse of the response in each bin is equal to the average jet energy scale correction factor [104]

The jet energy scale uncertainty for LCW+JES jets is determined using *in situ* techniques separately for various η regions.

The jet p_T resolution $\sigma(p_T)/p_T$, which at a fixed rapidity value corresponds to the jet energy resolution $\sigma(E)/E$, can be determined by two different techniques [109], both performed in situ in dijet events. The first method makes use of the approximate scalar p_T balance of the two leading (highest p_T) jets in such events, based on momentum balance in the transverse plane. The p_T asymmetry is given by

$$A(p_{T,1}, p_{T,2}) \equiv \frac{p_{T,1} - p_{T,2}}{p_{T,1} + p_{T,2}}, \tag{5.9}$$

$p_{T,1}$ and $p_{T,2}$ being the randomly ordered momenta of the two jets. The width $\sigma(A)$ of the asymmetry distribution is used to determine the energy resolution via the relation

$$\sigma(A) \simeq \frac{\sqrt{\sigma^2(p_{T,1}) + \sigma^2(p_{T,2})}}{\langle p_{T,1} + p_{T,2} \rangle} \simeq \frac{1}{\sqrt{2}} \frac{\sigma(p_T)}{p_T}, \tag{5.10}$$

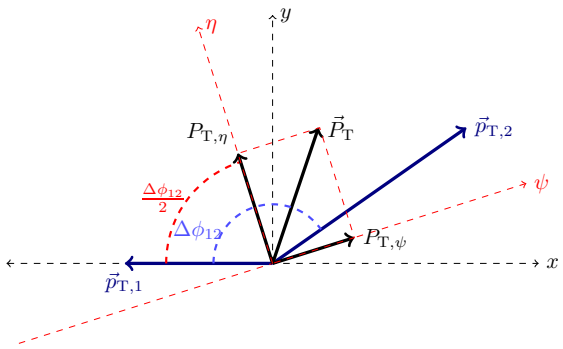

Figure 5.10.: Variables used in the bisector method. The η-axis corresponds to the azimuthal angular bisector of the dijet system in the plane transverse to the beam axis, while the ψ-axis is defined as the one orthogonal to the η-axis [109].

for two jets in the same rapidity range, with $\sigma(p_{T,1}) = \sigma(p_{T,2}) = \sigma(p_T)$. For jets in different rapidity intervals, a similar but slightly more involved formula determines the relation between the fractional jet p_T resolution and the width of the asymmetry function [109]. The calculation additionally takes into account corrections for the presence of additional soft jets in the event as well as for out-of-jet showering in the particle jets.

The second strategy to measure the jet energy resolution, the so-called bisector method, projects the vector sum of the p_T of the two leading jets onto a coordinate system in the transverse plane given by the bisector of the azimuthal angle difference of the two jets (η-axis) and an axis perpendicular to this one (ψ-axis), as depicted in Figure 5.10. This method makes use of the fact that for a perfectly balanced dijet event, the vector sum of the jet momenta would be zero. After correcting for detector effects and transferring all quantities from particle jet to calorimeter jet level, the fractional jet p_T resolution is given by the widths of the η and ψ momentum components measured in the calorimeter and the azimuthal angle difference of the two jets, $\Delta\Phi_{12}$, via the following relation:

$$\frac{\sigma(p_T)}{p_T} \simeq \frac{\sqrt{\sigma_{\psi}^{2\ calo} - \sigma_{\eta}^{2\ calo}}}{\sqrt{2}p_T\sqrt{\langle|cos\Delta\phi_{12}|\rangle}}. \tag{5.11}$$

The fractional p_T resolutions measured with the two methods in data and MC are shown in Figure 5.11 as a function of the mean p_T of the two jets used. Within statistical uncertainties the results of the two methods as well as data and MC results are in agreement and no additional smearing has to be applied.

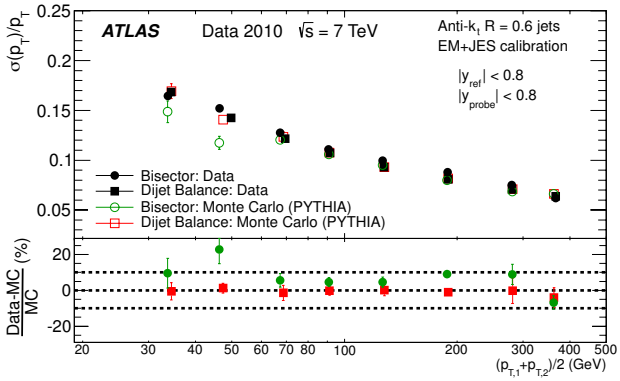

Figure 5.11.: Fractional jet p_T resolution for the dijet balance and the bisector methods as a function of the mean transverse momentum of the two jets for EM+JES calibrated jets. The lower panel shows the difference between data and MC results [109].

5.4.3. Jet Quality and Pile-up Suppression

Besides particles stemming from real proton-proton collisions, there is a number of different processes, that can also lead to energy depositions in the calorimeters, which might be picked up by the jet algorithms and therefore need to be discriminated against. These non-collision events can be spikes or other hardware problems in the calorimeters, LHC beam halo events or showers induced by cosmic rays entering the detector. A set of quality cuts has been established in order to label jets which are likely to stem from these processes as 'bad jets' [110]. Events containing a bad jet are not considered in the analysis.
Another source of jets not stemming from the hard interaction and thus from the primary vertex (PV) in the respective event is pile-up. These jets are rejected by introducing the so-called jet vertex fraction (JVF), which is a measure for the likelihood that a jet originates from the primary vertex. For every jet it is defined as the fraction of the sum of transverse momenta of associated[2] tracks pointing back to the PV and the transverse momentum sum of all associated tracks:

$$JVF = \frac{\sum_{tracks} p_T^{PV}}{\sum_{tracks} p_T}. \tag{5.12}$$

Figure 5.12 shows the JVF distribution for simulated dijet events. The separation between hard-scatter and pile-up jets is very clean. For rejecting pile-up jets, a requirement of $|JVF| > 0.5$ is therefore made. To reduce potential inefficiencies, this requirement is

[2]The association is done via a ΔR matching.

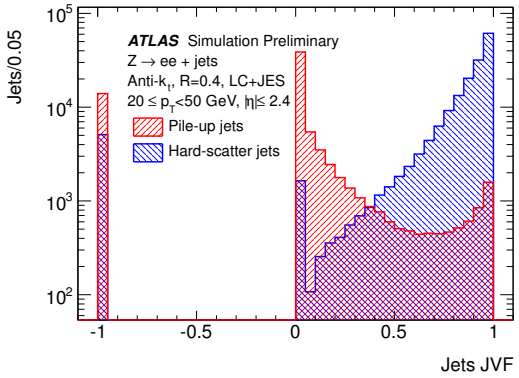

Figure 5.12.: JVF distribution for simulated hard-scatter and pile-up jets with 20 GeV $< p_T <$ 50 GeV in simulated Z+jets events [111]. A JVF value of -1 is assigned to calorimeter jets without associated tracks. As the cut is performed on the absolute value of JVF, these jets are not rejected by the JVF requirement.

only applied for jets within $|\eta| < 2.4$, as the association of tracks is only meaningful within the acceptance of the Inner Detector, and for jets with $p_T \leq 50$ GeV, as it could be shown that 99% of pile-up jets lie within that kinematic region [111].

Small data-MC differences in the hard scatter jet selection efficiency given by the JVF requirement, are accounted for by a scale factor in the analysis and its associated systematic uncertainty.

5.4.4. *b*-Jet Identification

Bottom quarks hadronise into so-called b hadrons, that have comparatively long lifetimes of $\tau \sim 1$ ps in the case of the Λ_b and even $\tau \sim 1.5$ ps for other b hadrons like B^0, $\bar{B}^0$, $B^{\pm}$ or B_s. Thus, the decay characteristics of those hadrons can be deployed in order to distinguish the resulting jets (so-called b-jets) from jets initiated from light quarks or gluons. This can be useful in searches involving top-quarks, like the one presented in this thesis, as top-quarks nearly exclusively decay into b quarks. The identification of b-jets is therefore a powerful means to suppress non-top background.
The long life time enables a b hadron with $p_T \sim 50$ GeV to travel ~3 mm before it decays, which leads to a displaced secondary vertex and large impact parameters, as shown in Figure 5.13, which can be used in order to identify b-jets. Other characteristics that should be noted are the high b-hadron mass (> 5 GeV) and the hard fragmentation process, which

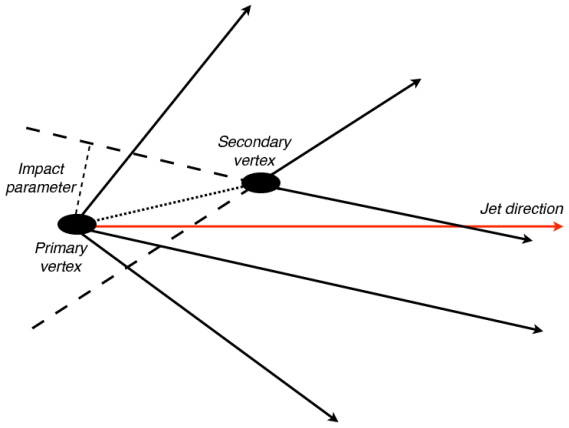

Figure 5.13.: Sketch of a displaced vertex coming from a b-jet with high impact parameter tracks (not to scale) [112].

leads to the fact that the b hadron carries on average about 70% of the original b-quark momentum [112].

Several algorithms are used in ATLAS, all of which use information on the impact parameters or on the displaced vertices in order to discriminate between b-quark induced jets and others. This procedure is commonly called *b-tagging*. As a first stage, a track selection is performed with somewhat looser criteria than the tracks used for primary vertex reconstruction (see section 3.2.2), e.g. a relaxed cut on the transverse track impact parameter [81], in order to enhance the selection efficiency for tracks from V^0 decays (e.g. Λ or K_s) and to reject those tracks. Another means of V^0 rejection is to sort out two-track vertices which have an invariant mass compatible with a V^0. The remaining tracks are used as input for two different kinds of b-tagging algorithms, which will be explained in the following:

- **Impact parameter tagging algorithms:**
  The impact parameters of the tracks are computed with respect to the primary vertex. Based on the assumption that the decay point of the b hadron must be lying on its flight path, the impact parameter is given a sign. That sign is defined by the jet direction $\overrightarrow{P_j}$ as measured by the calorimeter, the position $\overrightarrow{X_t}$ and the direction $\overrightarrow{P_t}$ of the track at the point of closest approach to the primary vertex and the position $\overrightarrow{X_{PV}}$

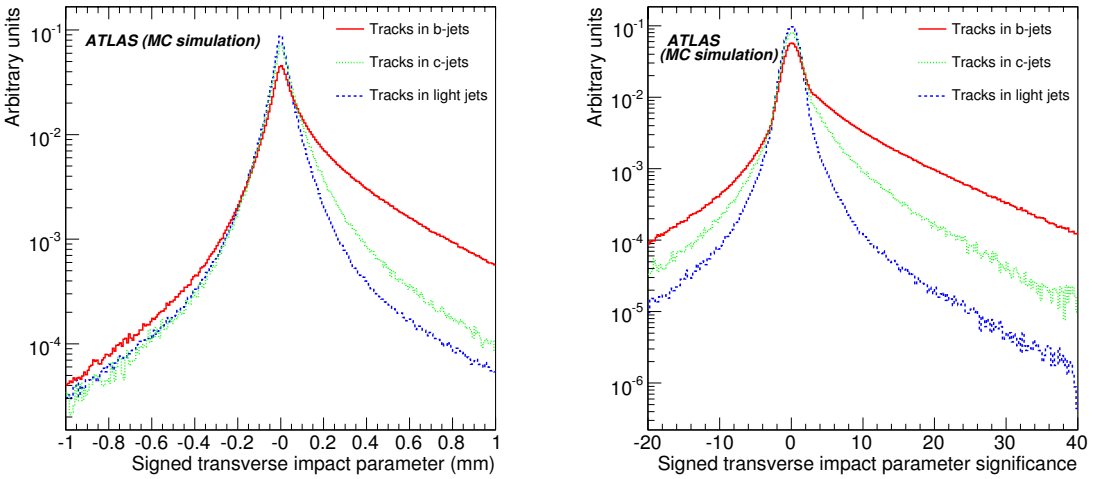

(a) (b)

Figure 5.14.: Distributions of the signed transverse impact parameter d_0 (a) and the signed transverse impact parameter significance d_0/σ_{d_0} (b) for b-jets, c-jets and light jets [113].

of the primary vertex in the following way [81]:

$$sign(d_0) = \left(\overrightarrow{P_j} \times \overrightarrow{P_t}\right) \cdot \left(\overrightarrow{P_t} \times \left(\overrightarrow{X_{PV}} - \overrightarrow{X_t}\right)\right). \tag{5.13}$$

This is a means to discriminate between heavy (b, c) and light-flavour jets, as the resolution randomly generates signs for the latter ones, while the impact parameters of the former ones tend to be positive. Another discriminating variable is the signed longitudinal impact parameter, of which the sign is given by $(\eta_j - \eta_t) \times z_{0_t}$, where again the subscript t (j) corresponds to track (jet) quantities. In order to give more weight to precisely measured tracks, eventually the significances of the impact parameters are used as discriminating variables instead of the quantities themselves. This comparison is shown in Figure 5.14, where the signed transverse impact parameter and its significance are shown for b-, c- and light jets.

Various algorithms make use of these quantities: `IP1D` uses the longitudinal impact parameter, `IP2D` the transverse one and `IP3D` combines information from both by using 2-dimensional histograms of the two quantities and thus taking their correlations properly into account.

- **Secondary vertex tagging algorithms:**
  Another approach for identifying b-jets is the reconstruction of the secondary vertex from the b-hadron decay. A vertex is formed of all pairs of tracks that are far enough from the primary vertex. In order to assure this, the significance of the 3-dimensional decay length $L_{3D} \equiv |\overrightarrow{X_{PV}} - \overrightarrow{X_t}|$ has to fulfil $L_{3D}/\sigma_{L_{3D}} > 2$. Such a two-track vertex is discarded if it does not obey certain quality criteria. For details, please refer to [81]. After removing the vertices with an invariant mass compatible with a V^0, the other two-track vertices are combined into a single one. This is done optimising the χ^2 by removing the respective worst track.
  The `SV0` algorithm uses the signed decay length significance as a discriminating variable. In order to enhance the discrimination power, other b-tagging algorithms exploit three different quantities related to the secondary vertex:

  – the invariant mass of all tracks associated to the vertex,

  – the total energy ratio of tracks associated to the vertex and all tracks in the jet and

  – the number of two-track vertices used to build the secondary vertex.

  The `SV1` algorithm makes use of a 2D distribution of the first two variables, and the 1D distribution of the last one, while `SV2` uses a 3-dimensional histogram of all three quantities, which is only possible with sufficient statistics.

- **Decay chain reconstruction:**
  A different algorithm, called `JetFitter`, which makes use of the topology of weak b- and subsequent weak c-decays, uses a Kalman Filter [53] to find the line connecting the primary and the secondary vertices. This gives rise to the possibility to also disentangle b- from c-jets in addition to light jets. A likelihood is used with variables similar to the ones used by the `SV` taggers, and additional discriminating variables such as flight length significances. A more recent version of decay chain algorithms, `JetFitterCombNN`, uses an artificial neural network to combine the various variables in order to achieve an optimal discrimination power.

Both, the impact parameter-based and the secondary vertex tagging algorithms make use of a likelihood ratio method, in which the measured value S_i of a discriminant is compared to pre-defined distributions $b(S_i)$ and $u(S_i)$ for the b- and light jet hypotheses [81].

A track or vertex weight is defined by the ratio of likelihoods $b(S_i)/u(S_i)$. The sum of the logarithms of the N_T individual track weights of the tracks in one jet yields the jet weight W_{jet}:

$$W_{jet} = \sum_{i=1}^{N_T} lnW_i = \sum_{i=1}^{N_T} ln\frac{b(S_i)}{u(S_i)}. \tag{5.14}$$

When no vertex is found, the `SV` taggers return a weight of $(1-\epsilon_b^{SV})/(1-\epsilon_u^{SV})$, depending on the secondary vertex finding efficiencies for b- and light jets, ϵ_b and ϵ_u, respectively.
The actual decision whether a given jet is b-tagged, is based on the choice of a cut value on W_{jet}, corresponding to a certain efficiency, which differs depending on the analysis in question. The efficiency for a given cut value depends on the transverse momentum and rapidity of the jet and is especially only calculated for jets with $p_T > 20\,\text{GeV}$ and $|\eta| < 2.5$ (Inner Detector acceptance). Usually, an increase in the b-tagging efficiency goes in line with an increase of wrongly tagged jets which do not actually stem from a b quark (enhancement of the mistag rate). A sizeable effort is made within ATLAS in order to find suitable *working points* for physics analyses, which provide a cut value on W_{jet} corresponding to a particular b-tagging efficiency and mistag rate.

Combinations of Algorithms

Due to the properties of likelihood methods, different tagging algorithms can easily be combined by just summing up the weights of the individual algorithms. The tagger used in this analysis, the so-called `MV1` algorithm [114], uses a combination of weights of `IP3D`, `JetFitter+IP3D` and `SV1`, which are fed into a neural network trained on simulated top-pair ($t\bar{t}$) events, in order to obtain an overall weight for every jet. The distribution of the `MV1` weight is shown in Figure 5.15 for b-, c- and light jets. In this analysis, a cut at an `MV1` weight of 0.7892 is chosen, corresponding to a b-tagging efficiency of 70% and a purity 92.28%. The rejection factor is 136.66 for light jets, 4.97 for c-jets and 13.24 for τ-jets.

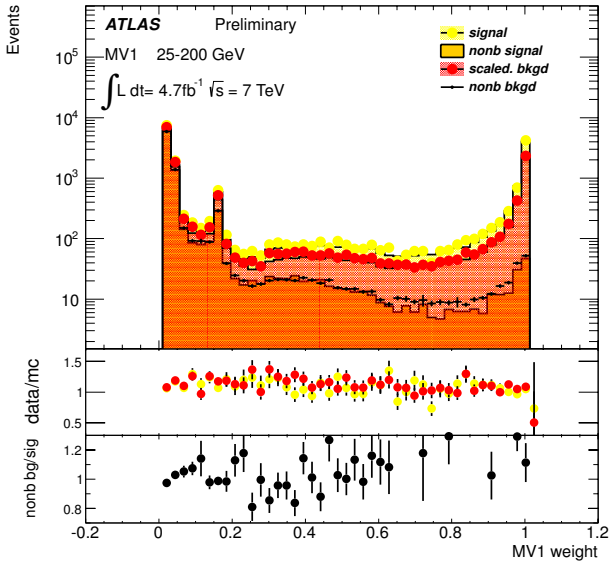

Figure 5.15.: MV1 weight distribution for simulated b-jet events (signal), simulated events without b-jets (non-b signal) and scaled simulated backgrounds for a centre-of-mass energy of 7 TeV [115]. A corresponding public plot for a centre-of-mass energy of 8 TeV was not available.

b-tagging Calibration

In order to account for potential differences between b-tagging efficiencies in data and MC, the algorithms have to be calibrated with data. For the `MV1` algorithm used in this analysis, this is done using dileptonic ($t\bar{t}$) events, i.e. events where the W bosons from both top-quark decays decay leptonically [116] via a procedure described in the following. Four channels are investigated separately and combined to obtain the final result (combinations of $e\mu$, same-flavour leptons and 2-, 3-jet events).
In order to obtain the b-tagging efficiency ϵ_b, one can use the following equation:

$$f_{tagged} = f_b\epsilon_b + (1 - f_b)\epsilon_j, \tag{5.15}$$

where the fraction of jets selected by the tagging requirement, f_{tagged}, is measured in data and the fraction of b-jets in the selected sample, f_b, as well as the non-b-jet efficiency, ϵ_j, are determined from MC simulations. For the case of events with exactly two jets, this extends to a system of two equations for one or two tagged jets, respectively. As the efficiencies usually depend on jet-related quantities like p_T, η and other kinematic variables, one wants

to bin in those variables. This generalisation leads to a large set of non-linear equations which can, in principle, be solved analytically, but in practice it is much simpler to use a likelihood function to model the system. This likelihood function is then maximised using numerical minimisation programs. The likelihood formalism will be described in the following.
The unbinned likelihood function used in this b-tagging calibration analysis is defined in the following way for the case of events with exactly two jets:

$$\begin{aligned}\mathcal{L}(p_{T,1}, p_{T,2}, w_1, w_2) = [&f_{bb}\mathcal{P}_{bb}(p_{T,1}, p_{T,2})\mathcal{P}_b(w_1|p_{T,1})\mathcal{P}_b(w_2|p_{T,2}) \\ &+ f_{bj}\mathcal{P}_{bj}(p_{T,1}, p_{T,2})\mathcal{P}_b(w_1|p_{T,1})\mathcal{P}_b(w_2|p\_T, 2) \\ &+ f_{jj}\mathcal{P}_{jj}(p_{T,1}, p_{T,2})\mathcal{P}_b(w_1|p_{T,1})\mathcal{P}_b(w_2|p\_T, 2) \\ &+ 1 \leftrightarrow 2]\,/2,\end{aligned} \tag{5.16}$$

with

- f_{bb}, f_{bj} and $f_{jj} = 1 - f_{bb} - f_{bj}$ being the two-jet flavour fractions,
- $\mathcal{P}_f(w|p_T)$ being the probability density function (PDF) for the b-tagging weight for a jet of flavour f with a given p_T and
- $\mathcal{P}_{f_1 f_2}(p_{T,1}, p_{T,2})$ being the 2-dimensional PDF for $[p_{T,1}, p_{T,2}]$ for the flavour combination $[f_1, f_2]$.

As the analysis uses binned histograms, the PDF have to be expressed as such histograms as well. All the PDF are determined from MC, except for the b-jet weight PDF, of which the information is extracted from data. In cases, where the efficiencies are only needed for a single cut on the b-tagging weight, a two-bin histogram is sufficient to describe the b-weight PDF. The bin above the cut value then corresponds to the b-tagging efficiency and this latter one can be expressed as

$$\epsilon_b(p_T) = \int_{w_{cut}}^{\text{inf}} dw' \mathcal{P}_b(w', p_T). \tag{5.17}$$

This procedure can be extended to the three-jet case similarly, which is also used in the calibration analysis. For details, please refer to [116].

Figure 5.16 shows the efficiency of the `MV1` tagger to select b-, c- and light jets as a function of the jet p_T and $|\eta|$, measured in a sample of simulated $t\bar{t}$ events.

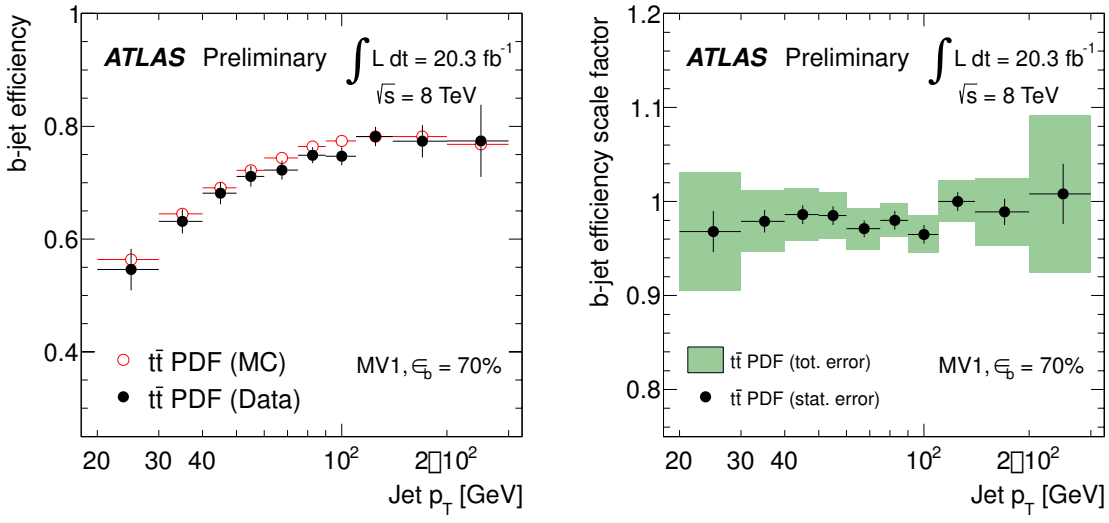

(a) (b)

Figure 5.16.: The b-jet efficiencies (a) and data-MC scale factors (b) obtained from all four channels for the `MV1` b-tagging algorithm at the 70% b-jet efficiency working point. The error bars on the data points in (a) represent the total statistical and systematic uncertainties, while in (b) the statistical-only uncertainties are shown by the error bars and the total errors by the green areas [116].

5.5. Overlap Between Lepton and Jet Objects

Even though the selection criteria for the various objects defined above are chosen in order to give a high purity, there is still a chance of misidentifying an object of one kind as one of another kind due to very similar residual detector responses. In order to avoid cases, where an object is reconstructed by several algorithms, the following set of so-called 'overlap removal' criteria has to be applied after having applied the full set of selection criteria of electrons, muons and jets:

- **electron-muon overlap removal:** If an electron and a muon share an ID track, which is closer than 0.005 in both, η and Φ, the lepton pair is flagged as overlapping. Events with at least one such pair are rejected from the analysis, as one can not distinguish which of the two was the 'real' particle and which one was misidentified.
- **electron-jet duplicates:** The closest jet to an electron has to be removed if it is within a distance of $\Delta R < 0.2$ to the electron. This accounts for the possibility that

electrons are reconstructed as jets, as the jet algorithm is seeded by energy deposits in the calorimeters, which are also left by electrons.

- **jet-electron overlap removal:** After the previously described electron-jet duplicate removal, all electrons within $\Delta R < 0.4$ to a jet are rejected. This accounts for the fact that electrons often occur as decay products inside jets, and thus have to be eliminated from the list of prompt electron candidates. As a consequence, the electron scale factors described earlier are only estimated for prompt electrons and are therefore only valid if there is no close-by jet.
- **jet-muon overlap removal:** As muons can also originate from hadron decays inside jets, muons with $\Delta R(\mu, jet) < 0.4$ are rejected as well.

5.6. Missing Transverse Momentum

In the semi-leptonic decays of heavy quarks, as they are considered in this analysis, one of the W bosons decays into a charged lepton and a neutrino. Even though neutrinos are not directly detectable in ATLAS, there is a measure for the amount of energy they carry away from the event. For this, momentum conservation is exploited: As the initial state in a collider has no transverse momentum components, an event only containing detectable particles would result in zero total momentum in the transverse plane after the collision. The variable used to quantify a momentum imbalance in the transverse plane, resulting from the presence of particles that escape the detection, is the missing transverse momentum, commonly referred to as 'missing transverse energy' or E_T^{miss}. It can be divided into a muon and a calorimeter term, while low-p_T tracks are used to recover particles which do not reach the calorimeter and ID muons are used to recover muons traversing regions which are not covered by the MS [117]:

$$E_{x(y)}^{miss} = E_{x(y)}^{miss,calo} + E_{x(y)}^{miss,\mu}. \tag{5.18}$$

The total missing transverse momentum is then given by

$$E_T^{miss} = \sqrt{\left(E_x^{miss}\right)^2 + \left(E_y^{miss}\right)^2}. \tag{5.19}$$

The algorithms used to calculate and calibrate the missing transverse momentum are developed and provided by the *ATLAS Jet and Etmiss Performance* working group.

5.6.1. The E_T^{miss} Calorimeter Term

The calorimeter term of the missing transverse momentum is calculated from energy deposits in calorimeter clusters that are associated with a physics object and calibrated accordingly. The order of this association with high-p_T parent objects is the following one: electrons, photons, hadronically decaying τ-leptons, jets, muons. Cells, which are not associated with such an object, but contain energy deposits, are also taken into account in the calculation via a term referred to as $E_T^{miss,CellOut}$, which plays an important role for the E_T^{miss} resolution. After the association with physics objects, the calorimeter term is calculated in the following way:

$$\begin{aligned} E_{x(y)}^{miss,calo} = & E_{x(y)}^{miss,e} + E_{x(y)}^{miss,\gamma} + E_{x(y)}^{miss,\tau} + E_{x(y)}^{miss,jets} + E_{x(y)}^{miss,softjets} \\ & + \left(E_{x(y)}^{miss,calo,\mu}\right) + E_{x(y)}^{miss,CellOut}, \end{aligned} \tag{5.20}$$

[117], the individual terms being described below, using only cells that belong to topological clusters in order to suppress noise contributions:

- $E_{x(y)}^{miss,e}$, $E_{x(y)}^{miss,\gamma}$, $E_{x(y)}^{miss,\tau}$ are reconstructed from cells in calorimeter clusters which are associated to electrons, photons or hadronic τ lepton decays, respectively.
- $E_{x(y)}^{miss,jets}$ is reconstructed from clusters associated to jets with calibrated $p_T > 20\,\text{GeV}$.
- $E_{x(y)}^{miss,softjets}$ is reconstructed from clusters associated to jets with $7\,\text{GeV} < p_T < 20\,\text{GeV}$.
- $E_{x(y)}^{miss,calo,\mu}$ is accounting for energy losses of muons in the calorimeter.
- $E_{x(y)}^{miss,CellOut}$ is calculated from cells that belong to calorimeter clusters which are not associated with any of the above mentioned physics objects.

The muon term in the calorimeter is only used in some cases (more information in the next section), which is why it is written in parentheses.

Each of the individual terms in Eq. 5.20 is calculated as the negative sum over the cells corresponding to the respective object:

$$E_x^{miss,term} = -\sum_i^{N_{cell}^{term}} E_i sin\theta_i cos\Phi_i \tag{5.21}$$

$$E_y^{miss,term} = -\sum_i^{N_{cell}^{term}} E_i sin\theta_i sin\Phi_i, \tag{5.22}$$

with E_i, θ_i and Φ_i being the energy, polar and azimuthal angle of the cells and the sum runs over all cells associated to objects with $|\eta| < 4.5$.

5.6.2. The E_T^{miss} Muon Term

The muon term is calculated from the momenta of tracks associated to muons reconstructed within $|\eta| < 2.7$ in the following way:

$$E_{x(y)}^{miss,\mu} = -\sum_{muons} p_{x(y)}^{\mu}. \tag{5.23}$$

Within the acceptance of the Inner Detector, $|\eta| < 2.5$, only combined muons (see section 5.3) are used in order to suppress contributions from fake muons. The muon term is calculated differently for isolated and non-isolated (within a ΔR of 0.3 to a reconstructed jet in the event) muons, in order to correctly deal with the energy deposit in the calorimeters, $E_{x(y)}^{miss,calo,\mu}$: For isolated muons, the p_T is obtained from the combined measurement of the MS and the ID and the energy deposit in the calorimeters is taken into account. Thus, in this case, the term $E_{x(y)}^{miss,calo,\mu}$ is not added in Eq. 5.20 in order to avoid double counting. For non-isolated muons, however, it is not possible to disentangle the muon's energy deposit in the calorimeter from the one of the close-by jet. The muon p_T is therefore determined from the MS information after a part of the energy has been lost in the calorimeter and thus the term $E_{x(y)}^{miss,calo,\mu}$ has to be added to the calorimeter term (Eq. 5.20). As there is no combined muon measurement for $|\eta| > 2.5$, in this region the p_T measured in the Muon Spectrometer is used.

5.6.3. Calibration of the Missing Transverse Momentum

Before calculating the total missing transverse momentum of an event, each term in Eq. 5.20 is calibrated, i.e. the cell energy is replaced by the refined calibrated energies according to the corresponding physics object. For electrons and photons, the EM scale corrections are applied (energy loss in front of the ECAL and lateral and longitudinal leakage corrections), for soft and high-p_T jets as well as for hadronic τ decays, the cell energies are calibrated according to the LCW+JES scheme. Topological clusters outside of reconstructed objects, which contribute to the $E_{x(y)}^{miss,CellOut}$ term, are also calibrated using the LCW scheme.
The missing transverse momentum obtained after applying all these calibrations, is referred to as 'refined' E_T^{miss}.
The corrections applied to the various physics objects, as described earlier in this chapter (mainly scaling and smearing) are also accounted for in the E_T^{miss} calculation, by applying corrections to the calculated E_T^{miss} depending on the changed kinematic quantities of the original objects. Another correction applied to the calculated missing transverse momentum accounts for energy losses of jets in the cryostat between the ECAL and the HCAL. This correction is applied to every jet. The E_T^{miss} calculation also has to be corrected for pile-up contributions which mainly affect the $E_{x(y)}^{miss,jets}$ and $E_{x(y)}^{miss,softjets}$ terms as they are reconstructed from comparatively large areas in the calorimeter and pile-up produces hadronic energy deposits. For the jet term, this is done by applying the jet vertex fraction criterion to low-p_T jets, as described in section 5.4, which in turn alters the E_T^{miss} value. For the soft-jet term a similar method is introduced, the so-called 'soft term vertex fraction' (STVF) [118].
The E_T^{miss} resolution has been studied in $Z \to e^+e^-$ and $Z \to \mu^+\mu^-$ events. The E_x^{miss} and E_y^{miss} resolution before and after pile-up suppression and compared between 2012 data and MC are shown in Figure 5.17.

After all the physics objects used in the analysis are defined, the analysis strategy and selection criteria using these objects is described in the next chapter.

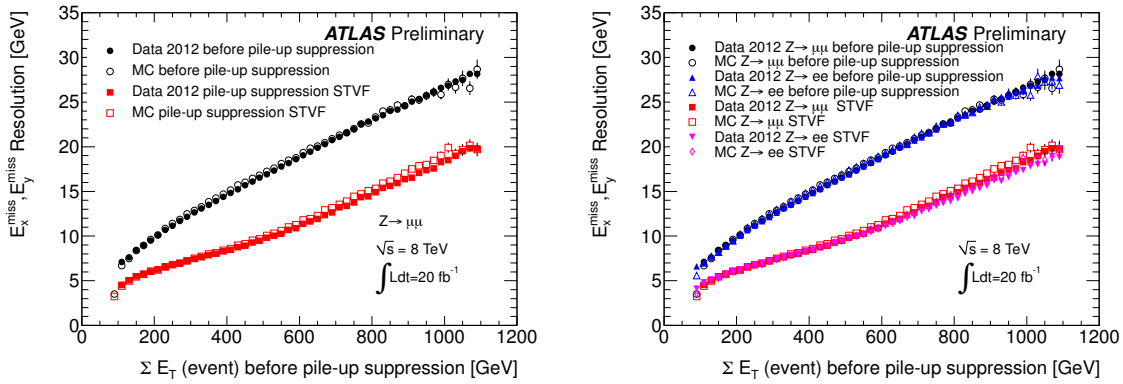

(a) (b)

Figure 5.17.: Missing transverse momentum resolution measured in the full 2012 data set compared to MC simulations before and after pile-up suppression in $Z \to \mu^+\mu^-$ events (a) and $Z \to \mu^+\mu^-$ as well as $Z \to e^+e^-$ events (b) [118].

Chapter 6.

Data Analysis and Results

In this chapter, the strategy and results of the analysis, a search for single production of two different new heavy quarks, b^* and B, in the decay mode to a W boson and a top quark in boosted single-lepton final states, are described. This analysis is part of a publication that was recently submitted to the Journal of High Energy Physics (JHEP) and which, besides the single-lepton channel described here, also covers an analysis in the dileptonic final state [119]. Final states of $b^*/B \to Wt \to WWb$ events in which both W bosons decay leptonically are generally clean signatures in terms of background processes, while the fraction of such events is relatively low ($\sim 4\%$). There are more events where only one of the W bosons decays leptonically ($\sim 30\%$) due to the higher branching fraction for hadronic W decays, while these events suffer from larger Standard Model backgrounds. This disadvantage, however, can be well compensated by selecting only events that contain a high-p_T jet with a large radius parameter, which is discussed further down in this chapter. While in the publication both channels were combined in order to obtain the final results, this thesis only focuses on the single-lepton results, which were obtained in the group at HU Berlin. The search in the dilepton channel was carried out by a team at Michigan State University and the statistical analysis, including the limit setting, was performed by a group from the University of Bonn.

Carrying out one combined search for both heavy quarks is well justified by the similarity of their decay kinematics, which is shown in section 6.2, after presenting the simulated signal samples in section 6.1, which were used to define and optimise the search strategy. The expected final state of such a heavy quark decay in the single-lepton channel is $Wt \to \ell + E_T^{miss} + jets$, with either the W boson or the top quark decaying hadronically. The selection has been optimised for relatively high vector-like quark masses. What this

implies for the analysis strategy, is discussed in section 6.3. In sections 6.4 and 6.5 the event selection and categorisation are described, while sections 6.6 through 6.8 discuss the modelling of the background by various techniques and systematic uncertainties of the method. Section 6.9 explains the signal extraction before closing with the statistical analysis in section 6.10.

6.1. Simulated Signal Processes

The signal selection was optimised using Monte-Carlo simulations of the signal and background processes. While the simulated background samples were produced by the ATLAS *Top* and *Exotics* groups, the simulation of the analysis-specific b^* process was carried out in the HU Berlin group and the B simulation was taken care of by the Michigan State University team.

b^* signal events [7] were simulated at leading order in QCD with the matrix-element generator MadGraph5 v1.5.12 [75] and interfaced to Pythia v8.175 [73] for hadronisation, parton shower and underlying event. This was done for 9 different signal masses between 600 GeV and 1800 GeV, in order to have some overlap with the mass range excluded by the preceding search (limit at ∼1 TeV [9]), while keeping some room to higher masses, which the changed search strategy of this analysis is expected to be sensitive to. The production was done in the 5-flavour scheme, allowing for the initial b quark to be taken from the b-quark PDF inside the proton and not only from gluon splitting processes. The only allowed decay mode of b^* in the produced samples is the one to W boson and top quark. The MSTW2008LO [66, 120] PDF set was used and the renormalisation scale μ_R and factorisation scale μ_F were set to the respective signal mass. As the exotic b^* quark can have purely left-handed ($f_g = f_L = 1,\ f_R = 0$) or purely right-handed couplings to the gauge bosons ($f_g = f_R = 1,\ f_L = 0$) or some arbitrary mixed case (including the vector-like quark scenario of $f_g = f_L = f_R = 1$)[1], see [7], and as the coupling slightly influences the decay kinematics, it was decided to produce two kinds of samples per mass point, corresponding to the two chiral cases: one with purely left-handed coupling (denoted as LH in the following) and another one with purely right-handed coupling (RH). The results can then be interpreted in terms of the vector-like case by normalising the sum of the two contributions to the theory cross section of that benchmark coupling scenario,

[1]Here, the unified notation $f_g = \kappa_L = \kappa_R$ is used for $\kappa_{L/R}$ as introduced in section 2.2.1 [7].

which is listed in Table 2.3 for various signal masses. Final results, as presented at the end of this chapter, are derived for the vector-like coupling scenario. In order to study effects of the choice of renormalisation and factorisation scale, which were set to the heavy quark mass in the production, μ_R and μ_R have been varied up and down by a factor of two in MadGraph and the resulting cross sections have been used as an uncertainty on the theory prediction. The cross-section values along with their variations for b^* for different coupling scenarios are listed in Table 6.1.

B signal events were simulated with Protos [6] using the MSTW2008LO PDF set, interfaced to Pythia v6.4 [72] for hadronisation, parton shower and underlying event. The samples were produced for 10 signal masses between 600 GeV and 1200 GeV, as the cross sections are lower than in the b^* case which leads to the expectation of a lower mass sensitivity in the B search. A singlet model and a mixing with the third generation of $V_{mix} = 0.1$ were assumed and all possible decay modes (Wt, Zb and Hb) were allowed in the production. For the B sample production, the MWST2008LO PDF set was used as well. While for the simulation the model described in [6] and the narrow-width approximation were used, for the final results a re-interpretation in terms of the composite Higgs model (as introduced in [44] and described in section 2.2.1) has been performed and thus, for the normalisation, theory cross-sections for a coupling parameter of $\lambda = 2$ have been used as a benchmark. Table 6.2 summarises the properties of the different signal samples, explicitly listing the cross sections for this B benchmark process. Cross sections for other λ values can be found in Table 2.2 in section 2.2.1. Please note, that cross sections for $\lambda > 3$ could not be used in the interpretation, as the composite Higgs model predicts significantly larger widths than the ones used in the production step. For larger values of λ the reconstructed width is no longer dominated by the experimental resolution, such that a usage of these samples within the presented analysis would lead to incorrect results. At the time the B Monte-Carlo samples were produced, unfortunately it was not yet known that the choice of the width would impose a restriction on the re-interpretation possibilities.
The simulated samples of the Standard Model background processes are described in section 6.5.

Table 6.1.: Characteristics of the generated b^* signal samples for various masses and purely left-handed (LH) and purely right-handed (RH) coupling scenarios: generator (hard process and shower), cross section times branching fraction to Wt (derived according to the model described in [7]) with its scale variations, as well as the total number of generated events. All samples were produced using the MSTW2008LO PDF set. MC samples were only produced for LH and RH cases, the vector-like (VL) case was obtained by making use of both chiral cases, which is why the last column is empty.

Process	Generator	$\sigma\cdot$ BF [pb]	$\sigma\cdot\mathrm{BF}_{down}$ [pb]	$\sigma\cdot\mathrm{BF}_{Up}$ [pb]	N_{events}
LH b^*, 600 GeV	MadGraph5	18.20	20.58	16.09	99998
LH b^*, 800 GeV	+Pythia8	3.864	4.463	3.357	100k
LH b^*, 1000 GeV		1.020	1.197	0.8738	99996
LH b^*, 1100 GeV		0.5560	0.6573	0.4735	99999
LH b^*, 1200 GeV		0.3128	0.3721	0.2649	99999
LH b^*, 1300 GeV		0.1807	0.2163	0.1523	99998
LH b^*, 1400 GeV		0.1069	0.1286	0.08959	99999
LH b^*, 1600 GeV		0.03952	0.04803	0.03284	99998
LH b^*, 1800 GeV		0.01553	0.01906	0.01280	99997
RH b^*, 600 GeV	MadGraph5	17.95	20.30	15.87	95000
RH b^*, 800 GeV	+Pythia8	3.781	4.368	3.285	99998
RH b^*, 1000 GeV		0.9907	1.163	0.8488	99998
RH b^*, 1100 GeV		0.5379	0.6358	0.4581	100k
RH b^*, 1200 GeV		0.3012	0.3583	0.2550	99997
RH b^*, 1300 GeV		0.1732	0.2072	0.1459	99997
RH b^*, 1400 GeV		0.1018	0.1225	0.08535	99998
RH b^*, 1600 GeV		0.03718	0.04521	0.03091	99998
RH b^*, 1800 GeV		0.01442	0.01769	0.01189	99998
VL b^*, 600 GeV	MadGraph5	34.742	39.307	30.715	–
VL b^*, 800 GeV	+Pythia8	7.5231	8.6895	6.5357	–
VL b^*, 1000 GeV		1.994	2.3408	1.7086	–
VL b^*, 1100 GeV		1.0868	1.2847	0.92564	–
VL b^*, 1200 GeV		0.61047	0.72629	0.51706	–
VL b^*, 1300 GeV		0.352	0.42123	0.29656	–
VL b^*, 1400 GeV		0.20755	0.24977	0.17403	–
VL b^*, 1600 GeV		0.076245	0.092718	0.063364	–
VL b^*, 1800 GeV		0.076245	0.036502	0.024528	–

Table 6.2.: Characteristics of the generated B signal samples for various masses: generator (hard process and shower), cross section times branching fraction to Wt (derived according to the model described in [44] for the benchmark coupling of $\lambda = 2$) with its scale variations, as well as the total number of generated events. All samples were produced using the MSTW2008LO PDF set.

Process	Generator	$\sigma\cdot$ BF [pb]	$\sigma\cdot\mathrm{BF}_{down}$ [pb]	$\sigma\cdot\mathrm{BF}_{up}$ [pb]	N_{events}
B ($\lambda = 2$), 600 GeV	Protos	0.2157	0.2717	0.1744	99999
B ($\lambda = 2$), 650 GeV	+Pythia6	0.1462	0.1838	0.1166	100k
B ($\lambda = 2$), 700 GeV		0.1035	0.1304	0.08246	99999
B ($\lambda = 2$), 750 GeV		0.07271	0.09214	0.05786	99999
B ($\lambda = 2$), 800 GeV		0.05229	0.06645	0.04196	99999
B ($\lambda = 2$), 850 GeV		0.03795	0.04814	0.03019	100k
B ($\lambda = 2$), 900 GeV		0.02751	0.03497	0.02183	100k
B ($\lambda = 2$), 950 GeV		0.02000	0.02548	0.01585	99999
B ($\lambda = 2$), 1000 GeV		0.01476	0.01904	0.01169	99999
B ($\lambda = 2$), 1200 GeV		0.004819	0.006237	0.003803	100k

6.2. Decay Kinematics of b^* and B

In order to validate the strategy of a combined search for the two models, the decay kinematics of both heavy quarks, b^* and B, were studied in detail. It was found that the kinematic distributions of the b^*/B decay products are sufficiently similar, such that a combined search is sensible. Figure 6.1 and Figure 6.2 show the Monte-Carlo truth information (cf. section 4.3.1) of p_T and η distributions of the heavy quark and its decay products (W boson and top quark) as well as the leading jet and electron p_T distributions for an example mass point of 900 GeV, none of which shows significant differences. The only major difference between the models that has to be accounted for in the selection is the different production modes resulting in additional (low-p_T and forward) jets in the B case which are not necessarily present in the production of b^* quarks.

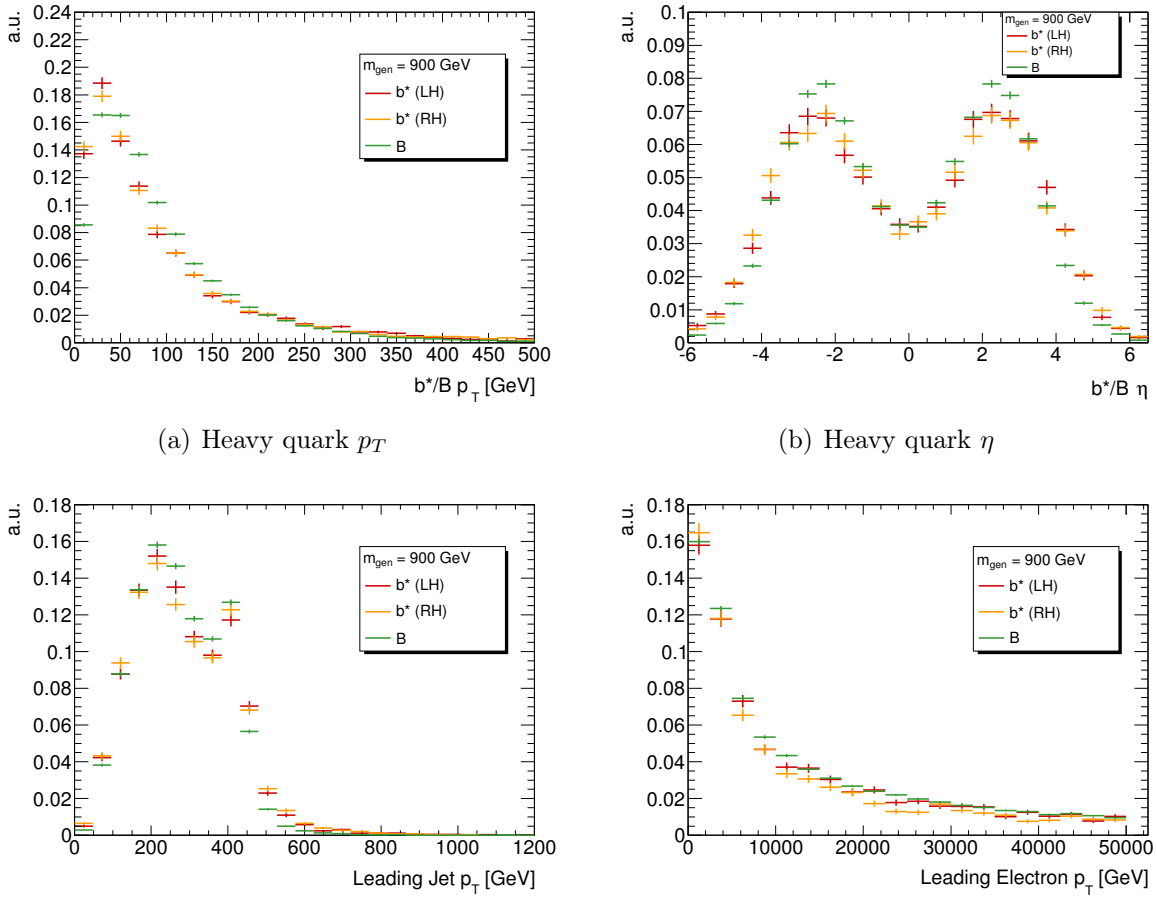

(a) Heavy quark p_T

(b) Heavy quark η

(c) Leading jet p_T

(d) Electron p_T

Figure 6.1.: Distributions of the truth information on p_T and η of the heavy quark (top row) and the leading jet and electron p_T (bottom) for simulated b^* (purely left- and purely right-handed couplings) and B signals with a mass of 900 GeV. The same set of distributions for a higher mass point can be found in Figure A.1 in Appendix A.

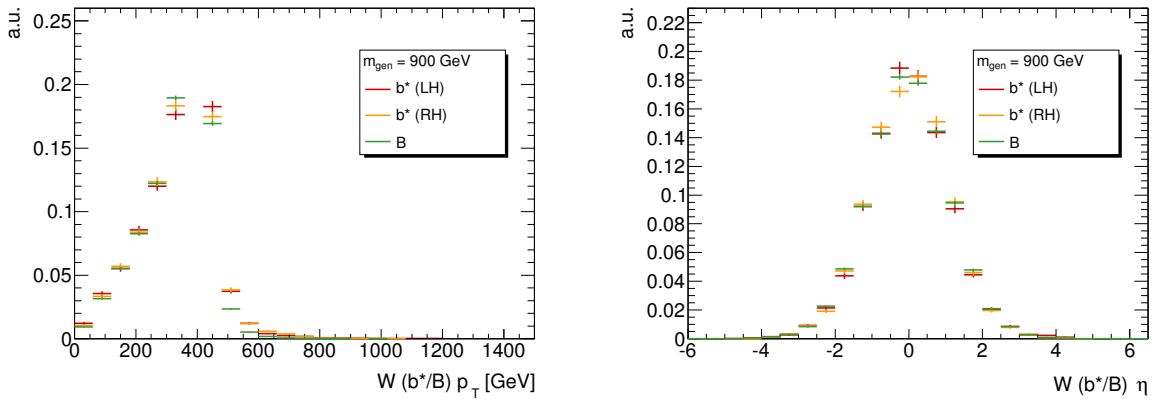

(a) W p_T (b) W η

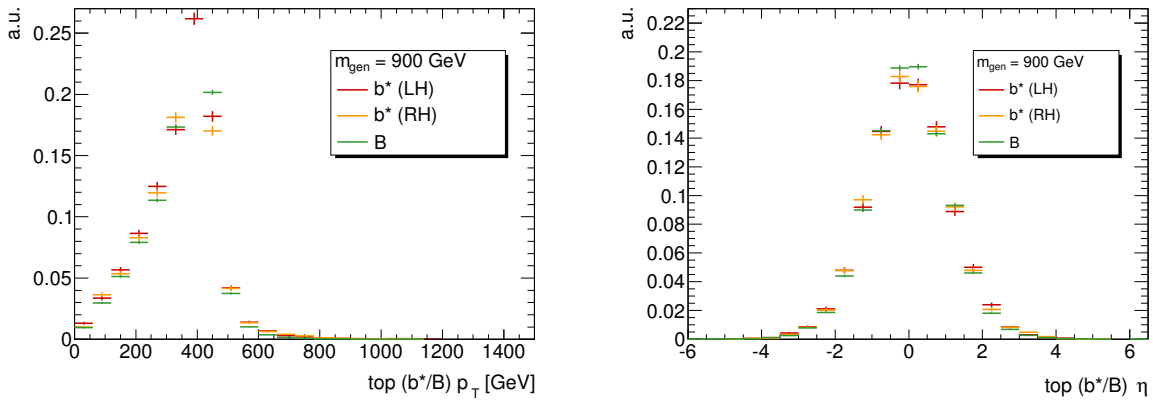

(c) top p_T (d) top η

Figure 6.2.: Distributions of the truth information on p_T and η of the heavy quark decay products W (top row) and top (bottom row) for simulated b^* (purely left- and purely right-handed couplings) and B signals with a mass of 900 GeV. The same set of distributions for a higher mass point can be found in Figure A.2 in Appendix A.

6.3. Analysis Strategy

Depending on the decay mode, there are different possible final states for b^*/B decays. Figure 6.3 shows the different types of heavy quark decays in the decay channel to Wt with at least one W boson decaying leptonically (the additional forward jet stemming from the production vertex in the B case is not shown as it does not influence the decay kinematics). For events with exactly one lepton, either the top quark or the W boson can decay hadronically, while the respective other one decays leptonically. As the top quark almost exclusively decays into a b quark, this leads to the final state of the heavy quark decay of $b^*/B \to tW \to bqq\ell\nu$. Fully hadronic decays are not considered in this search, while dileptonic decays were investigated in [119], alongside the single lepton ones described in this thesis.

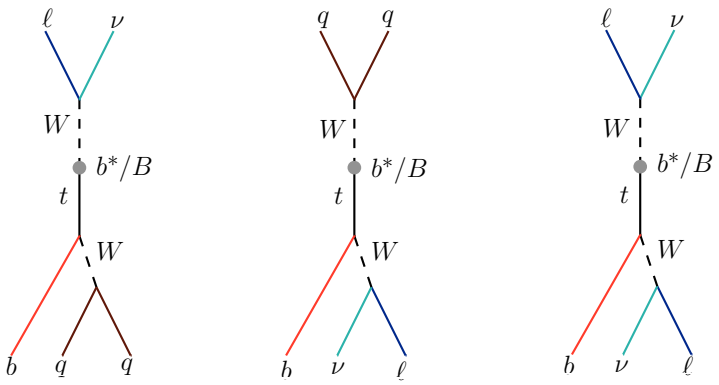

Figure 6.3.: Schematic representation of the possible heavy quark decay final states. The two different semi-leptonic final states and the dileptonic final state are shown. Fully hadronic final states are not displayed as they are not considered in this analysis.

In the semi-leptonic decay of a relatively light b^* quark, it is expected to find one isolated lepton, some amount of missing transverse momentum stemming from the undetected neutrino, and – in the case of no initial- or final-state radiation – three jets, one of which should be b-tagged. As the search has been carried out up to high signal masses (up to 1800 GeV in the b^* case), one has to consider the increasing Lorentz-boost of the b^*/B decay products for higher b^*/B masses. It increases the likelihood of jets stemming from hadronic decay products of W and t to merge in the detector. Therefore, despite the naive expectation of three jets in semi-leptonic final states, the requirement on the number of

jets (R = 0.4) is relaxed to also include events with only two jets, in order to also account for such boosted cases, in which two of the jets have merged. Otherwise, one would risk to loose good signal candidate events. Another means to optimise the selection for the high-mass region is the requirement for one high-momentum large-R jet (R = 1.0) to be present in the event. If not stated otherwise, the term *jet* denotes an anti-k_t jet with a radius parameter of R = 0.4 (anti-k_t4 jet or j_4) in the central part of the detector. Anti-k_t4 jets in the forward region will be referred to as *forward jets (FWjets)*, while anti-k_t jets with a radius parameter of R = 1.0 (anti-k_t10 jets or j_{10}) will be called *large-R jets*.
The focus on the high signal masses is the main difference between this search and the preceding search for b^* which was carried out by ATLAS on the $\sqrt{s} = 7\,\text{TeV}$ data set and which lead to a mass limit of 870 GeV for purely left-handed couplings ($f_g = f_L = 1$, $f_R = 0$) and of 1030 GeV for vector-like couplings ($f_g = f_L = f_R = 1$) in the combination of single-lepton and dilepton channels [9].
The selection criteria for both models are the same in this analysis, except that in the B case the presence of an additional jet in the forward region of the detector is required in order to account for the t-channel nature of its production and thus to further suppress the background.
For the discrimination between signal and background candidate events, the invariant mass of the heavy quark is used. It is calculated from the lepton kinematics, E_T^{miss}, and the kinematics of the central jets. The large-R jet is only used for the event selection and not for the calculation of the discriminating variable, as it is formed from the same topological clusters as the other jets, which are expected to partly overlap. Simulated signal and background as well as data distributions of the invariant mass in various signal-enriched and -depleted regions are then investigated for potential signal contributions in data and then fit to set an exclusion limit.
The following section contains a detailed description of all applied selection criteria.

6.4. Event Selection

In order to suppress background while keeping a high fraction of signal events, a set of selection criteria (*cuts*) is applied. All objects used in the event selection are introduced and described in section 5. On a technical level this procedure is divided into two steps: First, n-tuples provided by the *ATLAS Top group*, which contain information on uncalibrated

physics objects, are used as an input to a rather general pre-selection procedure, during which also all calibrations and overlap removals described in Chapter 5 are applied. The n-tuples of smaller size, written out after this step, are used as an input for the analysis-specific code developed and maintained in the group at HU Berlin, in which a refined event selection is performed, specifically optimised for the signal processes under consideration. At this stage histograms for further usage are written out. The selection criteria used in the two steps are described in the following.

6.4.1. Pre-Selection

Any event used in this analysis is required to have passed basic quality cuts, including removal of regions in the calorimeter, in which a high-quality particle reconstruction cannot be guaranteed due to technical failures. A single-lepton trigger must have fired (`EF_e24vhi_medium1` or `EF_e60_medium1` for electron events and `EF_mu24i_tight` or `EF_mu36_tight` for muon events, as described in sections 5.2.4 and 5.3.4) and the number of tracks with $p_T > 400\,\text{MeV}$ associated with the primary vertex has to be greater than four, to suppress non-collision backgrounds like beam-halo events. The event is required to contain exactly one good[2] electron or muon, which has to be matched to the object that fired the trigger, and no other good lepton. No dedicated category is established for semi-leptonic events with decays to tau leptons, due to the different detection properties caused by their high mass, short life time and decay modes to hadrons. However, a part of the events with leptonically decaying tau leptons will be picked up by this selection, as they fulfil the criteria for electron/muon events. Events with overlap between electrons and muons are removed, as are events which contain a jet that does not fulfil sufficient quality criteria (*'bad jets'*, as described in section 5.4). Details on overlap removals can be found in section 5.5. At least two good jets with $p_T > 25\,\text{GeV}$ and $|\eta| < 4.5$ are asked for. It can be seen from Figure 6.4 that a veto on events with less than 2 jets is justified as there are nearly no signal events at such low jet multiplicities. In addition, the presence of at least one large-R jet with $p_T > 200\,\text{GeV}$ and $|\eta| < 2.0$ is asked for. If there is more than one large-R jet in the event, the one with the highest p_T (the *leading* one) is considered for further usage. All pre-selection cuts are listed in Table 6.3. For this selection level, the product of raw acceptance and efficiency for selected signal masses can be found in

[2] good $\hat{=}$ isolated and fulfilling `tight++` or respectively `tight` selection criteria, as described in sections 5.2.1 and 5.3.1

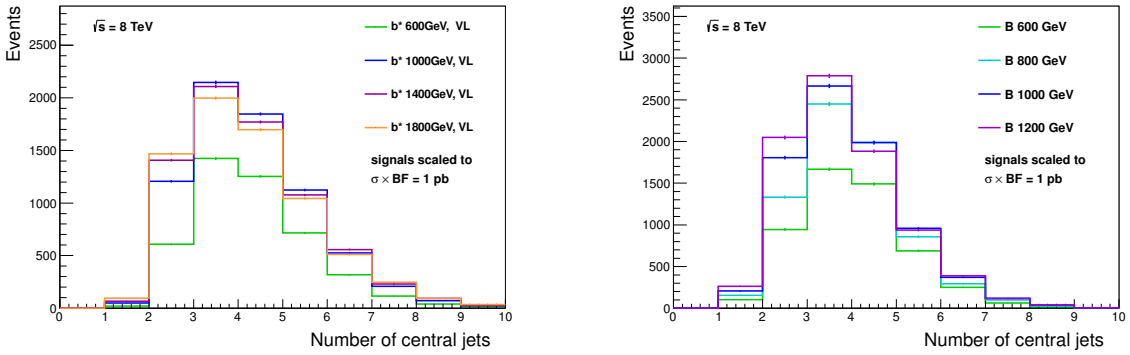

(a) Simulated b^* signals

(b) Simulated B signals

Figure 6.4.: Jet (j_4) multiplicity for various simulated b^* (left) and B (right) signal masses before applying a jet multiplicity, large-R jet or any of the signal selection cuts. Nearly no signal events contain only one jet. The product of signal cross-section and branching ratio has been scaled to 1 pb for better comparability.

Table 6.4. It can be noticed that already at this selection level, the product increases with increasing heavy quark mass, which shows that the requirement of a high-p_T large-R jet being present in the event already optimises for boosted scenarios.

Table 6.3.: Pre-selection cuts. The general selection criteria up to the removal of *'bad jets'* are widely used in single-lepton analyses within the *ATLAS Top group*, e.g. in the search for $t\bar{t}$ resonances described in [121].

cut	cut value (if applicable)
trigger	single-electron / single-muon
number of tracks associated to vertex	≥ 4
number of good leptons	$\equiv 1$
number of additional good leptons	$\equiv 0$
remove $e - \mu$ overlap	
remove *'bad jets'*	
number of good jets	≥ 2
number of large-R jets	≥ 1
(with $p_T > 200\,\text{GeV}$, $\lvert\eta\rvert < 2$)	

Table 6.4.: b^* and B signal raw acceptance×efficiency (based on raw Monte-Carlo event counts) after the pre-selection for the electron plus muon final states.

signal	el+mu
b^*, 600 GeV, LH	0.1043
b^*, 800 GeV, LH	0.1540
b^*, 1000 GeV, LH	0.1754
b^*, 1200 GeV, LH	0.1825
b^*, 1400 GeV, LH	0.1842
b^*, 1600 GeV, LH	0.1836
b^*, 1800 GeV, LH	0.1848
B, 600 GeV	0.1313
B, 800 GeV	0.1821
B, 1000 GeV	0.2053
B, 1200 GeV	0.2111

6.4.2. Signal Selection and Event Categorisation

A number of cuts, described in the following, are applied in order to further suppress background from SM processes and thus to enhance the signal-to-background ratio. To suppress QCD multijet background, a cut on the missing transverse energy of $E_T^{miss} > 20\,\text{GeV}$ is applied, and the sum of the transverse W mass (m_T^W) and the missing transverse energy has to satisfy $E_T^{miss} + m_T^W > 60\,\text{GeV}$. The transverse W mass is computed from the lepton and E_T^{miss} Lorentz-vectors, i.e. the W decay products if the neutrino is the only source of missing transverse energy, as $m_T^W = \sqrt{2p_T^\ell E_T^{miss}[1 - \cos\Delta\phi(p_T^\ell, E_T^{miss})]}$, with pt^ℓ being the lepton transverse momentum and $\Delta\phi(p_T^\ell, E_T^{miss})$ being the angular distance between the lepton direction and the missing transverse momentum vector. The cut values for these two criteria are commonly used in single-lepton analyses within the *ATLAS Top group* (e.g. in [121]) as they have shown a good performance in the past, such that the values were not specifically optimised in this search. As it is expected to find a b-jet from the top-quark decay, exactly one of the central jets is required to be b-tagged with the MV1 algorithm at the 70% b-tagging efficiency working point[3]. Events are selected separately depending on

[3] 70% is the recommended b-tagging working point by the *Top Group* in ATLAS. However, a working point of 80% with higher b-tagging efficiency but also higher mistag probability has also been tested for this analysis, but shown to result in slightly lower $S/\sqrt{B}$ values, such that this choice was discarded.

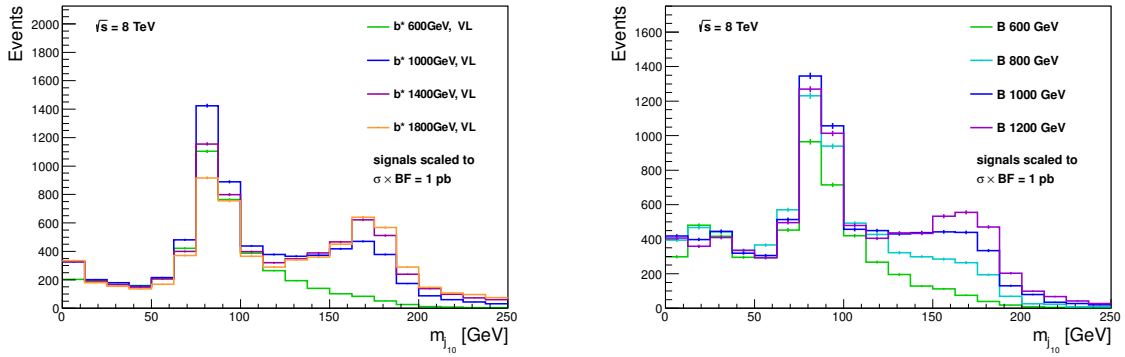

(a) b^* (b) B

Figure 6.5.: Leading large-R jet (j_{10}) mass for various simulated b^* (a) and B (b) signal masses after pre-selection cuts. Three distinct peaks (single parton, W boson and top quark) can be seen, indicating the high fraction of boosted W bosons and top quarks, especially with increasing signal mass. Signal cross-sections have been scaled to 1 pb for better comparability.

whether the lepton is an electron or muon. For the final results, both channels are merged. The number of jets in the event is further restricted to be smaller than four, in order to suppress background from top-pair production, while keeping about half of the signal events (cf. Figure 6.4). For top-pair background, higher jet multiplicities are expected, as each of the top quarks decays to a W boson and a b quark in most of the cases. Opening the cut to also allow for events with only two central jets gives room for signal events with a high enough boost for two jets to have merged.

For the selection of heavy particle decays, one can make use of the fact that the decay products are Lorentz-boosted. As the average p_T of the heavy quark decay products rises, the jets coming from hadronic top-quark or W-boson decays are likely to have small angular distances. This trend can be seen in Figure 6.5, which shows the leading large-R jet mass for simulated b^* and B events at various b^*/B signal masses. One can see that with increasing mass of the heavy quark, it becomes more and more likely to capture all W decay products in one single large-R jet (j_{10}), as the peak around the W mass grows. For really heavy b^*/B quarks, it is even possible for all hadronic top-quark decay products to be merged in one large-R jet, which can be seen from the growing peak around the top-quark mass. This behaviour, which can hardly be seen for SM processes (see Figure 6.6), can hence be used for suppressing the background by selecting only events that satisfy $m_{j_{10}} > 50\,\text{GeV}$.

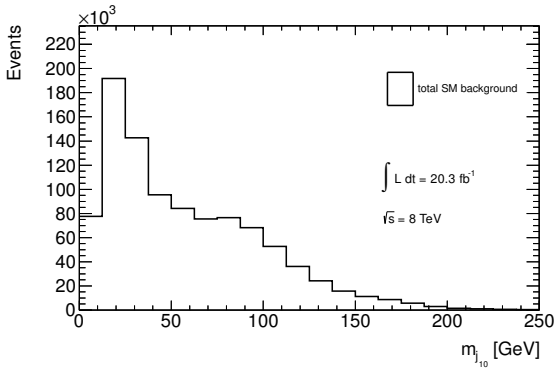

Figure 6.6.: Leading large-R jet mass for the simulated total SM background after pre-selection cuts. Only a small peak around the W mass can be seen, there is no sign for boosted top quarks in the spectrum.

The events selected by the described cuts are then further divided into multiple signal categories depending on the particle undergoing the hadronic decay (W boson or top quark). These pairwise disjoint categories are then statistically combined to enhance the sensitivity and thus to improve the final results. Studies have shown that the idea of cutting on the leading large-R jet mass in order to categorise the events into hadronic W-boson or top-quark events is too naive. As the clusters between both jet collections partly overlap, the systematic variation of the large-R jet mass and the one of the small-R jet energy scale cannot be treated as uncorrelated (a detailed discussion on systematic uncertainties is given in section 6.7), even though the fit of the background-only hypothesis to data (as described in section 6.10) assumes them to be. Applying cuts that are sensitive to large-R jet mass variations while at the same time calculating the discriminating variable only from small-R jets hence leads to an improper parametrisation of the involved systematic uncertainties and should therefore be avoided.

Another way of categorising the signal events by making use of their characteristic event topologies is to set restrictions on angular distances between the various objects in the final state. By different sets of so-called topology cuts, two categories are defined, to separate the events into hadronic W and hadronic top-quark decays. This is possible as the W boson and the top quark are expected to be back-to-back to each other in the transverse plane in b^*/B events. The definitions and values of these cuts are described in the following section and can be understood from Figure 6.7. As the B selection additionally contains a

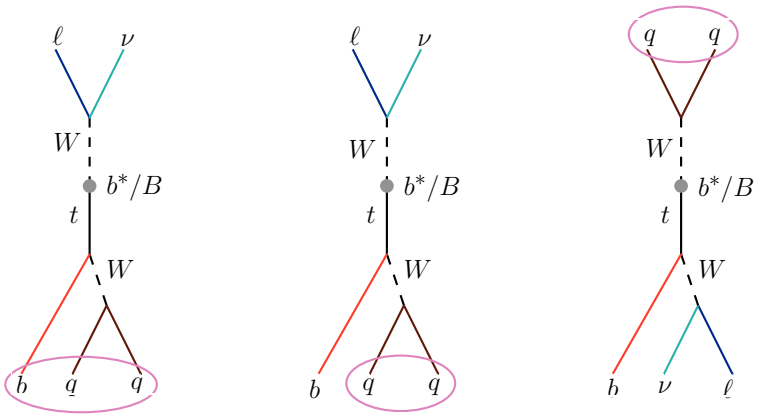

Figure 6.7.: Schematic representation of the possible semi-leptonic heavy quark decay final states. The ellipses denote which of the decay products could be captured within a single high-p_T large-R jet. From left to right: boosted hadronic top decay, semi-boosted hadronic top decay, hadronic W decay.

requirement of at least one forward jet being present, we end up with twice the number of signal categories.

Topology Cuts

The variables exploited to further enhance the signal fraction as well as for signal categorisation are three angular distances, the distributions of which are shown in Figure 6.8:

- The angular distance between the lepton and the large-R jet, $\Delta\Phi(\ell, j_{10})$:
  In signal events, the leptonic and hadronic decays of W and top are in different hemispheres, lepton and large-R jet are back-to-back in the transverse plane, which is why $\Delta\Phi$ is a natural choice for a variable to cut on. Cutting on ΔR between the two objects has been tested as well, but has shown to give no improvement. $\Delta\Phi(\ell, j_{10})$ tends to be close to π for both, hadronic W and hadronic top decays (see Figure 6.8(a) and 6.8(b)). A cut at $\Delta\Phi(\ell, j_{10}) > 1.5$ will therefore be applied for both categories.

- The angular distance between the lepton and the closest jet, $\min\Delta R(\ell, j_4)$:
  In signal events of hadronic top-quark decays, this distance is large, as the leptonic side does not contain any jets, while in events with hadronic W decays the b-jet is close to the leptonic W decay products, which is why this quantity should be small (see

Figure 6.8(c) and 6.8(d)). A cut value at $\min\Delta R(\ell, j_4) = 1.5$, which best separates the two peaks has been chosen to distinguish between the two categories.

- The maximum angular distance between the large-R jet and any of the narrow jets, $\max\Delta R(j_{10}, j_4)$:
  In signal events with hadronically decaying top quarks, this quantity is small as all jets (j_4 and j_{10}) are on the same side of the event (see Figure 6.7). In hadronic W decays (or leptonic top-quark decays respectively), the b-jet is on the opposite side from the large-R jet capturing the W decay products and this quantity should therefore be large (see Figure 6.8(e) and 6.8(f)). A value of $\max\Delta R(j_{10}, j_4) = 2.0$ is used to cut between the two peaks.

The distributions of these variables for various simulated signal masses are shown in Figure 6.8. One can nicely see that the distributions show the expected features, the more pronounced, the heavier the vector-like quark gets. For comparison, Figure 6.9 shows the same distributions for SM background as well as $S/\sqrt{B}$ (S being the number of signal and B the number of background events) as a measure for the expected sensitivity for one example signal mass point. One can see that cuts on these quantities are not only useful for the division into different signal regions, but that they also help to suppress a part of the background.

The cut values on the three angular distances were derived comparing signal and background distributions without taking into account systematic uncertainties. Cuts on $\min\Delta R(\ell, j_4)$ and $\max\Delta R(j_{10}, j_4)$ were chosen such that they divide the spectra at their minima in order to best distinguish hadronic W from hadronic top-quark decays. The same cut on $\Delta\Phi(\ell, j_{10})$ is applied for both categories, in order to select the bulk of the signal distribution while suppressing some of the background contribution. The exact values can be found in Table 6.7 in section 6.6. On top of this categorisation, the events are divided into a B selection in which at least one forward jet is asked for and a b^* selection without such a requirement. These different selections are specifically developed for the search of the respective heavy quark. All cuts described in this section are summarised in Table 6.5.

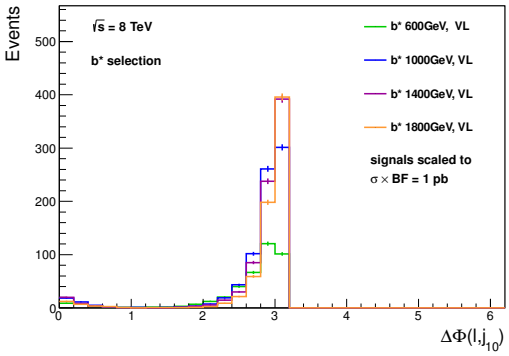

(a) $\Delta\Phi(\ell, j_{10})$, b^*

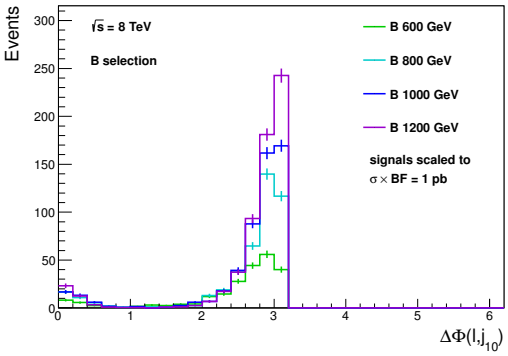

(b) $\Delta\Phi(\ell, j_{10})$, B

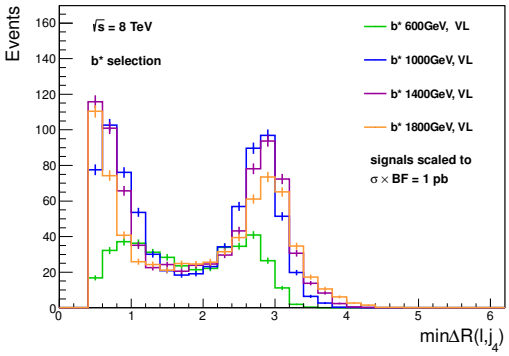

(c) $\min\Delta R(\ell, j_4)$, b^*

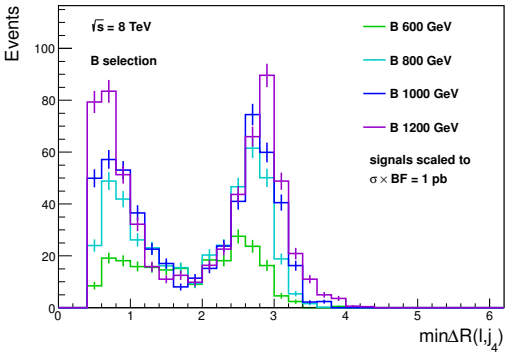

(d) $\min\Delta R(\ell, j_4)$, B

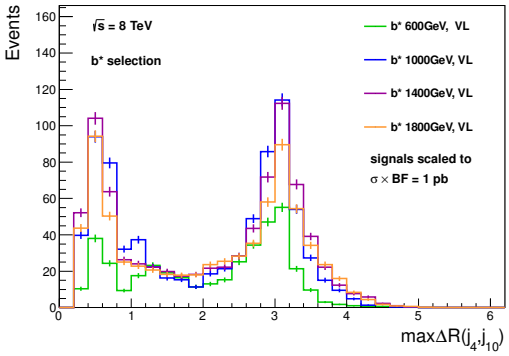

(e) $\max\Delta R(j_{10}, j_4)$, b^*

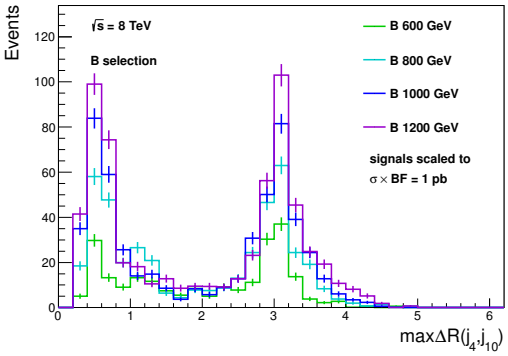

(f) $\max\Delta R(j_{10}, j_4)$, B

Figure 6.8.: $\Delta\Phi(\ell, j_{10})$ (top), $\min\Delta R(\ell, j_4)$ (middle) and $\max\Delta R(j_{10}, j_4)$ (bottom) distributions for various simulated b^* (left) and B (right) signal masses before applying any of the topology cuts. The features described in the text are the more pronounced the larger the signal mass gets. All signal cross-sections have been scaled to 1 pb for better comparability.

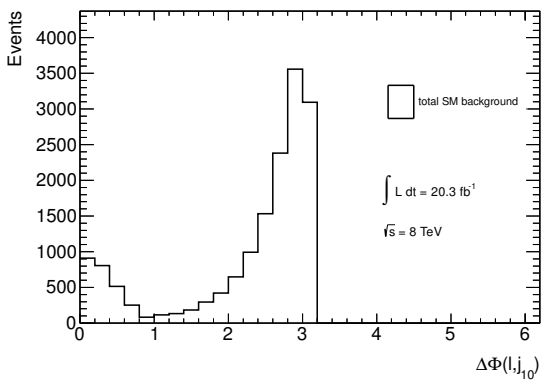

(a) $\Delta\Phi(\ell, j_{10})$

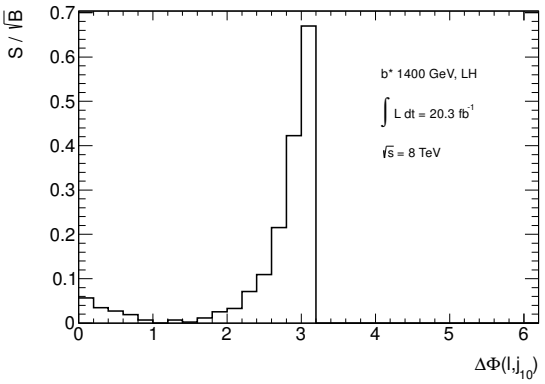

(b) $\Delta\Phi(\ell, j_{10})$

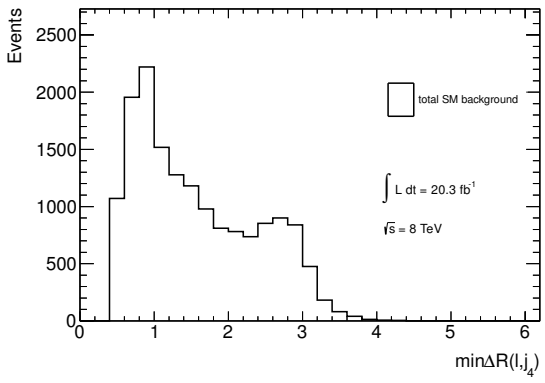

(c) $\min\Delta R(\ell, j_4)$

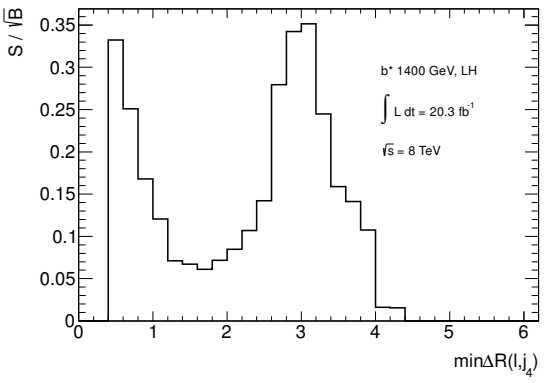

(d) $\min\Delta R(\ell, j_4)$

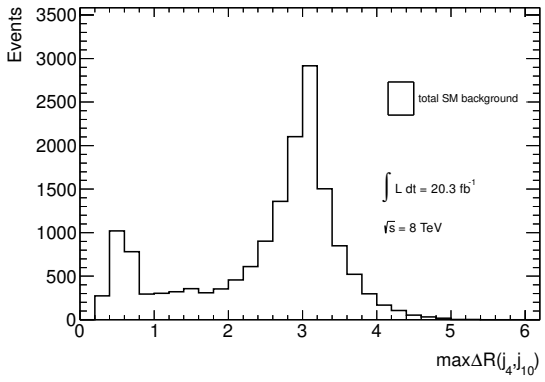

(e) $\max\Delta R(j_{10}, j_4)$

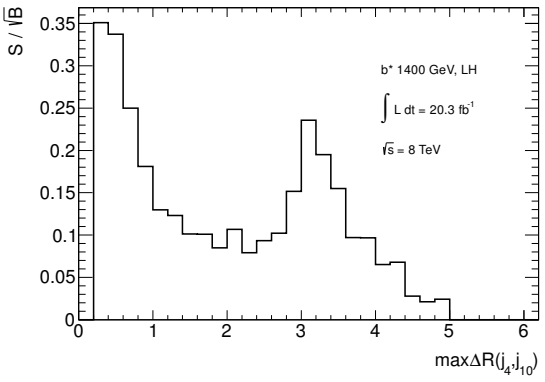

(f) $\max\Delta R(j_{10}, j_4)$

Figure 6.9.: $\Delta\Phi(\ell, j_{10})$ (top), $\min\Delta R(\ell, j_4)$ (middle) and $\max\Delta R(j_{10}, j_4)$ (bottom) distributions for the simulated total SM background before applying any of the topology cuts (left) and corresponding $S/\sqrt{B}$ distributions for an example simulated b^* signal of a generated mass of $m_{b^*}^{\text{gen}} = 1400\,\text{GeV}$ (right). It can be seen that cuts on these quantities can help to suppress the background.

Table 6.5.: Signal selection cuts

cut	cut value (if applicable)
number of jets	$\equiv 2$ or $\equiv 3$
E_T^{miss}	$\geq 20\,\text{GeV}$
$E_T^{miss} + m_T^W$	$\geq 60\,\text{GeV}$
number of b-tags	$\equiv 1$
number of forward jets	category-dependent (see Table 6.7)
$m_{j_{10}}$	$> 50\,\text{GeV}$
topology cuts	category-dependent (see Table 6.7)

6.5. Background Modelling

The cuts described in the previous sections are chosen such that they increase $S/\sqrt{B}$, especially for the higher signal masses. Ideally, the number of background events would be reduced to a minimum, while keeping a good fraction of signal events. Some background processes, however, can not be fully suppressed. The main sources of irreducible background in the semi-leptonic b^*/B search are top-pair production ($t\bar{t}$) and production of W bosons in association with jets (W+jets), followed by single top production (especially t-channel in the B selection and Wt associated production in the b^* selection, and a smaller s-channel contribution). Processes with smaller contributions are QCD multijet production, associated production of Z bosons and jets (Z+jets) as well as a small fraction of ZZ, WW, WZ (diboson) events. Example Feynman diagrams of these processes at LO are shown in Figure 6.10.

Most of the background processes are modelled using Monte-Carlo simulations, as described in Chapter 4. Table 6.6 lists which Monte-Carlo generators have been used to produce events for the various background processes. Only the multijet background is derived via a data-driven method, which is described in the next section.

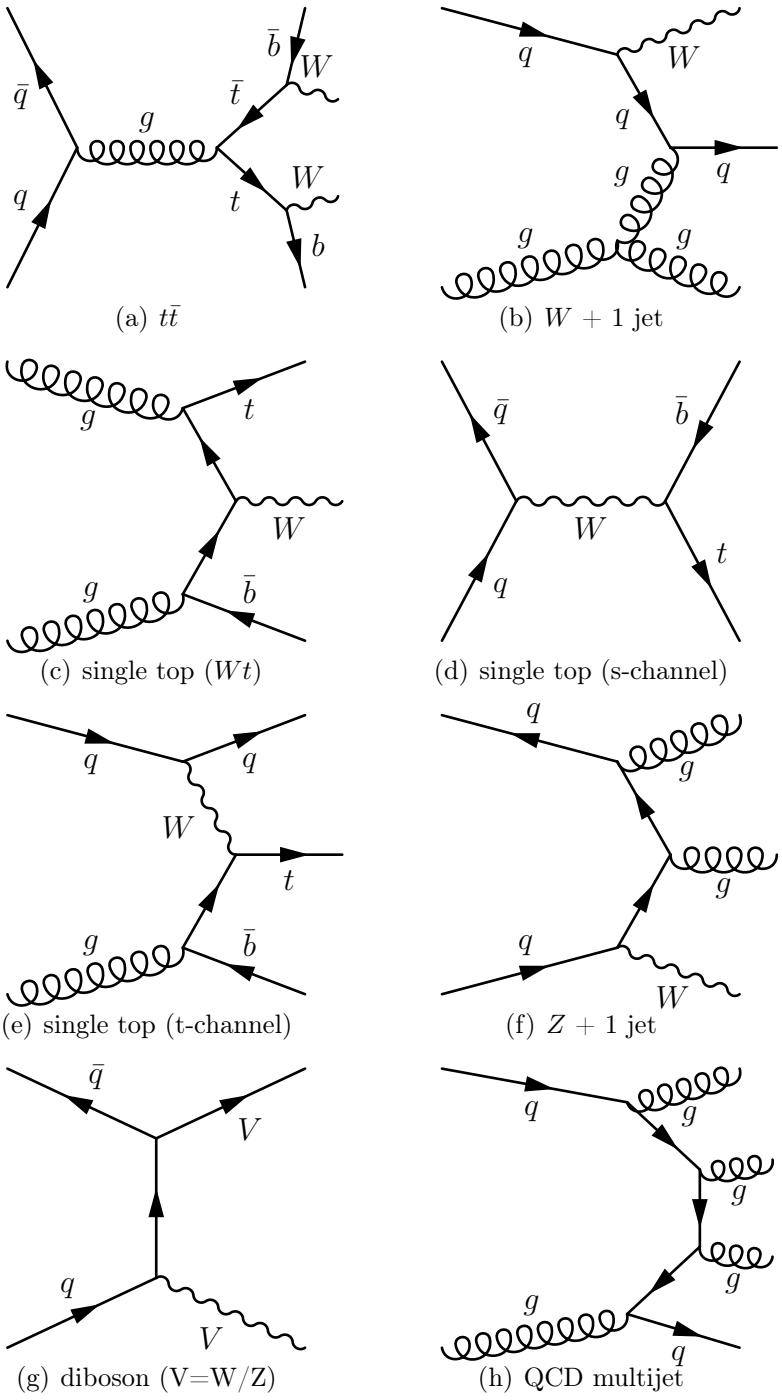

Figure 6.10.: One example Feynman diagram for each of the various sources of irreducible background. These processes enter the signal selection either because of the same final state particles being present (e.g. W and top associated production in 6.10(c)) or because of misidentification of light jets as b-jets (or vice versa) or leptons as jets (or vice versa) or loss of one or more final state particles (e.g. $t\bar{t}$ production in 6.10(a)).

Table 6.6.: Monte-Carlo generators and PDF sets used to simulate events for the various background processes. For a detailed listing of all sub-processes, including cross sections and numbers of generated events, please refer to Tables C.1 to C.3 in Appendix C.

Process	Hard Interaction generator	PDF	Shower Generator	PDF (Shower)
$t\bar{t}$	Powheg-Box (NLO)	CT10 [68] (NLO)	Pythia 6.426	CTEQ6L1 [67]
W+jets	Alpgen v2.14 (LO)	CTEQ6L1	Pythia 6.426	CTEQ6L1
single top	Powheg-Box (NLO)	CT10F4 [68]	Pythia 6.427	CTEQ6L1
Z+jets	Alpgen (LO)	CTEQ6L1	Pythia 6.426	CTEQ6L1
diboson	Herwig 6.520.2	CTEQ6L1	Herwig 6.520.2	CTEQ6L1

6.5.1. Data-Driven QCD Multijet Background Estimation

One source of potential background for single-lepton events are non-prompt (not stemming from the hard interaction) or fake leptons originating from QCD multijet production and some other processes. In these events, a lepton can e.g. emerge from semi-leptonic decays of b/c quarks and be mistaken for a prompt lepton, which in fact is not present. Jets with large electromagnetic energy ($\pi^0 \to \gamma\gamma$) can fake the signature of prompt electrons in the calorimeter and particles from high-energetic hadronic showers punching through the calorimeter system into the muon spectrometer can fake muon signatures. In addition to QCD multijet events, hadronic W-boson decays, which are not modelled by the Monte-Carlo, have to be accounted for as well as electrons from photon conversions that can be mistaken as prompt ones.

The method used to obtain a data-driven estimate for the number of such events, called the *Matrix Method* [122], will be described in the following.
The data sample is first divided into two parts, according to two different levels of lepton identification criteria: *loose* and *tight*. The *loose* electron selection requires `medium++` quality cuts for electrons (see section 5.2.1) and `medium` quality cuts for muons (see section 5.3.1), no isolation and a number of criteria preventing photon-conversion leptons to be picked up. In terms of η and p_T it satisfies the same criteria as the *tight* electrons. The *loose* muon selection is the same as the *tight* one except for the mini-isolation cut which is removed (see section 5.3).
The number of *loose* (N^{loose}) and *tight* leptons (N^{tight}) can be separated into the sum of events with real leptons, i.e. high-p_T isolated leptons stemming from W or Z decays, and events with fake leptons:

$$N^{loose} = N^{loose}_{real} + N^{loose}_{fake} \tag{6.1}$$

$$N^{tight} = \epsilon_{real} N^{loose}_{real} + \epsilon_{fake} N^{loose}_{fake} \tag{6.2}$$

with ϵ_{real} and ϵ_{fake} being the efficiency for fake and real leptons to move from the *loose* to the *tight* sample. These efficiencies are determined in regions enriched with real and fake leptons. One can then determine the number of *tight* lepton events actually stemming from

fakes from the combination of equations 6.1 and 6.2, by solving for $N_{fake}^{tight} = \epsilon_{fake} N_{fake}^{loose}$:

$$N_{fake}^{tight} = \frac{\epsilon_{fake}}{\epsilon_{real} - \epsilon_{fake}} \left(\epsilon_{real} N^{loose} - N^{tight} \right) \tag{6.3}$$

The electron real and fake efficiencies were determined as a function of η^e and ${p_T}^e$, $\Delta\Phi(e, E_T^{miss})$, $\min\Delta R(e, jet)$, $\sum E_T$ and $E_T^{miss}$and range from 74.6% to 81.4% for real electrons and from 21.4% to 41.6% for fake electrons [123]. The muon efficiencies were determined as a function of η^μ and ${p_T}^\mu$, $\min\Delta R(\mu, jet)$ and the number of b-tagged jets with the MV1 tagging algorithm at the 70% working point and are about 96.4% for real muons and ranges between 14.7% and 35.5% for fake muons [123].
As the vast majority of the non-prompt and fake lepton contribution stems from QCD multijet events, this background source will only be referred to *QCD* (*multijet*) background throughout this document for simplicity.

6.6. Signal and Control Regions

Table 6.7 summarises the selection in the four distinct signal regions (SR), which include hadronic top (referred to as *top*) and hadronic W decays (W) for the b^* and B scenarios. The B signal regions are the same as their b^* counterparts, except for the additional forward jet requirement.

To indicate which fraction of signal events passes all selection criteria, Table 6.8 and Table 6.9 show the products of acceptance and efficiency for b^* and B signal events in the respective signal regions. One can see that this analysis is better suited for higher signal masses than for lower ones.

Figure 6.11 and Figure 6.12 show the impact of the different selection criteria on the reduction of the various background processes in the two b^* and two B signal regions, respectively. Besides the cuts described earlier, they list three criteria, which were only included as cross checks: a cut to assure that none of the data events is processed twice (denoted as *remove duplicates* in the figures), a cut to make sure that the overlap between simulated events with W/Z bosons and heavy quarks stemming from the matrix element calculation heavy quarks being produced in the parton shower evolution is correctly removed

Table 6.7.: Event categorisation of the b^* or B decays in signal regions (SR) with hadronic top quark and hadronic W boson final states. The cut on the large-R jet mass of $m_{j10} > 50\,\text{GeV}$ and the topology cut $\Delta\phi(\ell, j_{10}) > 1.5$ are applied in all these categories.

category	number of b-tags	number of forward jets	topology cuts
b^* SR, top	$\equiv 1$	≥ 0	$\Delta\phi(\ell, j_{10}) > 1.5$ $\min\Delta R(\ell, j_4) > 1.5$ $\max\Delta R(j_{10}, j_4) < 2.0$
b^* SR, W	$\equiv 1$	≥ 0	$\Delta\phi(\ell, j_{10}) > 1.5$ $\min\Delta R(\ell, j_4) < 1.5$ $\max\Delta R(j_{10}, j_4) > 2.0$
B SR, top	$\equiv 1$	≥ 1	$\Delta\phi(\ell, j_{10}) > 1.5$ $\min\Delta R(\ell, j_4) > 1.5$ $\max\Delta R(j_{10}, j_4) < 2.0$
B SR, W	$\equiv 1$	≥ 1	$\Delta\phi(\ell, j_{10}) > 1.5$ $\min\Delta R(\ell, j_4) < 1.5$ $\max\Delta R(j_{10}, j_4) > 2.0$

Table 6.8.: b^* signal raw acceptance×efficiency (based on raw Monte-Carlo event counts) in the various signal regions for ℓ+jets events. As an example the numbers for the left-handed (LH) coupling scenario are shown, which are very close to the ones of the right-haded coupling scenario.

	b^* SR, top	b^* SR, W
b^*, 600 GeV, LH	0.00851	0.00634
b^*, 800 GeV, LH	0.0165	0.01061
b^*, 1000 GeV, LH	0.01855	0.01559
b^*, 1200 GeV, LH	0.01923	0.01698
b^*, 1400 GeV, LH	0.01797	0.01758
b^*, 1600 GeV, LH	0.01707	0.01589
b^*, 1800 GeV, LH	0.01584	0.01435

in an earlier stage (*HFOR*) and a cut to make sure, that the criterion on the large-R jet p_T of 200 GeV is correctly applied ($p_{T,10}$). If this is the case, the latter two cuts should not

Table 6.9.: B signal raw acceptance×efficiency (based on raw Monte-Carlo event counts) in the various signal regions for ℓ+jets events.

	B SR, top	B SR, W
B, 600 GeV	0.0084	0.0060
B, 800 GeV	0.0170	0.0126
B, 1000 GeV	0.0219	0.0186
B, 1200 GeV	0.0243	0.0225

have an influence on the event yield at that stage of the analysis, which is found to be confirmed in the figures.

Tables 6.10 and 6.11 list the event yields for all background processes as well as for a b^* example signal after the various cuts in the b^* signal regions. Tables 6.12 and 6.13 contain the corresponding information in the B signal regions with an example B signal.

In order to test whether the background is actually well-modelled, one can compare the data to the sum of backgrounds in regions enriched with a given background component, so-called *control regions*. In this analysis this is done for the two main backgrounds, top-pair and W+jets production. These regions are selected such that they are orthogonal to the signal selection, to assure that there are no overlapping events. The criterion altered to obtain orthogonal selections, is the number of b-tagged jets in each event. While exactly one b-tag is asked for in the signal regions, at least two are required in the $t\bar{t}$ control region and events with no b-tag end up in the W+jets control region. The control regions (CR) are divided into b^* and B via the forward jet requirement, as well as into hadronic top and hadronic W sub-regions via the cuts defined in Table 6.7, analogously to the signal regions. We therefore end up with four signal regions and eight control regions, an overview over which can be found in Table 6.14.

Even though the control regions ideally should not contain any signal events, in practice the separation is not perfect as there can also be signal events which fall into the $\equiv 0$ or ≥ 2 b-tag categories due to finite b-tagging efficiency and mistag probability. For the search to be powerful in discovering or excluding new physics processes, one needs to make sure that the signal contamination in the control regions is reasonably small. Table 6.15 and 6.16 show these numbers for various b^* ($f_g = f_L = 1$, $f_R = 0$) and B signal masses

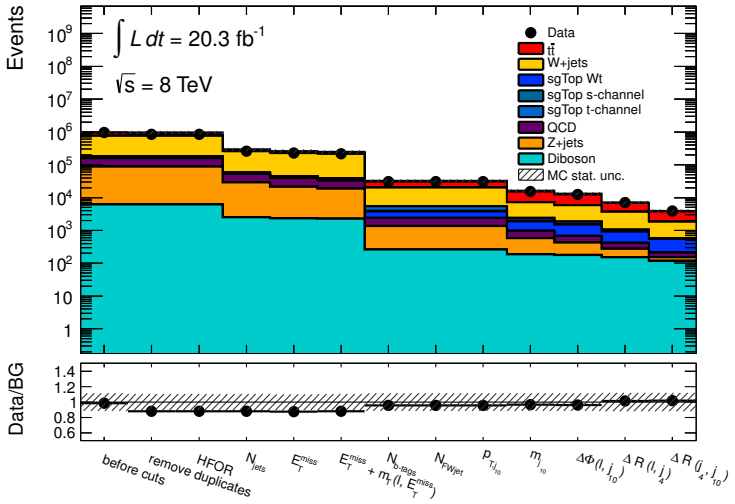

(a) b^* SR, top

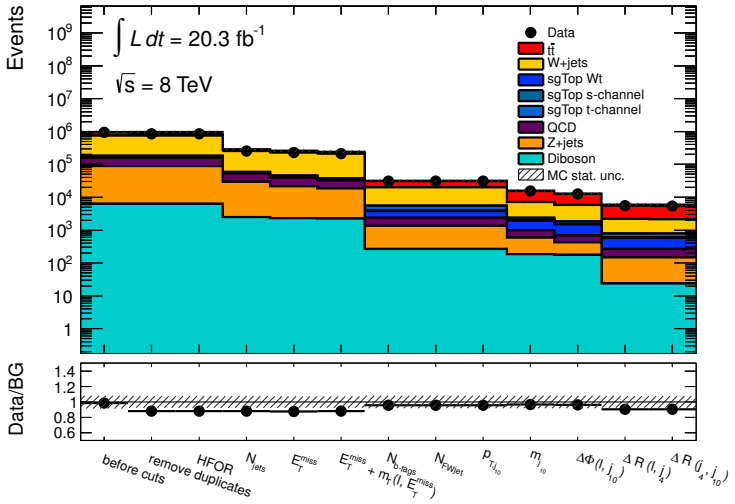

(b) b^* SR, W

Figure 6.11.: Impact of the signal selection cuts on the SM backgrounds in the b^* signal regions. One can see that after the last cut, the main backgrounds left are top-pair and W+jets production. At this stage, only the theory and MC statistical uncertainties are shown in the error band.
The second cut (HFOR) as well as the cut on $p_{T,j_{10}}$ were applied as cross checks and are expected to not influence the number of events. There is no requirement on the number of forward jets (N_{FWjet}), such that the event yield in the corresponding part of the histogram is not expected to change. All of these expectations are met.

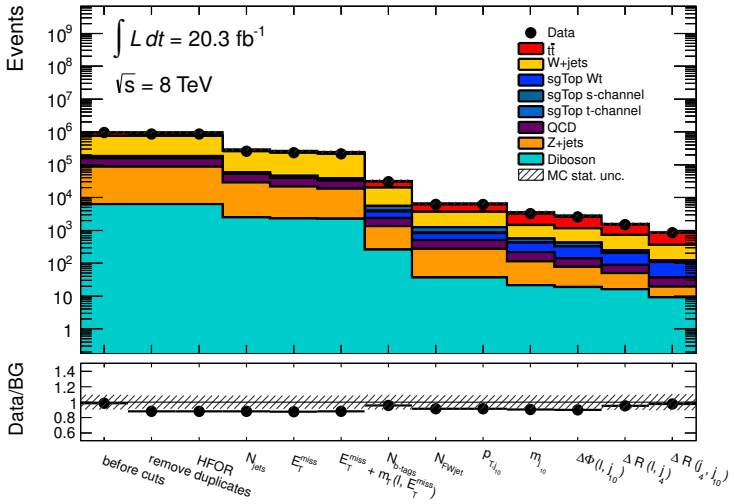

(a) B SR, top

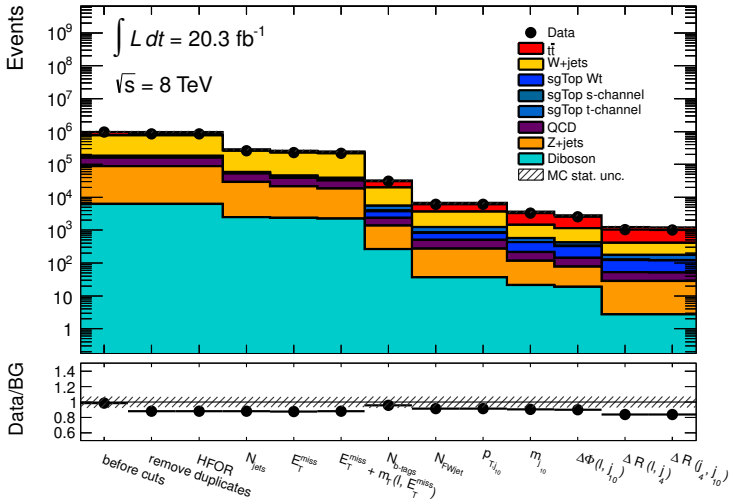

(b) B SR, W

Figure 6.12.: Impact of the signal selection cuts on the SM backgrounds in the B signal regions. One can see that after the last cut, the main backgrounds left are top-pair and W+jets production. At this stage, only the theory and MC statistical uncertainties are shown in the error band.
The second cut (HFOR) as well as the cut on $p_{T,j_{10}}$ were applied as cross checks and are expected to not influence the number of events. All of these expectations are met.

Table 6.10.: Event yields after the various selection steps for the background processes and a b^* signal with $m_{b^*}^{\text{gen}} = 1\,\text{TeV}$ (scaled to $20.3 fb^{-1}$) together with their statistical uncertainties in the e+jets channel in the b^* signal regions (top, W). The first line corresponds to events after the pre-selection cuts.

cut	process						
	b^* SR, top						
	signal $m_{b^*}^{\text{gen}} = 1\,\text{TeV}$	$t\bar{t}$	W+jets	single top	QCD	Z+jets	Diboson
==2 or ==3 j_4	839 ± 14	13187 ± 34	99593 ± 337	3173 ± 35	16613 ± 59	16467 ± 84	1295 ± 18
$E_T^{miss} > 20\,\text{GeV}$	827 ± 14	12549 ± 33	91186 ± 322	2973 ± 34	12118 ± 51	11275 ± 69	1186 ± 17
$E_T^{miss} + m_T^W > 60\,\text{GeV}$	818 ± 14	12121 ± 33	86756 ± 314	2860 ± 34	9454 ± 47	9509 ± 63	1135 ± 17
==1 b-tags	468 ± 10	6054 ± 23	7054 ± 95	1545 ± 24	552 ± 9	623 ± 16	128 ± 6
$m_{j10} > 50\,\text{GeV}$	387 ± 9	4553 ± 20	2474 ± 55	737 ± 19	229 ± 6	262 ± 10	84 ± 5
$\Delta\phi(\ell, j_{10}) > 1.5$	356 ± 9	3173 ± 17	1834 ± 48	525 ± 16	113 ± 4	119 ± 7	74 ± 4
$\min\Delta R(\ell, j_4) > 1.5$	215 ± 7	1489 ± 11	1236 ± 40	298 ± 13	67 ± 3	61 ± 5	64 ± 4
$\max\Delta R(j_4, j_{10}) < 2.0$	172 ± 6	925 ± 9	605 ± 28	174 ± 10	35 ± 2	16 ± 3	50 ± 4
	b^* SR, W						
	signal $m_{b^*}^{\text{gen}} = 1\,\text{TeV}$	$t\bar{t}$	W+jets	single top	QCD	Z+jets	Diboson
==2 or ==3 j_4	839 ± 14	13187 ± 34	99593 ± 337	3173 ± 35	16613 ± 59	16467 ± 84	1295 ± 18
$E_T^{miss} > 20\,\text{GeV}$	827 ± 14	12549 ± 33	91186 ± 322	2973 ± 34	12118 ± 51	11275 ± 69	1186 ± 17
$E_T^{miss} + m_T^W > 60\,\text{GeV}$	818 ± 14	12121 ± 33	86756 ± 314	2860 ± 34	9454 ± 47	9509 ± 63	1135 ± 17
==1 b-tags	468 ± 10	6054 ± 23	7054 ± 95	1545 ± 24	552 ± 9	623 ± 16	128 ± 6
$m_{j10} > 50\,\text{GeV}$	387 ± 9	4553 ± 20	2474 ± 55	737 ± 19	229 ± 6	262 ± 10	84 ± 5
$\Delta\phi(\ell, j_{10}) > 1.5$	356 ± 9	3173 ± 17	1834 ± 48	525 ± 16	113 ± 4	119 ± 7	74 ± 4
$\min\Delta R(\ell, j_4) < 1.5$	141 ± 6	1685 ± 12	597 ± 27	227 ± 10	46 ± 3	58 ± 5	10 ± 2
$\max\Delta R(j_4, j_{10}) > 2.0$	140 ± 6	1639 ± 12	588 ± 27	225 ± 10	45 ± 3	58 ± 5	10 ± 2

Table 6.11.: Event yields after the various selection steps for the background processes and a b^* signal with $m_{b^*}^{\text{gen}} = 1\,\text{TeV}$ (scaled to $20.3 fb^{-1}$) together with their statistical uncertainties in the μ+jets channel in the b^* signal regions (top, W). The first line corresponds to events after the pre-selection cuts.

cut	process						
	b^* SR, top						
	signal $m_{b^*}^{\text{gen}} = 1\,\text{TeV}$	$t\bar{t}$	W+jets	single top	QCD	Z+jets	Diboson
==2 or ==3 j_4	824 ± 14	12572 ± 34	107695 ± 356	3136 ± 34	7007 ± 92	10202 ± 73	1212 ± 18
$E_T^{miss} > 20\,\text{GeV}$	806 ± 14	12046 ± 33	100185 ± 343	2987 ± 34	5757 ± 85	7866 ± 64	1147 ± 18
$E_T^{miss} + m_T^W > 60\,\text{GeV}$	795 ± 14	11640 ± 33	96060 ± 336	2881 ± 33	4599 ± 78	6928 ± 60	1113 ± 17
==1 b-tags	457 ± 10	5874 ± 23	7576 ± 101	1586 ± 24	482 ± 17	475 ± 15	135 ± 6
$m_{j10} > 50\,\text{GeV}$	397 ± 10	4126 ± 19	2376 ± 56	670 ± 19	171 ± 10	135 ± 8	103 ± 5
$\Delta\phi(\ell, j_{10}) > 1.5$	391 ± 10	3942 ± 19	2224 ± 54	637 ± 18	148 ± 10	130 ± 8	102 ± 5
$\min\Delta R(\ell, j_4) > 1.5$	225 ± 7	1754 ± 13	1433 ± 44	338 ± 14	76 ± 6	64 ± 6	88 ± 5
$\max\Delta R(j_4, j_{10}) < 2.0$	184 ± 7	1048 ± 10	684 ± 31	189 ± 11	28 ± 4	20 ± 3	67 ± 4
	b^* SR, W						
	signal $m_{b^*}^{\text{gen}} = 1\,\text{TeV}$	$t\bar{t}$	W+jets	single top	QCD	Z+jets	Diboson
==2 or ==3 j_4	824 ± 14	12572 ± 34	107695 ± 356	3136 ± 34	7007 ± 92	10202 ± 73	1212 ± 18
$E_T^{miss} > 20\,\text{GeV}$	806 ± 14	12046 ± 33	100185 ± 343	2987 ± 34	5757 ± 85	7866 ± 64	1147 ± 18
$E_T^{miss} + m_T^W > 60\,\text{GeV}$	795 ± 14	11640 ± 33	96060 ± 336	2881 ± 33	4599 ± 78	6928 ± 60	1113 ± 17
==1 b-tags	457 ± 10	5874 ± 23	7576 ± 101	1586 ± 24	482 ± 17	475 ± 15	135 ± 6
$m_{j10} > 50\,\text{GeV}$	397 ± 10	4126 ± 19	2376 ± 56	670 ± 19	171 ± 10	135 ± 8	103 ± 5
$\Delta\phi(\ell, j_{10}) > 1.5$	391 ± 10	3942 ± 19	2224 ± 54	637 ± 18	148 ± 10	130 ± 8	102 ± 5
$\min\Delta R(\ell, j_4) < 1.5$	166 ± 6	2188 ± 14	791 ± 32	299 ± 12	72 ± 7	65 ± 5	14 ± 2
$\max\Delta R(j_4, j_{10}) > 2.0$	165 ± 6	2133 ± 14	782 ± 32	296 ± 12	45 ± 3	58 ± 5	14 ± 2

Table 6.12.: Event yields after the various selection steps for the background processes and a B example signal with $m_B^{\text{gen}} = 800\,\text{GeV}$ (scaled to $20.3 fb^{-1}$) together with their statistical uncertainties in the e+jets channel in the B signal regions (top, W). The first line corresponds to events after the pre-selection cuts.

cut	process						
	B SR, top						
	signal $m_B^{\text{gen}} = 800\,\text{GeV}$	$t\bar{t}$	W+jets	single top	QCD	Z+jets	Diboson
==2 or ==3 j_4	53 ± 0.8	13187 ± 34	99593 ± 337	3173 ± 35	16613 ± 59	16467 ± 84	1295 ± 18
$E_T^{miss} > 20\,\text{GeV}$	50 ± 0.8	12549 ± 33	91186 ± 322	2973 ± 34	12118 ± 51	11275 ± 69	1186 ± 17
$E_T^{miss} + m_T^W > 60\,\text{GeV}$	49 ± 0.8	12121 ± 33	86756 ± 314	2860 ± 34	9454 ± 47	9509 ± 63	1135 ± 17
==1 b-tags	29 ± 0.6	6054 ± 23	7054 ± 95	1545 ± 24	552 ± 9	623 ± 16	128 ± 6
≥ 1 FWjet	16 ± 0.4	1532 ± 12	1208 ± 38	368 ± 11	126 ± 4	152 ± 7	22 ± 2
$m_{j10} > 50\,\text{GeV}$	12 ± 0.4	1140 ± 10	459 ± 23	180 ± 9	57 ± 3	67 ± 5	12 ± 2
$\Delta\phi(\ell, j_{10}) > 1.5$	10 ± 0.4	738 ± 8	334 ± 19	121 ± 8	24 ± 2	33 ± 4	9 ± 1
$\min\Delta R(\ell, j_4) > 1.5$	7 ± 0.3	379 ± 6	224 ± 16	67 ± 6	13 ± 1	21 ± 3	8 ± 1
$\max\Delta R(j_4, j_{10}) < 2.0$	5 ± 0.3	235 ± 4	119 ± 12	41 ± 5	7 ± 1	7 ± 1	5 ± 1
	B SR, W						
	signal $m_B^{\text{gen}} = 800\,\text{GeV}$	$t\bar{t}$	W+jets	single top	QCD	Z+jets	Diboson
==2 or ==3 j_4	53 ± 0.8	13187 ± 34	99593 ± 337	3173 ± 35	16613 ± 59	16467 ± 84	1295 ± 18
$E_T^{miss} > 20\,\text{GeV}$	50 ± 0.8	12549 ± 33	91186 ± 322	2973 ± 34	12118 ± 51	11275 ± 69	1186 ± 17
$E_T^{miss} + m_T^W > 60\,\text{GeV}$	49 ± 0.8	12121 ± 33	86756 ± 314	2860 ± 34	9454 ± 47	9509 ± 63	1135 ± 17
==1 b-tags	29 ± 0.6	6054 ± 23	7054 ± 95	1545 ± 24	552 ± 9	623 ± 16	128 ± 6
≥ 1 FWjet	16 ± 0.4	1532 ± 12	1208 ± 38	368 ± 11	126 ± 4	152 ± 7	22 ± 2
$m_{j10} > 50\,\text{GeV}$	12 ± 0.4	1140 ± 10	459 ± 23	180 ± 9	57 ± 3	67 ± 5	12 ± 2
$\Delta\phi(\ell, j_{10}) > 1.5$	10 ± 0.4	738 ± 8	334 ± 19	121 ± 8	24 ± 2	33 ± 4	9 ± 1
$\min\Delta R(\ell, j_4) < 1.5$	4 ± 0.2	358 ± 6	110 ± 11	54 ± 5	11 ± 1	12 ± 2	1 ± 0.5
$\max\Delta R(j_4, j_{10}) > 2.0$	3 ± 0.2	345 ± 6	107 ± 11	54 ± 5	10 ± 1	12 ± 2	1 ± 0.5

Table 6.13.: Event yields after the various selection steps for the background processes and a B example signal with $m_B^{\text{gen}} = 800\,\text{GeV}$ (scaled to $20.3 fb^{-1}$) together with their statistical uncertainties in the μ+jets channel in the B signal regions (top, W). The first line corresponds to events after the pre-selection cuts.

cut	process						
	B SR, top						
	signal $m_B^{\text{gen}} = 800\,\text{GeV}$	$t\bar{t}$	W+jets	single top	QCD	Z+jets	Diboson
==2 or ==3 j_4	45 ± 0.8	12572 ± 34	107695 ± 356	3136 ± 34	7007 ± 92	10202 ± 73	1212 ± 18
$E_T^{miss} > 20\,\text{GeV}$	44 ± 0.8	12046 ± 33	100185 ± 343	2987 ± 34	5757 ± 85	7866 ± 64	1147 ± 18
$E_T^{miss} + m_T^W > 60\,\text{GeV}$	43 ± 0.8	11640 ± 33	96060 ± 336	2881 ± 33	4599 ± 78	6928 ± 60	1113 ± 17
==1 b-tags	24 ± 0.6	5874 ± 23	7576 ± 101	1586 ± 24	482 ± 17	475 ± 15	135 ± 6
≥ 1 FWjet	13 ± 0.4	1499 ± 12	1201 ± 38	382 ± 12	111 ± 8	83 ± 6	15 ± 2
$m_{j10} > 50\,\text{GeV}$	11 ± 0.4	1025 ± 10	418 ± 22	173 ± 9	46 ± 6	27 ± 3	10 ± 2
$\Delta\phi(\ell, j_{10}) > 1.5$	10 ± 0.4	961 ± 9	389 ± 21	160 ± 9	39 ± 5	26 ± 3	10 ± 2
$\min\Delta R(\ell, j_4) > 1.5$	7 ± 0.3	480 ± 7	260 ± 18	90 ± 7	26 ± 5	13 ± 2	8 ± 1
$\max\Delta R(j_4, j_{10}) < 2.0$	6 ± 0.3	286 ± 5	118 ± 13	46 ± 5	11 ± 3	4 ± 1	4 ± 1
	B SR, W						
	signal $m_B^{\text{gen}} = 800\,\text{GeV}$	$t\bar{t}$	W+jets	single top	QCD	Z+jets	Diboson
==2 or ==3 j_4	45 ± 0.8	12572 ± 34	107695 ± 356	3136 ± 34	7007 ± 92	10202 ± 73	1212 ± 18
$E_T^{miss} > 20\,\text{GeV}$	44 ± 0.8	12046 ± 33	100185 ± 343	2987 ± 34	5757 ± 85	7866 ± 64	1147 ± 18
$E_T^{miss} + m_T^W > 60\,\text{GeV}$	43 ± 0.8	11640 ± 33	96060 ± 336	2881 ± 33	4599 ± 78	6928 ± 60	1113 ± 17
==1 b-tags	24 ± 0.6	5874 ± 23	7576 ± 101	1586 ± 24	482 ± 17	475 ± 15	135 ± 6
≥ 1 FWjet	13 ± 0.4	1499 ± 12	1201 ± 38	382 ± 12	111 ± 8	83 ± 6	15 ± 2
$m_{j10} > 50\,\text{GeV}$	11 ± 0.4	1025 ± 10	418 ± 22	173 ± 9	46 ± 6	27 ± 3	10 ± 2
$\Delta\phi(\ell, j_{10}) > 1.5$	10 ± 0.4	961 ± 9	389 ± 21	160 ± 9	39 ± 5	26 ± 3	10 ± 2
$\min\Delta R(\ell, j_4) < 1.5$	4 ± 0.2	481 ± 7	129 ± 12	70 ± 6	14 ± 3	13 ± 2	2 ± 0.7
$\max\Delta R(j_4, j_{10}) > 2.0$	4 ± 0.2	465 ± 7	126 ± 12	69 ± 6	14 ± 3	13 ± 2	2 ± 0.7

Table 6.14.: Summary of the $t\bar{t}$ and W+jets control region selection requirements. For the $t\bar{t}$ CR ≥ 2 b-tagged narrow jets are required, while for the W+jets control region events with $\equiv 0$ b-tagged jets are selected. "All 4 SRs" refers to hadronic top and hadronic W as well as b^* (≥ 0 forward jets) and B (≥ 1 forward jet) regions. Two CR for each SR are defined, with the only difference being the cut on the number of b-tagged jets.

Region	# b-tags	Approx. fraction of particular background
all 4 SRs	$\equiv 1$	50-65% $t\bar{t}$, 20-35% W+jets
all 4 W+jets CRs	$\equiv 0$	70-80% W+jets
all 4 $t\bar{t}$ CRs	≥ 2	65-90% $t\bar{t}$

in the b^* and B control regions, respectively. While the $S/\sqrt{B}$ and S/B values for the B quark are negligible, they seem to be large for low b^* masses. It should be noted, that for this coupling scenario masses below 870 GeV are already excluded, such that the quoted numbers overestimate the true effect as they are derived using theory cross-sections larger than the current limits. The true signal contamination is thus much lower.

Table 6.15.: b^* signal contamination in the $t\bar{t}$ and W+jets control regions. As an example, b^* signals with purely left-handed couplings ($f_g = f_L = 1$, $f_R = 0$) are tested and normalised to their theoretical cross section. Higher values for $S/\sqrt{B}$ are only observed for the lowest mass points that are already excluded. In the signal regions the $S/\sqrt{B}$ numbers are about a factor of 4 higher than in the control regions.

b^* $t\bar{t}$ CR	b^* 600 GeV		b^* 800 GeV		b^* 1000 GeV		b^* 1200 GeV		b^* 1400 GeV	
	S/B	$S/\sqrt{B}$	S/B	$S/\sqrt{B}$	S/B	$S/\sqrt{B}$	S/B	$S/\sqrt{B}$	S/B	$S/\sqrt{B}$
top	0.821	16.23	0.365	7.206	0.100	1.977	0.029	0.577	0.010	0.203
W	0.125	6.335	0.048	2.444	0.017	0.835	0.005	0.265	0.002	0.084
b^* W+jets CR	b^* 600 GeV		b^* 800 GeV		b^* 1000 GeV		b^* 1200 GeV		b^* 1400 GeV	
	S/B	$S/\sqrt{B}$	S/B	$S/\sqrt{B}$	S/B	$S/\sqrt{B}$	S/B	$S/\sqrt{B}$	S/B	$S/\sqrt{B}$
top	0.098	15.26	0.032	5.016	0.009	1.436	0.003	0.470	0.001	0.177
W	0.062	8.467	0.022	3.045	0.009	1.164	0.003	0.415	0.001	0.155

Figure 6.13 and 6.14 show the leading jet p_T distributions as an example for data-MC comparisons in the $t\bar{t}$ and W+jets control regions. The uncertainty band does not cover all data points, as it only contains the theoretical and statistical uncertainty. A fair comparison can therefore not be made unless systematic uncertainties are included as well.

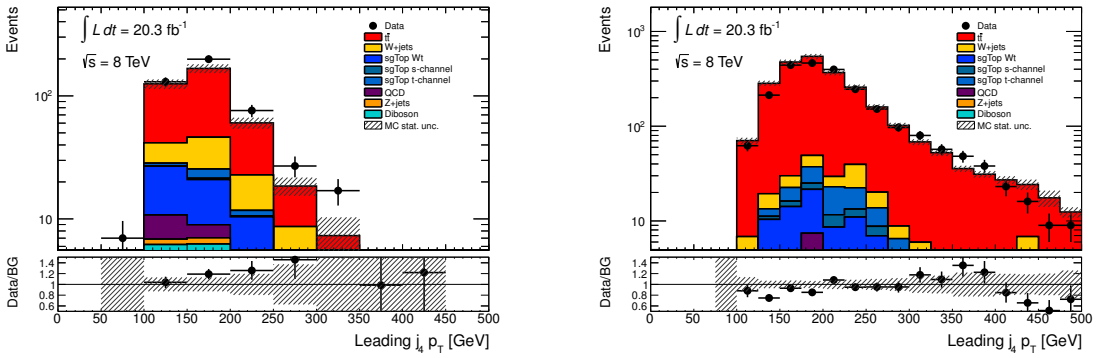

(a) b^* $t\bar{t}$ CR, top

(b) b^* $t\bar{t}$ CR, W

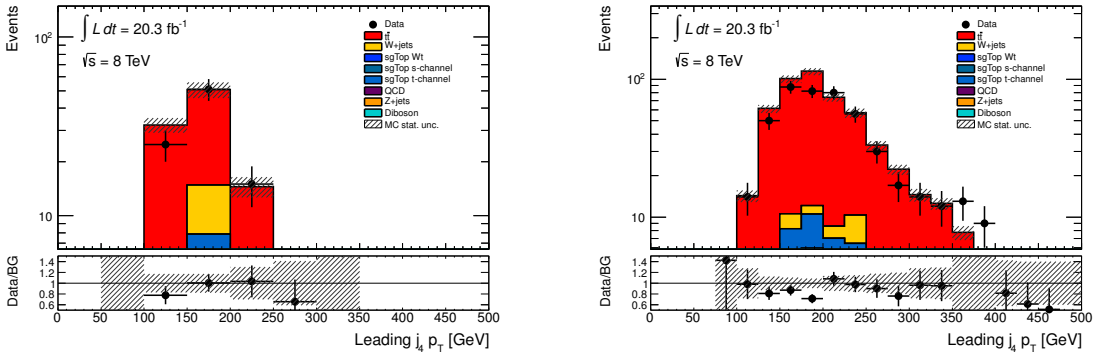

(c) B $t\bar{t}$ CR, top

(d) B $t\bar{t}$ CR, W

Figure 6.13.: Leading jet p_T distributions for data and the various SM backgrounds in the $t\bar{t}$ CR. The error band only shows the theory and MC statistical uncertainty. For plots with systematic uncertainties included, please refer to section 6.8. Separate distributions for electron and muon channel can be found in Figure B.1 and B.3 in Appendix B.

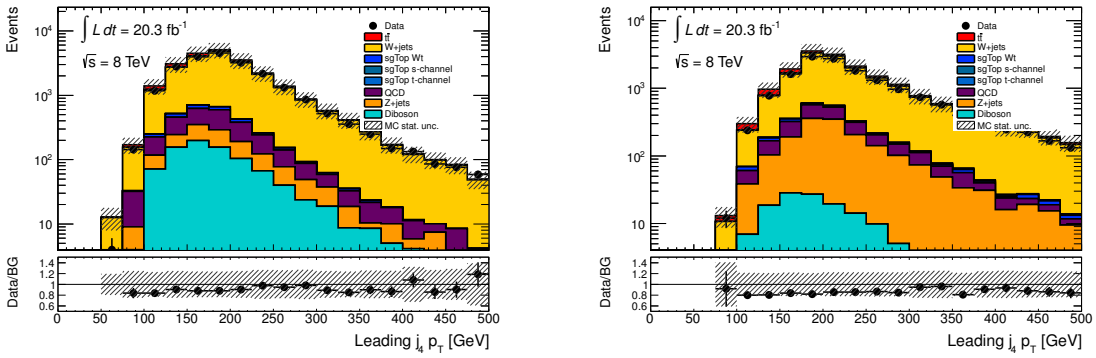

(a) b^* W+jets CR, top

(b) b^* W+jets CR, W

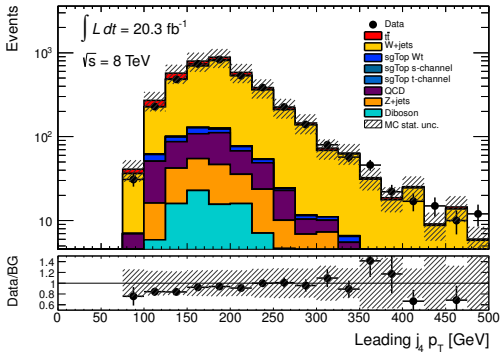

(c) B W+jets CR, top

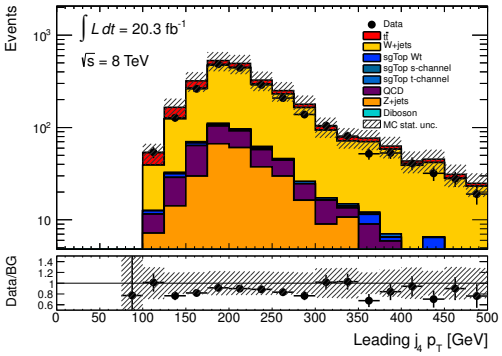

(d) B W+jets CR, W

Figure 6.14.: Leading jet p_T distributions for data and the various SM backgrounds in the W+jets CR. The error band only shows the theory and MC statistical uncertainty. For plots with systematic uncertainties included, please refer to section 6.8. Separate distributions for electron and muon channel can be found in Figure B.2 and B.4 in Appendix B.

Table 6.16.: B signal contamination in the $t\bar{t}$ and W+jets control regions. Signals are normalised to the theoretical cross section. In the signal regions the $S/\sqrt{B}$ numbers are about a factor of 4 higher than in the control regions.

B $t\bar{t}$ CR	B 600 GeV		B 800 GeV		B 1000 GeV		B 1200 GeV	
	S/B	$S/\sqrt{B}$	S/B	$S/\sqrt{B}$	S/B	$S/\sqrt{B}$	S/B	$S/\sqrt{B}$
top	0.0193	0.1981	0.0088	0.0900	0.0055	0.0562	0.0015	0.0149
W	0.0055	0.1278	0.0022	0.0502	0.0009	0.0215	0.0003	0.0073
B W+jets CR	B 600 GeV		B 800 GeV		B 1000 GeV		B 1200 GeV	
	S/B	$S/\sqrt{B}$	S/B	$S/\sqrt{B}$	S/B	$S/\sqrt{B}$	S/B	$S/\sqrt{B}$
top	0.0036	0.2330	0.0014	0.0932	0.0005	0.0341	0.0002	0.0131
W	0.0022	0.1154	0.0013	0.0686	0.0006	0.0310	0.0002	0.0096

In order to make a sound judgement on the level of agreement between data and MC in the control regions, it is necessary to take into account the statistical, theoretical and all possible systematic uncertainties, which are discussed in section 6.7. Section 6.8 shows a comparison between data and MC in various distributions considering these uncertainties.

6.6.1. Data-Driven Background Normalisation vs. Fit to Data

When studying the data-MC agreement in the control regions, one might find a poor description of the data by the simulation as a consequence of the generator settings not being optimised for the specific phase-space region selected in this analysis (e.g. by asking of at least one high-p_T large-R jet). This would require the use of an overall scale factor applied to the Monte-Carlo yield. One can e.g. see from Figure 6.14 that such a procedure would be applicable for the W+jets background, as the yield of these simulated events has shown to be generally too low to match the data. Such a factor can be derived by comparing data to simulated event yields in the control regions. However, in this analysis no such data-driven scale factors are directly calculated. Instead, in the statistical analysis (see section 6.10) an overall fit to data is performed, resulting in slightly modified background fractions.

6.7. Systematic Uncertainties

There are various sources of systematic uncertainties, stemming e.g. from insufficient theory knowledge or improper modelling of the observed data by the MC simulation. In order to reliably judge whether the measured data agrees with the SM prediction or whether one can claim to have seen signs for new physics phenomena, these effects have to be evaluated. In this section, the various sources of systematic uncertainties, some related technicalities as well as their impact on the predicted event yield are discussed. Most of the uncertainties are derived according to standard methods developed in the *ATLAS Top group*, as documented in [124] (restricted to ATLAS users). In most cases, the effect of single systematic uncertainties is quantified by running the analysis again, with a set of changed input parameters, comparing the result to the nominal one in terms of shape and normalisation of the discriminant distribution and using the maximum difference as an uncertainty.

6.7.1. Sources of Systematic Uncertainties

Electron Energy Scale and Resolution

In the nominal analysis, the electron energy scale in data (which is affected by energy losses outside the sensitive calorimeter volume) is corrected such that it matches the one in MC. The associated uncertainty is retrieved in MC, by calculating a scale factor for each electron from the difference of the nominal scale factor and the one varied within its uncertainty, which consists of the quadratic sum of the following contributions [88]:

- The electron energy scale is calibrated by a comparison of the Z peak in $Z \to e^+e^-$ events in data and MC and the derivation of a correction factor. The variation of this correction factor contains contributions from the statistical uncertainty in this comparison study as well as from the influence of the generator choice.
- Additionally, ECAL presampler uncertainties as well as uncertainties from electron interactions with the detector material have to be considered.

The event yield after application of the varied scale factor is then compared to the nominal one to obtain the size of the systematic uncertainty associated with the electron energy

scale [125].
In the nominal analysis, the electron energy is smeared in MC to obtain the resolution measured in data. This is done via a Gaussian of which the width equals the experimental resolution. To compute the uncertainty associated with this procedure, the width of the Gaussian used for smearing is enlarged by the measured uncertainty on the resolution. The resulting spectrum is then compared to the nominal one [126].

Muon Energy Scale and Resolution

The muon energy scale is corrected in MC to match what is observed in data. This scale factor is varied up and down within its uncertainties and the resulting distribution of the discriminating variable is compared to the nominal analysis outcome.
For muons, there are two separate resolutions: one from the momentum measurement in the ID and one from the muon spectrometer [127]. Both of them are smeared with a Gaussian enlarged in width by its measured uncertainty analogous to the electron case. The envelope of the largest deviation of the discriminating variable distribution from the nominal case is then taken as the final systematic uncertainty on the momentum resolution.

Lepton Scale Factors

For electrons and muons each, three scale factors are obtained from comparing trigger, reconstruction and identification efficiency in MC with the ones in data [84, 127]. These scale factors are scaled up and down individually within their measured uncertainties and the differences between the resulting distribution and the nominal ones are added in quadrature to obtain the systematic uncertainty associated with the lepton scale factors.

Jet Energy Resolution (JER)

As discussed in section 5.4.2, in the nominal analysis no smearing of the energy resolution is applied, as data and MC agree in terms of the resolution measured with two different methods (bisector method and in situ, as described in section 5.4.2) within the uncertainties. In order to obtain the total resolution uncertainty from the uncertainties on these two components, the respective differences between the measured resolutions in data and MC [109] are added in quadrature [128]. The result is applied as a smearing to the nominal

MC resolution to study the impact on the discriminating variable. The difference between the yield with and without that smearing applied is symmetrised (i.e. the size of the one-sided change is equally used for up and down variation) and used as a systematic uncertainty.

Jet Vertex Fraction (JVF)

In the nominal analysis, a scale factor is applied to correct for the difference in efficiencies between data and MC for the jet selection and pileup jet rejection by cutting on the jet vertex fraction (as explained in section 5.4.3). Uncertainties associated to the use of this scale factor are obtained by varying it within the measured uncertainty in both directions [129]. The relative difference in the event yield is used as the associated uncertainty.

Jet Reconstruction Efficiency (JEFF)

As stated in section 5.4.1, the jet reconstruction efficiency is 100% for jets with $p_T \geq 30\,\text{GeV}$ and agrees well between data and MC in this p_T region. Jets with smaller p_T are used to determine the uncertainty coming from the jet reconstruction efficiency [105]: This uncertainty is determined by varying parameters used in the efficiency determination via the T&P method. These parameters are the tag-jet p_T, which is changed to $p_T > 20\,\text{GeV}$ as well as the $\Delta\Phi$ window for the probe jet (varied within $\Delta\Phi < [2.6, 2.9]$) and the angular distance for the matching between probe track jet and calorimeter jet (varied within $\Delta R < [0.3, 0.5]$). The difference between the efficiency obtained using the varied input parameters to the nominal one is taken as a scale factor and the resulting yield difference is symmetrised and used as a systematic uncertainty in the analysis.

Jet Energy Scale (JES)

There are several sources of uncertainties on the jet energy scale, associated with the various techniques used to determine the size of the four corrections to the jet energy scale that were described in section 5.4.2. In total, the JES uncertainty is broken down into 26 components (listed in [130]), which are treated independently to account for the different parts entering the final jet energy scale factor for every jet. These components can be grouped into uncertainties arising from statistical limitations, modelling, detector effects,

η calibration, pileup, and b-jet response. For each of those components, the jet energy scale is varied within $\pm 1\sigma$ of the measured uncertainty corresponding to the particular method [104], before re-application of the event selection, leading to a changed event yield as well as a modified shape of the discriminating variable.

Large-R Jet Energy and Mass Resolution (JER, JMR)

Mass and energy resolution for large-R jets are not well measured and can be as high as 20% [131]. The impact of that uncertainty on the analysis is determined by binning the mass and energy resolution found in the nominal analysis in p_T and η of the large-R jets. For each large-R jet, the resolution from the corresponding phase space region is taken and smeared by 20% using a Gaussian distribution. The resulting yield difference is symmetrised and taken as an uncertainty.

Large-R Jet Energy and Mass Scale (JES, JMS)

Mass and energy uncertainties for large-R jets are obtained via a combination of methods: The double ratio method, where the ratios of jet and track jet (as introduced in section 5.4.1) distributions in data and MC are used, and the gamma-jet method, where the photon response p_T^{jet}/p_T^{γ} is compared in data and MC. Each method is only valid in a certain η and p_T region and an interpolation between the two is also taken into account. The data-MC ratios are varied within their measured uncertainties and the comparison between the nominal event yield and the ones with those methods applied, is taken as a systematic uncertainty [132]. It should be noted that with the provided tools, an uncertainty for large-R jets with $p_T < 200\,\text{GeV}$ could not be obtained, which would have resulted in asymmetries in the up and down variation because of missing events migrating from just below the threshold into the selected region for the up-variation. A pragmatic and conservative solution was chosen and jets below 200 GeV in p_T were assigned the relative uncertainty at $p_T = 200\,\text{GeV}$.

b-tagging

In the nominal analysis, scale factors are applied to account for the differences in b-tagging efficiency between data and MC. The same is done for differences in c-jet selection efficiency

and mistag rate, which need to be applied as there is a certain possibility of ranking a jet as a b-jet, while in fact it was a c-jet or a jet stemming from a light quark or gluon. The uncertainty associated with the usage of these scale factors is retrieved by varying the individual scale factors within their measured uncertainties [116] and comparing the nominal event yield with the ones obtained with varied scale factors [133].
The b- and c-tagging efficiencies are only provided (and thus compared to the ones in data) for jets with $p_T < 300\,\text{GeV}$. Beyond this value in p_T, the efficiency of the last defined value is taken. The corresponding uncertainty is estimated from an extrapolation of the increase of the b-tagging uncertainty over the calibration range [133].

E_T^{miss}

If an input variable for the E_T^{miss} calculation, e.g. the jet energy scale, is altered within its systematic variation, the E_T^{miss} is recalculated to account for the change in the particles' energies and momenta such that the systematic variations are propagated to an uncertainty of the missing transverse momentum [118].
The uncertainty on the E_T^{miss} itself is obtained using its *SoftJet* term, which covers all low-$p_T$jets with $10\,\text{GeV} < p_T < 20\,\text{GeV}$ (see section 5.6). Similar to the procedures to obtain JES and JER uncertainties, the scale and resolution uncertainties on this term are studied independently. Afterwards, the E_T^{miss} is recalculated, once with soft jets with a changed energy scale and once with soft jets with a changed resolution [118]. The difference between the yields obtained in those ways with the nominal yield is used as a systematic uncertainty.

Parton Distribution Function (PDF)

As stated earlier in section 4.2.1, parton distribution functions are not predicted by theory. They are extracted from various measurements by different groups, which provide PDF along with error PDF sets including experimental and theoretical uncertainties. The different groups analyse different data sets and differ in the chosen parametrisation, the analysis strategy and the theory uncertainties that they take into account. For the event generation of the various background and signal processes, one particular PDF has to be chosen, which slightly impacts the kinematic properties of the events. This choice therefore is a source of systematic uncertainty for the analysis which has to be evaluated. The most

straight-forward way to do this, would be to regenerate the MC samples with all different PDF, including the error sets. As this goes in line with unacceptably large CPU time, it is done via a procedure known as *PDF reweighting*, as e.g. described in [134] based on a method developed in [135]. The truth information of the x_1 and x_2 values is used to calculate a weighting factor w_i for each event i for an alternative PDF ($PDF2$) from the comparison with the nominal PDF ($PDF1$) as

$$w_i = \frac{g_{PDF2}(f_1, x_1, Q^2)}{g_{PDF1}(f_1, x_1, Q^2)} \cdot \frac{g_{PDF2}(f_2, x_2, Q^2)}{g_{PDF1}(f_2, x_2, Q^2)}, \tag{6.4}$$

with $g_{PDF1/2}$ being the parton distribution functions in the two protons, $f_{1/2}$ being the flavour of the partons and Q^2 the squared momentum transfer of the reaction. With this weight the event selection efficiency with $PDF2$, ϵ_2, can be expressed in terms of quantities related to $PDF1$:

$$\epsilon_2 = \epsilon_2^{gen} \frac{N_2^{cuts}}{N_2^{gen}} = \epsilon_2^{gen} \frac{\sum_{i=1}^{N_1^{cuts}} w_i}{\sum_{i=1}^{N_1^{gen}} w_i}, \tag{6.5}$$

with $N_{1/2}^{cuts}$ being the number of events after cuts for the two PDF and $N_{1/2}^{gen}$ the respective number of generated events.
This modified event selection efficiency is calculated for every error PDF of 3 different PDF sets (`MSTW2008nlo68cl`, `NNPDF2.3` and `CT10`) and compared to the nominal ones. As shape dependence is not expected to have a large impact, this is done in one single bin of the final discriminant, and the envelope of the multiple curves is taken as the systematic uncertainty. In order to keep the cross section for a given process constant, a scale factor is derived and applied during the procedure.

QCD Multijet Background Estimate

There are multiple sources of systematic uncertainties in the data-driven method to derive the QCD multijet background estimate which is described in section 6.5.1. This includes uncertainties estimated by varying the MC normalisation in the QCD control regions, the residual bias due to a lack of parametrisation of the real and fake efficiencies, and the different flavour compositions of the multijet events in the different control regions [122]. The analysis is run individually with each of these components varied within the respective uncertainty. The resulting uncertainties on the discriminating variable, which are then

added in quadrature, turned out to be high in some signal regions, but as the contribution from QCD multijet events in the signal regions is relatively low, this does not massively affect the final result (exact numbers will be shown at the end of this section in Table 6.17 and 6.18).

Initial and Final State Radiation (ISR/FSR)

Initial and final state radiation (ISR and FSR) produce additional partons to the ones which come from the hard interaction, by emissions of gluons from the initial and final state partons. The modelling of that radiation therefore has an influence on the selected events and is thus another source for systematic uncertainties. This effect is evaluated using special MC samples (produced with ALPGEN+PYTHIA) with more or less radiation. The number of additional partons is changed by varying the renormalisation scale associated with the strong coupling α_S up and down by a factor of 2 relative to the original scale between two partons in the matrix element calculation, which is set to the mass scale of the process. As such samples only exist for top-pair production and as this is the main background for this analysis, no other processes are used for this study. The analysis is run once on the high-radiation and once on the low-radiation sample. Half of the difference between the two is used as an uncertainty [136].

Generator Dependence and Parton Shower Modelling

As described in sections 4.2.2 and 4.2.3, different MC generators contain different implementations of the hard process and the parton shower model. The choice of a given generator can therefore have an influence on the kinematic distributions in the final state. To obtain a systematic uncertainty which accounts for these effects, the analysis is run on different MC samples of the same process and the outcome is compared. In this analysis, this is done for the two main backgrounds. For top-pair production two sets of samples are compared with one another to independently probe the influence of matrix element and shower generator:

- POWHEG (matrix element) + PYTHIA (shower) vs. POWHEG (matrix element) + HERWIG (shower)
- POWHEG (matrix element) + PYTHIA (shower) vs. MC@NLO (matrix element) + PYTHIA (shower)

The largest rate difference is symmetrised and taken as a systematic uncertainty [136]. For W+jets background, ALPGEN and SHERPA are compared, and the rate difference is symmetrised and used as systematic uncertainty.

W+jets Flavour Composition

As described in section 6.6, the W+jets modelling is tested in a control region enriched with this process. In a fit to data in the statistical analysis, this region is used to obtain scale factors to account for mismodellings in the Monte-Carlo simulation, which will then be applied in the signal region. However, the relative amount of the different flavours of jets produced in association with the W bosons ($W + c$, $W + c\bar{c}$ and $W + b\bar{b}$) differs in the signal and control regions: While the control region selection with exactly 0 b-tagged jets mainly selects W bosons produced in association with jets from light quarks or gluons, the requirement for exactly 1 b-tag leads to a higher contribution from c or b jets in the signal region. Shapes and yields of light and heavy-flavour jets produced in association with W bosons have therefore been compared, as shown in Appendix L of the backup documentation to the publication to this search [137], and the largest deviation of 10% in yields between different regions has been taken as a conservative uncertainty on the total W+jets count.

Background Normalisation

In order to match the MC yield and the data yield, the number of MC events has to be scaled to the luminosity of the dataset. This is done using the theoretical cross section of each simulated background component individually via the relation

$$N_{process} = \sigma_{process} \cdot \int Ldt \tag{6.6}$$

with $N_{process}$ being the number of expected events, $\sigma_{process}$ the cross section of the particular process and L the instantaneous luminosity. The theoretical cross sections have associated uncertainties, which translate to an uncertainty on the total yield. The theoretical uncertainties are of different sizes for the various background processes:

- For top-pair production the theory uncertainty (determined via scale, PDF and α_S variations) is assumed to be +5.7%/-5.3% [138, 139].

- For W+jets and Z+jets production, the uncertainty on the inclusive cross section is 4% [140] plus 24% per jet bin added in quadrature [141, 142]. For the selection used in this analysis, this yields an uncertainty of about 34% for each of the two background components.
  For diboson production, the same recipe is used as for Z+jets and W+jets, except that the uncertainty on the inclusive cross section is 5% in this case [140]. The uncertainties on the production of the three possible diboson pairs are assumed to be uncorrelated.

- For single-top production in the Wt channel, a cross-section uncertainty of $\pm 6.8\%$ is used [143]. For s- and t-channel, this uncertainty is assumed to be $\pm 3.9\%$ and uncorrelated between the processes [144].

The normalisation uncertainties are treated as independent between the various background processes.

Simulated signal distributions also have to be scaled to the correct luminosity and cross sections. The theory uncertainties retrieved by varying the renormalisation and factorisation scales, μ_R and μ_F, between half and twice the heavy quark mass can be found in Table 6.2 and Table 6.1 in section 6.1 for B and b^* respectively.

Luminosity

For the luminosity scaling described in the previous paragraph, the uncertainty on the measured luminosity has an influence as well. The measurement of the luminosity performed by ATLAS is described in section 3.4. The uncertainty on the integrated luminosity is $\pm 1.8\%$. It is derived, following the same methodology as that detailed in [56], from a preliminary calibration of the luminosity scale derived from beam-separation scans performed in November 2012.

Monte-Carlo Statistics

The statistical uncertainties on the Monte-Carlo samples is taken into account using the *Barlow-Beeston lite* method [145], in which one nuisance parameter in the statistical analysis

(as defined in section 6.10) is associated with the statistical uncertainty in each bin of the discriminating variable.

6.7.2. Impact of the Systematic Uncertainties

The impact of the previously discussed sources of systematic uncertainties on the background yield is shown in Table 6.17 and 6.18 for the various signal regions.

Table 6.17.: Summary of the total systematic uncertainties on the SM background yield in the b^* signal regions before the fit to data, which reduces the impact of most of the uncertainty sources and which is described in section 6.10.

systematic uncertainty	top		W	
	el	mu	el	mu
leptons	0.6% −0.7%	0.2% −0.2%	0.6% −0.7%	0.3% −0.3%
JER	0.3% −0.3%	1.8% −1.8%	0.8% −0.8%	1.3% −1.3%
JVF	1.2% −0.004%	0.6% −0.3%	1.4% −0.2%	1.1% −0.5%
JEFF	0.6% −0.6%	0.2% −0.2%	0.4% −0.4%	0.3% −0.3%
JES	3.4% −4.7%	3.3% −3.5%	4.1% −5.3%	4.0% −5.0%
large-R JMR, JER	3.9% −3.9%	4.3% −4.3%	2.2% −2.2%	2.4% −2.4%
large-R JMS, JES	14.8% −14.0%	17.5% −15.0%	10.2% −11.3%	11.4% −11.9%
b-tagging (b-, c-, mistag)	3.1% −3.1%	3.2% −3.2%	1.5% −1.5%	1.6% −1.5%
high p_T b and c-tagging	0.2% −0.2%	0.2% −0.2%	0.3% −0.3%	0.3% −0.3%
E_T^{miss}	0.9% −0.8%	0.1% −0.1%	0.8% −0.8%	0.1% −0.3%
PDF	1.7% −1.7%	2.7% −2.7%	1.3% −1.3%	1.8% −1.8%
QCD multijet background	6.4% −17.7%	1.9% −1.9%	5.5% −13.3%	1.6% −1.6%
ISR+FSR	3.6% −3.6%	2.7% −2.7%	4.9% −4.9%	3.3% −3.3%
$t\bar{t}$ generator (PowhegPythia vs. MCatNLO)	1.6% −1.6%	2.1% −2.1%	3.8% −3.8%	1.2% −1.2%
$t\bar{t}$ generator (PowhegPythia vs. PowhegHerwig)	4.3% −4.3%	3.3% −3.3%	5.7% −5/7%	6.7% −6.7%
W+jets generator (Alpgen vs. Sherpa)	15.8% −15.8%	17.9% −17.9%	8.9% −8.9%	2.8% −2.8%
W+light/W+HF difference	4.4% −4.4%	4.5% −4.5%	4.0% −4.0%	4.1% −4.1%

Table 6.18.: Summary of the total systematic uncertainties on the SM background yield in the B signal regions before the fit to data, which reduces the impact of most of the uncertainty sources and which is described in section 6.10.

systematic uncertainty	top, FWjet		W, FWjet	
	el	mu	el	mu
leptons	1.6% −1.8%	0.2% −0.2%	1.4% −1.3%	1.5% −1.5%
JER	3.2% −3.2%	0.5% −0.5%	1.5% −1.5%	5.1% −5.1%
JVF	0.5% −1.6%	0.6% −0.6%	1.9% −0.4%	0.3% −1.6%
JEFF	1.1% −1.1%	0.5% −0.5%	0.8% −0.8%	0.7% −0.7%
JES	6.8% −7.2%	3.1% −3.9%	5.6% −4.9%	5.3% −5.5%
large-R JMR, JER	3.5% −3.5%	3.3% −3.3%	1.3% −1.3%	0.9% −0.9%
large-R JMS, JES	16.6% −13.2%	17.7% −16.0%	9.5% −11.6%	11.0% −10.8%
b-tagging (b-, c-, mistag)	2.6% −2.7%	2.6% −2.6%	1.5% −1.5%	1.1% −1.1%
high p_T b and c-tagging	0.2% −0.2%	0.1% −0.1%	0.3% −0.3%	0.2% −0.2%
E_T^{miss}	1.5% −1.7%	0.2% −0.3%	1.5% −1.3%	1.0% −1.1%
PDF	4.4% −4.4%	5.7% −5.7%	2.2% −2.2%	3.1% −3.1%
QCD multijet background	7.7% −19.6%	5.5% −5.5%	7.9% −15.7%	2.0% −2.0%
ISR/FSR	0.6% −0.6%	2.4% −2.4%	2.5% −2.5%	2.9% −2.9%
$t\bar{t}$ generator (PowhegPythia vs. MCatNLO)	6.4% −6.4%	8.7% −8.7%	14.7% −14.7%	6.3% −6.3%
$t\bar{t}$ generator (PowhegPythia vs. PowhegHerwig)	5.6% −5.6%	1.9% −1.9%	6.1% −6.1%	8.8% −8.8%
W+jets generator (Alpgen vs. Sherpa)	9.3% −9.3%	18.4% −18.4%	2.0% −2.0%	7.0% −7.0%
W+light/W+HF difference	4.0% −4.0%	3.9% −3.9%	3.4% −3.4%	2.7% −2.7%

6.8. Data-MC Comparison in Control Distributions

Figure 6.15 through 6.22 show distributions for the leading jet p_T, lepton p_T, E_T^{miss} and the leading large-R jet mass for data and the various Standard Model background processes in the $t\bar{t}$ and W+jets control regions. One can see that the uncertainty band well covers data-MC differences. The uncertainty band includes all sources of systematic uncertainties mentioned in the previous sections, treated as independent sources. In the statistical analysis, which was not part of this work, but which is described in section 6.10, a fit of the sum of simulated background components to the measured data will be used to constrain some of the systematic uncertainties. This step will only be done at a later stage, and the shaded bands in Figure 6.15 through 6.22 therefore give conservative estimates on the total uncertainty.
Another feature which can be seen especially from the W+jets control region figures is that the MC prediction overestimates the W+jets contribution. This deviation is covered by the large normalisation uncertainty and the fit to data in regions without signal contribution (described in section 6.10) yields a scale factor for each background component to improve the background description. This scaling is not applied at that stage.

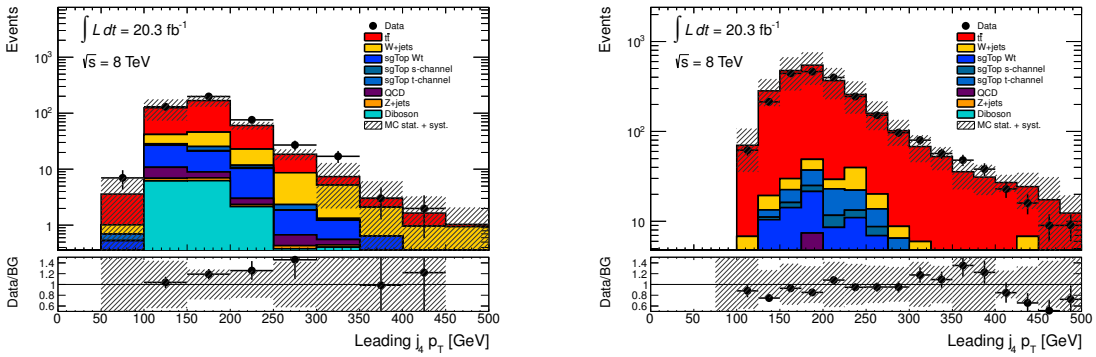

(a) b^* $t\bar{t}$ CR, top

(b) b^* $t\bar{t}$ CR, W

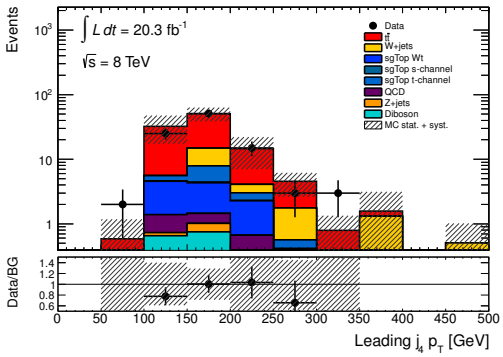

(c) B $t\bar{t}$ CR, top

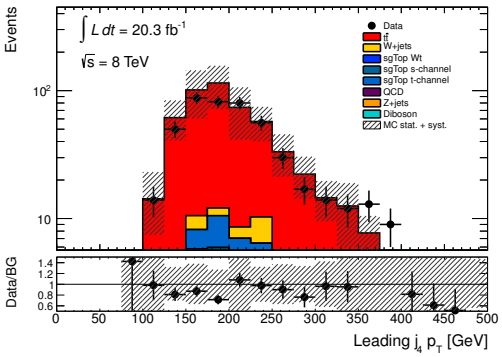

(d) B $t\bar{t}$ CR, W

Figure 6.15.: Leading jet p_T distributions for data and the various SM backgrounds in the $t\bar{t}$ CR. The error band includes the theoretical and MC statistical uncertainty and all systematic uncertainties described in section 6.7. Separate distributions for electron and muon channel can be found in Figure B.5 and B.7 in Appendix B.

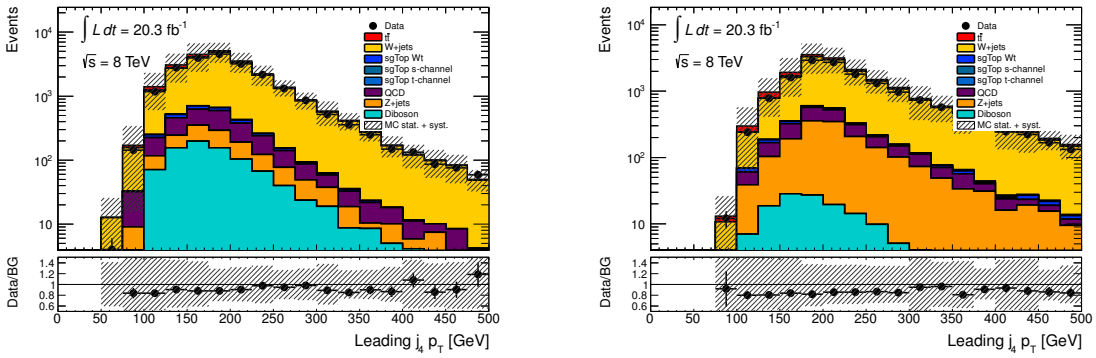

(a) b^* W+jets CR, top

(b) b^* W+jets CR, W

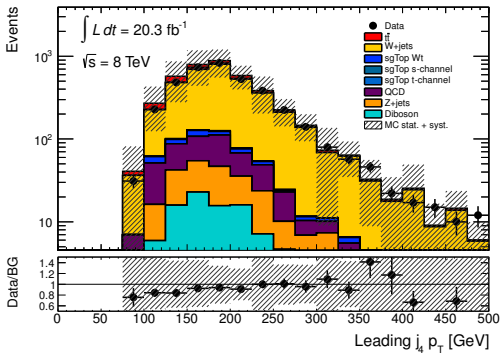

(c) B W+jets CR, top

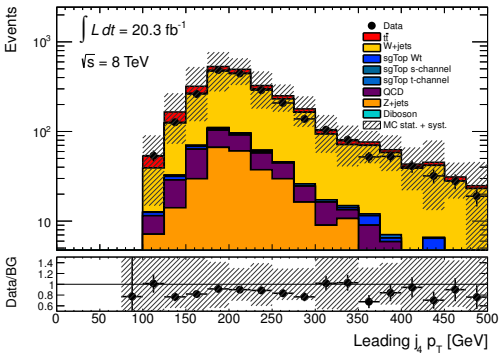

(d) B W+jets CR, W

Figure 6.16.: Leading jet p_T distributions for data and the various SM backgrounds in the W+jets CR. The error band includes the theoretical and MC statistical uncertainty and all systematic uncertainties described in section 6.7. Separate distributions for electron and muon channel can be found in Figure B.6 and B.8 in Appendix B.

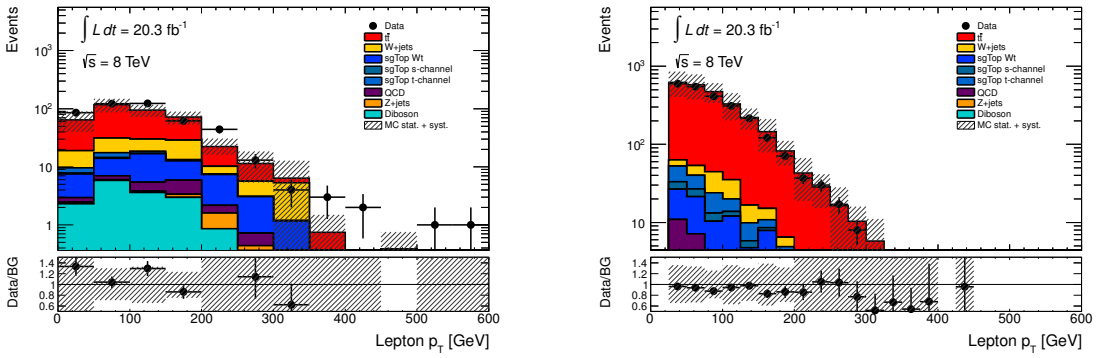

(a) b^* $t\bar{t}$ CR, top

(b) b^* $t\bar{t}$ CR, W

(c) B $t\bar{t}$ CR, top

(d) B $t\bar{t}$ CR, W

Figure 6.17.: Lepton p_T distributions for data and the various SM backgrounds in the $t\bar{t}$ CR. The error band includes the theoretical and MC statistical uncertainty and all systematic uncertainties described in section 6.7. Separate distributions for electron and muon channel can be found in Figure B.9 and B.11 in Appendix B.

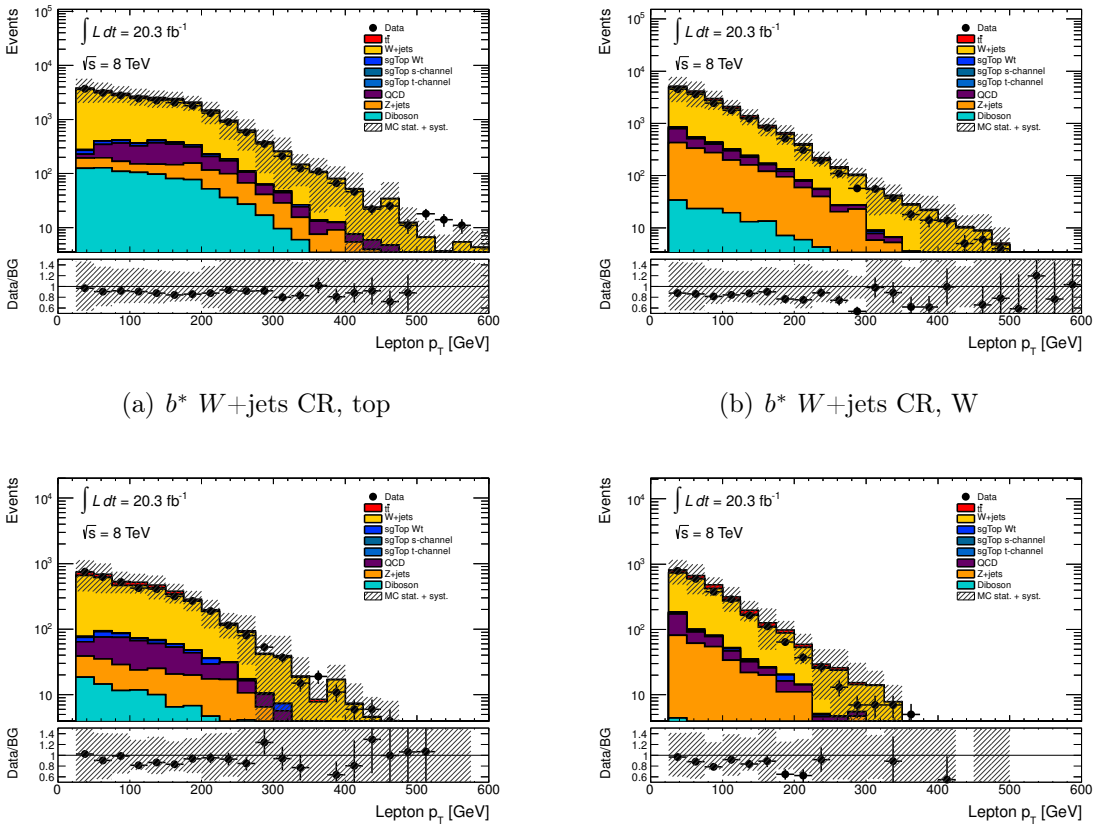

(a) b^* W+jets CR, top

(b) b^* W+jets CR, W

(c) B W+jets CR, top

(d) B W+jets CR, W

Figure 6.18.: Lepton p_T distributions for data and the various SM backgrounds in the W+jets CR. The error band includes the theoretical and MC statistical uncertainty and all systematic uncertainties described in section 6.7. Separate distributions for electron and muon channel can be found in Figure B.10 and B.12 in Appendix B.

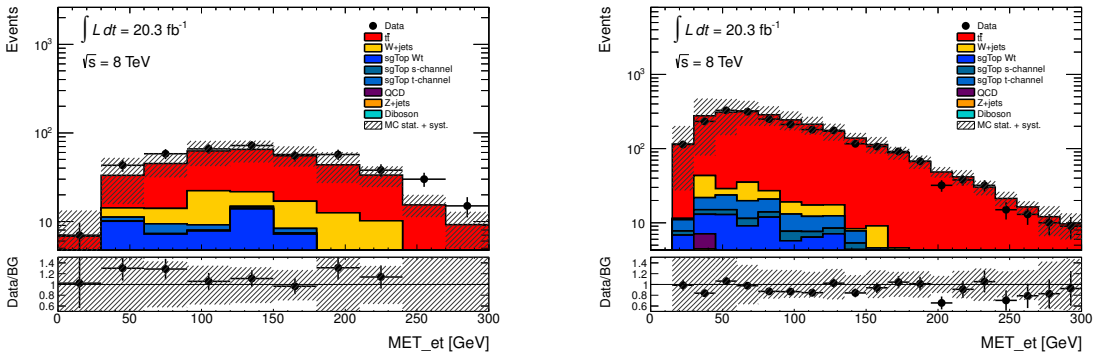

(a) b^* $t\bar{t}$ CR, top

(b) b^* $t\bar{t}$ CR, W

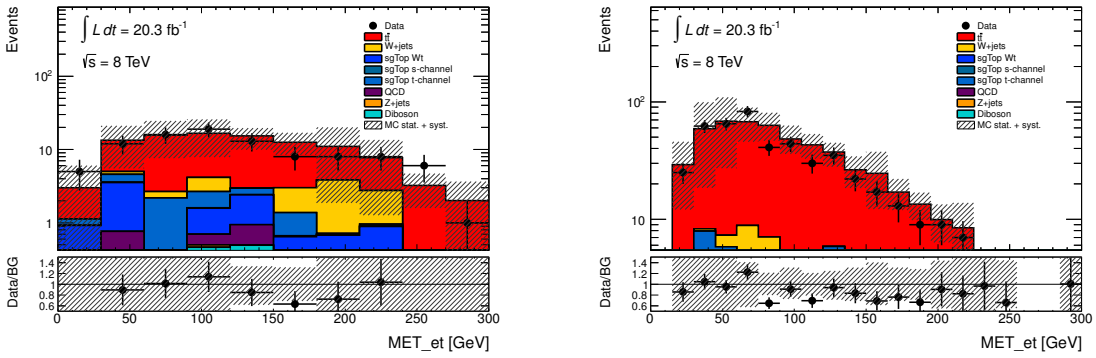

(c) B $t\bar{t}$ CR, top

(d) B $t\bar{t}$ CR, W

Figure 6.19.: E_T^{miss} distributions for data and the various SM backgrounds in the $t\bar{t}$ CR. The error band includes the theoretical and MC statistical uncertainty and all systematic uncertainties described in section 6.7. Separate distributions for electron and muon channel can be found in Figure B.13 and B.15 in Appendix B.

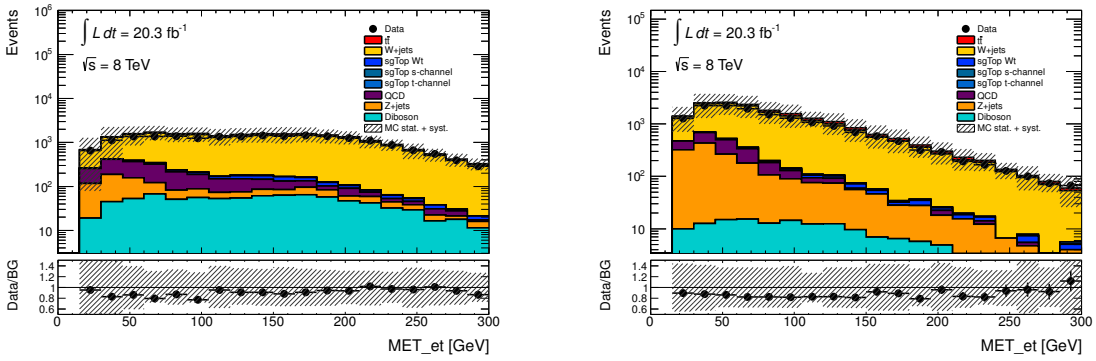

(a) b^* W+jets CR, top

(b) b^* W+jets CR, W

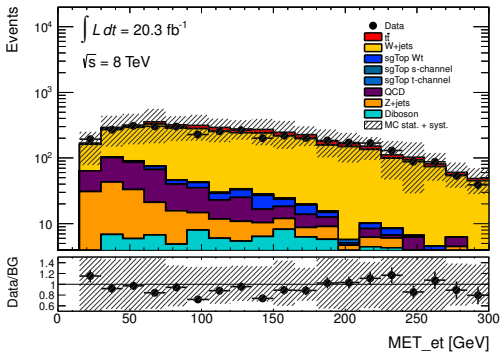

(c) B W+jets CR, top

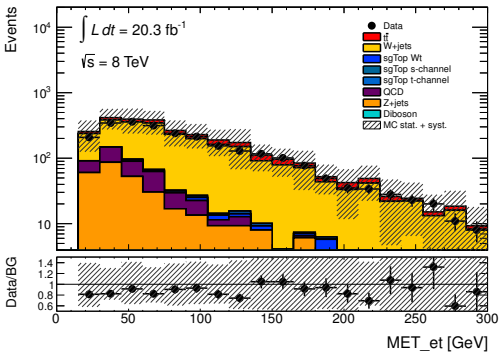

(d) B W+jets CR, W

Figure 6.20.: E_T^{miss} distributions for data and the various SM backgrounds in the W+jets CR. The error band includes the theoretical and MC statistical uncertainty and all systematic uncertainties described in section 6.7. Separate distributions for electron and muon channel can be found in Figure B.14 and B.16 in Appendix B.

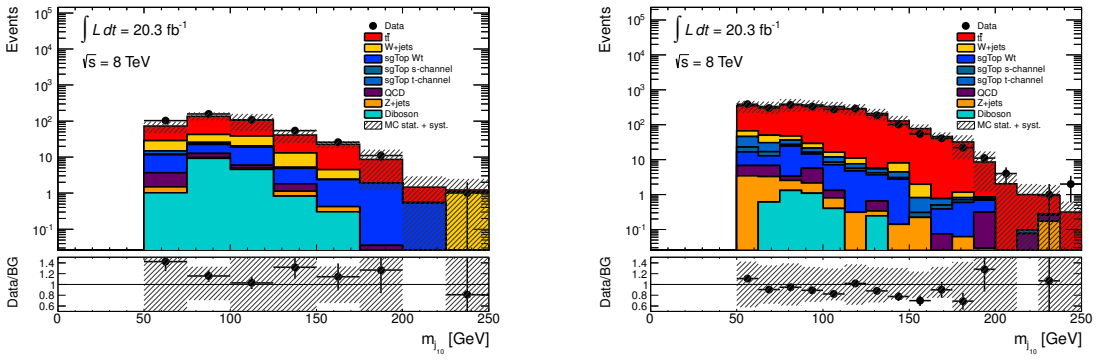

(a) b^* $t\bar{t}$ CR, top

(b) b^* $t\bar{t}$ CR, W

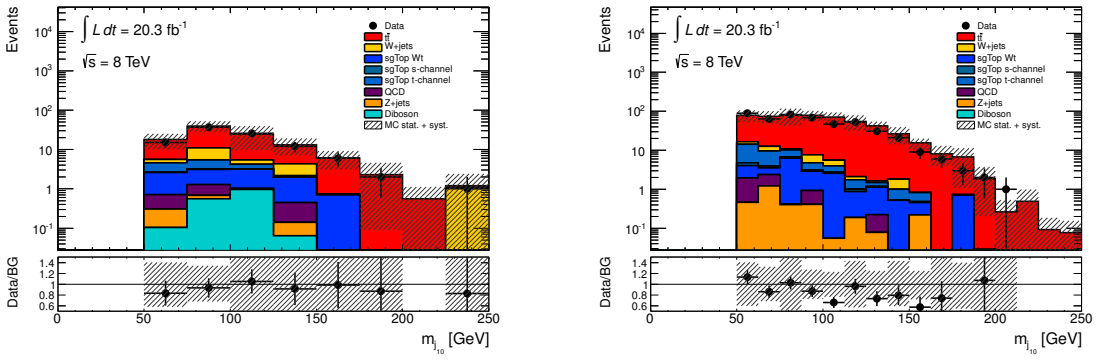

(c) B $t\bar{t}$ CR, top

(d) B $t\bar{t}$ CR, W

Figure 6.21.: Leading large-R jet mass distributions for data and the various SM backgrounds in the $t\bar{t}$ CR. The error band includes the theoretical and MC statistical uncertainty and all systematic uncertainties described in section 6.7. Separate distributions for electron and muon channel can be found in Figure B.17 and B.19 in Appendix B.

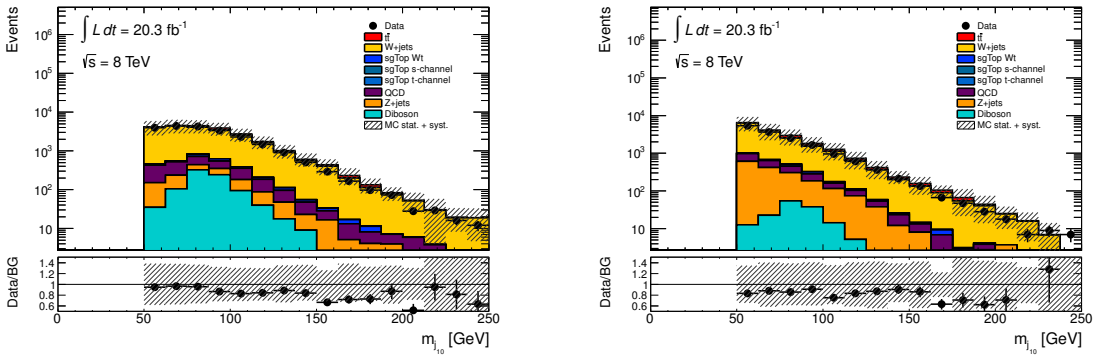

(a) b^* W+jets CR, top

(b) b^* W+jets CR, W

(c) B W+jets CR, top

(d) B W+jets CR, W

Figure 6.22.: Leading large-R jet mass distributions for data and the various SM backgrounds in the W+jets CR. The error band includes the theoretical and MC statistical uncertainty and all systematic uncertainties described in section 6.7. Separate distributions for electron and muon channel can be found in Figure B.18 and B.20 in Appendix B.

6.9. Discriminating Variable and Event Yields

A quantity often used in particle physics searches, is the invariant mass m of a particle, calculated from the Energies E and momenta $\mathbf{p}$ of its decay products as

$$m^2 = \left(\sum E\right)^2 - |\sum \mathbf{p}|^2. \tag{6.7}$$

In this analysis, the invariant mass of the heavy quark, m_{b^*} or m_B respectively, which is sensitive to resonance production of b^*/B, is used as a discriminating variable between signal and background. Data and background distributions of this quantity are used for the fit in the course of the statistical analysis, described in the next section. The invariant mass is calculated from the four-vectors of the lepton, E_T^{miss} and all (2 or 3) central jets in the event. The z-component of the neutrino 3-momentum vector is set to 0, as the usage of a W-boson mass-constrained reconstruction has shown no improvement in the preceding search at a centre-of-mass-energy of 7 TeV [146].
Figure 6.23 shows the distribution of the invariant heavy quark mass for the total SM background compared to distributions for various signal masses and Figure 6.24 shows the comparison of data and the individual SM backgrounds with two example signals for this variable. One can nicely see that with increasing heavy quark mass, the discriminating power increases as well.
Table 6.19 and 6.20 list the expected number of events in the b^* and B signal regions respectively for the various background processes as well as the total number of predicted SM backgrounds, the number of data events and the number of expected signal events with their theoretical and statistical uncertainties.

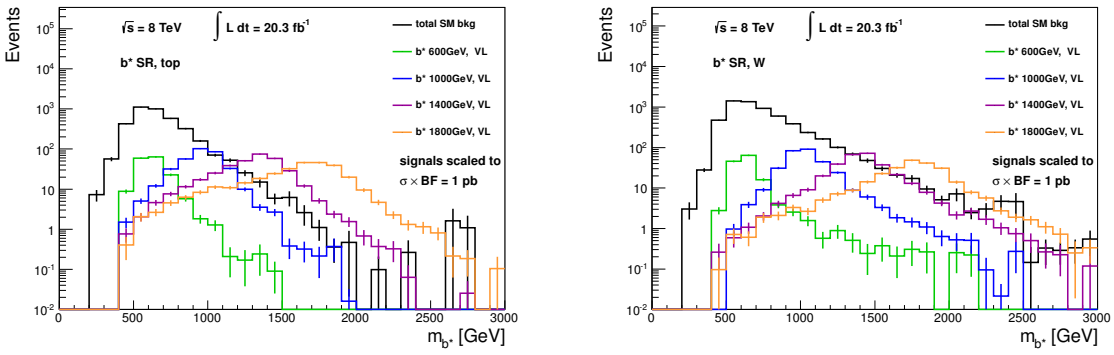

(a) b^* SR, top

(b) b^* SR, W

(c) B SR, top

(d) B SR, W

Figure 6.23.: Invariant mass distributions for the total SM background (black line) and various b^* and B signal masses (coloured lines) in the different signal regions. One can see that the discriminating power of this variable grows with increasing signal mass.

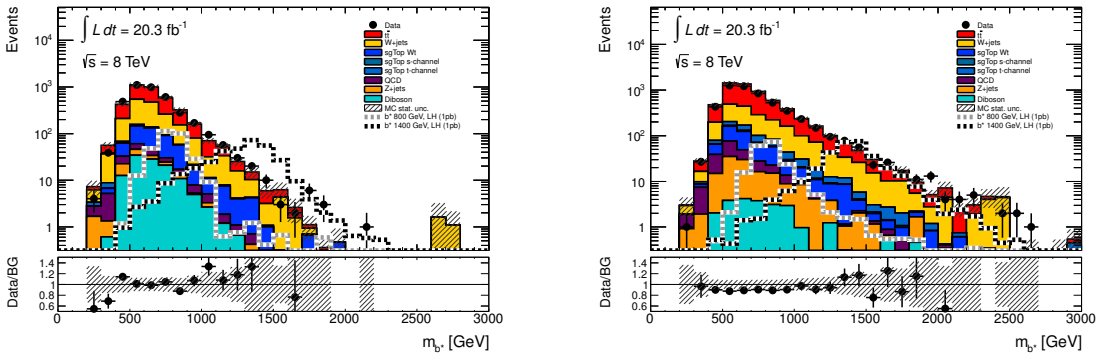

(a) b^* SR, top

(b) b^* SR, W

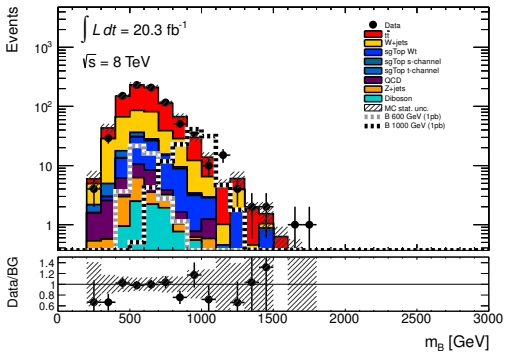

(c) B SR, top

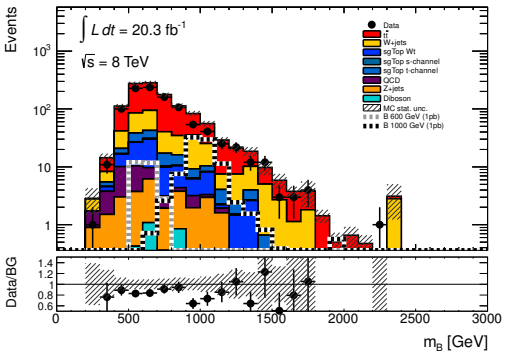

(d) B SR, W

Figure 6.24.: Invariant mass distributions for data and the various SM backgrounds as well as for different simulated signal masses. The error band only shows the theoretical and MC statistical uncertainty in order to keep the plot readable. One can see that the discriminating power of this variable grows with increasing signal mass.

Table 6.19.: Expected event yields in the b^* signal regions before the fit to data. Signals are normalised to their theory cross-sections. The total number of predicted SM background events and the number of data events are also presented. The uncertainties correspond to the data or MC statistical uncertainties. At this stage, none of the MC backgrounds has been fitted to data in the CRs, and thus the W+jets yield is about 10% higher than the contribution after the fit in the limit setting step (compare section 6.10).

SR	had top		had W	
Type	e	μ	e	μ
b^* 600, LH	1337.4 ± 73.7	1569.6 ± 81.8	1061.4 ± 66.9	1225.0 ± 72.2
b^* 800, LH	591.1 ± 22.6	638.6 ± 24.2	373.4 ± 17.9	400.6 ± 19.0
b^* 1000, LH	172.4 ± 6.2	184.0 ± 6.5	140.2 ± 5.6	165.1 ± 6.3
b^* 1100, LH	93.8 ± 3.4	98.1 ± 3.5	78.5 ± 3.1	99.1 ± 3.6
b^* 1200, LH	55.2 ± 2.0	56.8 ± 2.0	46.3 ± 1.8	53.9 ± 2.0
b^* 1300, LH	29.7 ± 1.1	31.3 ± 1.1	28.1 ± 1.1	32.1 ± 1.2
b^* 1400, LH	17.4 ± 0.6	18.4 ± 0.7	15.6 ± 0.6	18.9 ± 0.7
b^* 1600, LH	6.4 ± 0.2	6.2 ± 0.2	5.4 ± 0.2	6.6 ± 0.2
b^* 1800, LH	2.1 ± 0.1	2.1 ± 0.1	1.7 ± 0.1	2.2 ± 0.1
b^* 600, RH	1427.1 ± 77.8	1606.2 ± 84.5	1273.8 ± 74.0	1534.6 ± 82.5
b^* 800, RH	549.1 ± 21.6	554.6 ± 22.1	415.4 ± 18.7	533.0 ± 21.7
b^* 1000, RH	157.9 ± 5.9	180.7 ± 6.5	142.3 ± 5.7	180.3 ± 6.5
b^* 1100, RH	89.6 ± 3.3	90.5 ± 3.3	79.5 ± 3.1	94.1 ± 3.4
b^* 1200, RH	49.3 ± 1.8	56.4 ± 2.0	46.1 ± 1.8	56.5 ± 2.0
b^* 1300, RH	31.6 ± 1.1	32.4 ± 1.2	24.6 ± 1.0	31.0 ± 1.1
b^* 1400, RH	17.2 ± 0.6	18.5 ± 0.7	13.5 ± 0.6	18.1 ± 0.7
b^* 1600, RH	6.2 ± 0.2	6.4 ± 0.2	4.3 ± 0.2	5.9 ± 0.2
b^* 1800, RH	2.5 ± 0.1	2.5 ± 0.1	1.6 ± 0.1	2.2 ± 0.1
b^* 600, VL	2604.1 ± 100.9	2992.9 ± 110.8	2197.2 ± 93.8	2595.3 ± 103.1
b^* 800, VL	1132.5 ± 31.1	1184.7 ± 32.5	784.2 ± 25.7	929.0 ± 28.7
b^* 1000, VL	328.2 ± 8.5	362.6 ± 9.1	280.9 ± 7.9	343.7 ± 9.0
b^* 1100, VL	182.7 ± 4.7	187.8 ± 4.8	157.4 ± 4.4	192.3 ± 4.9
b^* 1200, VL	103.7 ± 2.6	112.5 ± 2.8	91.8 ± 2.5	109.7 ± 2.8
b^* 1300, VL	60.8 ± 1.5	63.0 ± 1.6	52.0 ± 1.4	62.4 ± 1.6
b^* 1400, VL	34.9 ± 0.9	37.2 ± 0.9	29.2 ± 0.8	37.3 ± 1.0
b^* 1600, VL	12.5 ± 0.3	12.6 ± 0.3	9.6 ± 0.3	12.4 ± 0.3
b^* 1800, VL	4.6 ± 0.1	4.8 ± 0.1	3.5 ± 0.1	4.6 ± 0.1
$t\bar{t}$	924.7 ± 8.9	1048.4 ± 9.6	1638.6 ± 12.1	2132.9 ± 14.2
W + light	284.1 ± 18.6	331.4 ± 21.3	228.2 ± 15.4	328.2 ± 19.0
W + c	176.1 ± 15.8	202.5 ± 17.9	211.7 ± 16.9	261.6 ± 19.5
$W + c\bar{c}$	61.2 ± 8.5	59.1 ± 8.9	59.2 ± 9.1	85.3 ± 10.9
$W + b\bar{b}$	84.1 ± 10.8	87.7 ± 10.7	83.6 ± 9.8	97.5 ± 10.9
single top	173.5 ± 10.4	189.1 ± 11.0	224.9 ± 9.8	295.7 ± 11.8
fakes	34.8 ± 2.5	27.7 ± 3.8	45.4 ± 2.6	72.3 ± 7.0
Z+jets	16.0 ± 2.7	20.5 ± 2.9	58.3 ± 5.0	65.1 ± 5.3
diboson	50.4 ± 3.6	67.2 ± 4.2	10.1 ± 1.5	13.7 ± 1.9
total SM bkg.	1802.0 ± 31.6	2033.4 ± 34.9	2553.6 ± 31.2	3346.3 ± 37.4
data	1785.0 ± 42.2	2147.0 ± 46.3	2387.0 ± 48.9	2975.0 ± 54.5

Table 6.20.: Expected event yields in the B signal regions before the fit to data. Signals are normalised to their theory cross sections. The total number of predicted SM background events and the number of data events are also presented. The uncertainties correspond to the data or MC statistical uncertainties. At this stage, none of the MC backgrounds has been scaled according to the fit in the CRs, and thus the W+jets yield is about 10% higher than the contribution after the fit in the limit setting step (compare section 6.10).

SR	FW jet, had top		FW jet, had W	
Type	e	μ	e	μ
B 600	4.7 ± 0.3	5.1 ± 0.4	2.5 ± 0.2	3.5 ± 0.3
B 650	4.4 ± 0.3	4.8 ± 0.3	2.6 ± 0.2	2.8 ± 0.2
B 700	3.5 ± 0.2	4.2 ± 0.2	2.2 ± 0.2	3.0 ± 0.2
B 750	2.9 ± 0.2	3.3 ± 0.2	1.9 ± 0.1	1.9 ± 0.1
B 800	2.5 ± 0.1	2.6 ± 0.1	1.6 ± 0.1	1.7 ± 0.1
B 850	2.0 ± 0.1	2.0 ± 0.1	1.4 ± 0.1	1.6 ± 0.1
B 900	1.5 ± 0.1	1.6 ± 0.1	1.1 ± 0.1	1.4 ± 0.1
B 950	1.2 ± 0.1	1.2 ± 0.1	0.8 ± 0.04	0.8 ± 0.04
B 1000	0.9 ± 0.04	0.9 ± 0.04	0.6 ± 0.03	0.7 ± 0.03
B 1200	0.4 ± 0.01	0.3 ± 0.01	0.2 ± 0.01	0.3 ± 0.01
$t\bar{t}$	235.0 ± 4.5	285.8 ± 5.0	344.7 ± 5.5	465.0 ± 6.6
W + light	41.8 ± 6.1	53.1 ± 8.2	49.4 ± 6.6	48.1 ± 5.8
W + c	45.6 ± 7.9	34.1 ± 7.2	36.1 ± 7.0	33.5 ± 6.8
$W + c\bar{c}$	13.4 ± 3.9	15.6 ± 5.0	12.8 ± 4.6	21.2 ± 5.6
$W + b\bar{b}$	18.3 ± 4.8	14.4 ± 4.5	7.7 ± 2.5	21.6 ± 5.2
single top	41.1 ± 5.2	45.6 ± 5.1	53.6 ± 4.6	68.9 ± 5.6
fakes	6.7 ± 1.1	10.5 ± 3.0	10.4 ± 1.2	13.8 ± 3.0
Z+jets	6.7 ± 1.4	3.5 ± 1.0	12.3 ± 2.0	13.1 ± 2.3
diboson	5.2 ± 1.1	4.1 ± 1.0	1.2 ± 0.5	1.6 ± 0.7
total SM bkg.	413.4 ± 13.8	466.8 ± 15.1	526.7 ± 13.3	685.1 ± 15.0
data	388.0 ± 19.7	468.0 ± 21.6	441.0 ± 21.0	576.0 ± 24.0

From Table 6.19 and Table 6.20 one can see, that the number of observed events in data is well in agreement with the Standard Model prediction already within the statistical uncertainties in all regions, which suggests that there is no sign of new physics phenomena in the analysed data. This seems to be confirmed for most regions by Figure 6.24. However, a small excess can be seen in the high-mass area of the b^* SR in the top category. In order to quantify that deviation and to test whether the observed data is statistically compatible with the SM background, a statistical analysis is deployed. If no significant excess is found in data, this setup can be used to set exclusion limits on the heavy quark production cross-section or other model parameters. This procedure is described in section 6.10.

6.10. Statistical Analysis and Limit Setting

As the invariant mass of the heavy quark, m_{b^*} or m_B respectively, is sensitive to resonance production of b^*/B, distributions of this variable for signal and backgrounds can be fit to the observed data in order to test for the presence of a signal. This is done via a likelihood fit using binned templates of the discriminating variable. As no significant excess of the data over the total SM background is found, the fit is used to set exclusion limits on the product $\sigma \cdot BF(b^*/B \to Wt)$ of the production cross-section of b^*/B and the branching fraction to Wt. Before presenting the results in section 6.11, the technicalities of this procedure are described in this section, starting from the construction of the likelihood function:
The expected number of events, ν_k, for signal and background process j in a single bin k can be expressed as

$$\nu_k \equiv \nu_k(\mu, \boldsymbol{\Theta}) = \mu\nu_k^{signal}(\boldsymbol{\Theta}) + \sum_j^{N_{backgrounds}} \nu_k^j(\boldsymbol{\Theta}) = \mu\nu_k^{signal}(\boldsymbol{\Theta}) + \nu_k^{background} \tag{6.8}$$

with ν_k^{signal} being the predicted number of signal events for a cross section times branching fraction of 1 pb and μ being the parameter of interest, the signal strength, measuring the the signal cross section times branching fraction in units of pb. $\boldsymbol{\Theta}$ is a vector of nuisance parameters, on which the signal and background contributions depend, as these parameters quantify the impact of the various sources of systematic uncertainties listed in section 6.7.1.

Every individual bin k can be seen as a counting experiment with an observed number of events N_k, which follows a multinomial distribution. As the total number of events is

Poisson-distributed, this is also true for the number of entries in an individual bin, N_k, which is distributed according to $Pois(N_k; \mu\nu_k^{signal} + \nu_k^{background})$, with $\nu_k^{background}$ being the total number of expected background counts in that bin. The corresponding likelihood $\mathscr{L}_k$ for ν_k expected and N_k observed events in bin k therefore is

$$\mathscr{L}_k(\mu, \boldsymbol{\Theta}) = \frac{\nu_k^{N_k} e^{-\nu_k}}{N_k!}, \tag{6.9}$$

which, by multiplying the likelihoods of all bins, yields the binned likelihood function $\mathcal{L}$:

$$\mathcal{L}(\mu, \boldsymbol{\Theta}) = \prod_k^{N_{bins}} \frac{\nu_k^{N_k} e^{-\nu_k}}{N_k!}. \tag{6.10}$$

This simple multiplicative approach is valid as the individual bins can be seen as independent experiments. As the various signal and control regions are independent from one another, the same multiplicative procedure can be used to combine their likelihood functions.

In a Bayesian approach, described in [147], a *Markov Chain Monte-Carlo* [148, p. 552] is used to estimate the posterior probability density $L(\mu)$ of the signal strength parameter and therefore on $\sigma \cdot BF(b^*/B \to Wt)$, while at the same time integrating out the nuisance parameters (a procedure known as *marginalisation*):

$$L(\mu) \propto \int_{\boldsymbol{\Theta}} \mathcal{L}(\mu, \boldsymbol{\Theta})\, \pi(\mu) \prod_i f(\Theta_i)\, d\Theta. \tag{6.11}$$

Each component of the systematic uncertainties discussed in section 6.7.1 gets assigned a nuisance parameter Θ_i. The prior probability density $f(\Theta_i)$ of each Θ_i is chosen to be a normal distribution centred around zero, $\mathcal{N}(0, 1)$, with 0 representing the nominal prediction and ± 1 the symmetric variations by one standard deviation of the systematic uncertainty. The prior probability density for the signal strength, $\pi(\mu)$, which is constrained to be positive, is taken to be uniform for $\mu \geq 0$ and zero otherwise.
To obtain the impact of the individual uncertainties, the analysis chain is re-evaluated once for the $\pm 1\sigma$ variations of each uncertainty, which is why the expected number of events $\nu_k^j(\boldsymbol{\Theta})$ is usually only known for the nominal value ($\boldsymbol{\Theta} = (0, ..., 0)$) and the $\pm 1\sigma$ variations ($\boldsymbol{\Theta} = (0, ..., 0, \pm 1, 0, ...0)$). Inter- and extrapolation strategies are used to obtain values in between and outside these points. Technically, the likelihood function was defined using

`RooStats` [149] and the integration over the nuisance parameters was carried out in the `Bayesian Analysis Toolkit` [150].

A Bayesian one-sided 95% credibility level (C.L.) exclusion limit on the signal strength, μ_{up}^{lim}, can be derived by integrating over the posterior density:

$$\int_0^{\mu_{up}^{lim}} L(\mu)\, d\mu = 0.95. \tag{6.12}$$

This step can be done for different fits in order to obtain different kinds of results. A fit of the signal-plus-background hypothesis to data yields the observed limit, while fitting this hypothesis to the nominal background expectation yields the expected limit. This latter step is usually done using large-statistics pseudo data, which is time- and CPU-intense. A less time-consuming procedure with an equally high precision as throwing pseudo experiments, is to use an asymptotic approximation (Asimov data [151]) instead, which means setting the observed number of events in a given bin in equation 6.8 to the expected one, while setting signal strength and nuisance parameters to zero: $N_k = \nu_k(\mu = 0, \boldsymbol{\Theta} = 0)$. An individual fit is performed for each signal hypothesis, i.e. for a fixed mass and coupling scenario, such that a value μ_{up}^{lim} is obtained for every simulated signal point. The uncertainties on the expected number of events per bin are propagated to μ via the nuisance parameters, resulting in a reduced limit.

As the control regions described in section 6.6 are defined such that the signal content is suppressed, they can be used to improve the background prediction and to constrain the associated systematic uncertainties. This is accomplished by fitting the background-only ($\mu = 0$) hypothesis to observed data in these regions. The uncertainty, of which the associated nuisance parameter gets most constrained, is the W+jets background normalisation, which is reduced to about 10% from its original size of about 40%. The largest uncertainties after the fit are stemming from JES, b-tagging, and the background normalisation, the latter one being dominant for small masses. After this fitting step, post-fit event yields can be computed. The expected yield for process j in region k is given by the expectation value of $\nu_k^j(\boldsymbol{\Theta})$ over the posterior sample and the associated error by the standard deviation. Table 6.21 summarises these numbers and Table 6.22 lists the ratio of post-fit

over pre-fit yields for the various processes. Please note that the expectations for the individual background contributions are highly correlated, leading to large uncertainties for the single components as there is no sensitivity for the individual fractions, while the total number of expected background events is constrained by data, such that its uncertainty is approximately the square root. One can use the information on the changed background normalisation as well, together with the set of updated nuisance parameters, for producing post-fit plots of various distributions in order to thoroughly check the agreement of of the observed data with the prediction after the fit. The ones for the invariant mass are shown in Figure 6.25. The updated background prediction is also used to quantify deviations of the observed data from the expectation. This is done using a moving-window algorithm [152], which leads to the result that the maximum local deviation can be found in the last bin of the top b^* signal region (Figure 6.25(a)) and amounts to 1.4 standard deviations [119].

It should be noted that the final fits, opposed to what is suggested above and as a result of an iterative procedure to make sure there is no significant deviation from the SM expectation, are performed in all signal and control regions (as introduced in section 6.6) simultaneously. This stabilises the nuisance parameters in the fits of the signal-plus-background hypothesis to (Asimov) data and can be used as a cross check whether the background is equally well modelled in signal and control regions in the fit of the background-only hypothesis to data.

The results of the fits of the signal-plus-background hypothesis can be interpreted in terms of exclusion of a certain parameter space of the given model. In this case, as stated earlier, the cross section of the process $pp \to b^*/B \to Wt$ is used dependent on the mass of the heavy quark, while interpolating between the simulated signal mass points. The region where the observed limit on the product of production cross-section and branching fraction, which is derived by the fit to real data, is smaller than the theoretical prediction is then excluded, such that a limit on the cross section translates into a limit on the mass. Graphical representations of this relation for the different models are shown in the next section[4]. As a cross check, the fits have been performed in the electron and muon channel individually. The results are comparable between the channels and none of the channels separately shows major deviations of the observed data from the SM background, such that the strategy to analyse them together was kept.

[4]The limits and the corresponding plotting code were kindly provided by the University of Bonn group [153].

Process	b^*, top	b^*, W	B, top	B, W
$t\bar{t}$	1863 ± 60	3390 ± 120	483 ± 27	746 ± 34
single t	368 ± 33	520 ± 40	94 ± 13	125 ± 13
W+jets	1360 ± 140	1290 ± 120	220 ± 40	152 ± 27
QCD multijet	60 ± 40	100 ± 40	18 ± 11	27 ± 14
WW, WZ, ZZ, Z+jets	230 ± 100	180 ± 50	22 ± 7	30 ± 11
signal m_{b^*}=600 GeV	5800 ± 270	4890 ± 230	-	-
signal m_{b^*}=800 GeV	2240 ± 90	1640 ± 70	-	-
signal m_{b^*}=1000 GeV	661 ± 30	591 ± 26	-	-
signal m_{b^*}=1200 GeV	209 ± 10	196 ± 10	-	-
signal m_{b^*}=1400 GeV	68.5 ± 3.2	63.4 ± 3.1	-	-
signal m_{b^*}=1600 GeV	23.8 ± 1.2	21.2 ± 1.0	-	-
signal m_B=600 GeV	-	-	22.4 ± 2.2	13.4 ± 1.5
signal m_B=800 GeV	-	-	11.1 ± 0.7	7.3 ± 0.5
signal m_B=1000 GeV	-	-	3.62 ± 0.29	2.78 ± 0.16
total SM bkg.	3881 ± 70	5480 ± 70	837 ± 34	1080 ± 35
data	3933	5380	856	1017

Table 6.21.: Predicted post-fit event yields for the background processes and various b^* and B signal masses in the various signal regions. The uncertainties (RMS of the respective posterior distribution) comprise theoretical, statistical and systematic uncertainties. The fact that the uncertainties on the single background components are large compared to the uncertainty on the total number of background events is a common feature of profile-likelihood fits. The expected number of total background events is constrained by data, so the associated uncertainty is of the order of its square root. However, the numbers for the individual components are (anti-) correlated, which leads to the large uncertainties. The numbers for the signal models have been evaluated with the signal strength fixed according to the respective theoretical cross sections (for $\lambda = 2$ in the B case and $f_g = f_L = f_R = 1$ in the b^* case). The factors by which the yields have changed due to the fit can be found in Table 6.22.

Process	b^*, top	b^*, W	B, top	B, W
	SR			
$t\bar{t}$	0.94±0.03	0.90±0.03	0.93±0.05	0.92±0.04
single t	1.01±0.09	1.00±0.08	1.09±0.15	1.02±0.11
W+jets	1.05±0.11	0.94±0.09	0.92±0.17	0.65±0.11
QCD multijet	1.00±0.61	0.87±0.35	1.04±0.64	1.13±0.56
Z+jets, diboson	1.51±0.63	1.25±0.32	1.15±0.38	1.07±0.40
	$t\bar{t}$ CR			
$t\bar{t}$	1.02±0.06	0.92±0.02	0.89±0.09	0.89±0.04
single t	1.11±0.16	0.98±0.08	1.03±0.23	0.89±0.11
W+jets	1.24±0.33	1.10±0.25	1.01±0.53	0.66±0.22
QCD multijet	1.98±1.00	1.16±0.83	1.72±1.00	1.91±1.30
Z+jets, diboson	1.60±0.76	1.35±0.41	0.98±0.42	0.93±0.47
	W+jets CR			
$t\bar{t}$	0.90±0.05	0.87±0.06	0.97±0.07	0.99±0.08
single t	1.01±0.10	0.97±0.10	1.02±0.17	1.14±0.25
W+jets	0.91±0.04	0.84±0.04	0.90±0.05	0.79±0.07
QCD multijet	0.32±0.31	0.45±0.28	0.79±0.47	0.95±0.37
Z+jets, diboson	1.38±0.44	1.16±0.33	1.12±0.31	1.08±0.36

Table 6.22.: Ratio of the event yields after and before the fit of the background-only hypothesis to real data for the b^* and B signal regions and the corresponding $t\bar{t}$ and W+jets control regions. For convenience, the small backgrounds (Z+jets and diboson production) are merged.

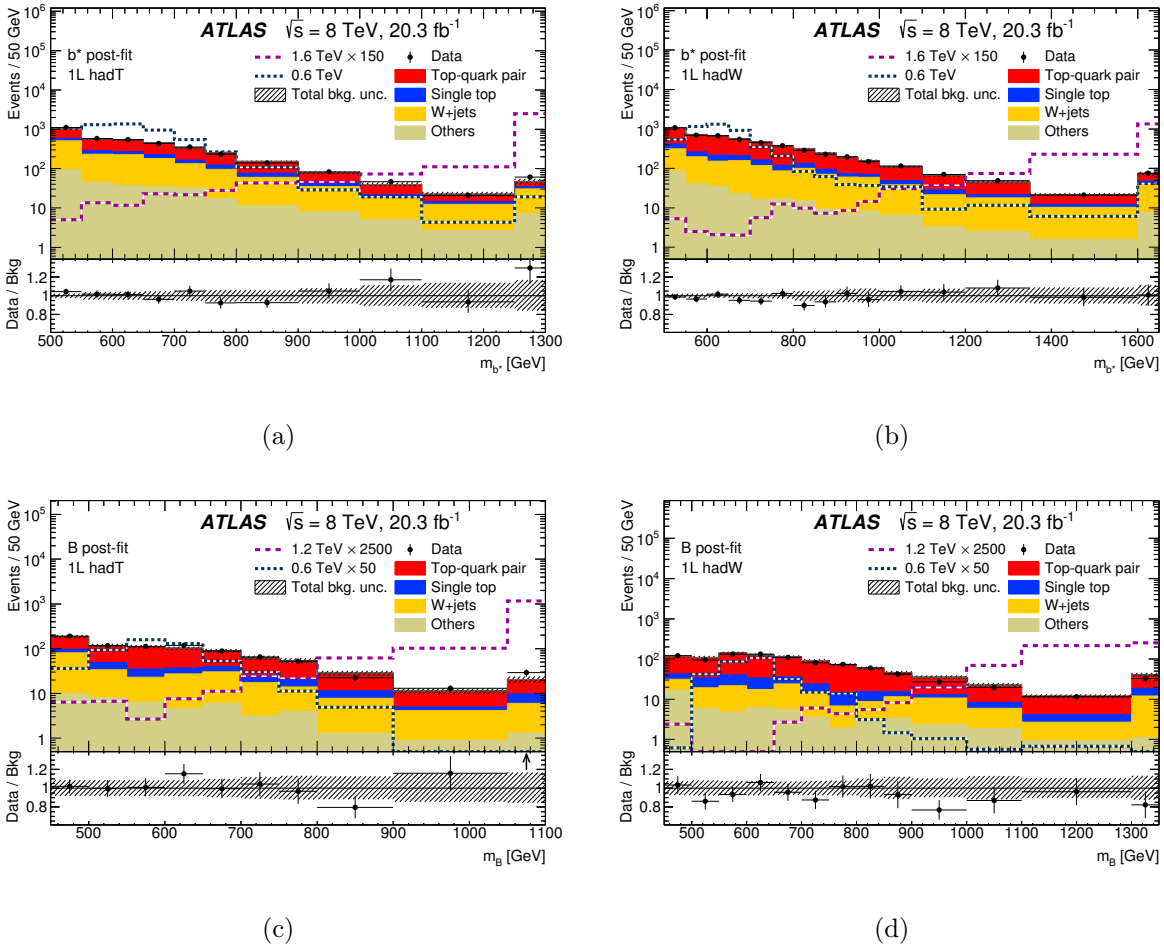

Figure 6.25.: Distributions of the discriminating variable in the b^* (top) and B (bottom) signal regions after the fit to data. The background normalisation is updated according to the fit and the uncertainty band is updated with the constrained nuisance parameters. "Others" refers to the remaining background contributions from Z+jets, diboson and QCD multijet production. The first and last bins contain under- and overflow, respectively [119].

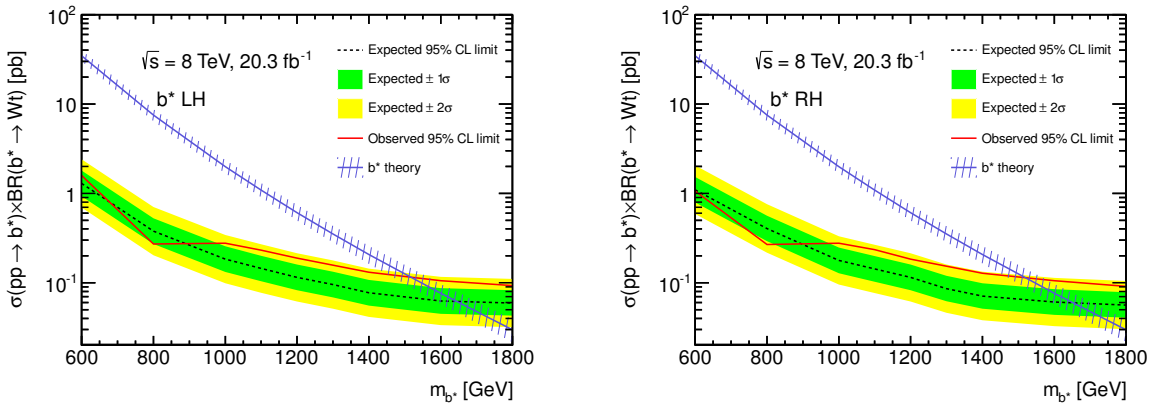

(a) (b)

Figure 6.26.: Mass-dependent cross-section limits for purely left-handed (a) and purely right-handed (b) b^* signals for the single-lepton analysis. The observed (expected) mass limit is 1517 GeV (1644 GeV) for purely left-handed and 1519 GeV (1652 GeV) for purely right-handed couplings. Details on the model and cross-section numbers to produce the theory line can be found in section 2.2.1 in Chapter 2.

6.11. Results

The results for the b^* case are shown in Figure 6.26 for purely left-handed and purely right-handed couplings and in Figure 6.27 for the vector-like coupling scenario of $f_g = f_L = f_R = 1$ as well as for the B case in Figure 6.28.

The dashed line shows the expected limit, the green and yellow bands are the 1σ and 2σ bands estimated to be $\mu_{up\pm N} = \mu_{up}^{exp}\left(\Phi^{-1}\left(1 - 0.05\Phi\left(\pm N\right)\right) \pm N\right)$ [154] with $N = 1\sigma \cdot BF$, $2\sigma \cdot BF$. The red line shows the observed limit. In the absence of a signal and for very high data and MC statistics, the observed limit line should be identical to the expected one. However, the strong selection cuts leave us with low data statistics, such that fluctuations play a role. This can be seen e.g. in the high-mass region (above ∼1100 GeV) in Figure 6.26, where the observed limit is slightly worse than the expected one, because the corresponding fits are sensitive to the above mentioned small excess in the last bin of the top signal region (of 1.4 standard deviations).

The observed (expected) limit on the heavy quark mass is given by the intersection points of the line of the theoretical cross section, shown in blue hashed, with the observed

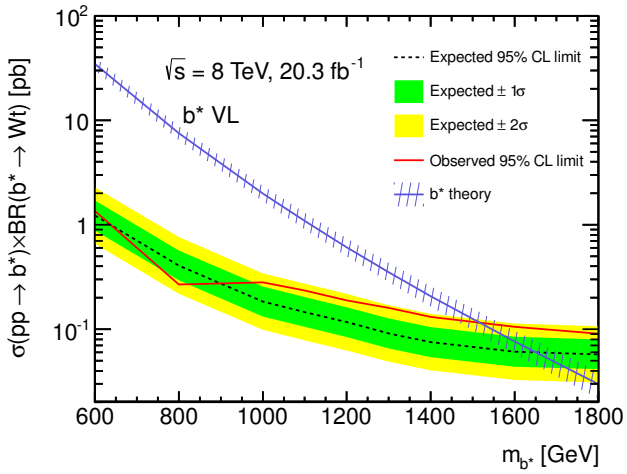

Figure 6.27.: Mass-dependent cross-section limits for b^* signals with vector-like couplings for the single-lepton analysis. The observed (expected) mass limit is 1517 GeV (1652 GeV). Details on the model and cross-section numbers to produce the theory line can be found in section 2.2.1 in Chapter 2.

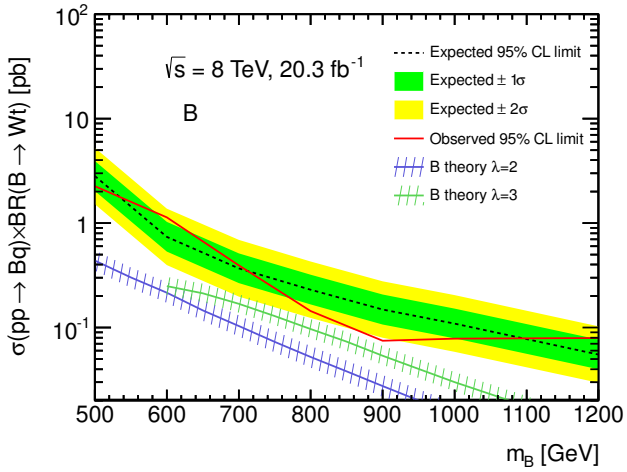

Figure 6.28.: Mass-dependent cross-section limits for B signals for the single-lepton analysis. A mass limit cannot be set for either of the coupling strength values λ. Cross sections for $\lambda > 3$ were not taken into account for the interpretation as in this region the decay width is no longer small compared to the experimental resolution, while the MC signal samples were produced with narrow-width approximation (as discussed in section 6.1). Details on the model and cross-section numbers to produce the theory line can be found in section 2.2.1 in Chapter 2.

(expected) limit of b^* production with subsequent decay to a W boson and a top quark. The observed (expected) mass limits are 1517 GeV (1652 GeV) for vector-like, 1517 GeV (1644 GeV) for purely left-handed and 1519 GeV (1652 GeV) for purely right-handed couplings. A comparison to the results of the preceding search on the 7 TeV data set shows that optimising the search strategy for boosted scenarios in the single-lepton channel has a large impact on the result. The observed mass limit for the purely left-handed coupling scenario is superseded by roughly 700 GeV in this search (no limit was provided for the vector-like coupling scenario in the single-lepton channel in the preceding search). It should also be noted that the combined observed limit from single- and dilepton searches for b^* as published in [119] is dominated by the single-lepton results in the high-mass region (The combined observed mass limit is 1.5 TeV [119]).

As one can see from Figure 6.28, the search is at the edge of sensitivity for the B model described in section 2.2.1, which is why the limits on the product of cross section and branching fraction to Wt can not be translated into mass limits for any of the investigated model parameters λ.

Chapter 7.

Summary and Outlook

In this thesis, a search for single production of two different new heavy down-type quarks, B and b^*, with vector-like couplings to W bosons in the decay channel to W bosons and top quarks has been presented, and the models predicting them as well as the instrumentation, simulation, reconstruction and analysis strategy used in this analysis have been described. No significant excess over the SM background has been found, and exclusion limits on the product of production cross-section and branching fraction to Wt have been derived for a wide range of signal masses. The observed mass limits for b^* in the single-lepton final-state search presented here of 1517 GeV to 1519 GeV (depending on the chosen coupling scenario) exceed the ones from the preceding search for b^* by ∼700 GeV, which is partly due to the slightly higher centre-of-mass energy and larger data set (20.3 fb^{-1} at $\sqrt{s} = 8$ TeV compared to 4.7 fb^{-1} at $\sqrt{s} = 7$ TeV), but can mainly be attributed to the exploitation of the large-R jets in the single-lepton search. This approach yields higher sensitivity for larger signal masses, as high-p_T large-R jets are well suited to detect the boosted W bosons and top quarks from b^*/B decays. The limits are very close to the mass limits for the b^* quark that were recently published by the CMS collaboration [10]. For B, the presented search is the first one to be carried out in the single-production mode. The sensitivity at $\sqrt{s} = 8$ TeV was not sufficient to translate the cross-section limits into mass limits, even when making use of the boosted topology. In the ongoing data taking period, however, at a centre-of-mass-energy of $\sqrt{s} = 13$ TeV, this will be different, as detailed in the next section.

7.1. Prospects for LHC Run 2

As the search for b^* and B on the 8 TeV data set yields good results, a similar analysis will also be carried out on the data set being collected at the moment with the higher centre-of-mass energy of $\sqrt{s} = 13\,\text{TeV}$ in the course of a succeeding PhD thesis at HU Berlin. Some improvements to the search strategy are currently being tested, like replacing large-R jets by groups of small-R jets, in order to eliminate unwanted correlations between the systematic uncertainties of the different jet collections (as discussed in section 6.4.2). The already quite high exclusion limits for the b^* model are expected to be superseded with the data being collected in 2015 and 2016, if no excess of the Standard Model background can be found in this run either. As the cross sections of the signal processes scale with increasing centre-of-mass energy with higher factors than the background processes, especially in the B case, for which so far no mass limit could be set, the results are expected to be improved. A back-of-the-envelope calculation based on the expected event yields for signal and background processes as listed in table 6.20 predicts that an integrated luminosity of about $9\,\text{fb}^{-1}$ will suffice for a claim of evidence (3σ or p-value of 0.003) for a B with a mass of 600 GeV, as the $t\bar{t}$ cross-section (as the main background component) roughly scales with a factor of 3 [155], while the B signal cross-section for that lowest mass point under investigation scales with a factor of 4 [40]. According to current plans, this goal will be achievable within the year 2016. For higher B masses, the cross sections scale more strongly with the increase in centre-of-mass energy, such that already a smaller data set will be sufficient for statistically significant results concerning this model. In addition, it will also be possible to investigate coupling scenarios for $\lambda > 3$, as future Monte-Carlo signal samples will either be produced taking into account the large width corresponding to higher λ values or containing enough statistics, such that a reweighting from a narrow width to the proper one is possible at a later stage of the analysis. This will further increase the sensitivity due to the larger cross sections for higher λ values. Promising results can thus be expected for the B analysis at a centre-of-mass energy of $\sqrt{s} = 13\,\text{TeV}$.

Appendix

Appendix A.

Additional Decay Kinematics Distributions of b^* and B quarks

Figure A.1 and figure A.2 show MC truth-based comparisons of b^* (purely left-handed and purely right-handed coupling) and B decay kinematics for a simulated signal mass of 1300 GeV. No significant difference can be seen, which once again motivates the strategy of a common search for both models.

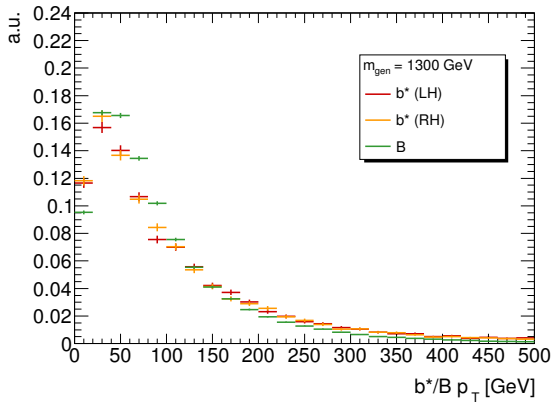

(a) Heavy quark p_T

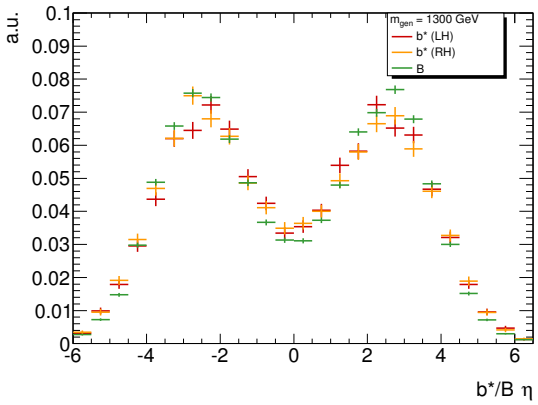

(b) Heavy quark η

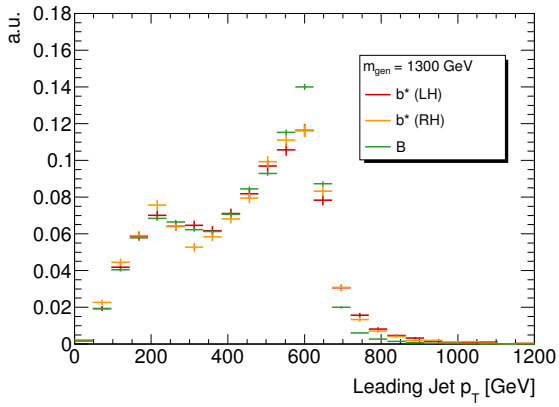

(c) Leading jet p_T

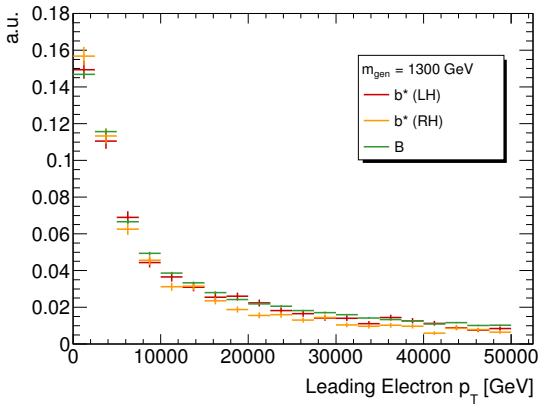

(d) Electron p_T

Figure A.1.: Distributions of the truth information on p_T and η of the heavy quark (top row) and the leading jet and electron p_T (bottom row) for simulated b^* and B signals with a mass of 1300 GeV.

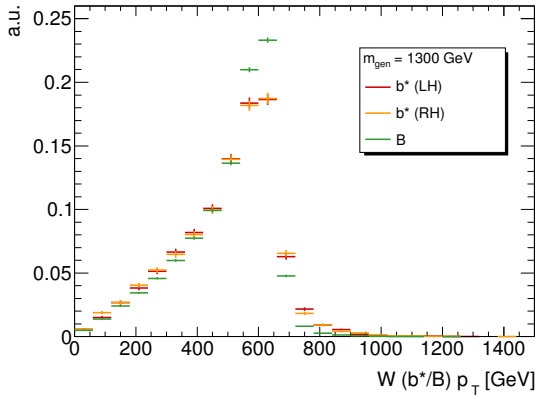

(a) W p_T

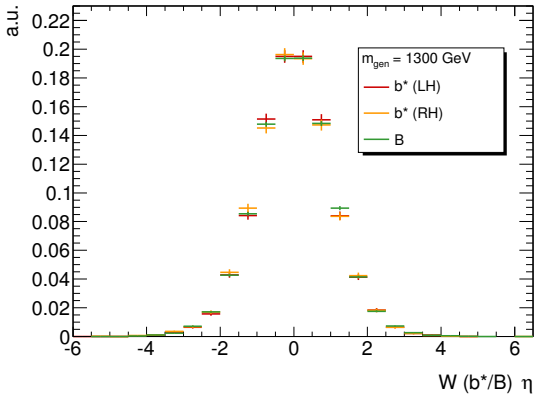

(b) W η

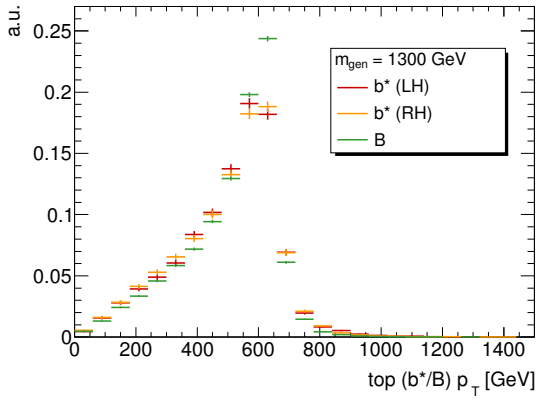

(c) top p_T

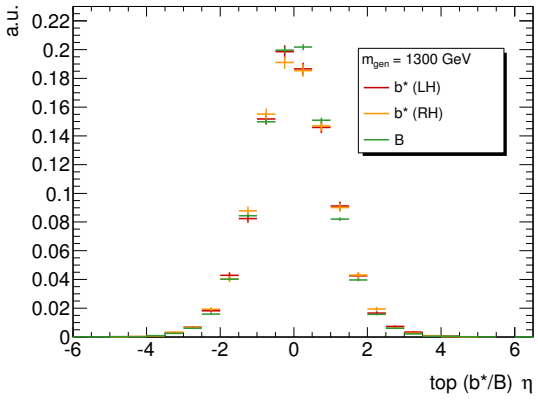

(d) top η

Figure A.2.: Distributions of the truth information on p_T and η of the heavy quark decay products, W (top row) and top (bottom row), for simulated b^* and B signals with a mass of 1300 GeV.

Appendix B.

Distributions for Electron and Muon Channel

B.1. Only Statistical and Theory Uncertainties

In the following, the distributions that were shown in section 6.6 for electron and muon channel merged, are shown for e+jets and μ+jets separately. One can see that not all differences between data and MC are covered by the uncertainty band. The same distributions taking into account also systematic uncertainties can be found in the next section.

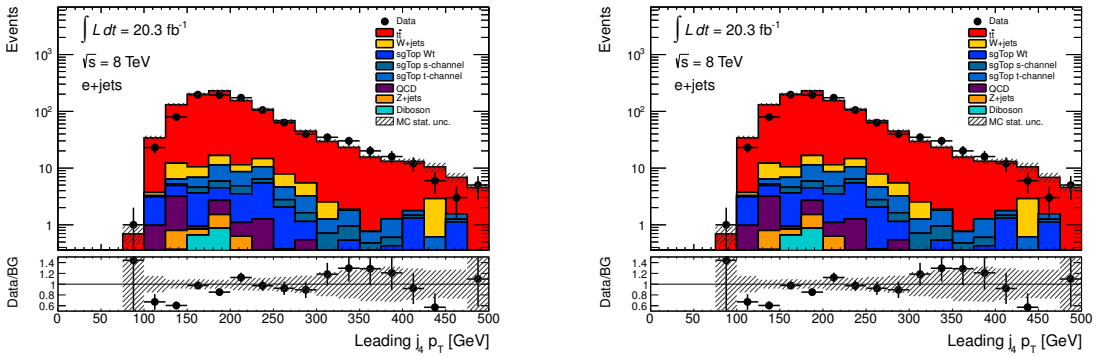

(a) b^* $t\bar{t}$ CR, top

(b) b^* $t\bar{t}$ CR, W

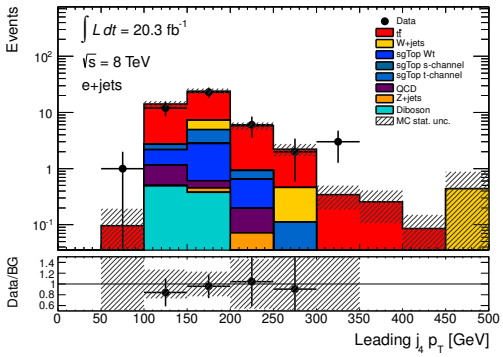

(c) B $t\bar{t}$ CR, top

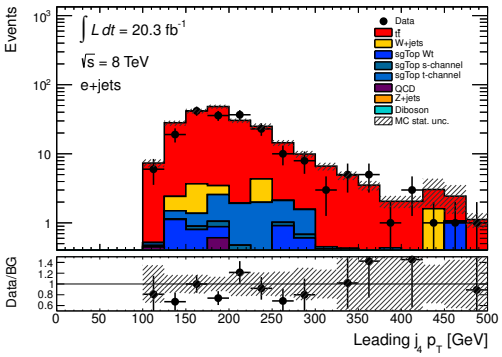

(d) B $t\bar{t}$ CR, W

Figure B.1.: Leading jet p_T distributions for data and the various SM backgrounds in the $t\bar{t}$ CR in the e+jets channel. The error band only shows the theory and Monte-Carlo statistical uncertainty. For plots with systematic uncertainties included, please refer to section B.2.

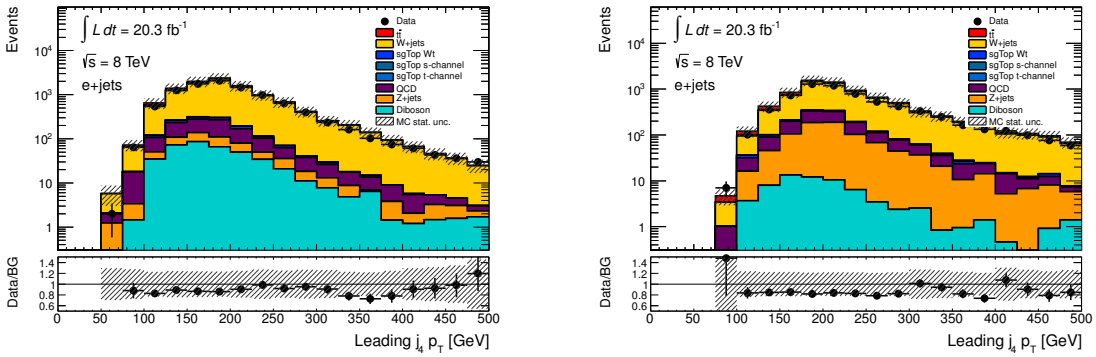

(a) b^* W+jets CR, top

(b) b^* W+jets CR, W

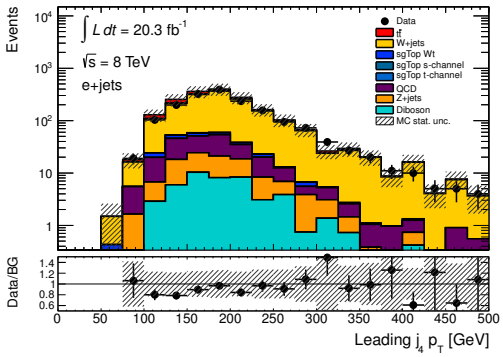

(c) B W+jets CR, top

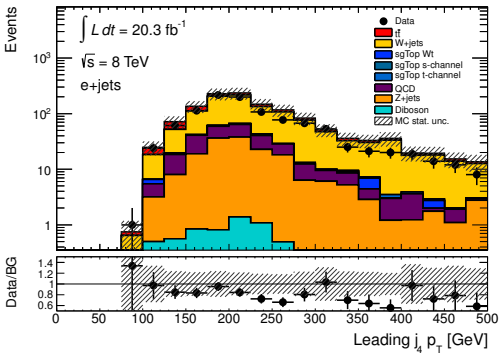

(d) B W+jets CR, W

Figure B.2.: Leading jet p_T distributions for data and the various SM backgrounds in the W+jets CR in the e+jets channel. The error band only shows the theory and Monte-Carlo statistical uncertainty. For plots with systematic uncertainties included, please refer to section B.2.

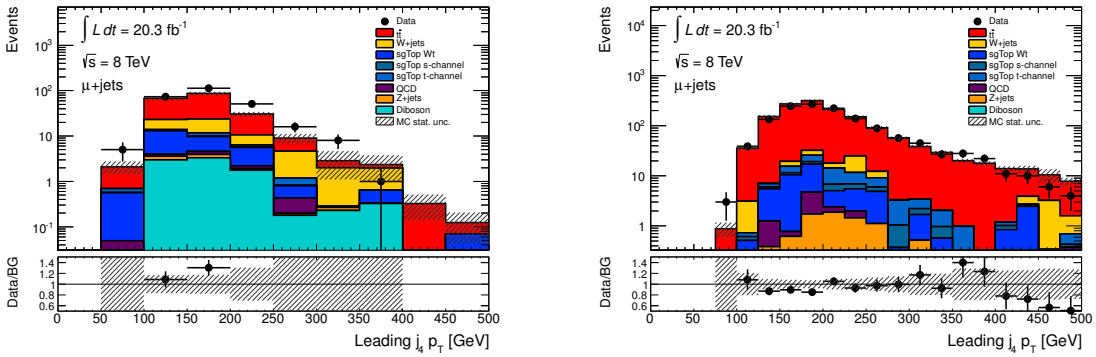

(a) b^* $t\bar{t}$ CR, top

(b) b^* $t\bar{t}$ CR, W

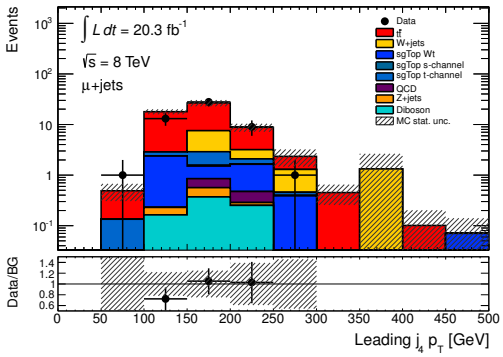

(c) B $t\bar{t}$ CR, top

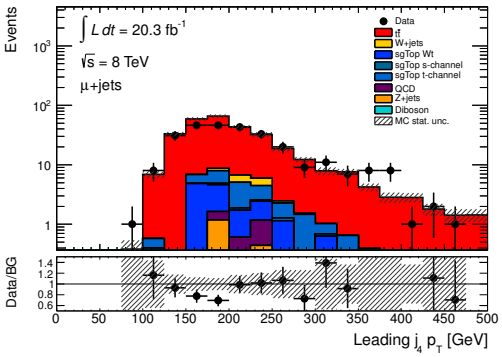

(d) B $t\bar{t}$ CR, W

Figure B.3.: Leading jet p_T distributions for data and the various SM backgrounds in the $t\bar{t}$ CR in the μ+jets channel. The error band only shows the theory and Monte-Carlo statistical uncertainty. For plots with systematic uncertainties included, please refer to section B.2.

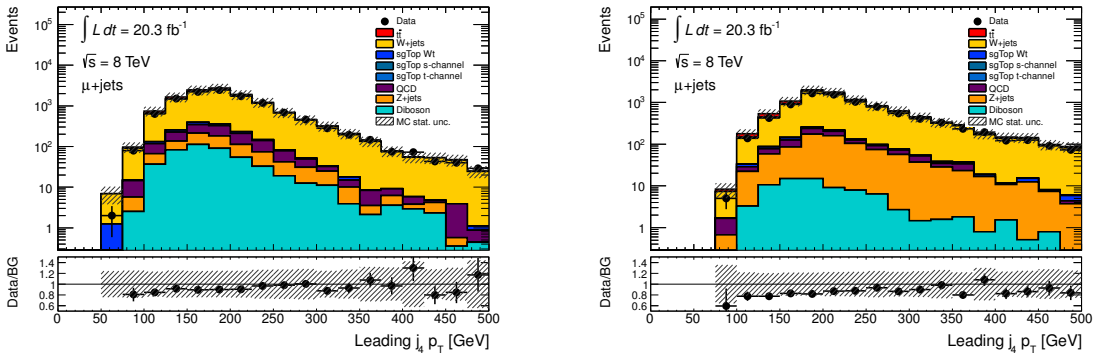

(a) b^* W+jets CR, top

(b) b^* W+jets CR, W

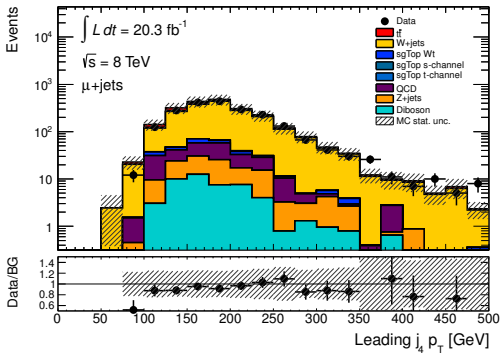

(c) B W+jets CR, top

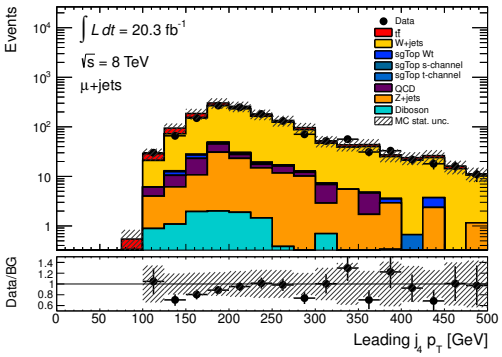

(d) B W+jets CR, W

Figure B.4.: Leading jet p_T distributions for data and the various SM backgrounds in the W+jets CR in the μ+jets channel. The error band only shows the theory and Monte-Carlo statistical uncertainty. For plots with systematic uncertainties included, please refer to section B.2.

B.2. Statistical, Theory and Systematic Uncertainties

This section contains distributions for data and the various SM background components for e+jets and μ+jets channel separately in order to complement the merged channels distributions in section 6.8. The error band includes the theory, statistical and all systematic uncertainties listed in section 6.7.1, unconstrained, before fitting the background to data in the control regions. None of the distributions shows significant differences between the observed data and the total SM background.

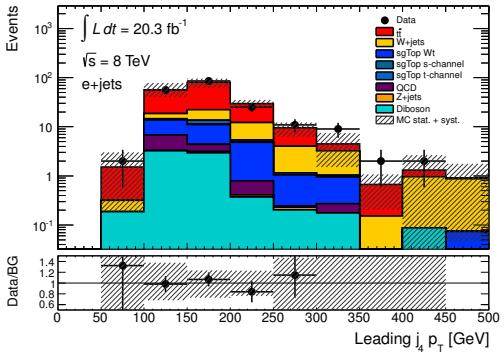

(a) b^* $t\bar{t}$ CR, top

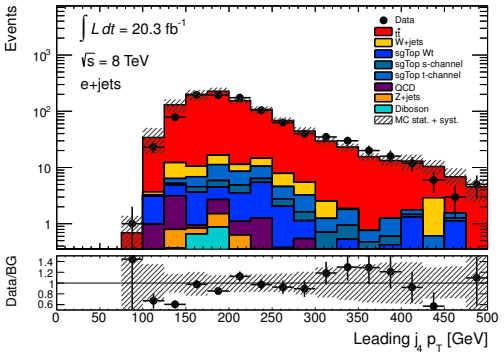

(b) b^* $t\bar{t}$ CR, W

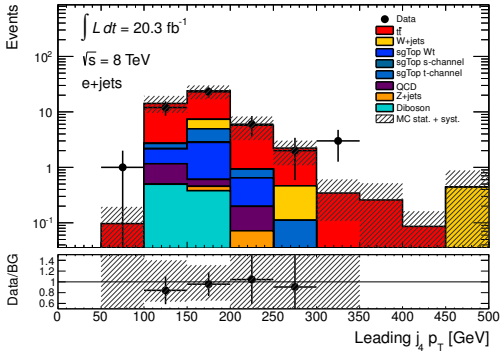

(c) B $t\bar{t}$ CR, top

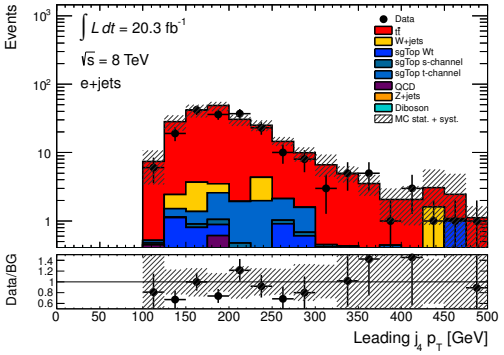

(d) B $t\bar{t}$ CR, W

Figure B.5.: Leading jet p_T distributions for data and the various SM backgrounds in the $t\bar{t}$ CR in the e+jets channel. The error band includes the theory and MC statistical uncertainty and all systematic uncertainties mentioned in section 6.7.1.

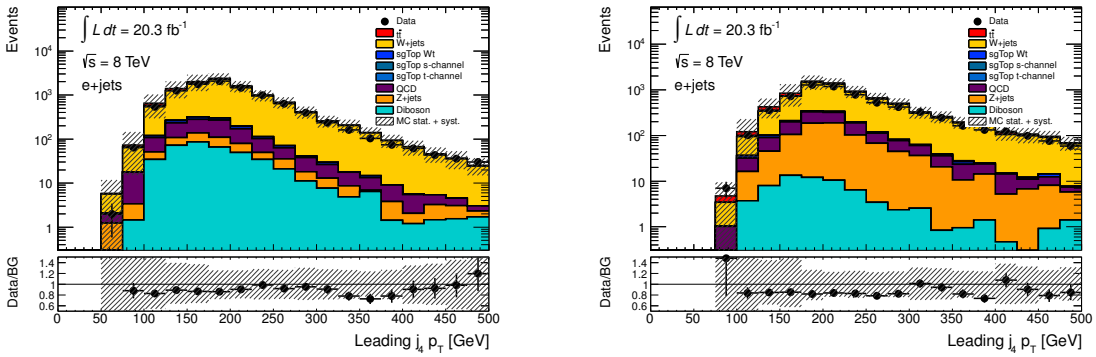

(a) b^* W+jets CR, top

(b) b^* W+jets CR, W

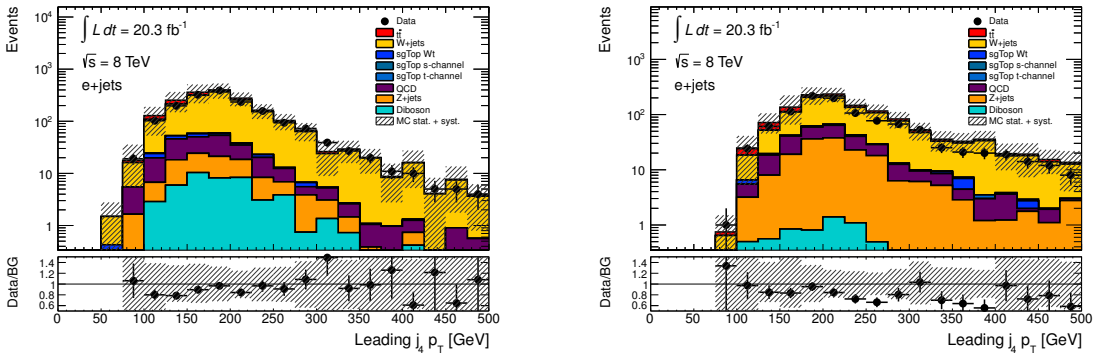

(c) B W+jets CR, top

(d) B W+jets CR, W

Figure B.6.: Leading jet p_T distributions for data and the various SM backgrounds in the W+jets CR in the e+jets channel. The error band includes the theory and MC statistical uncertainty and all systematic uncertainties mentioned in section 6.7.1.

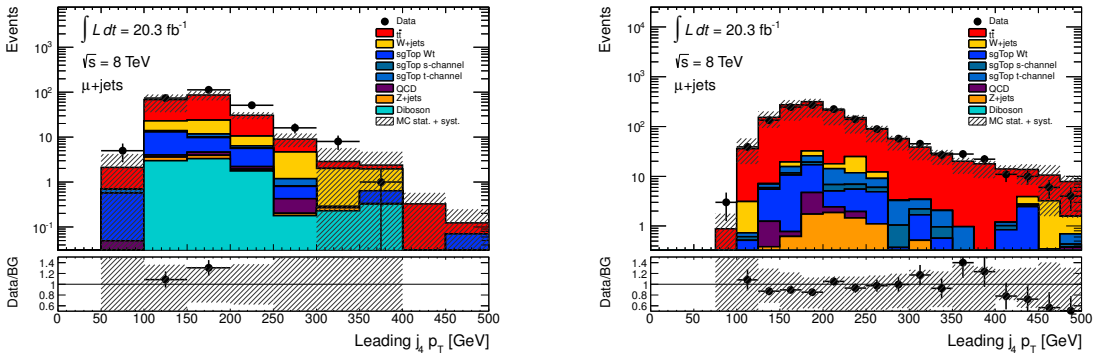

(a) b^* $t\bar{t}$ CR, top

(b) b^* $t\bar{t}$ CR, W

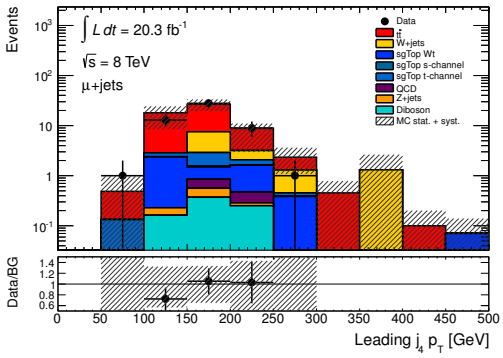

(c) B $t\bar{t}$ CR, top

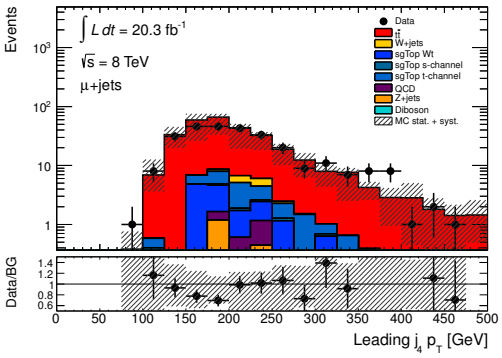

(d) B $t\bar{t}$ CR, W

Figure B.7.: Leading jet p_T distributions for data and the various SM backgrounds in the $t\bar{t}$ CR in the μ+jets channel. The error band includes the theory and MC statistical uncertainty and all systematic uncertainties mentioned in section 6.7.1.

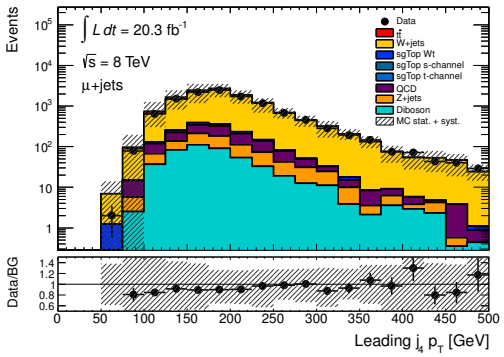

(a) b^* W+jets CR, top

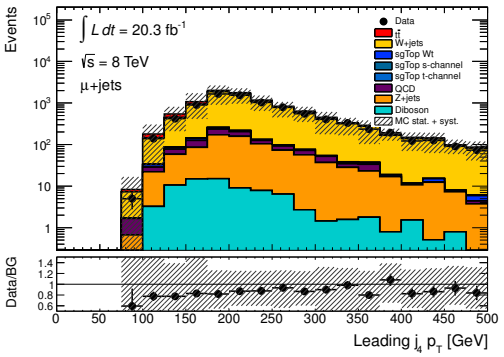

(b) b^* W+jets CR, W

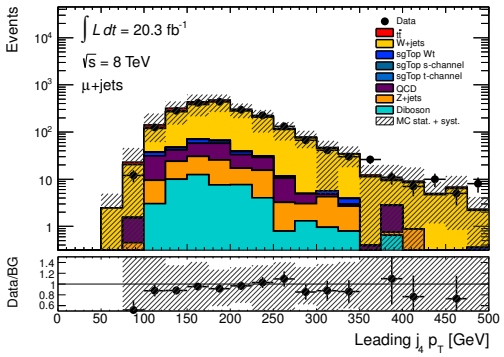

(c) B W+jets CR, top

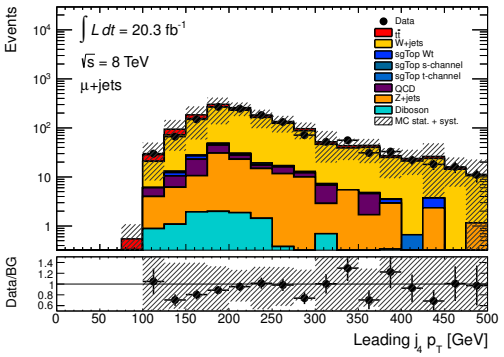

(d) B W+jets CR, W

Figure B.8.: Leading jet p_T distributions for data and the various SM backgrounds in the W+jets CR in the μ+jets channel. The error band includes the theory and MC statistical uncertainty and all systematic uncertainties mentioned in section 6.7.1.

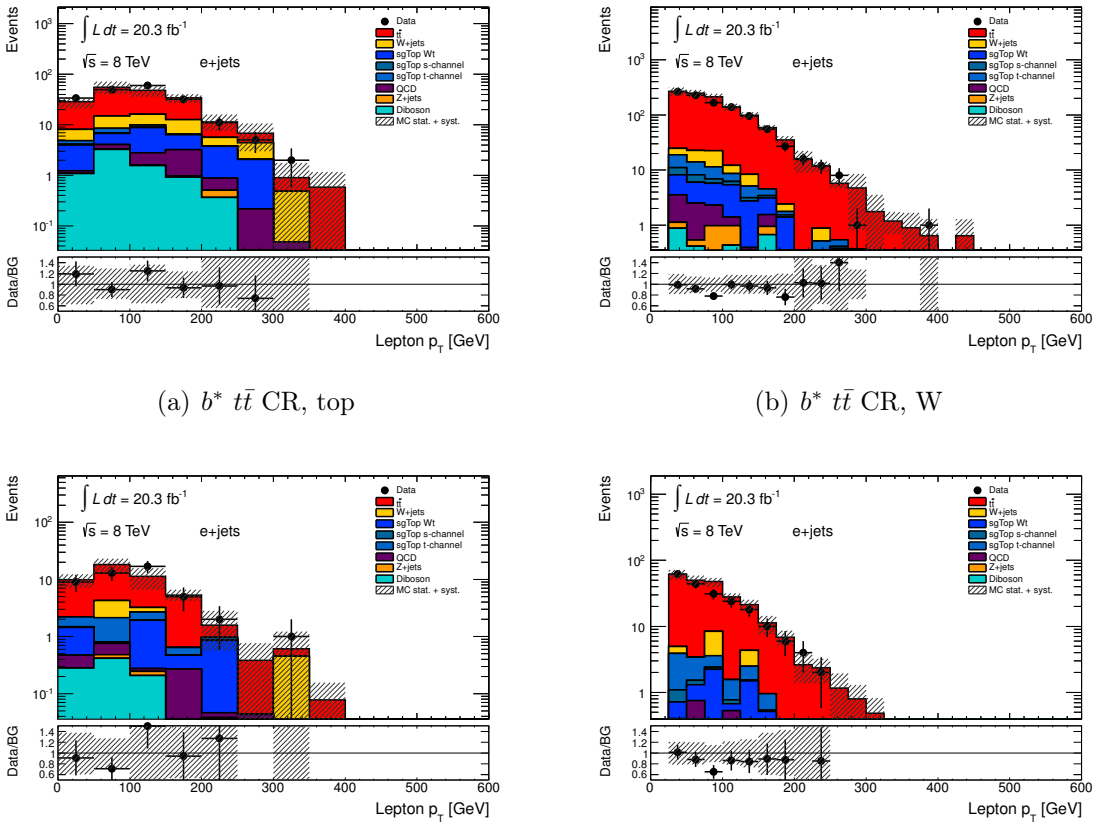

(a) b^* $t\bar{t}$ CR, top

(b) b^* $t\bar{t}$ CR, W

(c) B $t\bar{t}$ CR, top

(d) B $t\bar{t}$ CR, W

Figure B.9.: Lepton p_T distributions for data and the various SM backgrounds in the $t\bar{t}$ CR in the e+jets channel. The error band includes the theory and MC statistical uncertainty and all systematic uncertainties mentioned in section 6.7.1.

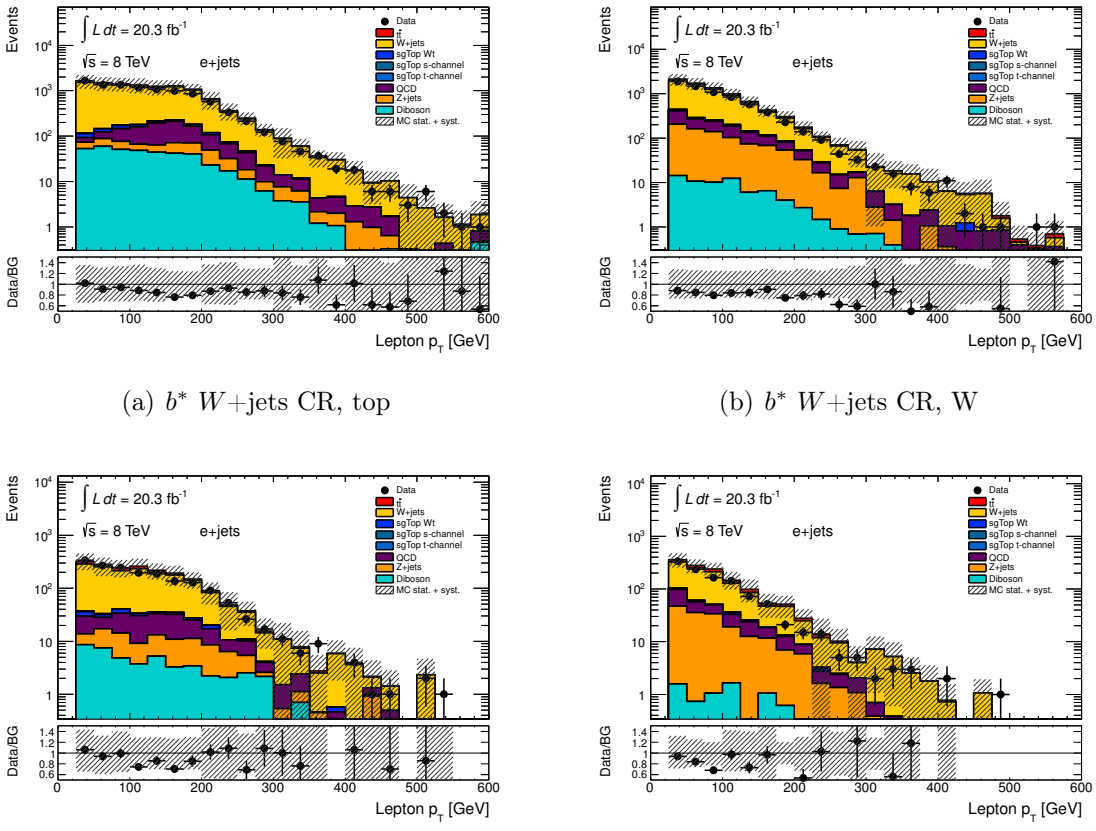

(a) b^* W+jets CR, top

(b) b^* W+jets CR, W

(c) B W+jets CR, top

(d) B W+jets CR, W

Figure B.10.: Lepton p_T distributions for data and the various SM backgrounds in the W+jets CR in the e+jets channel. The error band includes the theory and MC statistical uncertainty and all systematic uncertainties mentioned in section 6.7.1.

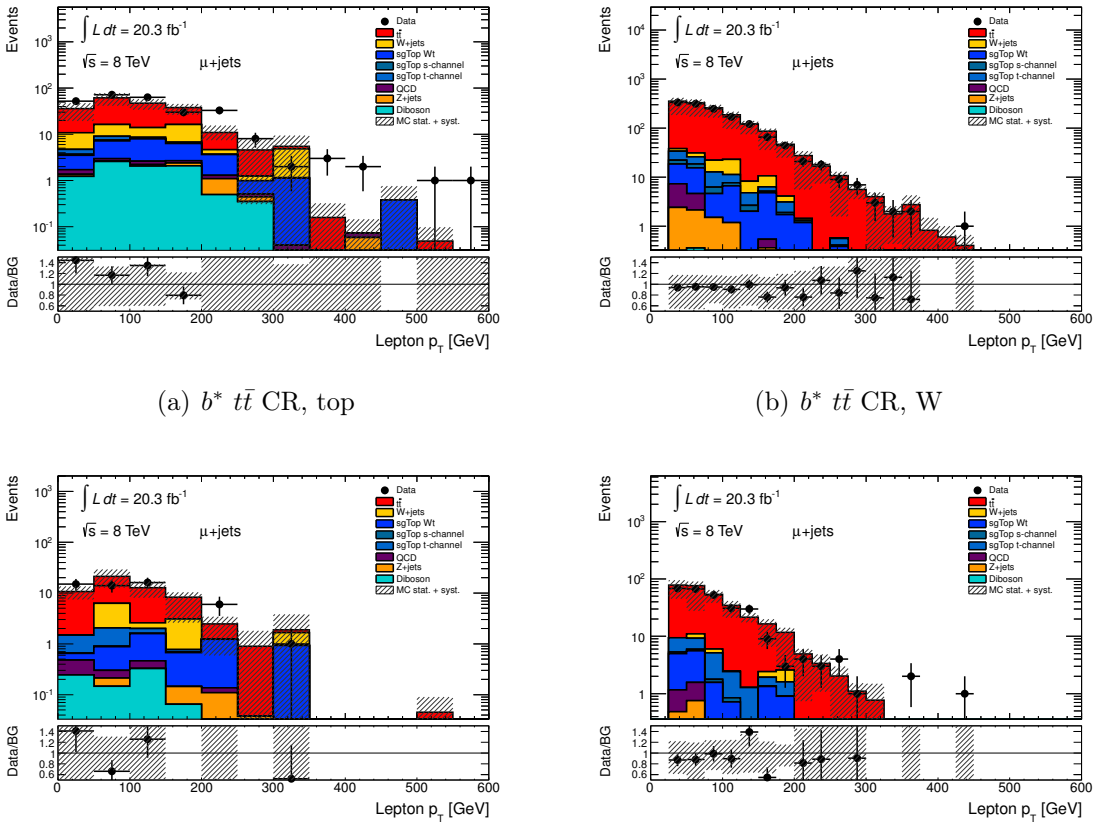

(a) b^* $t\bar{t}$ CR, top

(b) b^* $t\bar{t}$ CR, W

(c) B $t\bar{t}$ CR, top

(d) B $t\bar{t}$ CR, W

Figure B.11.: Lepton p_T distributions for data and the various SM backgrounds in the $t\bar{t}$ CR in the μ+jets channel. The error band includes the theory and MC statistical uncertainty and all systematic uncertainties mentioned in section 6.7.1.

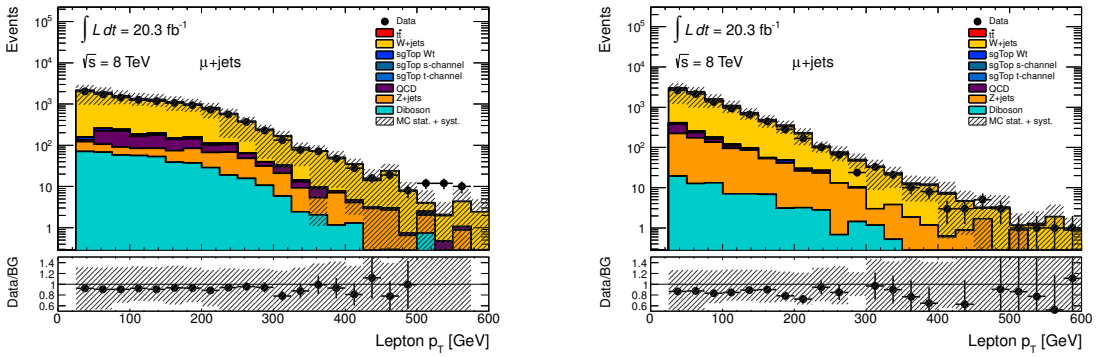

(a) b^* W+jets CR, top

(b) b^* W+jets CR, W

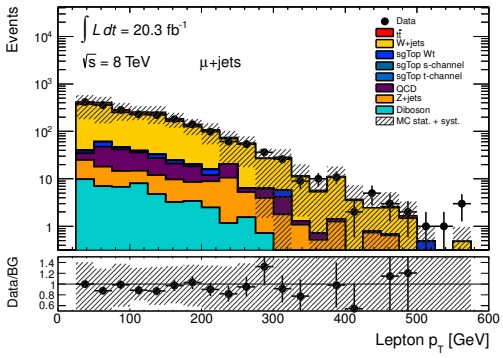

(c) B W+jets CR, top

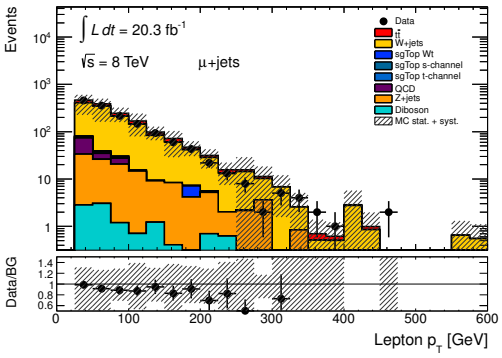

(d) B W+jets CR, W

Figure B.12.: Lepton p_T distributions for data and the various SM backgrounds in the W+jets CR in the μ+jets channel. The error band includes the theory and MC statistical uncertainty and all systematic uncertainties mentioned in section 6.7.1.

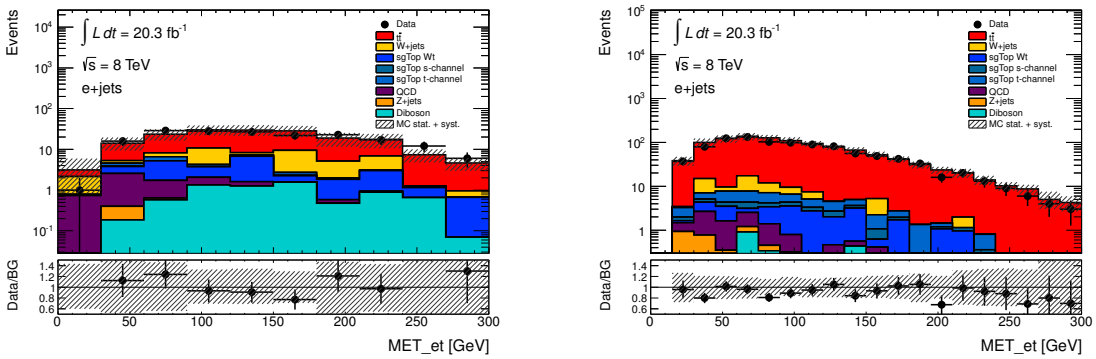

(a) b^* $t\bar{t}$ CR, top

(b) b^* $t\bar{t}$ CR, W

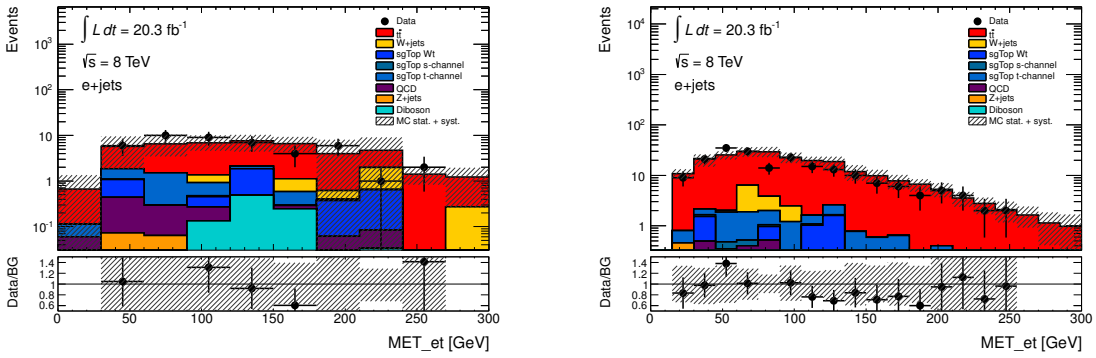

(c) B $t\bar{t}$ CR, top

(d) B $t\bar{t}$ CR, W

Figure B.13.: E_T^{miss} distributions for data and the various SM backgrounds in the $t\bar{t}$ CR in the e+jets channel. The error band includes the theory and MC statistical uncertainty and all systematic uncertainties mentioned in section 6.7.1.

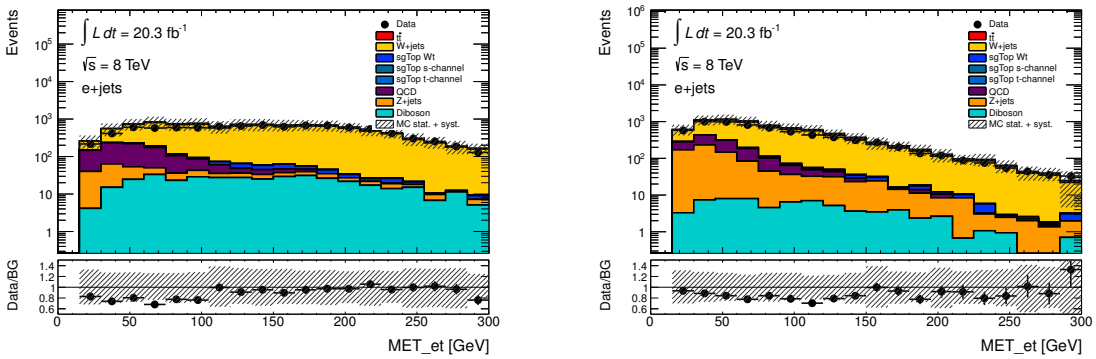

(a) b^* W+jets CR, top

(b) b^* W+jets CR, W

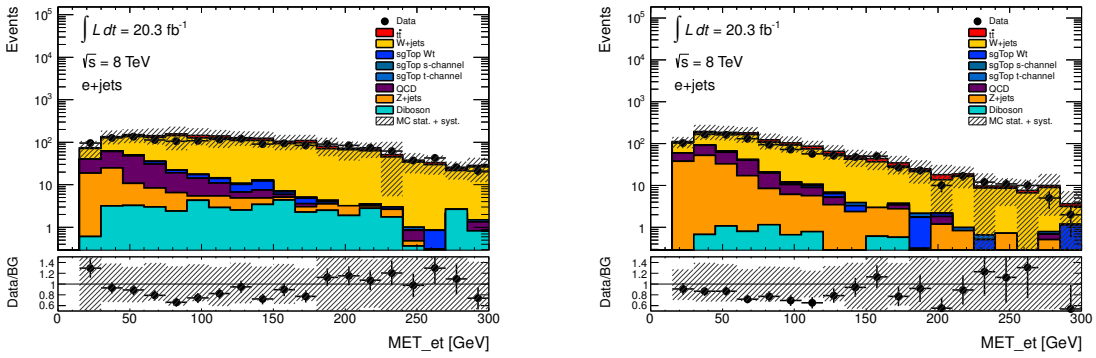

(c) B W+jets CR, top

(d) B W+jets CR, W

Figure B.14.: E_T^{miss} distributions for data and the various SM backgrounds in the W+jets CR in the e+jets channel. The error band includes the theory and MC statistical uncertainty and all systematic uncertainties mentioned in section 6.7.1.

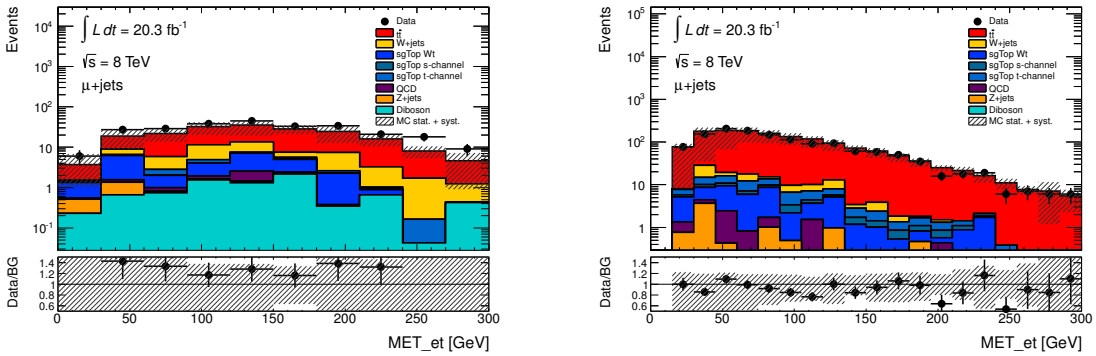

(a) b^* $t\bar{t}$ CR, top

(b) b^* $t\bar{t}$ CR, W

(c) B $t\bar{t}$ CR, top

(d) B $t\bar{t}$ CR, W

Figure B.15.: E_T^{miss} distributions for data and the various SM backgrounds in the $t\bar{t}$ CR in the μ+jets channel. The error band includes the theory and MC statistical uncertainty and all systematic uncertainties mentioned in section 6.7.1.

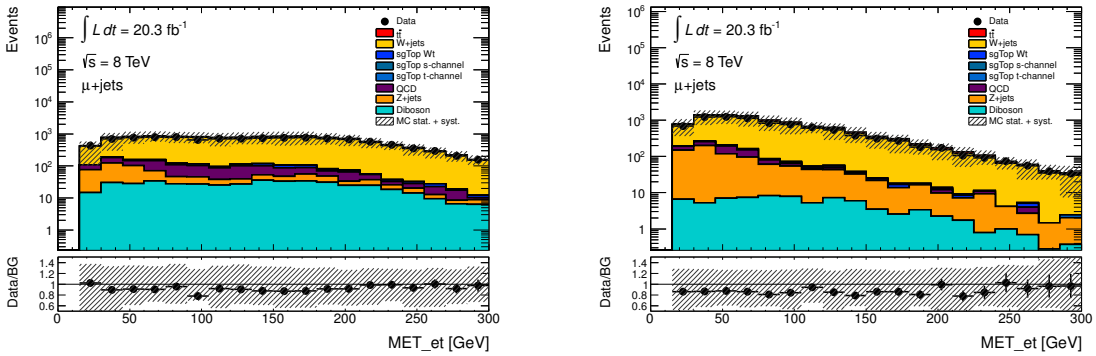

(a) b^* W+jets CR, top

(b) b^* W+jets CR, W

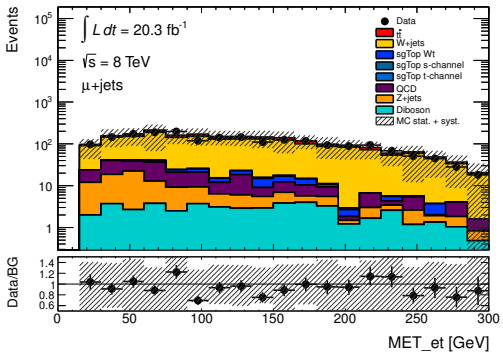

(c) B W+jets CR, top

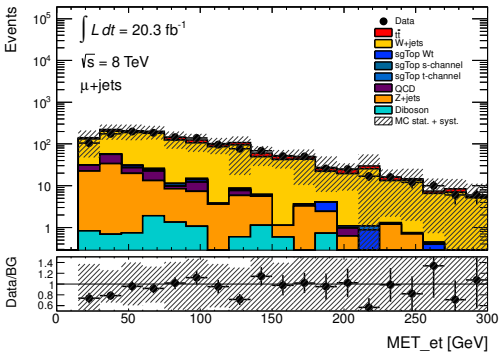

(d) B W+jets CR, W

Figure B.16.: E_T^{miss} distributions for data and the various SM backgrounds in the W+jets CR in the μ+jets channel. The error band includes the theory and MC statistical uncertainty and all systematic uncertainties mentioned in section 6.7.1.

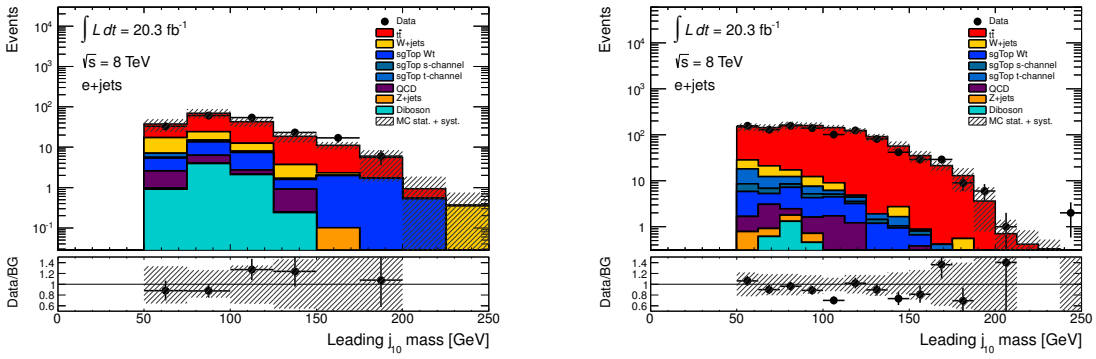

(a) b^* $t\bar{t}$ CR, top

(b) b^* $t\bar{t}$ CR, W

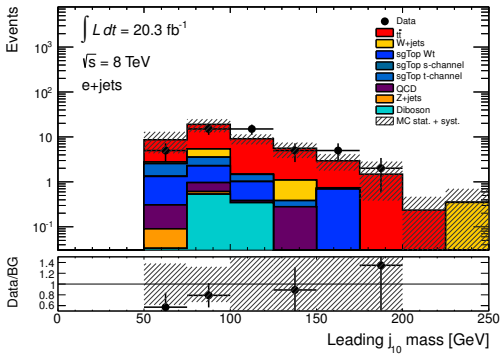

(c) B $t\bar{t}$ CR, top

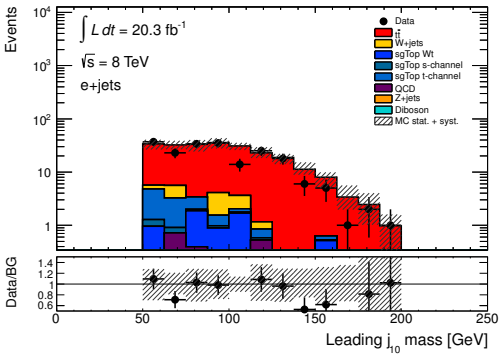

(d) B $t\bar{t}$ CR, W

Figure B.17.: Leading large-R jet p_T distributions for data and the various SM backgrounds in the $t\bar{t}$ CR in the e+jets channel. The error band includes the theory and MC statistical uncertainty and all systematic uncertainties mentioned in section 6.7.1.

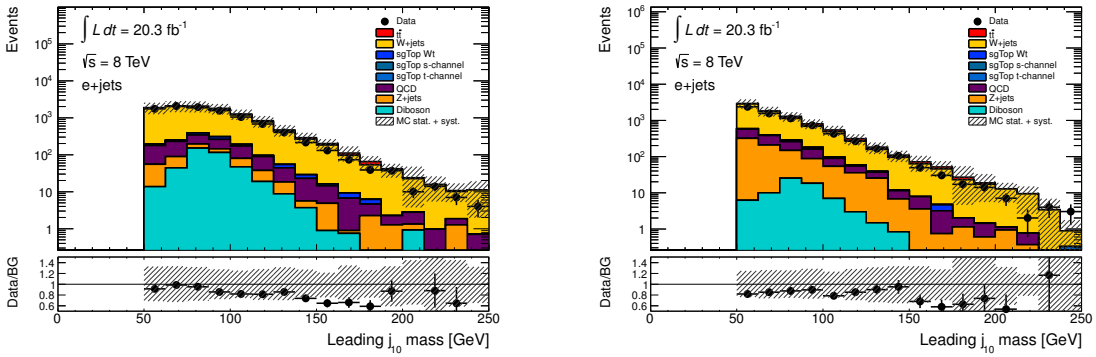

(a) b^* W+jets CR, top

(b) b^* W+jets CR, W

(c) B W+jets CR, top

(d) B W+jets CR, W

Figure B.18.: Leading large-R jet p_T distributions for data and the various SM backgrounds in the W+jets CR in the e+jets channel. The error band includes the theory and MC statistical uncertainty and all systematic uncertainties mentioned in section 6.7.1.

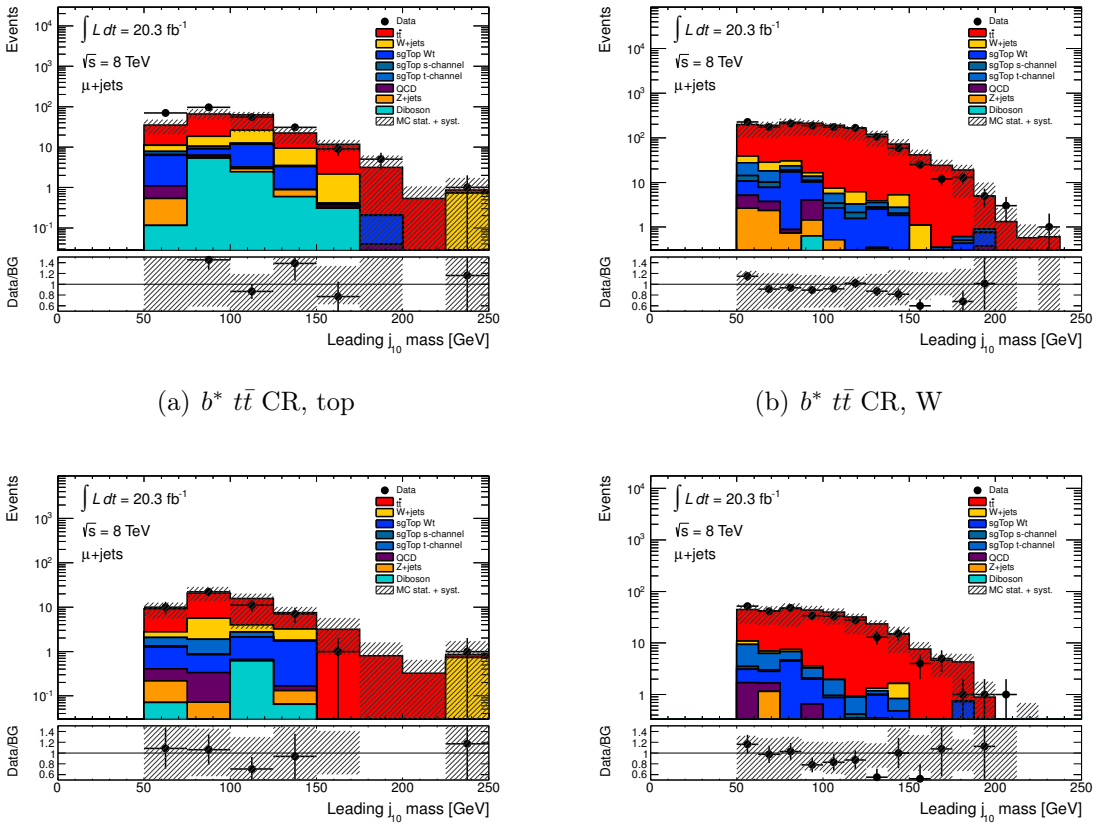

(a) b^* $t\bar{t}$ CR, top

(b) b^* $t\bar{t}$ CR, W

(c) B $t\bar{t}$ CR, top

(d) B $t\bar{t}$ CR, W

Figure B.19.: Leading large-R jet p_T distributions for data and the various SM backgrounds in the $t\bar{t}$ CR in the μ+jets channel. The error band includes the theory and MC statistical uncertainty and all systematic uncertainties mentioned in section 6.7.1.

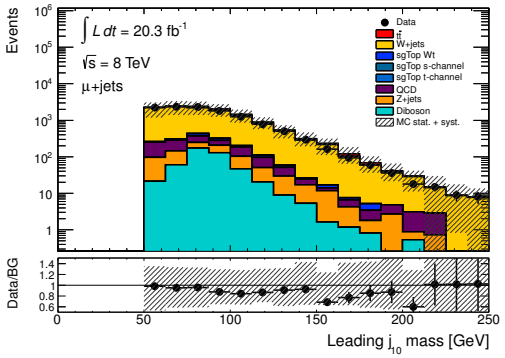

(a) b^* W+jets CR, top

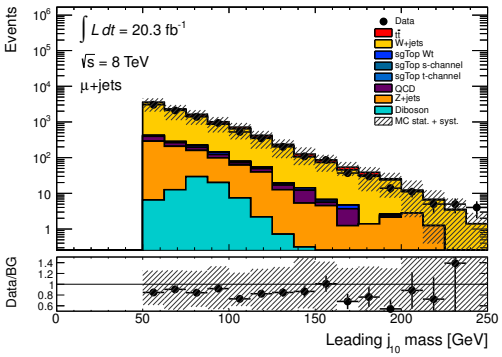

(b) b^* W+jets CR, W

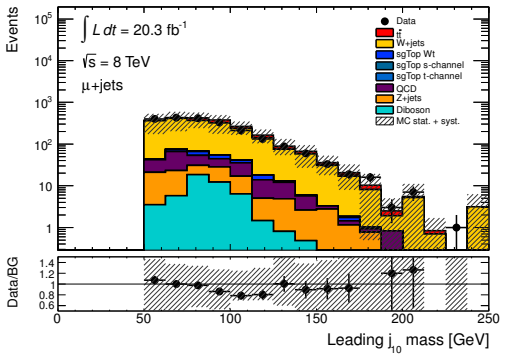

(c) B W+jets CR, top

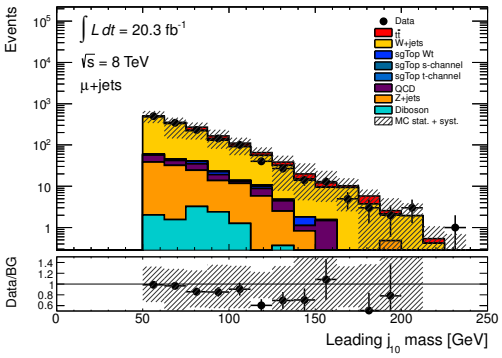

(d) B W+jets CR, W

Figure B.20.: Leading large-R jet p_T distributions for data and the various SM backgrounds in the W+jets CR in the μ+jets channel. The error band includes the theory and MC statistical uncertainty and all systematic uncertainties mentioned in section 6.7.1.

Appendix C.

Monte-Carlo Samples for Background Processes

Sample	DSID	Generator	PDF set	σ [pb]	k-factor	N_{MC}
$t\bar{t}$ (no full-had.)	117050	POWHEG+PYTHIA6	CT10	114.51	1.1992	14 996 424
Wt (DR)	110140	POWHEG+PYTHIA6	CT10	20.461	1.0933	999 692
t-channel (top)	110090	POWHEG+PYTHIA6	CT10	17.519	1.0501	4 994 481
t-channel (anti-top)	110091	POWHEG+PYTHIA6	CT10	9.3964	1.0613	4 999 879
s-channel	110119	POWHEG+PYTHIA6	CT10	1.6424	1.1067	1 199 895
$t\bar{t}$ (no full-had.)	105860	POWHEG+HERWIG	CT10	115.56	1.1883	29 960 959
$t\bar{t}$ (no full-had.)	105200	MC@NLO+HERWIG	CT10	112.94	1.2158	14 997 103
Wt	108346	MC@NLO+HERWIG	CT10	20.666	1.0825	1 999 194
$t\bar{t}$Np0 ktfac0.5 radHi (singlelept.)	201230	ALPGEN+PYTHIA	CTEQ6L1	15.017	2.0010	5 336 998
$t\bar{t}$Np1 ktfac0.5 radHi (singlelept.)	201231	ALPGEN+PYTHIA	CTEQ6L1	17.162	2.0010	6 183 996
$t\bar{t}$Np2 ktfac0.5 radHi (singlelept.)	201232	ALPGEN+PYTHIA	CTEQ6L1	12.372	2.0010	4 452 994
$t\bar{t}$Np3 ktfac0.5 radHi (singlelept.)	201233	ALPGEN+PYTHIA	CTEQ6L1	6.4212	2.0010	1 967 495
$t\bar{t}$Np4 (incl.) ktfac0.5 radHi (singlelept.)	201234	ALPGEN+PYTHIA	CTEQ6L1	4.3842	2.0010	1 530 499
$t\bar{t}$Np0 ktfac2.0 radLo (singlelept.)	201240	ALPGEN+PYTHIA	CTEQ6L1	18.995	2.0841	7 097 992
$t\bar{t}$Np1 ktfac2.0 radLo (singlelept.)	201241	ALPGEN+PYTHIA	CTEQ6L1	17.622	2.0841	6 672 995
$t\bar{t}$Np2 ktfac2.0 radLo (singlelept.)	201242	ALPGEN+PYTHIA	CTEQ6L1	10.161	2.0841	3 887 998
$t\bar{t}$Np3 ktfac2.0 radLo (singlelept.)	201243	ALPGEN+PYTHIA	CTEQ6L1	4.2490	2.0841	1 683 497
$t\bar{t}$Np4 (incl.) ktfac 2.0 radLo (singlelept.)	201244	ALPGEN+PYTHIA	CTEQ6L1	2.1198	2.0841	894 999

Table C.1.: All top-quark MC samples used in this analysis. The cross-section column includes the branching ratios but not the k-factors, which are given the next column. l indicates e, μ or τ.

Sample	DSID	Generator	PDF set	σ [pb]	k-factor	N_{MC}
$W \to e\nu$ + 0 parton	147025	Alpgen+Pythia6	CTEQ6L1	8127.3	1.1330	29 434 220
$W \to e\nu$ + 1 partons	147026	Alpgen+Pythia6	CTEQ6L1	1792.7	1.1330	48 155 904
$W \to e\nu$ + 2 partons	147027	Alpgen+Pythia6	CTEQ6L1	542.18	1.1330	17 554 347
$W \to e\nu$ + 3 partons	147028	Alpgen+Pythia6	CTEQ6L1	147.65	1.1330	4 985 287
$W \to e\nu$ + 4 partons	147029	Alpgen+Pythia6	CTEQ6L1	37.736	1.1330	2 548 292
$W \to e\nu$ + 5 partons	147030	Alpgen+Pythia6	CTEQ6L1	11.962	1.1330	799 192
$W \to \mu\nu$ + 0 parton	147033	Alpgen+Pythia6	CTEQ6L1	8127.1	1.1330	31 965 655
$W \to \mu\nu$ + 1 partons	147034	Alpgen+Pythia6	CTEQ6L1	1792.9	1.1330	43 677 615
$W \to \mu\nu$ + 2 partons	147035	Alpgen+Pythia6	CTEQ6L1	542.24	1.1330	17 611 454
$W \to \mu\nu$ + 3 partons	147036	Alpgen+Pythia6	CTEQ6L1	147.66	1.1330	4 956 077
$W \to \mu\nu$ + 4 partons	147037	Alpgen+Pythia6	CTEQ6L1	37.745	1.1330	2 546 595
$W \to \mu\nu$ + 5 partons	147038	Alpgen+Pythia6	CTEQ6L1	11.970	1.1330	788 898
$W \to \tau\nu$ + 0 parton	147041	Alpgen+Pythia6	CTEQ6L1	8127.1	1.1330	31 902 157
$W \to \tau\nu$ + 1 partons	147042	Alpgen+Pythia6	CTEQ6L1	1792.2	1.1330	48 255 178
$W \to \tau\nu$ + 2 partons	147043	Alpgen+Pythia6	CTEQ6L1	542.27	1.1330	17 581 943
$W \to \tau\nu$ + 3 partons	147044	Alpgen+Pythia6	CTEQ6L1	147.64	1.1330	4 977 982
$W \to \tau\nu$ + 4 partons	147045	Alpgen+Pythia6	CTEQ6L1	37.781	1.1330	2 548 295
$W \to \tau\nu$ + 5 partons	147046	Alpgen+Pythia6	CTEQ6L1	11.959	1.1330	789 096
$W \to l\nu + b\bar{b}$ + 0 parton	200256	Alpgen+Pythia6	CTEQ6L1	52.237	1.1330	1 599 997
$W \to l\nu + b\bar{b}$ + 1 partons	200257	Alpgen+Pythia6	CTEQ6L1	45.628	1.1330	1 398 396
$W \to l\nu + b\bar{b}$ + 2 partons	200258	Alpgen+Pythia6	CTEQ6L1	23.955	1.1330	699 398
$W \to l\nu + b\bar{b}$ + 3 partons	200259	Alpgen+Pythia6	CTEQ6L1	13.633	1.1330	398 397
$W \to l\nu + c\bar{c}$ + 0 parton	200156	Alpgen+Pythia6	CTEQ6L1	149.39	1.1330	4 299 592
$W \to l\nu + c\bar{c}$ + 1 partons	200157	Alpgen+Pythia6	CTEQ6L1	143.90	1.1330	3 987 891
$W \to l\nu + c\bar{c}$ + 2 partons	200158	Alpgen+Pythia6	CTEQ6L1	84.227	1.1330	2 394 394
$W \to l\nu + c\bar{c}$ + 3 partons	200159	Alpgen+Pythia6	CTEQ6L1	44.277	1.1330	985 295
$W \to l\nu + c$ + 0 parton	200056	Alpgen+Pythia6	CTEQ6L1	758.93	1.5200	22 769 047
$W \to l\nu + c$ + 1 partons	200057	Alpgen+Pythia6	CTEQ6L1	274.47	1.5200	8 198 769
$W \to l\nu + c$ + 2 partons	200058	Alpgen+Pythia6	CTEQ6L1	71.643	1.5200	2 090 290
$W \to l\nu + c$ + 3 partons	200059	Alpgen+Pythia6	CTEQ6L1	16.482	1.5200	499 498
$W \to l\nu + c$ + 4 partons	200060	Alpgen+Pythia6	CTEQ6L1	4.7824	1.5200	199 499

Table C.2.: All W+jets MC samples used in this analysis. The cross-section column includes the branching ratios but not the k-factors, which are given the next column. l indicates e, μ or τ.

Sample	DSID	Generator	PDF set	σ [pb]	k-factor	N_{MC}
$Z \rightarrow ee$ + 0 partons	147105	Alpgen+Pythia6	CTEQ6L1	718.97	1.1800	6 298 988
$Z \rightarrow ee$ + 1 parton	147106	Alpgen+Pythia6	CTEQ6L1	175.70	1.1800	8 169 476
$Z \rightarrow ee$ + 2 partons	147107	Alpgen+Pythia6	CTEQ6L1	58.875	1.1800	3 175 991
$Z \rightarrow ee$ + 3 partons	147108	Alpgen+Pythia6	CTEQ6L1	15.636	1.1800	894 995
$Z \rightarrow ee$ + 4 partons	147109	Alpgen+Pythia6	CTEQ6L1	4.0116	1.1800	398 597
$Z \rightarrow ee$ + 5 partons	147110	Alpgen+Pythia6	CTEQ6L1	1.2592	1.1800	229 700
$Z \rightarrow \mu\mu$ + 0 partons	147113	Alpgen+Pythia6	CTEQ6L1	719.16	1.1800	6 298 796
$Z \rightarrow \mu\mu$ + 1 parton	147114	Alpgen+Pythia6	CTEQ6L1	175.74	1.1800	8 188 384
$Z \rightarrow \mu\mu$ + 2 partons	147115	Alpgen+Pythia6	CTEQ6L1	58.882	1.1800	3 175 488
$Z \rightarrow \mu\mu$ + 3 partons	147116	Alpgen+Pythia6	CTEQ6L1	15.673	1.1800	894 799
$Z \rightarrow \mu\mu$ + 4 partons	147117	Alpgen+Pythia6	CTEQ6L1	4.0057	1.1800	388 200
$Z \rightarrow \mu\mu$ + 5 partons	147118	Alpgen+Pythia6	CTEQ6L1	1.2544	1.1800	229 200
$Z \rightarrow \tau\tau$ + 0 partons	147121	Alpgen+Pythia6	CTEQ6L1	718.87	1.1800	19 352 765
$Z \rightarrow \tau\tau$ + 1 parton	147122	Alpgen+Pythia6	CTEQ6L1	175.76	1.1800	10 669 582
$Z \rightarrow \tau\tau$ + 2 partons	147123	Alpgen+Pythia6	CTEQ6L1	58.856	1.1800	3 710 893
$Z \rightarrow \tau\tau$ + 3 partons	147124	Alpgen+Pythia6	CTEQ6L1	15.667	1.1800	1 091 995
$Z \rightarrow \tau\tau$ + 4 partons	147125	Alpgen+Pythia6	CTEQ6L1	4.0121	1.1800	398 798
$Z \rightarrow \tau\tau$ + 5 partons	147126	Alpgen+Pythia6	CTEQ6L1	1.2560	1.1800	229 799
$Z \rightarrow ee + b\bar{b}$ + 0 partons	200332	Alpgen+Pythia6	CTEQ6L1	6.5083	1.1800	1 799 992
$Z \rightarrow ee + b\bar{b}$ + 1 partons	200333	Alpgen+Pythia6	CTEQ6L1	3.2927	1.1800	999 896
$Z \rightarrow ee + b\bar{b}$ + 2 partons	200334	Alpgen+Pythia6	CTEQ6L1	1.2544	1.1800	994 594
$Z \rightarrow ee + b\bar{b}$ + 3 incl. partons	200335	Alpgen+Pythia6	CTEQ6L1	0.61711	1.1800	885 392
$Z \rightarrow \mu\mu + b\bar{b}$ + 0 partons	200340	Alpgen+Pythia6	CTEQ6L1	6.5056	1.1800	1 799 797
$Z \rightarrow \mu\mu + b\bar{b}$ + 1 partons	200341	Alpgen+Pythia6	CTEQ6L1	3.2904	1.1800	999 897
$Z \rightarrow \mu\mu + b\bar{b}$ + 2 partons	200342	Alpgen+Pythia6	CTEQ6L1	1.2601	1.1800	999 395
$Z \rightarrow \mu\mu + b\bar{b}$ + 3 incl. partons	200343	Alpgen+Pythia6	CTEQ6L1	0.61882	1.1800	880 894
$Z \rightarrow \tau\tau + b\bar{b}$ + 0 partons	200348	Alpgen+Pythia6	CTEQ6L1	6.5062	1.1800	300 000
$Z \rightarrow \tau\tau + b\bar{b}$ + 1 partons	200349	Alpgen+Pythia6	CTEQ6L1	3.2935	1.1800	100 000
$Z \rightarrow \tau\tau + b\bar{b}$ + 2 partons	200350	Alpgen+Pythia6	CTEQ6L1	1.2485	1.1800	50 000
$Z \rightarrow \tau\tau + b\bar{b}$ + 3 incl. partons	200351	Alpgen+Pythia6	CTEQ6L1	0.61363	1.1800	49 800
$Z \rightarrow ee + c\bar{c}$ + 0 partons	200432	Alpgen+Pythia6	CTEQ6L1	11.763	1.1800	284 999
$Z \rightarrow ee + c\bar{c}$ + 1 partons	200433	Alpgen+Pythia6	CTEQ6L1	7.1280	1.1800	499 500
$Z \rightarrow ee + c\bar{c}$ + 2 partons	200434	Alpgen+Pythia6	CTEQ6L1	3.3603	1.1800	498 997
$Z \rightarrow ee + c\bar{c}$ + 3 incl. partons	200435	Alpgen+Pythia6	CTEQ6L1	1.7106	1.1800	443 697
$Z \rightarrow \mu\mu + c\bar{c}$ + 0 partons	200440	Alpgen+Pythia6	CTEQ6L1	11.795	1.1800	298 998
$Z \rightarrow \mu\mu + c\bar{c}$ + 1 partons	200441	Alpgen+Pythia6	CTEQ6L1	7.1123	1.1800	499 799
$Z \rightarrow \mu\mu + c\bar{c}$ + 2 partons	200442	Alpgen+Pythia6	CTEQ6L1	3.3708	1.1800	499 500
$Z \rightarrow \mu\mu + c\bar{c}$ + 3 incl. partons	200443	Alpgen+Pythia6	CTEQ6L1	1.7059	1.1800	443 999
$Z \rightarrow \tau\tau + c\bar{c}$ + 0 partons	200448	Alpgen+Pythia6	CTEQ6L1	11.760	1.1800	299 000
$Z \rightarrow \tau\tau + c\bar{c}$ + 1 partons	200449	Alpgen+Pythia6	CTEQ6L1	7.1410	1.1800	199 998
$Z \rightarrow \tau\tau + c\bar{c}$ + 2 partons	200450	Alpgen+Pythia6	CTEQ6L1	3.3582	1.1800	99 800
$Z \rightarrow \tau\tau + c\bar{c}$ + 3 incl. partons	200451	Alpgen+Pythia6	CTEQ6L1	1.7046	1.1800	49 400
WW	105985	Herwig	CTEQ6L1	12.416	1.6833	2 499 890
ZZ	105986	Herwig	CTEQ6L1	0.99244	1.5496	245 000
WZ	105987	Herwig	CTEQ6L1	3.6666	1.9011	999 998

Table C.3.: Z+jets and diboson MC samples used in this analysis. The cross-section column includes the branching ratios but not the k-factors, which are given the next column. l indicates e, μ or τ.

Bibliography

[1] G. Aad et al. "The ATLAS Experiment at the CERN Large Hadron Collider". In: *Journal of Instrumentation* 3(08):S08003 (2008). URL: http://stacks.iop.org/1748-0221/3/i=08/a=S08003.

[2] S. Chatrchyan et al. "The CMS Experiment at the CERN LHC". In: *Journal of Instrumentation* 3(08):S08004 (2008). URL: http://stacks.iop.org/1748-0221/3/i=08/a=S08004.

[3] G. Aad et al. "Observation of a new particle in the search for the Standard Model Higgs boson with the ATLAS detector at the LHC". In: *Physics Letters B* 716.1 (2012), pp. 1 –29. ISSN: 0370-2693. DOI: http://dx.doi.org/10.1016/j.physletb.2012.08.020. URL: http://www.sciencedirect.com/science/article/pii/S037026931200857X.

[4] S. Chatrchyan et al. "Observation of a new boson at a mass of 125 GeV with the CMS experiment at the LHC". In: *Physics Letters B* 716.1 (2012), pp. 30 –61. ISSN: 0370-2693. DOI: http://dx.doi.org/10.1016/j.physletb.2012.08.021. URL: http://www.sciencedirect.com/science/article/pii/S0370269312008581.

[5] G. Aad et al. "Combined Measurement of the Higgs Boson Mass in *pp* Collisions at $\sqrt{s} = 7$ and 8 TeV with the ATLAS and CMS Experiments". In: *Phys. Rev. Lett.* 114 (2015), p. 191803. DOI: 10.1103/PhysRevLett.114.191803. eprint: 1503.07589.

[6] J. Aguilar-Saavedra. "Identifying top partners at LHC". In: *JHEP* 0911 (2009), p. 030. DOI: 10.1088/1126-6708/2009/11/030. eprint: 0907.3155.

[7] J. Nutter, R. Schwienhorst, D. Walker and J.-H. Yu. "Single Top Production as a Probe of B-prime Quarks". In: *Phys. Rev. D* 86 (2012), p. 094006. DOI: 10.1103/PhysRevD.86.094006. eprint: 1207.5179.

[8] N. Vignaroli. "Discovering the composite Higgs through the decay of a heavy fermion". In: *JHEP* 1207 (2012), p. 158. DOI: 10.1007/JHEP07(2012)158. eprint: 1204.0468.

[9] ATLAS Collaboration.
"Search for single b^*-quark production with the ATLAS detector at $\sqrt{s} = 7\,\text{TeV}$".
In: *Phys. Lett. B* 721 (2013), p. 171. DOI: 10.1016/j.physletb.2013.03.016.
eprint: 1301.1583.

[10] V. Khachatryan et al. "Search for the production of an excited bottom quark decaying to tW in proton-proton collisions at $\sqrt{s} = 8$ TeV". In: (2015).
eprint: 1509.08141.

[11] C. N. Yang and R. L. Mills.
"Conservation of Isotopic Spin and Isotopic Gauge Invariance".
In: *Phys. Rev.* 96 (1 1954), pp. 191–195. DOI: 10.1103/PhysRev.96.191.
URL: http://link.aps.org/doi/10.1103/PhysRev.96.191.

[12] E. Noether. "Invariant Variation Problems". In: *Gott. Nachr.* 1918 (1918).
[Transp. Theory Statist. Phys.1,186(1971)], pp. 235–257.
DOI: 10.1080/00411457108231446. eprint: physics/0503066.

[13] S. Weinberg. "A Model of Leptons". In: *Phys. Rev. Lett.* 19 (21 1967),
pp. 1264–1266. DOI: 10.1103/PhysRevLett.19.1264.
URL: http://link.aps.org/doi/10.1103/PhysRevLett.19.1264.

[14] Wikimedia Commons. *Standard Model of Elementary Particles*. October 2014.
URL: https://commons.wikimedia.org/wiki/File:
Standard_Model_of_Elementary_Particles.svg#/media/File:
Standard_Model_of_Elementary_Particles.svg.

[15] F. Halzen and A. D. Martin.
Quarks and leptons: an introductory course in modern particle physics. Wiley, 1984.

[16] S. L. Glashow. "Partial Symmetries of Weak Interactions".
In: *Nucl. Phys.* 22 (1961), pp. 579–588. DOI: 10.1016/0029-5582(61)90469-2.

[17] A. Salam. "Weak and Electromagnetic Interactions".
In: *Conf. Proc.* C680519 (1968), pp. 367–377.

[18] G. 't Hooft. "Renormalization of Massless Yang-Mills Fields".
In: *Nucl. Phys.* B33 (1971), pp. 173–199. DOI: 10.1016/0550-3213(71)90395-6.

[19] F. Englert and R. Brout.
"Broken Symmetry and the Mass of Gauge Vector Mesons".
In: *Phys. Rev. Lett.* 13 (9 1964), pp. 321–323. DOI: 10.1103/PhysRevLett.13.321.
URL: http://link.aps.org/doi/10.1103/PhysRevLett.13.321.

[20] P. W. Higgs. "Broken Symmetries and the Masses of Gauge Bosons".
In: *Phys. Rev. Lett.* 13 (16 1964), pp. 508–509. DOI: 10.1103/PhysRevLett.13.508.
URL: http://link.aps.org/doi/10.1103/PhysRevLett.13.508.

[21] G. S. Guralnik, C. R. Hagen, and T. W. B. Kibble.
"Global Conservation Laws and Massless Particles".
In: *Phys. Rev. Lett.* 13 (20 1964), pp. 585–587. DOI: 10.1103/PhysRevLett.13.585.
URL: http://link.aps.org/doi/10.1103/PhysRevLett.13.585.

[22] M. E. Peskin and D. V. Schroeder. *An Introduction to Quantum Field Theory.*
Westview Press, 1995.

[23] N. Cabibbo. "Unitary Symmetry and Leptonic Decays".
In: *Phys. Rev. Lett.* 10 (12 1963), pp. 531–533. DOI: 10.1103/PhysRevLett.10.531.
URL: http://link.aps.org/doi/10.1103/PhysRevLett.10.531.

[24] M. Kobayashi and T. Maskawa.
"CP-Violation in the Renormalizable Theory of Weak Interaction".
In: *Progress of Theoretical Physics* 49.2 (1973), pp. 652–657.
DOI: 10.1143/PTP.49.652.
eprint: http://ptp.oxfordjournals.org/content/49/2/652.full.pdf+html.
URL: http://ptp.oxfordjournals.org/content/49/2/652.abstract.

[25] J. Beringer et al. "Review of Particle Physics*". In: *Phys. Rev. D* 86 (1 2012),
p. 010001. DOI: 10.1103/PhysRevD.86.010001.
URL: http://link.aps.org/doi/10.1103/PhysRevD.86.010001.

[26] B. Pontecorvo.
"Neutrino Experiments and the Problem of Conservation of Leptonic Charge".
In: *Sov. Phys. JETP* 26 (1968). [Zh. Eksp. Teor. Fiz.53,1717(1967)], pp. 984–988.

[27] P. A. R. Ade et al.
"Planck 2013 results. I. Overview of products and scientific results".
In: *Astron. Astrophys.* 571 (2014), A1. DOI: 10.1051/0004-6361/201321529.
eprint: 1303.5062.

[28] S. Fajfer et al. "Light Higgs and Vector-like Quarks without Prejudice".
In: *JHEP* 07 (2013), p. 155. DOI: 10.1007/JHEP07(2013)155. eprint: 1304.4219.

[29] B. Holdom et al. "Four Statements about the Fourth Generation".
In: *PMC Phys. A* 3 (2009), p. 4. DOI: 10.1186/1754-0410-3-4. eprint: 0904.4698.

[30] A. K. Alok, A. Dighe and D. London. "Constraints on the Four-Generation Quark
Mixing Matrix from a Fit to Flavor-Physics Data". In: *Phys. Rev. D* 83 (2011),
p. 073008. DOI: 10.1103/PhysRevD.83.073008. eprint: 1011.2634.

[31] L. Randall and R. Sundrum.
"A Large mass hierarchy from a small extra dimension".
In: *Phys. Rev. Lett.* 83 (1999), pp. 3370–3373.
DOI: 10.1103/PhysRevLett.83.3370. eprint: hep-ph/9905221.

[32] S. P. Martin. "Extra vector-like matter and the lightest Higgs scalar boson mass in
low-energy supersymmetry". In: *Phys. Rev.* D81 (2010), p. 035004.
DOI: 10.1103/PhysRevD.81.035004. eprint: 0910.2732.

[33] D. B. Kaplan, H. Georgi, and S. Dimopoulos. "Composite Higgs Scalars". In: *Phys. Lett. B* 136 (1984), p. 187. DOI: 10.1016/0370-2693(84)91178-X.

[34] R. Nevzorov and A. W. Thomas. "E6 inspired composite Higgs model". In: (2015). eprint: 1507.02101.

[35] M. Schmaltz and D. Tucker-Smith. "Little Higgs review". In: *Ann. Rev. Nucl. Part. Sci.* 55 (2005), p. 229. DOI: 10.1146/annurev.nucl.55.090704.151502. eprint: hep-ph/0502182.

[36] O. Eberhardt et al. "Impact of a Higgs Boson at a Mass of 126 GeV on the Standard Model with Three and Four Fermion Generations". In: *Phys. Rev. Lett.* 109 (24 2012), p. 241802. DOI: 10.1103/PhysRevLett.109.241802. URL: http://link.aps.org/doi/10.1103/PhysRevLett.109.241802.

[37] M.-L. Xiao and J.-H. Yu. "Stabilizing electroweak vacuum in a vectorlike fermion model". In: *Phys. Rev.* D90.1 (2014). [Addendum: Phys. Rev.D90,no.1,019901(2014)], p. 014007. DOI: 10.1103/PhysRevD.90.014007,10.1103/PhysRevD.90.019901. eprint: 1404.0681.

[38] J. A. Aguilar-Saavedra. "Mixing with vector-like quarks: constraints and expectations". In: *EPJ Web Conf.* 60 (2013), p. 16012. DOI: 10.1051/epjconf/20136016012. eprint: 1306.4432.

[39] L. Panizzi and Y. Okada. "LHC Signatures of Vector-Like Quarks". In: *Advances in High Energy Physics* 2013 (2012). DOI: 10.1155/2013/364936. URL: http://www.hindawi.com/journals/ahep/2013/364936/.

[40] J. Aguilar-Saavedra et al. "Handbook of vectorlike quarks: Mixing and single production". In: *Phys.Rev.* D88.9 (2013), p. 094010. DOI: 10.1103/PhysRevD.88.094010. eprint: 1306.0572.

[41] F. del Aguila and M. J. Bowick. "The Possibility of New Fermions With Δ I = 0 Mass". In: *Nucl. Phys.* B224 (1983), p. 107. DOI: 10.1016/0550-3213(83)90316-4.

[42] O. Matsedonskyi, G. Panico, and A. Wulzer. "On the interpretation of Top Partners searches". English. In: *Journal of High Energy Physics* 2014.12, 97 (2014). DOI: 10.1007/JHEP12(2014)097. URL: http://dx.doi.org/10.1007/JHEP12%282014%29097.

[43] A. De Simone et al. "A First Top Partner Hunter's Guide". In: *JHEP* 04 (2013), p. 004. DOI: 10.1007/JHEP04(2013)004. eprint: 1211.5663.

[44] N. Vignaroli. "Δ F=1 constraints on composite Higgs models with LR parity". In: *Phys.Rev.* D86 (2012), p. 115011. DOI: 10.1103/PhysRevD.86.115011. eprint: 1204.0478.

[45] G. Aad et al. "Search for vectorlike B quarks in events with one isolated lepton, missing transverse momentum and jets at $\sqrt{s} = 8$ TeV with the ATLAS detector". In: *Phys. Rev.* D91.11 (2015), p. 112011. DOI: 10.1103/PhysRevD.91.112011. eprint: 1503.05425.

[46] V. Khachatryan et al. "Search for pair-produced vector-like B quarks in proton-proton collisions at $\sqrt{s} = 8$ TeV". In: (2015). eprint: 1507.07129.

[47] U. Baur, I. Hinchliffe, and D. Zeppenfeld. "Excited Quark Production at Hadron Colliders". In: *Int. J. Mod. Phys.* A2 (1987), p. 1285. DOI: 10.1142/S0217751X87000661.

[48] C. Lefèvre. "The CERN accelerator complex. Complexe des accélérateurs du CERN". 2008. URL: http://cds.cern.ch/record/1260465.

[49] A. A. Alves Jr. et al. "The LHCb Detector at the LHC". In: *JINST* 3 (2008), S08005. DOI: 10.1088/1748-0221/3/08/S08005.

[50] K. Aamodt et al. "The ALICE experiment at the CERN LHC". In: *JINST* 3 (2008), S08002. DOI: 10.1088/1748-0221/3/08/S08002.

[51] Wikimedia Commons. *A graphic showing the relationship between angle and pseudorapidity.* May 2007. URL: https://en.wikipedia.org/wiki/File:Pseudorapidity2.png.

[52] T. Cornelissen et al. *Concepts, Design and Implementation of the ATLAS New Tracking (NEWT).* Tech. rep. ATL-SOFT-PUB-2007-007. ATL-COM-SOFT-2007-002. Geneva: CERN, 2007. URL: http://cds.cern.ch/record/1020106.

[53] R. Fruhwirth. "Application of Kalman filtering to track and vertex fitting". In: *Nucl. Instrum. Meth.* A262 (1987), pp. 444–450. DOI: 10.1016/0168-9002(87)90887-4.

[54] ATLAS Collaboration. *Performance of the ATLAS Inner Detector Track and Vertex Reconstruction in High Pile-Up LHC Environment.* ATLAS-CONF-2012-042. 2012. URL: http://cdsweb.cern.ch/record/1435196.

[55] ATLAS Collaboration. *Performance of primary vertex reconstruction in proton–proton collisions at* $\sqrt{s} = 7$ TeV *in the ATLAS experiment.* ATLAS-CONF-2010-069. 2010. URL: http://cdsweb.cern.ch/record/1281344.

[56] G. Aad et al. "Improved luminosity determination in pp collisions at sqrt(s) = 7 TeV using the ATLAS detector at the LHC". In: *Eur.Phys.J.* C73.8 (2013), p. 2518. DOI: 10.1140/epjc/s10052-013-2518-3. eprint: 1302.4393.

[57] S. van der Meer. "Calibration of the Effective Beam Height in the ISR". In: (1968).

[58] P. Jenni et al.
ATLAS Forward Detectors for Measurement of Elastic Scattering and Luminosity.
Technical Design Report. Geneva: CERN, 2008.
URL: https://cds.cern.ch/record/1095847.

[59] M Bruschi. "The ATLAS luminosity monitor". In: *Nucl. Instrum. Methods Phys. Res., A* 623.ATL-LUM-PROC-2009-001. ATL-COM-LUM-2009-006 (2009). Deadline: April 20th 2009, 371–373. 3 p.
URL: https://cds.cern.ch/record/1171462.

[60] V. Cindro et al. "The ATLAS beam conditions monitor". In: *JINST* 3 (2008), P02004. DOI: 10.1088/1748-0221/3/02/P02004.

[61] ATLAS Collaboration.
Integrated luminosity summary plots for 2011-2012 data taking.
Geneva: CERN, 2012. URL: https://twiki.cern.ch/twiki/bin/view/AtlasPublic/LuminosityPublicResults.

[62] ATLAS Collaboration. *ATLAS Stand-Alone Event Displays.* Geneva: CERN, 2012.
URL: https://twiki.cern.ch/twiki/bin/view/AtlasPublic/EventDisplayStandAlone.

[63] A. Buckley et al. "General-purpose event generators for LHC physics".
In: *Phys. Rept.* 504 (2011), pp. 145–233. DOI: 10.1016/j.physrep.2011.03.005.
eprint: 1101.2599.

[64] G. Aad et al. "The ATLAS Simulation Infrastructure". In: *Eur. Phys. J.* C70 (2010), pp. 823–874. DOI: 10.1140/epjc/s10052-010-1429-9. eprint: 1005.4568.

[65] M. A. Dobbs et al.
"Les Houches guidebook to Monte Carlo generators for hadron collider physics".
In: *Physics at TeV colliders. Proceedings, Workshop, Les Houches, France, May 26-June 3, 2003.* 2004, pp. 411–459. eprint: hep-ph/0403045.
URL: http://lss.fnal.gov/cgi-bin/find_paper.pl?conf-04-183.

[66] A. Martin et al. "Parton distributions for the LHC". In: *Eur. Phys. J. C* 63 (2009), p. 189. DOI: 10.1140/epjc/s10052-009-1072-5. eprint: 0901.0002.

[67] J. Pumplin et al. "New generation of parton distributions with uncertainties from global QCD analysis". In: *JHEP* 0207 (2002), p. 012.
DOI: 10.1088/1126-6708/2002/07/012. eprint: hep-ph/0201195.

[68] H.-L. Lai et al. "New parton distributions for collider physics".
In: *Phys.Rev.* D82 (2010), p. 074024. DOI: 10.1103/PhysRevD.82.074024.
eprint: 1007.2241.

[69] F. Maltoni et al. "Choosing the Factorization Scale in Perturbative QCD".
In: (2007). eprint: hep-ph/0703156.

[70] T. Gleisberg et al. "Event generation with SHERPA 1.1". In: *JHEP* 02 (2009), p. 007. DOI: 10.1088/1126-6708/2009/02/007. eprint: 0811.4622.

[71] G. Corcella et al. "HERWIG 6: An Event generator for hadron emission reactions with interfering gluons (including supersymmetric processes)". In: *JHEP* 0101 (2001), p. 010. DOI: 10.1088/1126-6708/2001/01/010. eprint: hep-ph/0011363.

[72] T. Sjostrand, S. Mrenna, and P. Skands. "PYTHIA 6.4 Physics and Manual". In: *JHEP* 05 (2006), p. 026.

[73] T. Sjostrand, S. Mrenna, and P. Z. Skands. "A Brief Introduction to PYTHIA 8.1". In: *Comput. Phys. Commun.* 178 (2008), pp. 852–867. DOI: 10.1016/j.cpc.2008.01.036. eprint: 0710.3820.

[74] M. L. Mangano et al. "ALPGEN, a generator for hard multiparton processes in hadronic collisions". In: *JHEP* 0307 (2003), p. 001. DOI: 10.1088/1126-6708/2003/07/001. eprint: hep-ph/0206293.

[75] J. Alwall, M. Herquet, F. Maltoni, O. Mattelaer and T. Stelzer. "MadGraph 5 : Going Beyond". In: *JHEP* 1106 (2011), p. 128. DOI: 10.1007/JHEP06(2011)128. eprint: 1106.0522.

[76] D. Amati and G. Veneziano. "Preconfinement as a Property of Perturbative QCD". In: *Phys. Lett.* B83 (1979), p. 87. DOI: 10.1016/0370-2693(79)90896-7.

[77] S. Alioli et al. "A general framework for implementing NLO calculations in shower Monte Carlo programs: the POWHEG BOX". In: *JHEP* 1006 (2010), p. 043. DOI: 10.1007/JHEP06(2010)043. eprint: 1002.2581.

[78] S. Frixione, P. Nason, and G. Ridolfi. "A Positive-weight next-to-leading-order Monte Carlo for heavy flavour hadroproduction". In: *JHEP* 0709 (2007), p. 126. DOI: 10.1088/1126-6708/2007/09/126. eprint: 0707.3088.

[79] S. Agostinelli et al. "GEANT4: A Simulation toolkit". In: *Nucl. Instrum. Meth.* A506 (2003), pp. 250–303. DOI: 10.1016/S0168-9002(03)01368-8.

[80] M. Dobbs and J. B. Hansen. "The HepMC C++ Monte Carlo event record for High Energy Physics". In: *Comput. Phys. Commun.* 134 (2001), pp. 41–46. DOI: 10.1016/S0010-4655(00)00189-2.

[81] G. Aad et al. *Expected performance of the ATLAS experiment: detector, trigger and physics.* Geneva: CERN, 2009. URL: http://cds.cern.ch/record/1125884.

[82] G. Aad et al. "Electron performance measurements with the ATLAS detector using the 2010 LHC proton-proton collision data". English.
In: *The European Physical Journal C* 72.3, 1909 (2012). ISSN: 1434-6044.
DOI: 10.1140/epjc/s10052-012-1909-1.
URL: http://dx.doi.org/10.1140/epjc/s10052-012-1909-1.

[83] ATLAS Collaboration. *Improved electron reconstruction in ATLAS using the Gaussian Sum Filter-based model for bremsstrahlung*. ATLAS-CONF-2012-047. 2012.
URL: http://cdsweb.cern.ch/record/1449796.

[84] *Electron efficiency measurements with the ATLAS detector using the 2012 LHC proton-proton collision data*. Tech. rep. ATLAS-CONF-2014-032.
Geneva: CERN, 2014. URL: http://cds.cern.ch/record/1706245.

[85] J. Alison. "The road to discovery: Detector alignment, electron identification, particle misidentification, WW physics, and the discovery of the Higgs boson". PhD thesis. University of Pennsylvania, 2012.
URL: http://search.proquest.com/docview/1287097601.

[86] ATLAS Collaboration. *Electron reconstruction and identification efficiencies*.
ATL-COM-PHYS-2011-783. Geneva: CERN, 2012.
URL: https://atlas.web.cern.ch/Atlas/GROUPS/PHYSICS/EGAMMA/PublicPlots/20120611/ElectronEfficiency2012/ATL-COM-PHYS-2011-783/ATL-COM-PHYS-2011-783.pdf.

[87] B. Acharya et al. *Object selection and calibration, background estimations and MC samples for the Winter 2013 Top Quark analyses with 2012 data*.
Tech. rep. ATL-COM-PHYS-2013-088. Geneva: CERN, 2013.
URL: https://cds.cern.ch/record/1509562.

[88] D. Banfi, L. Carminati, and L. Mandelli.
Calibration of the ATLAS electromagnetic calorimeter using calibration hits.
Tech. rep. ATL-LARG-PUB-2007-012. ATL-COM-LARG-2007-007.
Geneva: CERN, 2007. URL: https://cds.cern.ch/record/1046248.

[89] G. Unal and D. Froidevaux.
Higgs mass measurements and uncertainties in 2011 and 2012 data.
Tech. rep. ATL-COM-PHYS-2012-1774. Geneva: CERN, 2012.
URL: https://cds.cern.ch/record/1498240.

[90] "Precision electroweak measurements on the Z resonance".
In: *Physics Reports* 427.5–6 (2006), pp. 257 –454. ISSN: 0370-1573.
DOI: http://dx.doi.org/10.1016/j.physrep.2005.12.006. URL:
http://www.sciencedirect.com/science/article/pii/S0370157305005119.

[91] R. O. Duda and P. E. Hart.
"Use of the Hough Transformation to Detect Lines and Curves in Pictures".
In: *Commun. ACM* 15.1 (Jan. 1972), pp. 11–15. ISSN: 0001-0782.
DOI: 10.1145/361237.361242.
URL: http://doi.acm.org/10.1145/361237.361242.

[92] T. Lagouri et al. "A muon identification and combined reconstruction procedure for the ATLAS detector at the LHC at CERN".
In: *Nuclear Science, IEEE Transactions on* 51.6 (2004), pp. 3030–3033.
ISSN: 0018-9499. DOI: 10.1109/TNS.2004.839102.

[93] *Muons in the Calorimeters: Energy Loss Corrections and Muon Tagging.*
Tech. rep. ATL-PHYS-PUB-2009-009. ATL-COM-PHYS-2009-153.
Geneva: CERN, 2009. URL: https://cds.cern.ch/record/1169055.

[94] M. Schott et al.
Impacts of misalignment effects on the Muon Spectrometer Performance.
Tech. rep. ATL-MUON-PUB-2007-006. ATL-COM-MUON-2007-007.
Geneva: CERN, 2007. URL: https://cds.cern.ch/record/1035445.

[95] *ATLAS muon spectrometer: Technical Design Report.*
Technical Design Report ATLAS. Geneva: CERN, 1997.
URL: https://cds.cern.ch/record/331068.

[96] ATLAS Collaboration. *Plots of Muon Performance in 2012 Data.*
Tech. rep. ATL-COM-PHYS-2012-716. Geneva: CERN, 2012.

[97] *Muon Momentum Resolution in First Pass Reconstruction of pp Collision Data Recorded by ATLAS in 2010.* Tech. rep. ATLAS-CONF-2011-046.
Geneva: CERN, 2011. URL: http://cds.cern.ch/record/1338575.

[98] F. Sforza et al. *MCP Mass Performance plots - HCP dataset 2012.*
Tech. rep. ATL-COM-MUON-2013-006. Geneva: CERN, 2013.
URL: https://cds.cern.ch/record/1517605.

[99] K. Rehermann and B. Tweedie.
"Efficient Identification of Boosted Semileptonic Top Quarks at the LHC".
In: *JHEP* 1103 (2011), p. 059. DOI: 10.1007/JHEP03(2011)059.
eprint: 1007.2221.

[100] ATLAS Collaboration. *Efficiency of the primary single muon trigger separately for L1, L2, EF -barrel region, data-.* Geneva: CERN, 2012.
URL: https://twiki.cern.ch/twiki/pub/AtlasPublic/MuonTriggerPublicResults/CHEP13_eff_L1L2EF_barrel.eps.

[101] S. Catani, Y. L. Dokshitzer, and B. Webber. "The K^- perpendicular clustering algorithm for jets in deep inelastic scattering and hadron collisions".
In: *Phys.Lett.* B285 (1992), pp. 291–299. DOI: 10.1016/0370-2693(92)91467-N.

[102] G. S. M. Cacciari G. P. Salam. "The anti-k_T jet clustering algorithm". In: *JHEP* 04(2008) (2008). URL: http://iopscience.iop.org/1126-6708/2008/04/063. DOI: doi:10.1088/1126-6708/2008/04/063.

[103] Y. L. Dokshitzer et al. "Better jet clustering algorithms". In: *JHEP* 9708 (1997), p. 001. DOI: 10.1088/1126-6708/1997/08/001. eprint: hep-ph/9707323.

[104] G. Aad et al. "Jet energy measurement and its systematic uncertainty in proton-proton collisions at $\sqrt{s} = 7$ TeV with the ATLAS detector". In: *Eur.Phys.J.* C75.1 (2015), p. 17. DOI: 10.1140/epjc/s10052-014-3190-y. eprint: 1406.0076.

[105] "Jet energy resolution and selection efficiency relative to track jets from in-situ techniques with the ATLAS Detector Using Proton-Proton Collisions at a Center of Mass Energy $\sqrt{s} = 7$ TeV". In: (2010).

[106] G. Bellettini, ed. *Jet reconstruction and spectroscopy at hadron colliders. Proceedings, Workshop, Pisa, Italy, April 18-19, 2011*. 2011. URL: http://iopscience.iop.org/1742-6596/323/1.

[107] W. Lampl et al. *Calorimeter Clustering Algorithms: Description and Performance*. Tech. rep. ATL-LARG-PUB-2008-002. ATL-COM-LARG-2008-003. Geneva: CERN, 2008. URL: https://cds.cern.ch/record/1099735.

[108] Y. A. Kulchitskii et al. *Electromagnetic Cell Level Calibration for ATLAS Tile Calorimeter Modules*. Tech. rep. ATL-TILECAL-PUB-2007-001. ATL-COM-TILECAL-2006-013. CERN-ATL-TILECAL-PUB-2007-001. Geneva: CERN, 2006. URL: http://cds.cern.ch/record/1004187.

[109] G. Aad et al. "Jet energy resolution in proton-proton collisions at $\sqrt{s} = 7$ TeV recorded in 2010 with the ATLAS detector". In: *Eur.Phys.J.* C73.3 (2013), p. 2306. DOI: 10.1140/epjc/s10052-013-2306-0. eprint: 1210.6210.

[110] *Data-Quality Requirements and Event Cleaning for Jets and Missing Transverse Energy Reconstruction with the ATLAS Detector in Proton-Proton Collisions at a Center-of-Mass Energy of sqrts = 7 TeV*. Tech. rep. ATLAS-CONF-2010-038. Geneva: CERN, 2010. URL: https://cds.cern.ch/record/1277678.

[111] *Pile-up subtraction and suppression for jets in ATLAS*. Tech. rep. ATLAS-CONF-2013-083. Geneva: CERN, 2013. URL: https://cds.cern.ch/record/1570994.

[112] A. C. on behalf of the ATLAS Collaboration. "Track reconstruction and b-jet identification for the ATLAS trigger system". In: *J. Phys. Conf. Ser.* 368 012034 (2012). URL: http://iopscience.iop.org/1742-6596/368/1/012034. DOI: doi:10.1088/1742-6596/368/1/012034.

[113] *Impact parameter-based b-tagging algorithms in the 7 TeV collision data with the ATLAS detector: the TrackCounting and JetProb algorithms.* Tech. rep. ATLAS-CONF-2010-041. Geneva: CERN, 2010. URL: http://cds.cern.ch/record/1277681.

[114] *Calibration of the performance of b-tagging for c and light-flavour jets in the 2012 ATLAS data.* Tech. rep. ATLAS-CONF-2014-046. Geneva: CERN, 2014. URL: https://cds.cern.ch/record/1741020.

[115] *Measuring the b-tag efficiency in a top-pair sample with 4.7 $fb^{-}1$ of data from the ATLAS detector.* Tech. rep. ATLAS-CONF-2012-097. Geneva: CERN, 2012. URL: http://cds.cern.ch/record/1460443.

[116] *Calibration of b-tagging using dileptonic top pair events in a combinatorial likelihood approach with the ATLAS experiment.* Tech. rep. ATLAS-CONF-2014-004. Geneva: CERN, 2014. URL: https://cds.cern.ch/record/1664335.

[117] G. Aad et al. "Performance of Missing Transverse Momentum Reconstruction in Proton-Proton Collisions at 7 TeV with ATLAS". In: *Eur.Phys.J.* C72 (2012), p. 1844. DOI: 10.1140/epjc/s10052-011-1844-6. eprint: 1108.5602.

[118] *Performance of Missing Transverse Momentum Reconstruction in ATLAS studied in Proton-Proton Collisions recorded in 2012 at 8 TeV.* Tech. rep. ATLAS-CONF-2013-082. Geneva: CERN, 2013. URL: https://cds.cern.ch/record/1570993.

[119] G. Aad et. al. *Search for the production of single vector-like and excited quarks in the Wt final state in pp collisions at $\sqrt{s} = 8$ TeV with the ATLAS detector.* Tech. rep. CERN-PH-EP-2015-235. arXiv:1510.02664. Comments: submitted to JHEP, All figures including auxiliary figures are available at https://atlas.web.cern.ch/Atlas/GROUPS/PHYSICS/PAPERS/EXOT-2014-13/. Geneva: CERN, 2015. URL: https://cds.cern.ch/record/2058159.

[120] A. Martin et al. "Uncertainties on α_S in global PDF analyses and implications for predicted hadronic cross sections". In: *Eur. Phys. J. C* 64 (2009), p. 653. DOI: 10.1140/epjc/s10052-009-1164-2. eprint: 0905.3531.

[121] G. Aad et al. "A search for $t\bar{t}$ resonances using lepton-plus-jets events in proton-proton collisions at $\sqrt{s} = 8$ TeV with the ATLAS detector". English. In: *Journal of High Energy Physics* 2015.8, 148 (2015). DOI: 10.1007/JHEP08(2015)148. URL: http://dx.doi.org/10.1007/JHEP08%282015%29148.

[122] *Estimation of non-prompt and fake lepton backgrounds in final states with top quarks produced in proton-proton collisions at $\sqrt{s}$=8 TeV with the ATLAS detector.* Tech. rep. ATLAS-CONF-2014-058. Geneva: CERN, 2014. URL: http://cds.cern.ch/record/1951336.

[123] B. Acharya et al. *Object selection and calibration, background estimations and MC samples for the Summer 2012 Top Quark analyses with 2011 data.* Tech. rep. ATL-COM-PHYS-2012-499. Geneva: CERN, 2012.

[124] ATLAS Top group. *Twiki page: TopSystematicUncertainties for 8 TeV 2012 analyses.* https://twiki.cern.ch/twiki/bin/view/AtlasProtected/TopSystematicUncertainties?rev=249. 2015.

[125] ATLAS Jet/EtMiss group. *Twiki page: Calibration recommendations for 2011 and 2012 analyses using GEO-20 MC samples and Calibration-Hits-based calibration.* https://twiki.cern.ch/twiki/bin/view/AtlasProtected/EGammaCalibrationGEO20?rev=90. 2014.

[126] ATLAS Jet/EtMiss group. *Twiki page: Scale Factors For Use in Rel 17.2 2012 Autumn and 2013 Winter analyses based on 8 TeV data.* https://twiki.cern.ch/twiki/bin/view/AtlasProtected/TopCommonScales?rev=146. 2014.

[127] G. Aad et al. "Muon reconstruction efficiency and momentum resolution of the ATLAS experiment in proton-proton collisions at $\sqrt{s} = 7$ TeV in 2010". In: *Eur. Phys. J.* C74.9 (2014), p. 3034. DOI: 10.1140/epjc/s10052-014-3034-9. eprint: 1404.4562.

[128] ATLAS Jet/EtMiss group. *Twiki page: JetEnergyResolutionProvider2012: Current preliminary tag for 2012 dataset.* https://twiki.cern.ch/twiki/bin/view/AtlasProtected/JetEnergyResolutionProvider2012?rev=10. 2014.

[129] ATLAS Jet/EtMiss group. *Twiki page: JVFUncertaintyTool.* https://twiki.cern.ch/twiki/bin/view/AtlasProtected/JVFUncertaintyTool?rev=8. 2013.

[130] ATLAS Jet/EtMiss group. *Twiki page: Twiki page: JetUncertainties2012: Moriond 2013 recommendations.* https://twiki.cern.ch/twiki/bin/viewauth/AtlasProtected/JetUncertainties2012?rev=36. 2012.

[131] A. R. Davison and I Ochoa. *Validating the ATLAS Large R-parameter Jet Mass Scale and Resolution with Hadronically Decaying Boosted W Bosons Using the 2012 Dataset.* Tech. rep. ATL-COM-PHYS-2013-865. Geneva: CERN, 2013. URL: https://cds.cern.ch/record/1557901.

[132] *Performance of large-R jets and jet substructure reconstruction with the ATLAS detector.* Tech. rep. ATLAS-CONF-2012-065. Geneva: CERN, 2012. URL: http://cds.cern.ch/record/1459530.

[133] ATLAS Flavour Tagging group. *Twiki page: Calibration Data Interface.* https://twiki.cern.ch/twiki/bin/view/AtlasProtected/BTaggingCalibrationDataInterface?rev=72. 2014.

[134] ATLAS Top group. *Twiki page: TopPdfUncertainty*. https://twiki.cern.ch/twiki/bin/view/AtlasProtected/TopPdfUncertainty?rev=36. 2015.

[135] M. Botje et al. "The PDF4LHC Working Group Interim Recommendations". In: (2011). eprint: 1101.0538.

[136] ATLAS Top group. *Twiki page: Systematics affecting Top MC for 8 TeV 2012 analyses*. https://twiki.cern.ch/twiki/bin/view/AtlasProtected/TopSystematics2012?rev=13. 2012.

[137] A. Bandyopadhyay et al. *Search for excited b^* quark and singly-produced vector-like B quarks in the Wt final state with one or two leptons*. Tech. rep. ATL-COM-PHYS-2014-1207. Geneva: CERN, 2014. URL: https://cds.cern.ch/record/1756878.

[138] M. Czakon, P. Fiedler, and A. Mitov. "Total Top-Quark Pair-Production Cross Section at Hadron Colliders Through $O(\alpha_S^4)$". In: *Phys. Rev. Lett.* 110 (2013), p. 252004. DOI: 10.1103/PhysRevLett.110.252004. eprint: 1303.6254.

[139] M. Czakon and A. Mitov. "Top++: A Program for the Calculation of the Top-Pair Cross-Section at Hadron Colliders". In: *Comput. Phys. Commun.* 185 (2014), p. 2930. DOI: 10.1016/j.cpc.2014.06.021. eprint: 1112.5675.

[140] C. Anastasiou et al. "High precision QCD at hadron colliders: Electroweak gauge boson rapidity distributions at NNLO". In: *Phys. Rev.* D69 (2004), p. 094008. DOI: 10.1103/PhysRevD.69.094008. eprint: hep-ph/0312266.

[141] C. Berger et al. "Precise Predictions for W+4 Jet Production at the Large Hadron Collider". In: *Phys. Rev. Lett.* 106 (2011), p. 092001. DOI: 10.1103/PhysRevLett.106.092001. eprint: 1009.2338.

[142] F. A. Berends et al. "On the production of a W and jets at hadron colliders". In: *Nucl. Phys. B* 357 (1991), p. 32. DOI: 10.1016/0550-3213(91)90458-A.

[143] N. Kidonakis. "Two-loop soft anomalous dimensions for single top quark associated production with a W- or H-". In: *Phys. Rev.* D82 (2010), p. 054018. DOI: 10.1103/PhysRevD.82.054018. eprint: 1005.4451.

[144] N. Kidonakis. "Next-to-next-to-leading-order collinear and soft gluon corrections for t-channel single top quark production". In: *Phys. Rev.* D83 (2011), p. 091503. DOI: 10.1103/PhysRevD.83.091503. eprint: 1103.2792.

[145] R. Barlow and C. Beeston. "Fitting using finite Monte Carlo samples". In: *Computer Physics Communications* 77.2 (1993), pp. 219–228.

[146] H. Lee et al. *Search for single B' production in the decay to Wt lepton+jets final states at $\sqrt{s} = 7$ TeV*. Tech. rep. ATL-COM-PHYS-2012-1040. Geneva: CERN, 2012. URL: https://cds.cern.ch/record/1461576.

[147] K. Nakamura et al. (PDG).
"Particle Data Group and partial update for 2012 edition".
In: *J. of Phys. G* 37 (2010), p. 075021. DOI: 10.1088/0954-3899/37/7A/075021.

[148] A. Markov. "Extension of the Limit Theorems of Probability Theory to a Sum of Variables Connected in a Chain".
In: *Dynamic Probabilistic Systems (Volume I: Markov Models)*. Ed. by R. Howard. New York City: John Wiley & Sons, 1971, pp. 552–577.

[149] K. Cranmer et al.
HistFactory: A tool for creating statistical models for use with RooFit and RooStats.
Tech. rep. 2012.

[150] A. Caldwell, D. Kollár, and K. Kröninger. "BAT–The Bayesian analysis toolkit".
In: *Computer Physics Communications* 180.11 (2009), pp. 2197–2209.

[151] G. Cowan et al. "Asymptotic formulae for likelihood-based tests of new physics".
In: *The European Physical Journal C-Particles and Fields* 71.2 (2011), pp. 1–19.

[152] G. Choudalakis.
On hypothesis testing, trials factor, hypertests and the BumpHunter. 2011.
eprint: 1101.0390.

[153] A. Bandyopadhyay, S. Mergelmeyer, and R. Zhang. private communication. 2015.

[154] "Frequentist Limit Recommendation, Draft 1.6". In: *ATLAS Statistics Forum*. 2011.

[155] LHCPhysics. "Twiki page: NNLO+NNLL top-quark-pair cross sections".
https://twiki.cern.ch/twiki/bin/view/LHCPhysics/TtbarNNLO?rev=16. 2015.

Danksagung

In den fast vier Jahren, in denen diese Dissertation entstanden ist, habe ich von vielen Seiten Unterstützung erhalten. Hierfür möchte ich mich herzlich bedanken. Insbesondere gilt dieser Dank meinem Doktorvater, Prof. Heiko Lacker, der mich in seine Gruppe aufgenommen hat, obwohl ich keinen Hintergrund in der Hochenergiephysik hatte. Die engmaschige Betreuung und die vielen Erklärungen weiß ich sehr zu schätzen, ebenso wie seine Genauigkeit in Kombination mit seinem Anspruch an die Qualität unserer Arbeit. All dies führt dazu, dass ich viel gelernt habe in meiner Zeit in dieser Gruppe. Meinem Zweitbetreuer im Graduiertenkolleg, Prof. Michael Kobel, möchte ich für die netten und produktiven Gespräche über meine Arbeit danken. Das Einbringen einer weiteren Sichtweise war an manchen Punkten sehr hilfreich. Des Weiteren möchte ich Dr. Janet Dietrich vor allem dafür danken, dass sie mir in meiner Schreibezeit den Rücken dadurch freigehalten hat, dass sie sich um das Schreiben unserer Publikation gekümmert hat. Außerdem für die vielen teils hitzigen Diskussionen, in denen ich nicht nur inhaltlich, sondern auch über mich viel lernen konnte. I would also like to thank Dr. Elin Bergeås Kuutmann for sharing knowledge and relations, but especially for providing kind and supportive words, even from abroad. Dr. Ingo Bloch möchte ich dafür danken, dass er mich zu Beginn meiner Berliner Zeit so freundlich in die Zeuthener Hardware-Gruppe aufgenommen hat, in der ich einen realistischeren und respektvolleren Blick für Detektoren entwickelt habe. Danken möchte ich außerdem dem gesamten b^*/B-Analyseteam, insbesondere Sebastian (auch für Last-Minute-Erklärungen), Anji und Rui, die meine Ergebnisse in Ausschlussgrenzen verwandelt haben. Mein Dank gilt auch allen Mitgliedern der beiden Gruppen EE1 und EE2 für viel Unterstützung auf verschiedenen Ebenen. Insbesondere möchte ich mich bei Dennis S. und Sören für die geduldige Hilfe bei technischen Problemen verschiedenster Natur bedanken, sowie bei Dustin, der mit vielen ebenfalls geduldigen Erklärungen entschieden dazu beigetragen hat, meine Defizite im Theorie-Verständnis zu reduzieren. Many thanks to my office mate Geoff for technical help, physics discussions and for being a partner in misfortune concerning Run-1 deadlines and other stuff as well as for countless fun discussions and plenty of (more or less useful) vocabulary. Ferner möchte ich meinen ehemaligen Bürokollegen Holger, Dennis W. und Rocco für die Einführung in ATLAS-, HU- und Gruppeninterna, sowie viele kurzweilige Bürogespräche danken, obwohl ich so hartnäckig daran gearbeitet habe, mit ihrer Feierabendbierkultur zu brechen. Ähnliches gilt für Patrick, der außerdem so nett war, sein Wissen um die organisatorischen Hürden bei der Abgabe einer Doktorarbeit mit mir zu teilen. Ein besonderer Dank gilt auch Veronika, der Seele der beiden Arbeitsgruppen, für die Hilfe im Bürokratiedschungel, aber vor allem für viele erhellende und lustige Gespräche in den Arbeitspausen. Ebenfalls bedanke ich mich bei Conrad und Christoph. Nicht zuletzt möchte ich meinen Eltern für ihre Unterstützung und stärkenden Worte vor allem in den Durststrecken danken. Insbesondere meine Mutter hat immer mal wieder meinen Blick auf mich selbst zurechtrücken müssen. Meinem Vater, der mit seinen Physikerklärungen in meiner Kindheit sicherlich nicht unwesentlich zu meiner Begeisterung für dieses Feld beigetragen hat, und der leider nicht an meiner Disputation teilnehmen kann, da er in meinem letzten Promotionsjahr verstorben ist, ist diese Arbeit gewidmet.